Satellites as Probes of Dark Matter and Gravitational Theories

Inauguraldissertation

zur
Erlangung der Würde eines Doktors der Philosophie
vorgelegt der
Philosophisch-Naturwissenschaftlichen Fakultät
der Universität Basel

von

Katrin Jordi

aus Huttwil, BE

Basel, 2010

Genehmigt von der Philosophisch-Naturwissenschaftlichen Fakultät

auf Antrag von

Prof. Dr. Eva K. Grebel und Dr. Michael Hilker

Basel, den 23. Juni 2009

Prof Dr. Eberhard Parlow
Dekan

Meinen Eltern

Contents

List of Figures

List of Tables

Nichts war so wie ich es mir vorgestellt hatte.

Alberto Giacometti, 1947

The Milky Way hosts ~ 150 globular clusters, and at least 17 dwarf spheroidal galaxies. These satellites experience a constantly changing gravitational field on their orbits. Close encounters with the Galactic bulge and passages through the Galactic disk enhance the effect of the constantly changing tidal field. As a consequence satellite member stars can leave their host's gravitational potential. For globular clusters, internal mechanisms, such as 2-body relaxation are also resulting in a loss of stars. Hence, the globular clusters are constantly losing stars and are being dissolved. In this thesis I investigate 17 globular cluster for signs of dissolution. I.e., we are studying the two-dimensional distribution of (potential) cluster member stars on the sky using photometric data from the Sloan Digital Sky Survey. We use a color-magnitude weighted counting algorithm to count the stars around the globular clusters. We detect the known tidal tails of Pal 5 and NGC 5466. Further, we also confirm some previous finding of possible tidal features for NGC 5053 and NGC 6341. For NGC 4147, we observe for the first time complex two-dimensional features, resembling a multiple-arm morphology. For almost all clusters in our sample we observe a halo of extra tidal stars. We observe no new large scale tidal features for our sample of clusters containing stars brighter than 22.5 mag. The lack of large scale tidal tails is compatible with theoretical predictions of the destruction timescales for the clusters in our sample.

We also observe the two-dimensional distribution of stars around three dwarf spheroidal galaxies: Sextans, Leo II, and Ursa Minor. Each galaxy reveals a unique structure. The main, luminous body of Sextans is not filling the tidal radius. We observe an off-center peak of highest stellar density. For Leo II, we observe an almost symmetric structure, compatible with the theory that Leo II has never come close to the Milky Way. We detect the complex structure of Ursa Minor, with two off-center peaks. We observe no large scale structure emanating from this dwarf galaxy. We further investigate the possibility of a line-of-sight depth of Sextans and Ursa Minor. We study the thickness of the blue horizontal branch. For Sextans, we observe an increasing thickness with increasing radius, comparable with the photometric error. Only detailed modeling will be able to show the significance of this varying thickness. For Ursa Minor, the increase in horizontal branch thickness is negligible, compared to the photometric error. Hence, Ursa Minor shows no sign of a significant line-of-sight depth. The distribution of red and blue horizontal stars was investigated for Sextans. The "red" population is much more concentrated. The peak of the density of the two populations does not coincide.

Further, we investigated one globular cluster in particular, Pal 14. This cluster is sparse and at a remote location in the Galaxy. We aim to answer the question whether Pal 14 is governed by classical or modified Newtonian dynamics. We measured the radial velocity of 17 red giant branch stars and (probable) AGB stars with UVES@ VLT and the Keck I telescope. The resulting line-of-sight velocity dispersion is comparable to the theoretical predictions for the case of classical dynamics. The predicted value for modified dynamics is about twice as large as the observed value. With HST images we derived the cluster's mass function and computed its total mass. The main sequence mass function slope is flatter than the canonical value, the cluster seems to be depleted in lower mass stars. N-body simulations predict for a given mass of the cluster its line-of-sight velocity dispersion in modified dynamics. The measured mass for Pal 14 is requiring a much larger velocity dispersion in modified Newtonian dynamics than we have measured. This leads to the conclusion that if Pal 14 is on a circular orbit, modified dynamics cannot explain the low velocity dispersion and the measured mass simultaneously.

1

Introduction

1.1 Milky Way globular clusters

A globular cluster (GC) is a gravitationally bound concentration of stars which have a common chemical and dynamical history. Today, we know of ~ 150 GCs in the Milky Way (MW) (Harris 1996). We do expect to have about 160 ± 20 GCs in our Galaxy (van den Bergh 1999). Ivanov et al. (2005) investigated the number of missing GCs by assuming a radial symmetric distribution of the GCs around the Galactic center. They concluded that at least 10 ± 3 GCs are still undiscovered. These unknown GCs are most likely located towards the Galactic center, behind the bulge or in the disk, where they are obscured by dust. All-sky infrared surveys discover new star clusters in the Galactic disk from time to time, some of which are believed to be true GCs (e.g., Kurtev et al. 2008). GCs are not only found in the MW, but also in galaxies of all Hubble types in the Universe (Brodie & Strader 2006).

Figure 1.1 shows two examples of GCs in the MW. The left panel shows Pal 1, a very sparse cluster. The right panel is an image of NGC 5272 (M3), a more "typical" GC. Both GCs are about 10 kpc away from the Sun and the two images show the same area on the sky, $7' \times 7'$. An average GC appears roughly circular in the projection on the sky, hence in three dimension it is a sphere. White & Shawl (1987) studied the appearance of 100 GCs and measured a mean ellipticity of $e = 0.07$. Only 5% of the GCs in their sample are more elongated than $e = 0.2$. A typical GC also seems to be a pure stellar system without any gas or dust. All searches for gas and dust in a GC have only resulted in upper limits for the mass of these components. These limits are usually far smaller than what one would expect due to the ongoing mass loss from evolved stars (Barmby et al. 2009). GCs contain no dark matter. Stellar population studies of a large number of GCs in the MW, the Small & Large Magellanic Clouds, and Fornax have shown that their mass-to-light ratios are comparable to the expectations of purely old single stellar populations (McLaughlin & van der Marel 2005). The usual number of stars in a GC is between 10^3 and 10^6. Therefore, GCs have an absolute magnitude in the range of $M_V = -10.4 \ldots -3.0$ mag. The size of a GC is best described by its half-light radius r_h, the radius within which it contains half of its light. Most GCs have $r_h < 10$ pc, with some exeptions like NGC 2419 ($r_h = 23.2$ pc, (Bellazzini 2007)) or Pal 14 ($r_h = 27.8$ pc, (Hilker 2006)).

Globular cluster system of the Milky Way

The stars in a GC were all born at one "instant" some $8 - 13$ Gyr ago. Marín-Franch et al. (2009) investigated the relative ages for all GCs in the MW located within ~ 20 kpc. They found two distinct populations of GCs: an old group with a relative age spread of 5% around an absolute age of ~ 12.8 Gyr, and a clearly younger group, where the absolute ages differ by ~ 0.4 Gyr and a clear age-metallicity relation was observed. The relatively younger GCs are more metal-rich than the relatively older GCs in the subpopulation. The absolute

Figure 1.1: *Left panel:* Image of Pal 1. *Right panel:* Image of NGC 5272 (M3). The two globular clusters are roughly 10 kpc distant to the Sun. Both images are taken from the Sloan Digital Sky Survey and span $7' \times 7'$.

age determination is very dependent on the choice of isochrones used (Glatt et al. 2008a). Therefore the distinction into two absolute age groups is not very straightforward.

The separation based on metallicity is a more robust method. It also reveals a bimodal distribution. There is the metal-poor group with a mean metallicity of $[Fe/H] = -1.6$ dex and a dispersion of $\sigma = 0.3$ dex, while the metal-rich group has a mean of $[Fe/H] = -0.6$ dex and dispersion of $\sigma = 0.2$ dex (Harris 2001). These two populations are not only distinct in their metallicity but also in their kinematics and spatial distribution (Zinn 1985). The metal-rich GCs form a subsystem with a smaller spatial extent and are associated with the Galactic bulge. They form a subsystem which resembles a flattened bulge population. The metal-poor GCs are distributed as far as the edge of the Galaxy in a spherical population. Investigating the rotation of these two subpopulation reveals even more subpopulations. The metal-rich GCs can be divided in two groups: an inner $(0-4$ kpc) bulge-like group with a rotation speed of $v_{rot} \sim 90$ km s^{-1}, and an outer $(4-8$ kpc) thick-disk-like group with $v_{rot} \sim 150$ km s^{-1}. The metal-poor GCs have no net rotation, but the most metal-poor clusters ($[Fe/H] < -1.7$ dex) show a prograde rotation with $v_{rot} \sim 80-100$ km s^{-1}. Individual clusters have a retrograde orbit. These kinematic information are all taken from the Saas-Fee course summary by Harris (2001). Some GCs are known to have been "donated" by accreted dwarf galaxies, e.g., Sagittarius contained initially several GCs which are now members of the Galactic GC system (Da Costa & Armandroff 1995; Bellazzini et al. 2003).

Color-magnitude diagram

Today for the majority of the GCs in the Galaxy multi-band images exist and the properties of the GCs' stellar component have been studied in great detail. The color-magnitude diagram (CMD) of a GC has a distinct appearance. In Figure 1.2 we show a sample CMD of NGC 5272. The prominent features are the main sequence (MS), the red giant branch (RGB), the red and blue horizontal branch (RHB, BHB) and the asymptotic giant branch (AGB). The CMD demonstrates that the GC contains only one stellar population. All the stars were born at the same time and they only differed in their initial mass. This difference led to differences in the
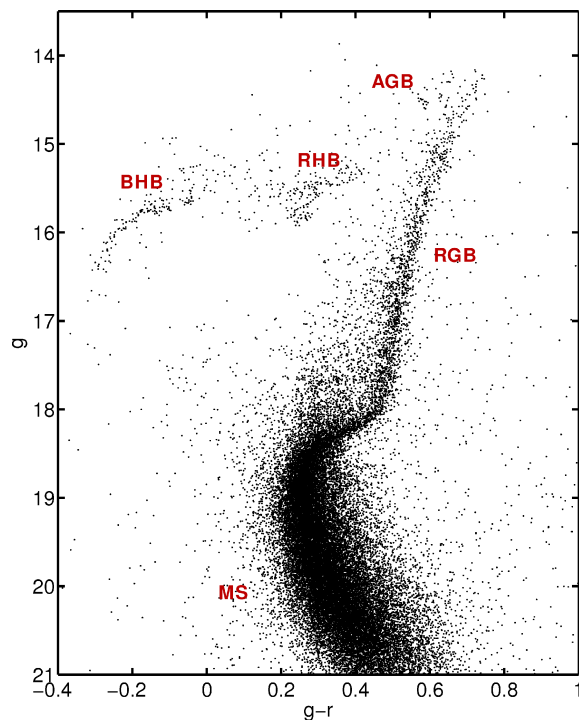
Figure 1.2: Color-magnitude diagram of NGC 5272. The prominent features typical for a GC CMD are labeled: main-sequence (MS), red giant branch (RGB), asymptotic giant branch (AGB), red and blue horizontal branch (RHB, BHB). The data is taken from the Sloan Digital Sky Survey and from An et al. (2008).

time spent on the MS burning hydrogen. The more massive stars evolved faster away from the MS towards the RGB. Hence, the turnoff point, in our example roughly at $g - r = 0.3$ mag, $g = 18.5$ mag, is an indicator of cluster age (e.g., Glatt et al. 2008b).

For some GCs, particularly those with large masses, multiple main sequences, subgiant branches or RGBs have been observed, calling the single stellar population paradigm into question (see Piotto (2009) for a summary of the observations). In the case of NGC 5272 this cannot be excluded, as the MS is very broad due to photometric errors. The stars shown in Figure 1.2 were only selected by position on the sky and no foreground subtraction was done.

Luminosity & mass function

To construct a CMD of a GC is a "simple" task, especially because at the location of the GC itself cluster member stars are outnumbering potential contaminants. The typical features are observable although not all observed stars are cluster members. As well as examining the CMD one can also investigate how many stars occupy each region of a CMD. The number of stars of different types tells us something about the efficiency at which stars with different luminosity (hence stellar types) were formed. The construction of a luminosity function is not as straight forward as the construction of the CMD was, since for the luminosity function source confusion plays a much bigger role. The luminosity function Φ is defined as follows: $dN = -\Phi(M)dM$, where dN is the number of stars with absolute magnitudes in $(M, M + dM)$.

The true luminosity function Φ is never observed. First, the observations have a detection limit in luminosity, implying that stars fainter than this minimum magnitude are not observed. Second, in the center of a GC stars might be projected onto each other. E.g., a

bright star in front might hide a fainter star behind it. Third, in GC centers stars are packed very tightly. Magnitudes of single stars in crowded fields are affected by higher uncertainties and faint stars in particular will not be detected. Overall, mainly faint stars go uncounted and have to be added to the observed luminosity function. Fourth, foreground stars have to be eliminated from the observed luminosity function, as only the distribution of cluster member stars is of interest. The observed luminosity function Φ_{obs} has to be corrected for all the effects mentioned above. Nevertheless, these corrections are mostly straightforward and they increase the error on the number of stars per magnitude bin. Luminosity functions of different GCs can be compared, but different GC metallicities complicate the comparison. The luminosity of a single star depends on its metallicity, therefore also the luminosity function is a reflection of the overall metallicity of the cluster. There is also a variation of the luminosity function within a GC. Due to 2-body relaxation the higher mass stars sink to the cluster center, whereas lower mass stars are left in the cluster halo. A phenomenon called mass segregation. As a consequence the luminosity function measured in the cluster center shows more bright stars compared to faint stars. The luminosity function in the cluster's outer parts has fewer bright stars compared to the faint stars (e.g., Koch et al. 2004).

From the corrected Φ_{obs} we can derive the present-day mass function Ξ, $dN = \Xi(m)dm$, (dN is the number of stars with masses in the mass interval $(m, m + dm)$), of a GC:

$$\Xi(m) = -\Phi(M)(dm/dM)^{-1} \qquad \boxed{1.1}$$

This derivation strongly depends on the assumed mass-luminosity relation. Any uncertainty in the assumption on stellar structure and evolution, as well as on the observed mass-luminosity data influences the resulting mass function. The mass-luminosity relation depends on the star's metallicity, its age, and also its rotation. Stars are brighter if they contain less metals than the Sun. Stars on the main sequence brighten with time and lose mass. Rotation dims a star (depending on the inclination angle). A debate is still going on whether initially all star clusters have the same mass function regardless of the differences their initial molecular clouds inhibited. See Kroupa (2002) for a detailed discussion on the universality of the initial mass function.

In a GC the present day mass function Ξ is not equal to the initial mass function (IMF) (but also see Paresce & De Marchi 2000). The higher mass stars evolved faster and lost most of their mass, the highest mass stars already became white dwarfs or neutron stars. In the low mass regime the present day mass function might still resemble or even be equal to the IMF. Besides stellar evolution, the dynamical evolution of the GC influences the mass function. This leads preferentially to the loss of low mass stars (Baumgardt & Makino 2003; Koch et al. 2004), therefore also the low mass end of the present day mass function evolved away from the IMF. In summary, mass segregation plus evaporation transform the IMF of the inner and outer parts of a GC into the present day mass function.

Radial density profile

Here, the distribution of stars within a GC is discussed. As said before, the GCs are mostly spherical, i.e., their distribution of light is specified by the radial brightness profile. The distribution of single stars is represented by a radial number density profile. Usually, for the outer parts of a GC, where crowding is not an issue, single stars are summed up to a number density profile or their brightnesses are added to a surface brightness profile. The fraction of contamination due to the foreground field stars can be estimated by measuring density of the field stars sufficiently far away from the cluster. This number can then be subtracted from the observations. In the central parts single stars can not easily be resolved. Therefore the
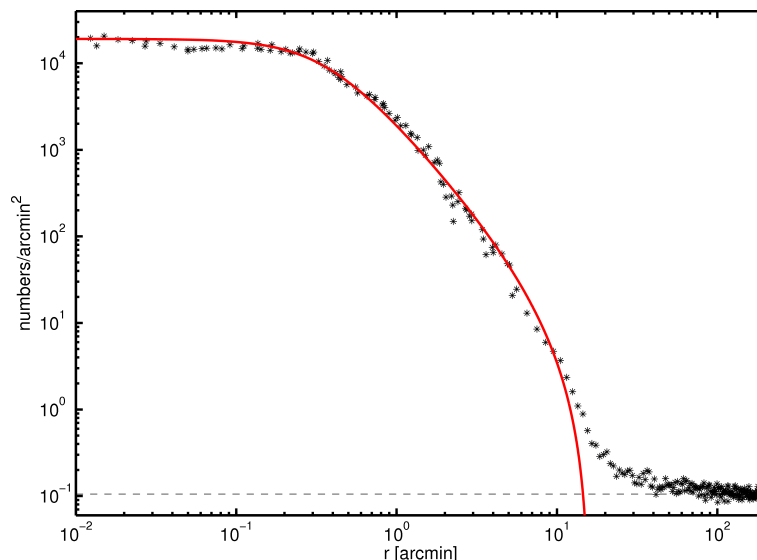
Figure 1.3: Number density profile of NGC 5024. The horizontal line is the measured background. The red line is a fitted King model.

integrated light is measured to obtain a radial profile. The light is always dominated by the very few bright stars.

In Figure 1.3 the number density profile of NGC 5024 is shown. This profile is a combination of number counts in the outer parts (this work) and integrated photometry in the center (Trager et al. 1995). The profile traces the distribution of stars from the center to the outer most points. Outside of $r \approx 80'$ the flat background of the field stars is observed. The transition from the declining cluster profile to the flat background is smooth and not sudden. The red line is a King profile (King 1962) overlaid onto the data points:

$$f_K(r) = k \cdot \left(\frac{1}{\sqrt{1 + (r/r_c)^2}} - \frac{1}{\sqrt{1 + (r_t/r_c)^2}} \right)^2 + b, \qquad \boxed{1.2}$$

where r_c is the core radius, r_t is the limiting (tidal) radius, k is a constant and b parametrizes the background. The core radius, r_c, is defined as the value of r at which the projected surface brightness is about half of its central value. At the tidal radius, r_t, the surface brightness has dropped to zero. In reality this value is never reached, because the field star background starts to dominate the surface brightness profile. The concentration c of a GC is given by $c = \log(r_t/r_c)$. The King profile in equation 1.2 is an empirical description of the distribution of light from stars in a spherically symmetric system. In contrast, King models (King 1966) are physically motivated models for the case of densely populated GCs placed in an external tidal field. These models evolve naturally to the profile shown in equation 1.2. The King profile is applicable to relaxed systems, like GCs. The King profile makes the assumption that the most energetic stars have already left the cluster's tidal field. This leads to a tidal truncation of the GC at a finite radius, the tidal radius,r_t.

Observations already have shown that the change from the cluster profile to the background is a smooth variation of the slope of the profile. This implies that there are constantly stars leaving the cluster. As the cluster orbits the galaxy the external tidal field is constantly changing, hence the limiting radius is also constantly changing. The current observations are not representative of the entire cluster orbit. The overabundance of stars around the current tidal radius is interpreted as a halo of extra-tidal stars. These stars might leave the cluster

or at the next apogalacticon these stars might become bound members again.

1.2 Dynamical evolution of globular clusters

GCs are the oldest stellar systems in our Galaxy. They were, very likely, born during the early formation of the MW and should still have information of these ancient times hidden in their orbital information. E.g., their global dynamics should give clues to these early formation times. In this Section the dynamical evolution of a GC in an external tidal field is discussed. Numerous N-body simulations have studied the evolution of a GC (e.g., Vesperini & Heggie 1997; Baumgardt & Makino 2003). Internal and external processes drive the dynamical evolution and the resulting mass loss in a GC. The internal processes to consider are: stellar evolution, 2-body relaxation, more-body encounters, core collapse, cluster re-expansion due to the 2-body relaxation, formation and destruction of binary systems. The external processes are: tidal disruption, disk & bulge shocking. The different processes act on different time scales and also at different points in time after the cluster's formation. The relaxation time in a GC is of the order of $t_{rel} \approx 10^8$ yr. I.e., after this time the cluster has lost all memory of its initial internal dynamical state. The crossing time $t_{cr} \approx 10^6$ yr, the time it takes one star to move across the GC. Within the lifetime of a typical GC, a star crosses several times, hence stellar encounters play a significant role in its dynamical evolution.

Stellar evolution is the main driver of the cluster's evolution right after formation. High mass, early type stars lose a large fraction of their mass, either by strong winds, ionization or in supernova explosions. Such a "instantaneous" gas expulsion reduces the binding energy of the initial system and suddenly stars that have remained in place have velocities higher than the local escape velocity and leave the cluster. This sudden mass loss might disrupt the entire cluster, a.k.a. infant mortality (Geyer & Burkert 2001; Kroupa 2001). The star formation efficiency, the rate at which the gas is removed and the strength of the external tidal field have a big influence on the survival of the cluster (Baumgardt & Kroupa 2007). If the cluster survives, it is expanding by up to a factor of 4. The external tidal field has only an influence on the GCs evolution if the ratio r_h/r_t is larger than 0.05, where r_h is the half-mass radius, the value within which half of the cluster's mass is found [1]. In Figure 1.4 the evolution of the bound mass is shown for a GC on an eccentric orbit (Baumgardt & Makino 2003). Right after the cluster's formation the loss due to stellar evolution is the main influence.

Evaporation due to 2-body relaxation redistributes the energy between stars, resulting in a mass segregated cluster: high-mass stars will sink to the cluster center and low-mass stars populate the cluster halo. If a star gains enough energy it eventually leaves the potential of the cluster and drifts into the host galaxy's stellar field. It is important to note that stars which gain enough energy to leave the cluster do not instantly leave. Stars can only leave the cluster at the Lagrange points L1 and L2. E.g., these stars usually cross within the cluster several times before leaving at one of these two points or maybe even never leaving the cluster (Fukushige & Heggie 2000).

For GCs on eccentric orbits the perigalactic passage is a place of enhanced mass loss. At this point on the orbit the stars at the tidal radius gain much energy from the varying external tidal field. Most of these stars are stripped away. The bound mass of the cluster decreases. As the cluster moves outward on its orbit, the tidal radius expands and the stars outside the perigalactic tidal radius are bound again, the cluster mass increases. In this phase the cluster will occupy a larger volume. The expansion is driven by relaxation (Baumgardt & Makino 2003). The distribution of lost stars has been modeled by various authors. Figure 1.5 shows

---

[1]r_h can also denote the projected half-light radius, the value within which half of the cluster's luminosity is encompassed. This is more the observer's variable, where as the 3d-half-mass radius is a theoretician's value.
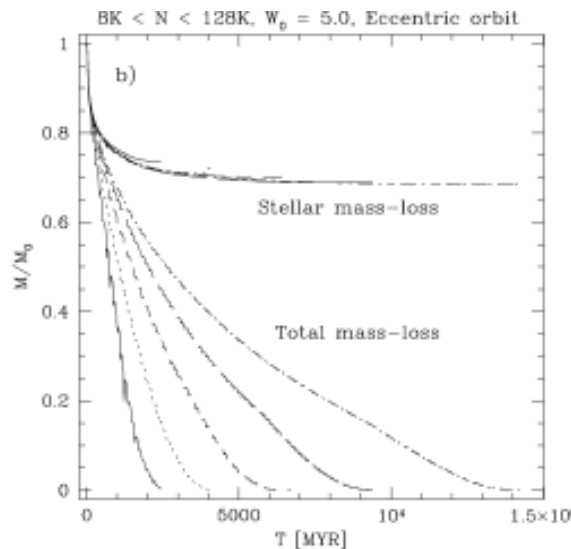
Figure 1.4: Simulated evolution of the bound mass of a GC on an eccentric orbit. The upper curves show the stellar mass loss from bound stars. (Baumgardt & Makino 2003, Fig. 1)

one example of Capuzzo Dolcetta et al. (2005). It illustrates how tidal tails form and how they are oriented with respect to the GC's orbit. In Section 2.1.1 the formation of tidal tails is explained in more detail.

As already mentioned above, relaxation segregates stars of different masses within the cluster. The heavier stars sink to the cluster center. The radius containing 90% of the cluster mass expands due to the growth of the halo as a consequence of the relaxation process in the cluster core. At the same time the radius containing 10% of the mass decreases. Hence the central density of the cluster grows. It even seems that the central density could become infinite in a finite time (the core collapse). The formation of binaries, either through two- or three-body encounters leads to an eventual reversal of the core collapse into a core expansion. In the post-core-collapse phase the GC undergoes gravothermal oscillations. Whether an individual GC is in the pre- or post-core-collapse phase is observationally determinable from the cluster's radial density profile. In Figure 1.6 the surface brighness profiles of NGC 7078 and NGC 7089 are shown. For NGC 7078, the density towards the center is constantly increasing. NGC 7078 is in the post-collapse phase. In the case of NGC 7089 a flat core is observed, the cluster is in the pre-collapse phase. For a detailed discussion of all effects influencing the dynamical evolution of a GC see Spitzer (1987); Heggie & Hut (2003).

So far the N-body simulations here only considered the baryonic matter content of the host galaxy to account for the external tidal field. Praagman et al. (2009) made simulations including a static dark matter halo in addition to the standard baryonic disk and bulge. GCs lose mass faster if the DM halo is considered. The increase of the mass loss is bigger for larger, and more concentrated DM halos.

1.3 Dwarf spheroidal galaxies

Today, nine dwarf spheroidal (dSph) galaxies around the Milky Way are known with absolute magnitudes brighter than $M_V = -8$ mag (Mateo 1998), these are the classical dSph galaxies. In the last three years, eight new dSph galaxies have been found in the vicinity of the MW which are all fainter than $M_V = -8$ mag. The study of the new, ultra-faint dSphs is based
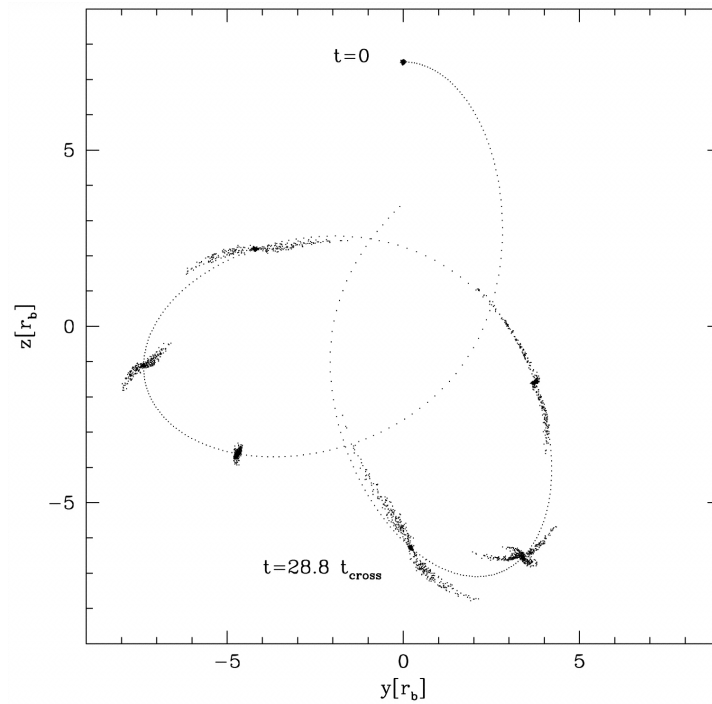
Figure 1.5: Simulation of a globular cluster in our Galaxy. Tidal tails are forming. (Capuzzo Dolcetta et al. 2005, Fig. 8)
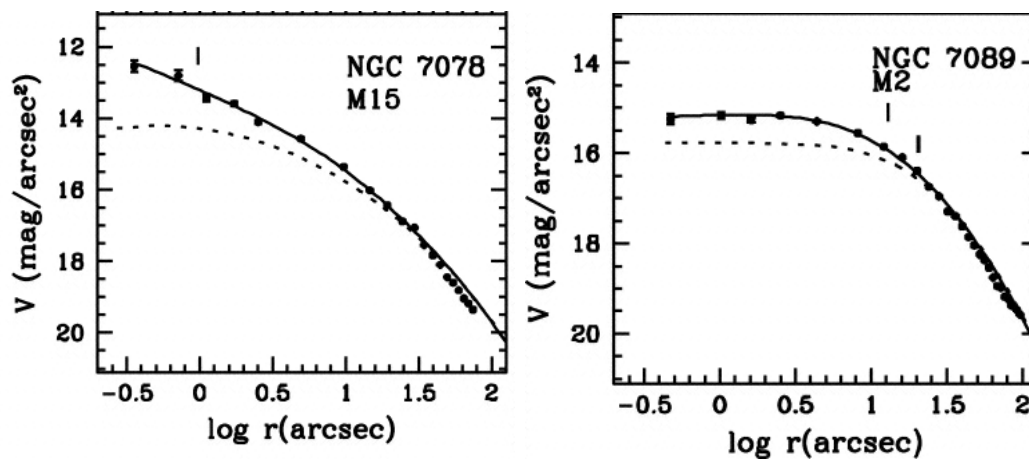
Figure 1.6: Surface brightness profile of NGC 7078 and NGC 7089. NGC 7078 is in the post-core-collapse phase, NGC 7089 in the pre-core-collapse phase. (Noyola & Gebhardt 2006, Fig. 7)

Figure 1.7: *Left panel:* Image of Leo I spanning $13' \times 13'$. *Right panel:* Image of Leo II spanning $7' \times 7'$. Both images are taken from the Sloan Digital Sky Survey.

on only a small number of stars for each galaxy. Therefore, the following characteristics of dSph galaxies are certainly true for the classical dSphs. These might not be fully true for the ultra-faint dSphs, because they have just become the aim of many observations and theoretical investigations. Figure 1.7 shows the dSph galaxies Leo I (left panel) and Leo II (right panel) as two examples of the classical dSphs. The typically low surface brightness $(\mu_{V,0} > 22$ mag arcsec$^{-2})$ of these objects is clearly visible.

DSph galaxies are essentially free of gas and dust (Mateo 1998; Grcevich & Putman 2009). They contain hardly any stars younger than ~ 2 Gyr. In all classical dSphs RR Lyrae stars are found, i.e., these systems began to form stars at least 10 Gyr ago. Main sequence age dating showes that these galaxies are actually as old as the oldest MW GCs (Grebel & Gallagher 2004). The total luminosity of dSphs is comparable to the total luminosity of GCs, but the galaxies are much more extended. DSphs are not a different kind of star cluster. Indeed some of them have globular clusters of their own, e.g., Fornax (Hodge 1961) and Sagittarius (Bellazzini et al. 2003b). A further difference to GCs, dSph galaxies did not form all their stars at one point in time. They experienced star formation over several gigayears, from gas with differing metallicities (Smecker-Hane et al. 1996). For each dSph galaxy the star formation history is unique (Grebel 1997). In a number of dSphs a population gradient has been observed, such that red HB stars are more centrally concentrated than blue HB stars (Harbeck et al. 2001). The general explanation for this trend is the deeper central potential well, in which the gas is retained for longer, allowing the star formation to continue for a longer period in the center compared to the outer regions.

Dark matter dominated?

According to standard stellar population models the mass-to-light ratio of a stellar system is expected to be ~ 2. I.e., the system is composed of only stars. But dSph galaxies have larger observed mass-to-light ratios, $\mathcal{M}/\mathcal{L} = 6 - 100 \, (\mathcal{M}/\mathcal{L})_\odot$ (Mateo 1998), impling that the dSph galaxies have a large DM content. At the same time for some Milky Way dSphs extratidal features were found (Palma et al. 2003, e.g.,). While having a large DM content today it is unlikly that tidal effects are observable in the galaxy's luminous matter. Different theories

were proposed to explain the large $\mathcal{M}/\mathcal{L}$ and the tidally shaped structure, simultaneously. Different mechanisms were proposed which artificially increase the velocity dispersion[2]: binaries (e.g., Kleyna et al. 2002), velocity jitter of the giant stars (e.g., Bizyaev et al. 2006; Carney et al. 2003). But these authors showed that these effects are not responsible for the large dispersion value. Another explanation questioned the assumed virial equilibrium. Extreme models proposed the dSphs to be in complete or near complete tidal disruption and their appearance is an artifact of other dynamical processes. In these explanations no DM is necessary (Fleck & Kuhn 2003).Today, for each classical dSph galaxy the spectra of several hundred red giants have been measured. The derived radial velocities and velocity dispersion profiles give insight into the internal kinematics of these galaxies. These measurements supported the earlier findings that dSphs are DM dominated, e.g., Ursa Minor (Wilkinson et al. 2004; Muñoz et al. 2005), Sextans (Walker et al. 2006), or Leo II (Koch et al. 2007).

An alternative explanation for the flat dispersion profiles and the measured large central velocity dispersion was proposed by Kroupa (1997) and Klessen & Kroupa (1998). The internal kinematics might be influenced by the tidal torques the dSph galaxy experiences on its orbit around the MW. Therefore the virial equilibrium, assumed in the above determinations, is not true anymore. The general idea of this "tidal scenario" is that the remnant of the satellite galaxy contains only a few percent of the initial mass and prevails as a long-lived and distinguishable entity for several billion years. Kroupa (1997) and Klessen & Kroupa (1998) proposed that what we observe as a bound dSph galaxy might in fact be the an unbound remnant of a tidally disrupted satellite galaxy on an eccentric orbit. In this way the high velocity dispersion is obtained without any DM. This model predicts a large spread in stellar distances along the line of sight. Klessen & Zhao (2002) suggested using the HB of the dSph galaxy to test for the depth extent. Klessen et al. (2003) investigated the width of the blue HB of Draco and concluded that the predicted increase of HB thickness with increasing radius was not observed. Therefore, Draco is not a remnant of a disrupted satellite.

Although for Draco the "tidal scenario" was excluded, for other dSphs it might still be possible. Meanwhile, the models describing dSph galaxies usually assume the galaxies to be bound objects, but they also have to incorporate the presence of unbound stars. Unbound material has been found for some dSphs, e.g., Ursa Minor (Martínez-Delgado et al. 2001; Palma et al. 2003; Muñoz et al. 2005) or Carina (Muñoz et al. 2008). The Sagittarius dwarf galaxy is a unique case in the vicinity of the MW. It is currently being accreted by the MW (Ibata et al. 1994; Majewski et al. 2003). The remaining parts resemble a dSph galaxy, but were initially a different type of dwarf galaxy. Unbound material of Sagittarius has been found all over the sky (Majewski et al. 2003; Belokurov et al. 2006).

Peñarrubia et al. (2008) performed N-body simulations where dSphs are composed of a stellar component within a DM halo. They showed that the galaxy's luminous radial density profile is very resilient to tides. First the DM halo is stripped, before the luminous component is affected by the tides. On the other hand, DM-dominated-mass-follows-light models describe the dSph galaxies as luminous component within a DM halo, but which is affected by tides Muñoz et al. (2008). The true nature of the dSphs is not yet uncovered and the amount and distribution of DM in these galaxies is a subject of ongoing study.

1.4 Modified Newtonian dynamics

In Figure 1.8 the rotation curve of the Milky Way is shown out to ~ 60 kpc. The measured data points show only a slight decline towards larger radii. The solid line is the best fit

---

[2]The mass of a dSph is not an observable quantity as the luminosiy (light) is. But the mass is connected to the velocity dispersion via the viral theorem: $\sigma^2 = GM/r$.
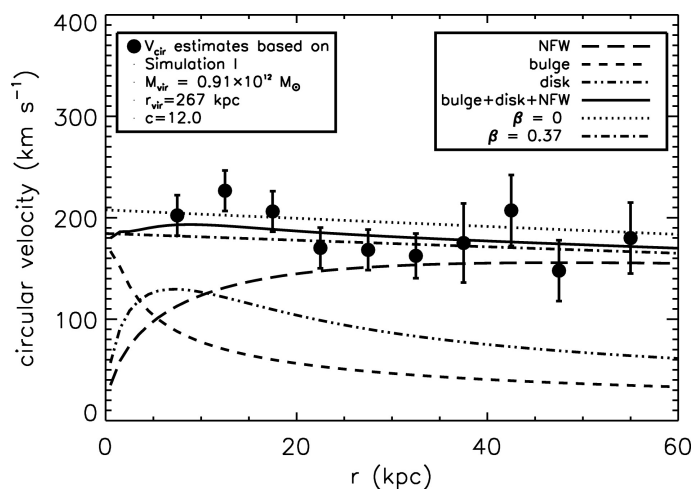
Figure 1.8: Rotation curve of the Milky Way from Xue et al. (2008, Fig. 16a). The black dots are the estimated circular velocities, the solid line is the best fit model.

circular velocity model. The short dashed line is the contribution of the Galactic bulge, the dash-dotted line the contribution of the Galactic disk. These two components show the typical Keplerian fall-off for increasing radii, as an observer expects from the distribution of baryonic matter in the Galaxy. The sum of the two baryonic components cannot fully reproduce the observed (roughly) flat curve. The flat rotation curve of the Milky Way is not a special case, it is an example of a typical rotation curve of a spiral galaxy in the Universe (Sofue & Rubin 2001). The observed mass in stars, gas and dust is not sufficient for spiral galaxies to have flat rotation curves in their outer parts.

A possible explanation is the introduction of a new kind of matter - dark matter (DM). DM only interacts with the ordinary (baryonic) matter by gravitational interaction. DM itself is believed to be not self-interacting, in contrast to baryonic particles. In the outer regions of spiral galaxies the amount of DM is larger than the amount of baryonic matter, therefore the total mass is larger than the observable mass and the rotation curves are flat. The standard general solution is that disk galaxies are embedded in massive DM halos.

In large clusters of galaxies, the mass inferred via the classical Newtonian virial theorem is very large compared to the mass seen directly as galaxies and intra-cluster gas (Zwicky 1933, 1937). This mass discrepancy is also observed when the cluster mass is determined by gravitational lensing in the framework of General Relativity. The standard general solution is that galaxy clusters are dominated by DM.

The observations with the WMAP satellite (Hinshaw et al. 2009) of the cosmic microwave background, the baryonic acoustic oscillations (Percival et al. 2007) measured with SDSS galaxies and the supernova studies (Kowalski et al. 2008) are consistent with a model of our Universe which contains 75% dark energy, 21% dark matter, and 4% baryonic matter (Komatsu et al. 2009). The nature of dark matter is still unknown: different baryonic candidates, like neutrinos and MACHOs (massive compact halo objects) were ruled out. Many candidate particles exist, but so far none has been found in accelerators or other high-energy experiments (Bertone et al. 2005). Nevertheless, a potential DM candidate particle has to fulfill a large set of constrains summarized in Taoso et al. (2008).

An alternative explanation for the flat rotation curve is the introduction of new physics - Modified Newtonian Dynamics (MOND, Milgrom 1983a,b; Bekenstein & Milgrom 1984). According to MOND, Newtonian dynamics breaks down for accelerations lower than $a_0 \simeq 1 \times 10^{-8}$ cm s^{-2} (Begeman et al. 1991; Sanders & McGaugh 2002). The acceleration $\boldsymbol{a}$ in

MONDian dynamics is given by the (heuristic) equation:

$$\mu\left(\frac{|\boldsymbol{a}|}{a_0}\right)\boldsymbol{a} = \boldsymbol{a}_N, \qquad \boxed{1.3}$$

where $\mu(x)$ is an arbitrary function with the following limits:

$$\mu\left(x\right) = \left\{ \begin{array}{ll} x & \text{if} \quad x \ll 1 \\ 1 & \text{if} \quad x \gg 1. \end{array} \right. \qquad \boxed{1.4}$$

Here, $\boldsymbol{a}_N$ is the standard Newtonian acceleration and a_0 is the acceleration limit below which MOND is applicable. MOND was introduced to explain the flat rotation curves of spiral galaxies, as a side effect it can explain the well-defined relationship between rotation velocities and luminosity of spiral galaxies, the Tully-Fisher law (Tully & Fisher 1977; Aaronson et al. 1982). A recent review on MOND is written by Sanders & McGaugh (2002).

TeVeS is the relativistic expansion of MOND (Bekenstein 2004, 2009). It reproduces strong lensing as well as General Relativity (Bekenstein 2006; Chen 2008), but it meets problems dealing with weak lensing (Feix et al. 2008). Recent observations of the "Bullet Cluster" (Clowe et al. 2006), where the baryonic matter is distributed differently than the DM, was only explainable with MOND when hot DM is introduced (Angus et al. 2006, 2007). The treatment of cluster dynamics has been a problem for MOND as well as for *TeVeS*.

Neither MOND, nor DM has so far been falsifiable.

"If a physical law, when extended to a regime in which it has never before been tested, implies the existence of a medium (e.g., an ether) that cannot be detected by any other means, then it would not seem unreasonable to question that law." (Sanders & McGaugh 2002).

"Est enim galaxia nihil aliud, quam innumerarum Stellarum coacervatim consitarum congeries [...]"

Galileo Gallilei, "Sidereus Nuncius" (1609)

2

Tidal Structure of Globular Clusters

Today, the Milky Way is home to ~ 150 globular clusters. Each of them is a unique object. Studying all clusters in our Galaxy reveals their wide range of observables. We study the 17 globular clusters in the Sloan Digital Sky Survey (SDSS). They are experiencing the constantly changing tidal field of the Milky Way. Further internal mechanisms are driving the globular clusters' dissolution. We use a color-magnitude weighted counting algorithm to study the two-dimensional distribution of globular cluster stars on the sky. The large area coverage of the SDSS allows us to study their extensions much further out than their nominal tidal radius. We observe the known extended tidal tails of Pal 5 and NGC 5466, as well as the small scale tidal features of NGC 5053 and NGC 6341. For NGC 4147 we detect a multiple-arm morphology which is predicted by theoretical simulations. Theoretical predictions concerning the destruction times of the globular clusters in our sample predict only for NGC 4147 a definite destruction within the next Hubble time. The lack of any new large scale tidal features in our sample is a confirmation of these predictions.

2.1 Introduction

Globular clusters (GCs) are the oldest stellar objects found in the Milky Way (MW), with ages in the range of $12 - 15$ Gyr. They represent tracers of the early formation history of our Galaxy. GCs are the ideal systems to study stellar dynamics in high-density systems as their relaxation times are much smaller than their age. We expect, at least in the core, the stars to have lost memory about their initial conditions. The GCs we see today are only the lucky survivors of an initially much larger population. Several different mechanisms can destroy a GC: internal processes are infant mortality by stellar evolution and two-body relaxation; external mechanisms, mainly, the interaction of the GC with the constantly changing tidal field of its host galaxy. Different processes are dominant at different ages of the cluster. For young clusters stellar evolution is the main driver. More massive stars are evolving rapidly, have high winds and explode in supernovae within the first million years. The sudden change, due to the mass loss, in the GC's internal gravitational field can destroy the GC. Two-body relaxation arises from close encounters between cluster stars, leading to a slow diffusion of stars over the tidal boundary. This process is taking place from the beginning to the final dissolution of the cluster. Equipartition of energy by two-body encounters leads to mass-segregation, the more massive stars sink to the center, less massive stars remain in the outer parts of the cluster. This leads to a preferential loss of low-mass stars, which can be observed today in declining mass-function slopes of GCs. On the other side, the mass loss due to the cluster's encounter with the Galactic disk and bulge is strongest at pericenter passages, especially for GCs on elliptical orbits (Baumgardt & Makino 2003). *See Section 1.2 for further details.*

2.1.1 Theoretical studies on globular cluster destructions by external tidal fields

Destruction of globular clusters

Gnedin & Ostriker (1997, GO97) studied the dynamical evolution of the entire Galactic GC system. They derived the destruction rates due to the different internal and external mechanisms. The total destruction rate of the entire GC system is such that more than half of the present day GCs will not survive the next Hubble time. GO97 did not include any information on the GCs proper motion, they only used the known present day distance to the Galactic center and the GC's radial velocity. The GC's tangential velocity was derived statistically (see GO97 for details). They constructed *vital diagrams* in the plane cluster mass vs. radial extent ($\mathcal{M}_{GC}$,r_h). In Figure 2.1 we show Fig. 21 from GO97 and marked the GCs in our sample (see Table 2.1) by using the parameters given by the authors. The GCs inside the triangular shapes are likely to survive the next Hubble time, while the GCs outside the triangles are destroyed by the mechanism stated in the diagram. The lowest mass cluster is Pal 1. The clusters on the right side of the triangles are Pal 3, 4, 5, and 14. The GC on the left side of the triangles is NGC 4147.

The survival triangle can be understood as follows: During the dynamical evolution of the GC, it is constantly losing mass eventually leading to the cluster's dissolution. Two-body relaxation acts on time scales of the half-mass relaxation time

$$t_{rh} \sim \frac{M_c^{1/2} r_h^{3/2}}{G^{1/2} m},$$

(2.1)

where m is the individual stellar mass, M_c the cluster mass, and r_h the half-mass radius. Setting this timescale equal to the present day age of the GCs, we obtain values for which
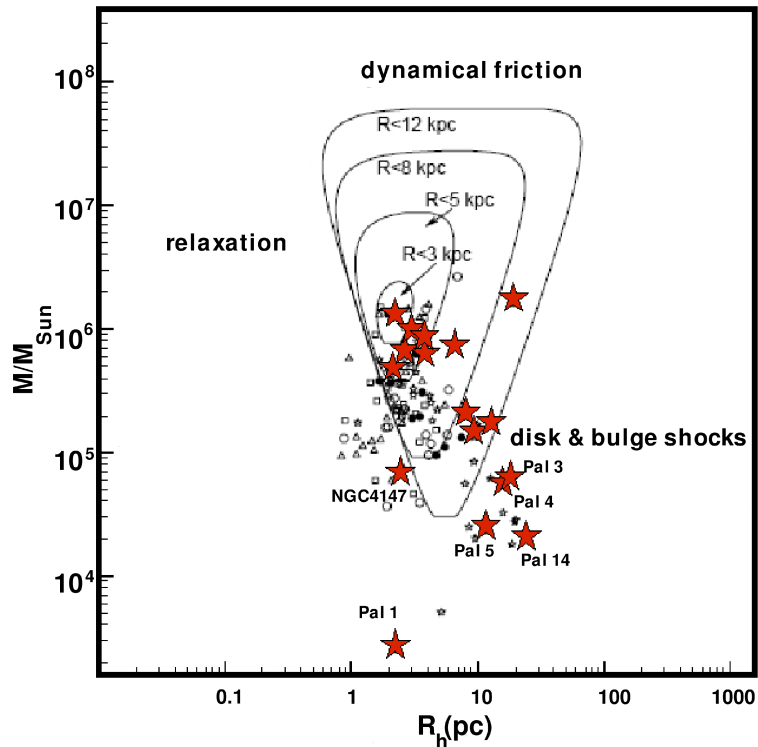
Figure 2.1: Vital diagram from GO97. The red stars are the GCs in our sample, Cluster mass and half-light radius were taken from GO97. GCs within the triangles are most likely surviving the next Hubble time.

GCs survived this process. It results in the lower left boundary of the survival triangle. As it is only an internal process it is independent of the cluster's position in the Galaxy. The main external process is disk shocks. The energies of the individual stars are changed on the time scale of shock relaxation:

$$t_{sr} \sim \frac{M_c R V}{G \Sigma^2 r_h^3}, \qquad (2.2)$$

where R is the cluster's galactocentric distance, V its orbital speed around the Galaxy and Σ the surface density of the Galactic disk. Setting this equal to the typical lifetime of GC gives lines at the lower right boundary of the survival triangles (different lines for different galactocentric distances). The upper horizontal border is the result of dynamical friction. Massive clusters are slowed down by dynamical friction and have circled into the Galactic center (Heggie & Hut 2003).

Dinescu et al. (1999, DG99) derived the destruction rates for a smaller sample of Galactic GCs including the proper motion data. They concluded that the destruction processes for the clusters in their sample are mostly dominated by internal relaxation and stellar evaporation. Tidal shocks due to the bulge and disk are only dominant for a small number of GCs in their sample. From our sample this is only the case for Pal 5 (see columns 11 &12 in Table 2.1). Comparing their destruction rates with the numbers of GO97, they find that the GO97 total rates are larger. The destruction rates due to internal processes (2-body relaxation, stellar evaporation) are in both catalogs comparable, therefore only the destruction rate due to tidal shocks is incompatible. DG99 conclude that the statistical approach of assigning tangential velocities (the method used by GO97) results in more destructive orbits than are actually observed.

A similar conclusion is drawn by Allen et al. (2006). These authors derive the orbits of Galactic GCs, also based on observed proper motions, in a axisymmetrical potential and in a barred potential (resembling the MW). They derived the destruction rates for the GCs in their sample in an almost identical way to DG99. It is logical that these destruction rates are also smaller than the rates from GO97. Allen et al. (2006) further investigated the influence of the bar on the clusters' orbits and destruction rates. The bar does not influence the orbits of clusters, which have a pericenter distance greater than ~ 4 kpc. Therefore none of our clusters are influenced by the bar.

Emerging tidal tails in simulations

Combes et al. (1999) studied the tidal effects experienced by GCs on their orbits around the MW. In general, they find that two large tidal tails emerge extending out to $5\,r_t$. They conclude by stating *i)* GCs are always surrounded by tidal tails and tidal debris, *ii)* the tails are preferentially composed of low mass stars, *iii)* mass loss in a GC is enhanced if the cluster is in direct rotation with respect to its orbit, *iv)* extended tidal tails trace the cluster's orbit, and *v)* stars are not distributed homogeneously along the tidal tails, but clump.
Capuzzo Dolcetta et al. (2005) investigated the clumpy structure of the tidal tails. They saw that the clumpy structure is not associated with an episodic mass loss or tidal shocks with Galactic substructure, as stars are continuously lost. The clumps are not self-gravitating systems. Further, they confirmed the earlier finding that the cluster's leading tail develops inside the orbit, while the trailing tail follows outside the orbital path. They also saw that for clusters on elliptical orbits the tidal tails trace the orbital path only near perigalacticon. On the other hand for circular orbits the tails are clear tracers of the cluster path. Further the length of the tails is not constantly growing. On eccentric orbits the leading tail tends to be longer than the trailing tail on the cluster's motion from apogalacticon to perigalacticon and vice versa on the other half of the cluster's orbit. The clumps are a result of epicyclic motion of the stars lost by the cluster (Küpper et al. 2008).
Montuori et al. (2007) investigated the direction of tidal tails with respect to the GC's orbit. They found that in the outer parts of the tails ($> 7 - 8$ tidal radii away from the cluster center), the tails are very well aligned with the cluster's orbit regardless of the cluster's location on the orbit. On the other hand, in the inner parts, the orientation of the tidal tails is strongly correlated with the orbital eccentricity and the GC's location on the orbit. Only if the cluster is near perigalacticon, the inner tidal tails are aligned with the orbital path. Therefore, only if long tidal tails are detected, it is possible to well constrain the cluster's orbit from those. Detecting only small, short tidal extensions just outside the GC's tidal radius does not give any hint on the cluster's orbit unless the cluster's proper motion has been measured before. In Figure 1.5 we show an example of their calculations.
DG99 have measured proper motions of a large number of GCs and added values from the literature to their catalog. From this they derived orbital parameters, such as ellipticity e, perigalacticon R_{peri}, apogalacticon R_{apo}, etc. The eleven clusters we have in common with DG99 have orbital eccentricities larger than ~ 0.3, i.e., there are no circular-like orbits for our sample.
The formation and typical $\mathcal{S}$-shape of tidal tails around a GC can be understood by the motion of a star which escapes from a cluster moving in a spherical potential. Montuori et al. (2007) gave a qualitative description. We are following their line of thoughts and reproduce their calculations here. We introduce a rotating frame of reference (x', y', z'), originating in the cluster's center of mass. The (x', y')-plane coincides with the orbital plane, while x' points to the Galactic center (e.g., this reference frame is rotating with the GC's angular velocity ω with respect to the inertial reference system (x, y, z)). See Figure 2.2 for a visualization of
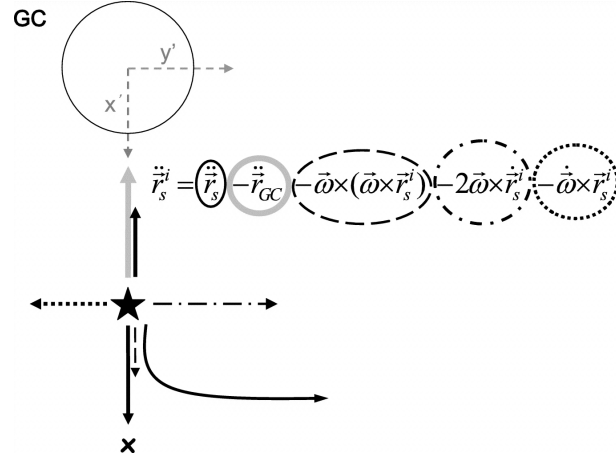
Figure 2.2: Interpretation of the $\mathcal{S}$-shape of the inner tidal tail around a globular cluster. The different terms in the right-hand side of equation 2.8 are represented as arrows of different styles. The last term in the equation is plotted antiparallel to the Coriolis term (as it occurs when the globular cluster moves from peri- to apogalacticon. The black cross in the lower left marks the Galactic center. (Montuori et al. 2007, Fig. 5)

the coordinate systems.

The position of the ith star in the galactocentric reference frame (x, y, z) can thus be given by

$$\mathbf{r}_i = \mathbf{r}_{GC} + \mathbf{r}'_i, \tag{2.3}$$

$\boldsymbol{r}_{GC}$ is the position vector of the cluster's center of mass in the inertial system. We rewrite the above definitions and we omit the z-component for simplicity:

$$x_i\hat{\mathbf{x}} + y_i\hat{\mathbf{y}} = x_{GC}\hat{\mathbf{x}} + y_{GC}\hat{\mathbf{y}} + x'_i\hat{\mathbf{x}}' + y'_i\hat{\mathbf{y}}'. \tag{2.4}$$

Here $\hat{\mathbf{x}}, \hat{\mathbf{y}}$, and $\hat{\mathbf{x}}', \hat{\mathbf{y}}'$ are the unit vectors in the two reference frames, respectively. We now take the derivative of equation 2.4 with respect to time t:

$$
\begin{aligned}
\dot{x}_i\hat{\mathbf{x}} + \dot{y}_i\hat{\mathbf{y}} &= \dot{x}_{GC}\hat{\mathbf{x}} + \dot{y}_{GC}\hat{\mathbf{y}} + \dot{x}'_i\hat{\mathbf{x}}' + \dot{y}'_i\hat{\mathbf{y}}' + x'_i\dot{\hat{\mathbf{x}}}' + y_i\dot{\hat{\mathbf{y}}}' \tag{2.5}\\
&= \dot{x}_{GC}\hat{\mathbf{x}} + \dot{y}_{GC}\hat{\mathbf{y}} + \dot{x}'_i\hat{\mathbf{x}}' + \dot{y}'_i\hat{\mathbf{y}}' + \omega \times (x'_i\hat{\mathbf{x}}' + y'_i\hat{\mathbf{y}}') \tag{2.6}
\end{aligned}
$$

where $\dot{\hat{\mathbf{x}}}' = \omega \times \hat{\mathbf{x}}'$, $\dot{\hat{\mathbf{y}}}' = \omega \times \hat{\mathbf{y}}'$. We take the derivative of equation 2.5 with respect to time t and use the two equations before and get

$$\ddot{x}_i\hat{\mathbf{x}} + \ddot{y}_i\hat{\mathbf{y}} = \ddot{x}_{GC}\hat{\mathbf{x}} + \ddot{y}_{GC}\hat{\mathbf{y}} + \ddot{x}'_i\hat{\mathbf{x}}' + \ddot{y}'_i\hat{\mathbf{y}}' + 2\omega \times (\dot{x}'_i\hat{\mathbf{x}}' + \dot{y}'_i\hat{\mathbf{y}}') + \omega \times [\omega \times (x'_i\hat{\mathbf{x}}' + y'_i\hat{\mathbf{y}}')] + \dot{\omega} \times (x_i\hat{\mathbf{x}}' + y_i\hat{\mathbf{y}}'). \tag{2.7}$$

To better understand equation 2.7, we rewrite it in a more compact form and solve for $\ddot{\mathbf{r}}'_i$:

$$\ddot{\mathbf{r}}'_i = \ddot{\mathbf{r}}_i - \ddot{\mathbf{r}}_{GC} - 2\omega \times \dot{\mathbf{r}}'_i - \omega \times (\omega \times \mathbf{r}'_i) - \dot{\omega} \times \mathbf{r}'_i. \tag{2.8}$$

Stars escape through the unstable Lagrangian points L1 and L2, which are located along the x' axis. In equation 2.8, the first, second and fourth term are directed along the x' direction. The third term, the Coriolis force, as well as the fifth term are directed along y'. The fifth term is parallel to the Coriolis force when $|\omega|$ increases, i.e., when the cluster moves from apo- to perigalacticon, and anti parallel on the other half of the cluster's orbit. Therefore, these two terms are responsible for the initial deviation of the tails from a radial direction and for the formation of the known $\mathcal{S}$-shape. In Figure 2.2 the different terms are visualized for a better understanding.
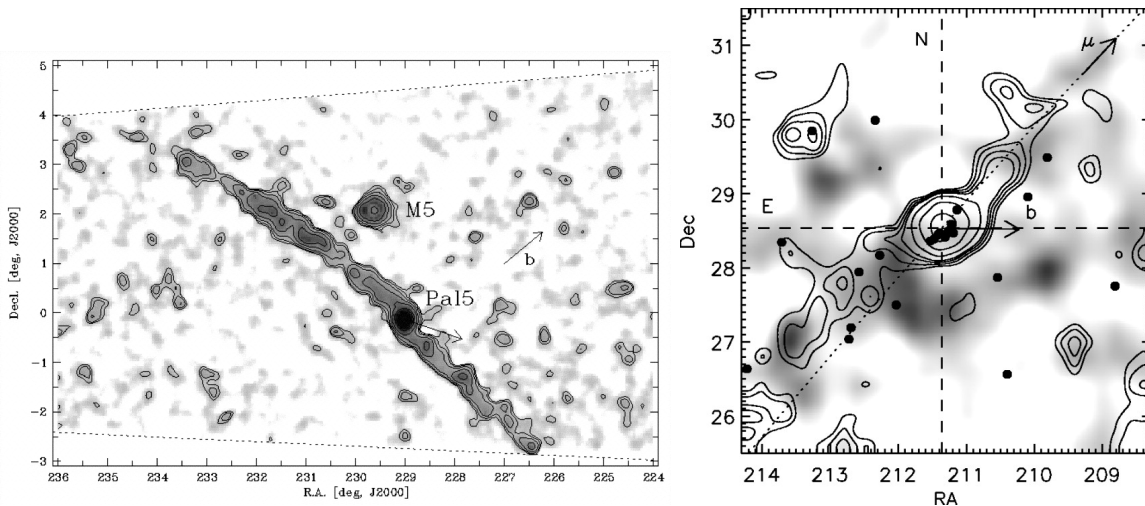
Figure 2.3: *Left:* Tidal tails of Pal 5 as detected by Odenkirchen et al. (2003). *Right:* Tidal tails of NGC 5466 as detected by Belokurov et al. (2006). *Figures from Odenkirchen et al. (2003) & Belokurov et al. (2006)*

2.1.2   Observational studies on tidal tails of globular clusters

Grillmair et al. (1995) performed deep two-color star counts to examine the outer structure of 12 GCs using photographic Schmidt plates. They detected a halo of extra tidal stars around most of their clusters. The tidal tails are not in all cases purely of stellar-origin, as the morphological identification galaxy/star, especially for faint objects, was not perfect. In other cases random overdensities of foreground stars induced features into the cluster's contours. Leon et al. (2000) studied the tidal tails of 20 GCs, using Schmidt plates as well. These authors also find halos of extra tidal stars as well as tidal tails for most of their clusters. The two studies have three GCs in common. For two out of the three clusters Grillmair et al. (1995) detect tidal tails where Leon et al. (2000) did not see such a strong signal and in the third case it is the opposite. In Section 2.5 we will compare the tidal structure of Grillmair et al. (1995) and Leon et al. (2000) with our tidal maps for each cluster separately.

Besides the two studies mentioned above, for individual clusters different authors determined the 2d distribution of cluster stars on the sky. The two most prominent cases are Pal 5 and NGC 5466, as for these two clusters extended tidal tails have been found. The large area-coverage with CCDs by the SDSS is a large database for tidal tail studies of GCs. Pal 5 was the first cluster for which extended tidal tails were discovered (Odenkirchen et al. 2001; Rockosi et al. 2002; Odenkirchen et al. 2003; Grillmair & Dionatos 2006) using SDSS data. NGC 5466 was the second cluster found to have extended tidal tails (Belokurov et al. 2006; Grillmair & Johnson 2006). In Figure 2.3 we show the tidal tails of Pal 5 and NGC 5466. Not only spectacular tidal tails, but simpler tidal features were also detected for NGC 5053 (Lauchner et al. 2006) and for NGC 6341 (M92) by Testa et al. (2000). Further, Kiss et al. (2007) studied the kinematics of red giants around five GCs. For M55, M30 and NGC 288, they did not find any strong signs for tidal debris. Recently, Chun et al. (2010) studied the spatial configuration of stars around five metal-poor GCs (M15, M30, NGC 5024 (M53), NGC 5053, and NGC 5466). They used deep images obtained at the Canada-France-Hawaii Telescope. Around all GCs extratidal overdensities and extratidal halos were observed. Between NGC 5024 and NGC 5053 they detect a tidal-bridge like feature and an envelope structure.

To perform a study on the 2d structure of GCs a large area coverage is needed. For smaller
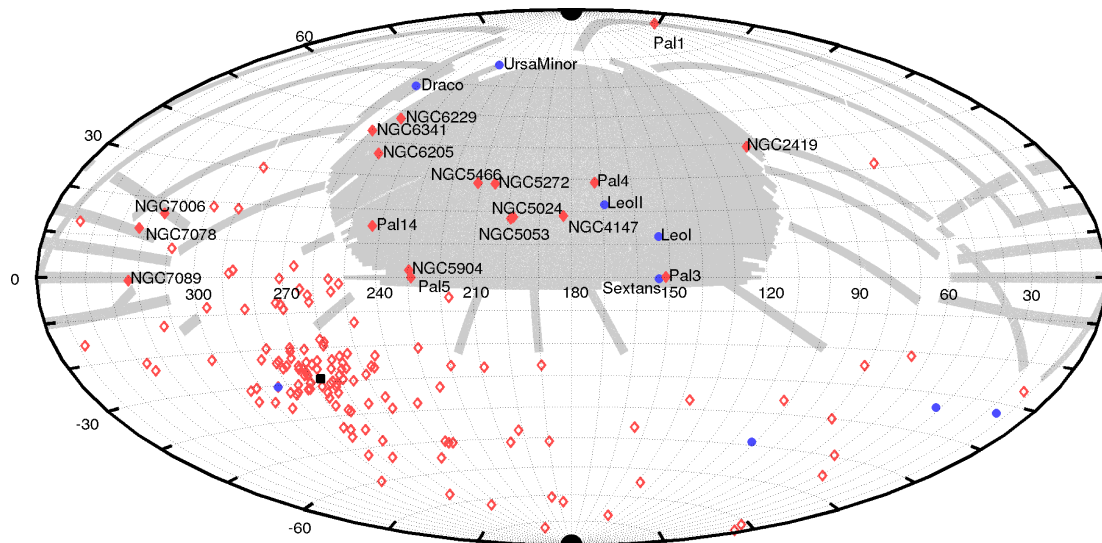
Figure 2.4: Aitoff projection of the sky in RA-Dec centered on $RA = 180°$. The light gray shaded area indicates the sky coverage of SDSS DR7. The red and blue symbols mark the Galactic GCs and dSph galaxies, respectively. The red filled diamonds are the GCs in the SDSS DR7, the blue labelled dots are the dSphs in the SDSS DR7, the black filled square marks the Galactic center.

areas, the surface brightness profile or number density profile of a GC can give a hint on a halo of extra tidal stars. Usually, one assumes that the GC's profile follows a King profile (King 1962). An excess of observed stars compared to the outer parts of a theoretical King profile is interpreted as a halo of extra tidal stars and as an indication of tidal features. Grillmair et al. (1995) did not only study the 2d structure but also the number density profiles of the clusters in their sample. They were able to confirm the connection between the overabundance at larger radii with a halo of extra tidal stars or in some cases even with tidal features.

This chapter is organized as follows: Section 2.2 introduces the GC sample. In Section 2.3 we explain the algorithm used to derive the 2d-contour maps. We will discuss and show the number density profiles for the GCs in our sample in Section 2.4. Finally in Section 2.5 we present the contour maps for our clusters. The discussion in Section 2.6 of the results concludes this chapter.

2.2 Data

The Sloan Digital Sky Survey (SDSS) is an imaging and spectroscopic survey in the Northern hemisphere (York et al. 2000). SDSS imaging data are produced in the five bands *ugriz* (Fukugita et al. 1996; Gunn et al. 1998, 2006; Hogg et al. 2001; Smith et al. 2002; Ivezic et al. 2004; Tucker et al. 2006). The data are automatically processed to measure photometric and astrometric properties (Photo; Lupton et al. 2002; Pier et al. 2003) and are publicly available on the SDSS web pages[1]. Figure 2.4 is an Aitoff projection of the sky in RA-Dec, showing the sky coverage of the latest SDSS Data Release 7 (DR7; Abazajian et al. 2009) in gray and the Galactic GCs as red open and filled symbol. The clusters labeled are those which lie in the DR7 footprint and are studied here. The blue symbols are the Galactic "classical" dwarf spheroidal (dSph) galaxies. The blue labelled symbols mark the DR7 dSph galaxies.

---

[1]www.sdss.org

In Table 2.1 we list the GCs found in the SDSS DR7 footprint. Columns (3) and (4) contain the RA, Dec coordinates of the cluster center mainly taken from Harris (1996), except for Pal 14 (Hilker 2006) and NGC 7089 (Dalessandro et al. 2009). In column (5) we list the clusters' distance to the Sun and in column (6) the cluster's distance to the center of the MW from Harris (1996), except for Pal 14 (Hilker 2006). Columns (7) and (8) contain the core and tidal radii from McLaughlin & van der Marel (2005, M05). For almost all GCs in our sample proper motions have been measured. Only for three of the most distant GCs, NGC 2419, Pal 4 and Pal 14, as well as for NGC 5053 this information is lacking. Columns (9) and (10) list the proper motion taken from Dinescu et al. (1999). In columns (11) and (12) we report the destruction rates calculated by GO97.

We downloaded all photometric data on point-sources from the DR7 database in areas of $\sim 9° \times 9°$ centered on the GCs. We only used stars with "clean photometry"[2].

The automatic SDSS pipeline Photo was initially designed to process high Galactic latitude fields with a low density of Galactic field stars. Fields on and around GCs are too crowded for Photo to process, so the automatic pipeline does not provide photometry for these most crowded regions. An et al. (2008) used the DAOPHOT crowded-field photometry package to derive accurate photometry for the stars in these crowded areas. This photometry is published on the SDSS web pages as a value-added catalog[3]. From this sample we only considered stars with photometry flags set to 0. The An sample and the original SDSS sample are overlapping in some regions. If a star is measured in both samples, we used the original SDSS photometry. Finally, we merged the two samples into one catalog for each GCs. The magnitudes in the final catalog were corrected for extinction. The SDSS catalog provides the extinction values from Schlegel et al. (1998). The fields with An photometry, the extinction values were derived by a cubic interpolation of the values listed in the SDSS.

In Figure 2.5 (left panel) we show a $3° \times 3°$ field around NGC 6205. In black we drew all stars extracted from the DR7 database. It is clearly visible that the automatic SDSS pipeline does not provide photometry for most of the cluster. The gray area marks the fields processed by An et al. (2008), filling the hole at the center of NGC 6205. The diagonal stripes result from the SDSS scans. After cleaning the sample for bad photometry flags these artificial features vanish.

2.3   Color-magnitude weighted star counts

To map cluster member stars on the sky we used the same method as Odenkirchen et al. (2003) to follow the tidal tails of Pal 5. We defined the *cluster sample* to contain all stars within $2/3 \cdot r_t$ and the *field sample* to contain all stars outside $3/2 \cdot r_t$. In some cases, e.g., for NGC 5024 and NGC 5053, two clusters are close neighbors in the projection on the sky. In these cases, we excluded all stars within the tidal radius of the neighboring cluster from the *field sample*.

2.3.1   Selecting stars in color & magnitude

We are only interested in the distribution of cluster member stars on the sky. Therefore, we selected our stars in color-magnitude (C-M) space to minimize the contamination by field stars. In order to achieve a minimum contamination, we defined new orthogonal color indices

$$c_1 \;=\; k_1 \cdot (g - r) + k_2 \cdot (g - i) + k_3 \qquad\qquad (2.9)$$

$$c_2 \;=\; -k_2 \cdot (g - r) + k_1 \cdot (g - i) + k_4. \qquad\qquad (2.10)$$

---

[2]http://cas.sdss.org/astro/en/help/docs/algorithm.asp?key=flags
[3]http://www.sdss.org/dr7/products/value_added/index.html

Table 2.1: Globular clusters in the SDSS footprint

NGC	Name	RA hh mm ss.s	Dec ° ′ ″	$R_\odot$ kpc	R_{MW} kpc	r_c ′	r_t ′	$\mu_\alpha \cos(\delta)$ mas/yr	μ_δ mas/yr	ν_{evap} t^{-1}_{Hubble}	ν_{tot} t^{-1}_{Hubble}
(1)	(2)	(3)	(4)	(5)	(6)	(7)	(8)	(9)	(10)	(11)	(12)
2419		07 38 08.5	+38 52 55	84.2	91.5	0.32	8.34	...	...	7.97e-3	7.98e-3
4147		12 10 06.2	+18 32 31	19.3	21.3	0.09	6.32	-1.85 ± 0.82	-1.3 ± 0.82	4.83e-1	4.84e-1
5024	M 53	13 12 55.3	+18 10 09	17.8	18.3	0.35	16.06	$+0.5 \pm 1$	-0.1 ± 1	2.88e-2	2.88e-2
5053		13 16 27.0	+17 41 53	16.4	16.9	1.91	13.85	...	...	1.07e-1	1.39e+1
5272	M 3	13 42 11.2	+28 22 32	10.4	12.2	0.37	30.15	-1.1 ± 0.51	-2.3 ± 0.54	3.41e-2	3.98e-2
5466		14 05 27.3	+28 32 04	15.9	16.2	1.53	13.64	-4.65 ± 0.82	0.80 ± 0.82	1.88e-2	3.01e+0
5904	M 5	15 18 33.8	+02 04 58	7.5	6.2	0.42	22.45	$+5.07 \pm 0.68$	-10.7 ± 0.56	6.76e-2	1.08e-1
6205	M 13	16 41 41.5	+36 27 37	7.7	8.7	0.55	19.49	-0.9 ± 0.71	$+5.5 \pm 1.12$	9.13e-2	1.47e-1
6341	M 92	17 17 07.3	+43 08 11	8.2	9.6	0.26	12.96	-3.3 ± 0.55	-0.33 ± 0.70	2.56e-1	2.66e-1
7006		21 01 29.5	+16 11 15	41.5	38.8	0.32	12.75	-0.96 ± 0.35	-1.14 ± 0.40	8.72e-2	9.02e-2
7078	M 15	21 29 58.3	+12 10 01	10.3	10.4	0.07	21.50	-0.95 ± 0.51	-5.63 ± 0.5	6.23e-2	2.03e-1
7089	M 2	21 33 27.3	-00 49 23	11.5	10.4	0.32	12.75	$+5.9 \pm 0.56$	-4.95 ± 0.86	5.51e-2	8.13e-2
	Pal 1	03 33 23.0	+79 34 50	10.9	17.0	2.28	12.04	...	...	4.37e+0	2.26e+1
	Pal 3	10 05 31.4	+00 04 17	92.7	95.9	0.35	4.89	0.33 ± 0.23	0.30 ± 0.31	5.88e-2	5.88e-2
	Pal 4	11 29 16.8	+28 58 25	109.2	111.8	0.33	3.30	...	...	1.16e-1	1.16e-1
	Pal 5	15 16 05.3	-00 06 41	23.2	18.6	2.28	12.04	-1.78 ± 0.17	-2.32 ± 0.23	1.64e-1	9.62e+0
	Pal 14	16 11 00.6	+14 57 28	74.7	69.0	0.77	7.20	...	...	1.78e-1	1.96e-1
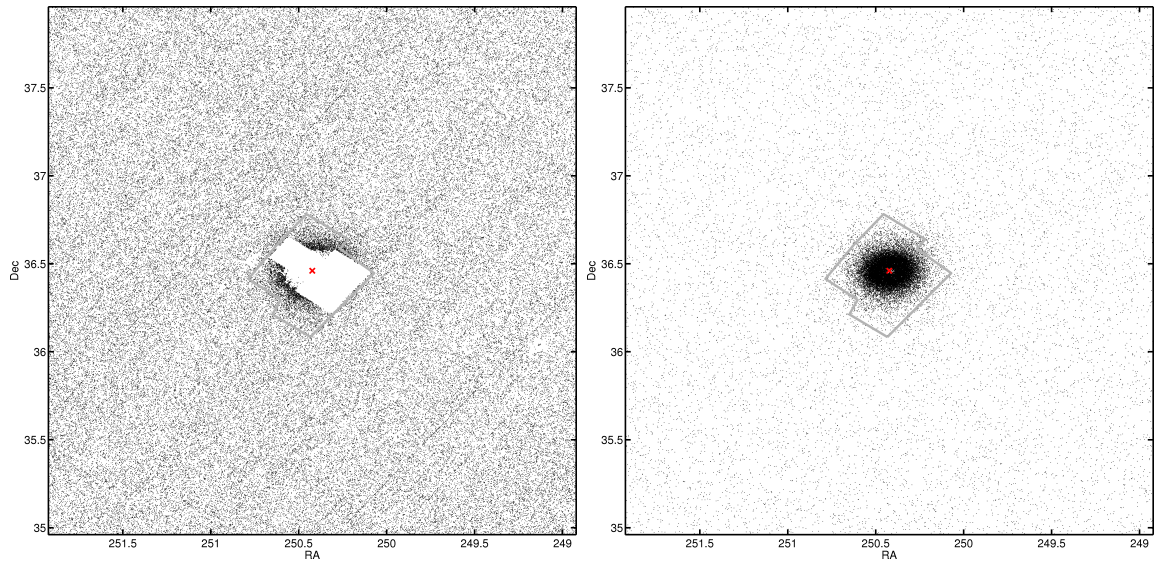
Figure 2.5: *Left Panel:* Distribution of all stars extracted from the SDSS DR7 database for NGC 6205 in black. The gray lines show the fields with photometry from An et al. (2008), which is not shown here. The red cross marks the cluster center. *Right Panel:* Distribution of all stars of NGC 6205 pre-selected in the colors c_1 and c_2. The red cross marks the cluster center.

Table 2.2: Parameters to derive the new Color Indices.

NGC	2419	4147	5024	5053	5272	5466	5904	6205	6341
$\tan(\alpha)$	1.472	1.462	1.495	1.434	1.473	1.531	1.447	1.381	1.345
b	-0.039	0.004	-0.053	-0.006	-0.053	-0.047	-0.016	-0.010	-0.001

NGC/Name	7006	7078	7089	Pal 1	Pal 3	Pal 4	Pal 5	Pal 14	
$\tan(\alpha)$	1.540	1.522	1.473	1.545	1.404	1.534	1.553	1.767	
b	-0.028	-0.035	-0.054	0.007	0.017	-0.147	-0.034	-0.190	

In a color-color plot the cluster stars are distributed along a straight line. The indices were now chosen in such a way, that the color c_1 goes along this straight line and c_2 is perpendicular to that. To derive these indices for each GC we used its *cluster sample*. We fitted a straight line $y = \tan(\alpha) \cdot x + b$ to the distribution of stars in the color-color diagram $(g-r)$ *vs.* $(g-i)$. In Table 2.2 we list the fitted parameters $\tan(\alpha)$ and b from which we derived $k_1 = \cos(\alpha)$, $k_2 = \sin(\alpha)$, $k_3 = -b \cdot \sin(\alpha)$, and $k_4 = -b \cdot \cos(\alpha)$ for each GC.

We selected our stars in the color-magnitude diagrams (c_1, g) and (c_2, g) to minimize the contamination by Galactic field stars. From the cluster sample we derived the GCs ridge line and selected all stars within 3σ of this ridge line. The ridge line of a GC traces the location of highest density of stars in a color-magnitude diagram (CMD). The CMDs of NGC 5272's *cluster sample* are plotted in Figure 2.6 to illustrate the selection criteria. We only considered stars with $g \leq 22.5$ mag and within the red borders. In blue we show the stars before and in black the stars after preselection. This preselection leaves us with the final catalog, where all stars are explicitly chosen to have the same photometric properties as the GC, but are located not only at the position of the cluster but also in the wide field around it. The final catalog is again split in a *final cluster sample* and a *final field sample*, with which we are continuing. In the right panel of Figure 2.5 we show the stars of NGC 6205 after preselection in c_1 and
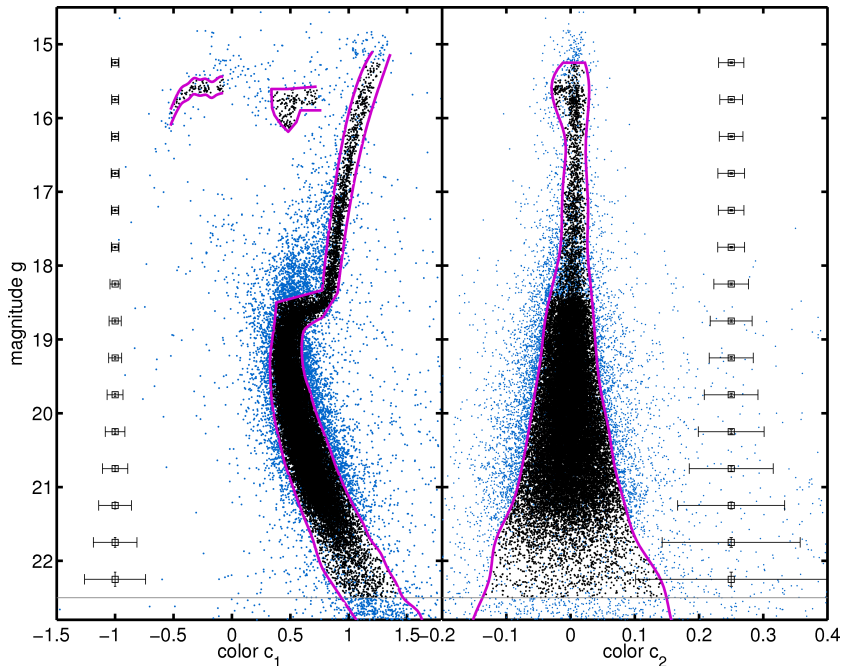
Figure 2.6: CMDs (c_1, g) (*left panel*) and (c_2, g) (*right panel*) of NGC 5272. In blue we show all stars of the *cluster sample*. The black dots are the remaining stars in the *cluster sample* after the C-M selection. In red we show the borders within which we selected the stars. The gray line is at $g = 22.5$ mag, only stars above this line were selected.

c_2. Comparing to the left panel in Figure 2.5 it is clearly visible how many (foreground) stars we are eliminating by these color and magnitude cuts.

Distribution of selected stars in a CMD

We define a grid in C-M space (c_1, g) with cells spanning 0.01×0.05 mag^2. These cells are labeled by the index j. We construct normalized C-M density diagrams for the cluster (ρ_C) and the field (ρ_F). We corrected the cluster C-M density distribution for the presence of possible field stars by subtracting the field C-M distribution in appropriate proportion. I.e., the field contribution was multiplied by the ratio of "cluster area" and "field area", the areas from which the two samples were drawn from.

$$\rho_C = \rho_C - \frac{A_C}{A_F} \cdot \rho_F \qquad (2.11)$$

In Figure 2.7 we show the Hess diagrams for the *cluster sample* NGC 5272 in the left panel and the *field sample* of the same cluster in the right panel. For these Hess diagrams the stars are already selected in C-M space as described above. For the *cluster sample* we can easily observe the different features typical for a CMD of a GC: main sequence, red giant branch, red and blue horizontal branch. It is also clear that the density of stars varies across the diagram, with the highest density in the center of the main sequence. For the *field sample* the density across the selected areas is approximately constant. At the location of the cluster's blue horizontal branch there are hardly any field stars. This is not only the case for the example NGC 5272, but a feature common to all clusters which have a blue horizontal branch.
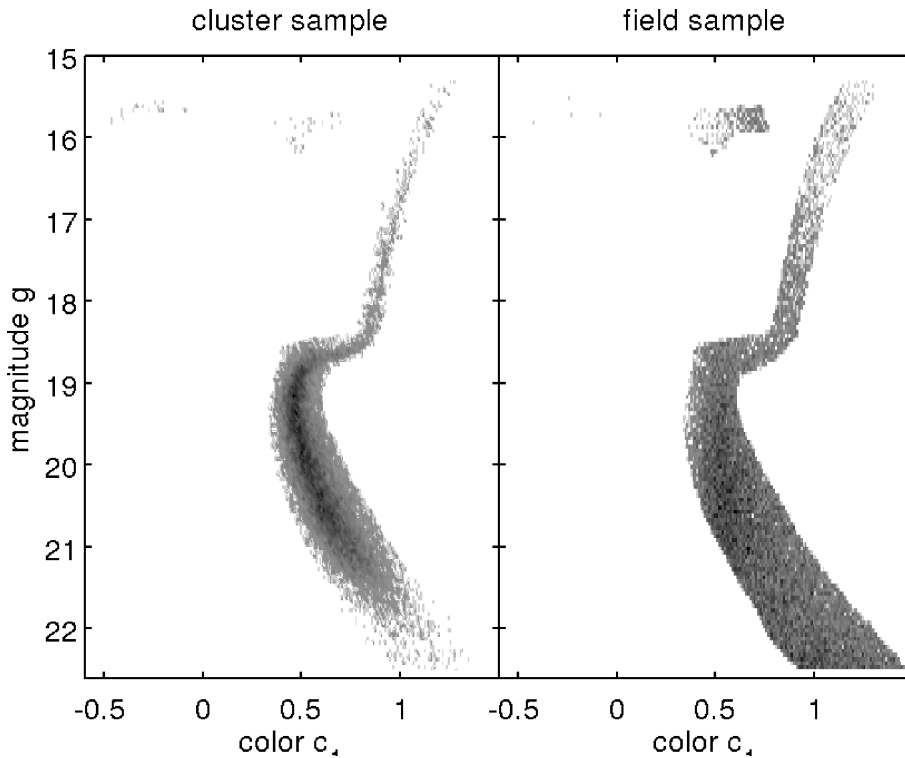
Figure 2.7: Hess diagrams in (c_1, g) of the cluster (*left panel*) and field (*right panel*) sample of NGC 5272.

2.3.2   Counting algorithm[5]

To derive the surface density distribution of cluster stars on the sky we need a model. The general model we use describes the stellar density in the space spanned by the celestial sphere and the C-M plane to be the sum of the densities of the cluster (S_C) and field (S_F) stars in this hyperspace

$$S(\alpha, \delta, color, magnitude) = S_C + S_F.$$

Each addend is the product of the surface density Σ on the sky and a position-dependent normalized C-M density Φ. For the *cluster sample* we assume that *i)* the sample is composed of the same stellar mix at all positions on the sky and *ii)* all stars are at the same distance to us. For extended tidal tails this second assumption might not be true far away from the cluster, as the cluster's orbit does not have to be in the plane of the sky. As we, in a first try, look for signs of tidal tails in the vicinity of the cluster, our assumption is valid. Therefore, Φ_C does not depend on the position (α, δ) on the sky. The *field sample* is composed of stars of different types at different points in the sky and the distribution along the line-of-sight is also spatially variable. In principle, Φ_F must vary with position on the sky. Thus we can write $S_C = \Sigma_C(\alpha, \delta) \cdot \Phi_C(color, magnitude)$ and $S_F = \Sigma_F(\alpha, \delta) \cdot \Phi_F(\alpha, \delta, color, magnitude)$. We introduce a grid on the sky with each cell spanning $3' \times 3'$. The cells are labeled by the index k. $\nu(k, j)$ is the expected number of stars lying in the solid angle Ω_k centered on (α_k, δ_k) with magnitudes and colors falling in cell j:

$$\nu(k, j) = \nu_C(k) f_C(j) + \nu_F(k) f_F(j). \tag{2.12}$$

---

[5]taken from Odenkirchen et al. (2003)

It is the sum of the expected number of cluster stars at the given position k with colors & magnitudes of cell j and the expected number of field stars at the same position k with identical colors and magnitudes.

The distribution of field stars in C-M space f_F does in principle depend on the position index k, but in our fields we can assume that substantial changes in the characteristics of the field population only occur on larger scales than we observe. Thus f_F and f_C can be represented by the observed, normalized (average) C-M distributions ρ_F and ρ_C, respectively.

The quantity $\nu_C(k)$, the number of cluster stars in Ω_k, is the target of our analysis. We name it $n_C(k)$. For $\nu_F(k)$, the number of field stars in Ω_k, we can assume that it must be a smoothly varying function of position. We derived the density of field stars in cells of size $3' \times 3'$. We described the density distribution by a simple polynomial model: $\nu_F(k) = n_F(k) = m_1 + m_2 \cdot \alpha_k + m_3 \cdot \delta_k$. The coefficients m_1, m_2, m_3 are determined in a least-squares fit to the derived density distribution.

Inserting all these inputs from the observations into the model in equation 2.12, we can determine $n_C(k)$ by minimizing the square sum of the noise-weighted deviations between the observed number $n(k, j)$ and the expected number $\nu(k, j)$ of stars given by equation 2.12, summed over the C-M grid.

Since the contribution of the cluster population to the total counts is small outside the cluster, we assume the noise to be dominated by the field stars, that is, we expect $\sigma_n^2(k, j) = \nu_F(k)f_F(j)$. The sum of weighted squares to be minimized thus is:

$$\chi^2(k) = \sum_j \frac{[n(k, j) - \nu_C(k)f_C(j) - \nu_F(k)f_F(j)]^2}{\nu_F(k)f_F(j)}. \qquad \boxed{2.13}$$

We derive the least-squares solution for the number of cluster stars $n_C(k)$ at a given position and its variance $\sigma_{n_C}^2(k)$ by solving $\partial\chi^2/\partial\nu_C = 0$ and plugging in the observed numbers for all the theoretical variables:

$$n_C(k) = \frac{\sum_j n(j, k) \cdot \rho_C(j)/\rho_F(j) - n_F(k)}{\sum_j \rho_C^2(j)/\rho_F(j)} \qquad \boxed{2.14}$$

$$\sigma_{n_C}^2(k) = \frac{n_F(k)}{\sum_j \rho_C^2(j)/\rho_F(j)} \qquad \boxed{2.15}$$

From Equation 2.14 we see that each star in a given cell on the sky k and in C-M space j is weighted according to its position in the CMD by the factor $\rho_C(j)/\rho_F(j)$. This weighted number of stars per cell on the sky is then summed and divided by the factor $a = \sum_j \rho_C^2(j)/\rho_F(j)$. This gives the estimated number of cluster stars n_C plus a term n_F/a, the number of contaminating field stars attenuated by a.

2.3.3 Possible contaminations

Before presenting all contour maps in Section 2.5, we briefly discuss the possible sources for contaminations. Without being aware of them we could not interpret our results as real or artificial tidal features.

Background galaxies, galaxy clusters & quasars
The SDSS automatic Star/Galaxy separation seems to be very reliable. As we only use data considered to be a point source we, in principle, do not have to worry about contaminating background galaxies or galaxy clusters. In the fields with An photometry this may be an issue, but these fields do have a high stellar density, outnumbering contaminating galaxies.

As quasars are point sources and are included in the SDSS database together with stars, these might influence our data. We have looked at the SDSS quasar catalog IV (Schneider et al. 2007), which contains 77 429 quasars from SDSS DR5. We applied the same selection criteria in color and magnitude to select possible contaminating quasars for each GCs, respectively. E.g., for NGC 5272 we end up with 54 quasars contaminating our sample of 51 964 stars in total. The contamination due to quasars can be neglected.

Dust
The extinction by dust might also influence our tidal features. All our magnitudes are corrected for extinction as given in the SDSS database by values from Schlegel et al. (1998). In a first look, we do not expect a strong contamination by dust, as the SDSS mainly observed the sky around the North Galactic pole (NGP), where less dust is expected. But, in previous studies a correlation between tidal tails and dust was found for some GCs. We show for each GC the distribution of dust in the field we observed. In this way we can investigate a possible correlation between the detected tidal features and the foreground dust. In Appendix A (Figures A.1-A.4), we show the derived contour maps plotted on top of the extinction maps for each dSph. The extinction maps show the mean extinction value from Schlegel et al. (1998).

Foreground stars
In Section 2.3.1 we explained our criteria to select stars in C-M space to minimize the number of foreground contaminants. For all GCs we have only selected stars within 3σ of the cluster's ridge line to assure that the majority of stars counted are likely cluster members. The 2d distribution of these selected stars shows in all cases a unique maximum at the GC's position. The area around the GC is in all cases not perfectly flat, but shows density peaks of various significances. I.e., we are able to clean our stellar sample, but not perfectly. A more accurate exclusion of foreground contaminants can only be achieved with spectroscopic confirmations for each single star. A task which seems almost impossible if thought of the vast number of objects to be observed.

2.4 Number density profiles

The large area coverage of the SDSS data allows us to observe the number density profiles of GCs much further out than the cluster's tidal radii. By using a large area "far away" from the cluster we are able to determine the mean background contamination and to investigate in detail the *outer edge* of the GCs. For the denser clusters the SDSS and the SDSS+An-extension are not suited to observe the number density profile in the clusters central part due to crowding. Therefore we combined the number density profiles from the SDSS with previously published profiles for the central parts of the clusters.

We derived the number density profiles by counting the stars in annuli of constant width dr. We used only the stars preselected in C-M space as described above. We used annuli of width $2'$ outside the published tidal radius. Within the cluster's tidal radius we chose either $0.5'$ or $1'$ as width of the annuli, depending on the surface density of the cluster. For the final number density profile we counted all stars in each annulus and divided by the area of the annulus. The error on the number density was derived by dividing the annulus in 20 segments. We then derived the number of stars in each segment and used the standard deviation of these 20 values as the error. For clusters with a small number of stars we divided the annuli in 8 segments to minimize the effect of small number statistics. In Figure 2.8 we plot the SDSS number density profile of NGC 6205 as blue crosses. The effect of incompleteness within the
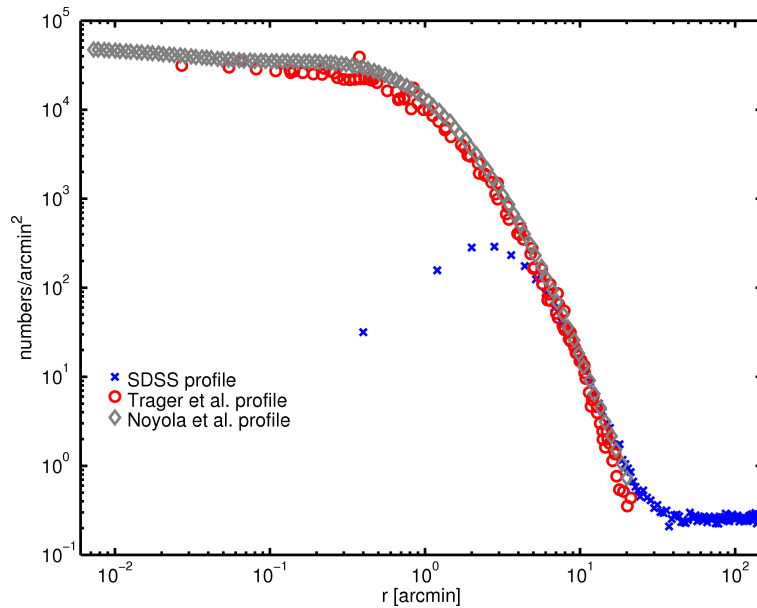
Figure 2.8: Number density profile of NGC 6205. The profile derived from SDSS data is shown as blue crosses. The Trager et al. (1995) profile is shown as red squares and the Noyola & Gebhardt (2006) profile as gray diamonds.

inner $4'$ is evident, as well as the flat density of the Galactic background outside $30'$.

The surface brightness profiles by Trager et al. (1995, T95) and the revised study of the same data by McLaughlin & van der Marel (2005, M05) are the only large catalogs of surface brightness profiles of Galactic GCs. We combined the older dataset from T95 with our new SDSS profiles to get profiles spanning from the cluster center out to several times the tidal radius.

In order to combine the two datasets, we converted the surface brightness $\mu(r)$ of T95 into a number density $\log(N(r)) = -\mu(r)/2.5 + C$. C is a constant derived separately for each GC in the following way. The T95 profile and the SDSS profile overlapped in some radial range. This overlap was used to derive the vertical shift C between the profiles. The T95 profiles were shifted by C to match the SDSS profiles. In Figure 2.8 we also show the T95 profile of NGC 6205 in red. For GCs which have T95 profiles far out, the outermost points were not taken into account, because these data points are the most affected by the background contamination or subtraction. Further, differences in the outer parts of the different profiles can also be explained by mass segregation in the clusters, unveiled by different limiting magnitudes. This effect might be visible in Figure 2.8.

For the GCs NGC 5272 (M3), NGC 5904 (M5), NGC 6205 (M13), NGC 6341 (M92), NGC 7078 (M15), and NGC 7089 (M2) Noyola & Gebhardt (2006, N06) published surface brightness profiles derived from HST observations. They tested the influence of the chosen filter on the profiles and found no dependences. The profiles looked the same in each observed filter. For 50% of their clusters the photometric data points are brighter in the central parts of the clusters than the fitted King profiles (King 1962). The discrepancy between the observations and the fit increases as the radius decreases. They conclude that the inner parts are not suited to be fit with a King profile.

For these six GCs we combined the Noyola & Gebhardt (2006) profiles and our SDSS profiles to span the largest possible range in radius. The combination was done in an identical way as for the combination of the T95 sample with our SDSS sample. In Figure 2.8 we also show

the N06 profile of NGC 6205 in gray.

We fitted King profiles (King 1962) of the form

$$f_K(r) = k \cdot \left(\frac{1}{\sqrt{1 + (r/r_c)^2}} - \frac{1}{\sqrt{1 + (r_t/r_c)^2}} \right)^2 + b, \qquad \boxed{2.16}$$

where the variables have the following meaning: r_c is the cluster's core radius, the radius at which the surface brightness drops to half of its central value; r_t is the tidal radius, the theoretical radius at which the density of cluster stars drops to zero, b is the average number density of the field, and k is a constant shifting the profile in y-direction not altering the overall shape of the profile at all.

We performed two fits. First, we only fitted the number density profile derived from the SDSS data. We adopted the core radii r_c from M05 and the background b from our observations. The tidal radius r_t and the constant factor k were the fitted parameters. For some clusters, e.g., NGC 6205, the effect of incompleteness was very easily seen in the inner most radial bins. Such data points were not considered for the fitting process. Also at larger radii, where we expect a flat "profile" for some cluster a drop in the profile was observed. This drop was caused by a "hole" in the observations, e.g. for some region on the sky we did not have any data. These data points were also neglected. Second, we fitted a King profile to the combined number density profiles, either T95+SDSS or N06+SDSS. For this fit we adopted the background b from our observations and fitted the remaining three parameters. As N06 described the discrepancy between the King models and the observed profiles for the inner parts of the profile, we did not attempt to fit the central parts. We did not adopt a consistent way of choosing a radius up to which the central data points were not considered. For each GCs this was done individually by visual inspection.

Could the fact that we are fitting the number density profile of pre-selected stars influence our result? In Figure 2.9 we show the number density profiles of a high-concentrated GC (NGC 2419) and of a low-concentrated GC (NGC 5053) for different stellar samples. The original stellar sample is shown as the gray squares. If we subtract from this profile the constant stellar background we get the profile drawn with blue, filled squares. The black, open squares are the resulting profile if we only count the preselected stellar sample. The shape of the blue and the black profiles are the same (neglecting the radial range outside the tidal radius). Therefore, we conclude that our approach by fitting the King profile to the pre-selected stellar sample and fixing the background to the observed value results in a trustworthy result.

In Figure 2.10–2.18 we show the number density profiles for the clusters in our sample. In the left panel we show the profile derived from the SDSS data. In green we show the profile fitted to the SDSS profile. In the right panel the combined profile is shown, in red the best fit King profile. In both panels we plot in blue the profile based on the parameters from M05. The dashed vertical line is the average background. The filled squares denote the data points, which were included in the fit, the empty squares were not fitted. The errorbars shown are representative. The errorbars are drawn for the declining cluster profile and for a small number of data points in the (flat) background. The errorbars are not drawn anymore if they stay the same. The quoted core and tidal radii for each profile have arcmin as units. The fit to the SDSS profile always resulted in a larger tidal radius r_t with respect to the combined one. Comparing this profile to the observed combined profile the fits are usually rather poor, especially in the inner parts. This is to be expected, as the SDSS profiles lack these inner parts. Further, we have no measure for the completeness of our sample. In some clusters, e.g., NGC 5024, we see the effect of missing stars in the central parts via an unphysical decline for decreasing radius. But we also expect an effect of incompleteness in
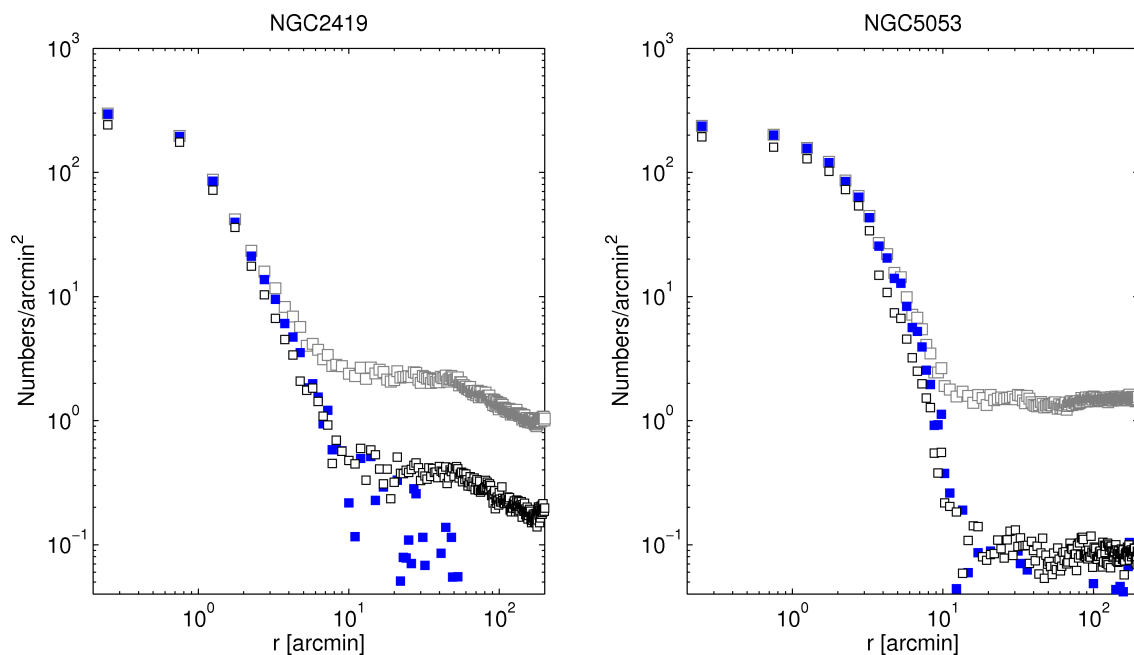
Figure 2.9: Number density profiles of NGC 2419 (left panel) and NGC 5053 (right panel). The profiles drawn in gray are derived from the entire stellar sample. The profiles in blue are the profiles of the entire stellar sample corrected for a constant background. In black we show the profile for the preselected stellar sample.

the other data points: in fact, we fit to an incomplete profile resulting in a steeper slope, in turn increasing the tidal radius.

Special profiles

NGC 7078 is the only post-core-collapsed cluster in our sample. A specific feature of a post-core-collapsed cluster is a steep central cusp in its surface brightness profile. In Figure 2.17 (lower panel) we show the number density profile of NGC 7078. The steep central cusp cannot be traced with the SDSS data. For NGC 7078 no data from M05 is available, therefore we used the values published in Harris (1996). We adopted a fixed core radius $r_c = 0.07'$ (Harris 1996) to fit the SDSS profile. The fit did not result in any reasonable profile. Fitting the combined profile, SDSS+N06, was more successful and resulted in a similar tidal radius as published in Harris (1996). Although the profile drawn with the Harris (1996) parameters does not match the observed profile.

Pal 1 is a very sparse GC. Due to its unique CMD there is a discussion if it is a real GC (Rosenberg et al. 1998). Its CMD is shown in the left panel of Figure 2.32. Above the main sequence only a sparse red giant branch is observed. A crucial issue to obtain a number density profile is to obtain the accurate center of the cluster (N06) and for such a sparse cluster this is not a negligible issue. We used the center published in Harris (1996). The number density profile of Pal 1 is shown in Figure 2.18. It was not possible to fit a King model to the SDSS profile, which shows almost no rising slope for decreasing radius. If we use the central coordinates from SIMBAD[6] the profile does not significantly change. The fit to the combined data is also very questionable. The combined profile shows a rising slope for decreasing radius, but it seems as if the top is not reached. There is definitely no crowding

---

[6]http://simbad.u-strasbg.fr/simbad/

Table 2.3: Measured structural parameters.

NGC		n_{bkg} stars/arcmin^2	Fit to combined profile		Fit to SDSS profile	
			r_c arcmin	r_t arcmin	r_c^* arcmin	r_t arcmin
2419		0.35	0.30 ± 0.05	8.07 ± 0.87	0.32	11.98 ± 0.52
4147		0.14	0.14 ± 0.01	6.29 ± 1.53	0.089	8.36 ± 0.60
5024	M 53	0.11	0.37 ± 0.01	14.79 ± 7.19	0.35	23.64 ± 1.04
5053		0.08	2.23 ± 0.36	12.52 ± 4.49	1.91	13.26 ± 0.82
5272	M 3	0.12	0.41 ± 0.003	31.81 ± 12.30	0.37	32.32 ± 0.92
5466		0.03	1.19 ± 0.09	14.64 ± 2.41	1.53	13.36 ± 0.86
5904	M 5	0.52	1.04 ± 0.06	18.91 ± 2.71	0.42	23.82 ± 1.11
6205	M 13	0.25	0.68 ± 0.02	13.91 ± 0.84	0.55	24.31 ± 0.74
6341	M 92	0.15	0.37 ± 0.01	12.55 ± 0.90	0.26	19.01 ± 0.86
7006		0.99	0.14 ± 0.01	3.62 ± 0.56	0.17	6.57 ± 0.46
7078	M 15	0.16	0.27 ± 0.03	18.35 ± 1.97	0.07	...
7089	M 2	0.13	0.29 ± 0.002	11.72 ± 0.63	0.32	13.18 ± 0.44
	Pal 1	0.13	0.005 ± 1.06	4.09 ± 0.92	0.01	...
	Pal 3	0.03	0.37 ± 0.02	5.75 ± 0.92	0.35	4.27 ± 0.50
	Pal 4	0.15	0.26 ± 0.10	5.30 ± 0.65	0.33	7.86 ± 1.97
	Pal 5	0.15	2.34 ± 0.14	16.03 ± 2.24	2.30	18.24 ± 0.82
	Pal 14	0.07	0.72 ± 0.08	8.82 ± 3.20	0.72	14.0 ± 1.95

[*] Values from McLaughlin & van der Marel (2005)

issue for Pal 1. There is always the issue of completeness, but the SDSS profiles is flat, regardless of the used cluster center.

In Table 2.3 we list the fitted and adopted parameters. In Column (3) we list the observed mean background level. Columns (4) and (5) contain the core and tidal radius fitted to the combined profiles. In column (6) the core radius from M05 is reported, and column (7) contains the fitted tidal radius to the SDSS profiles.
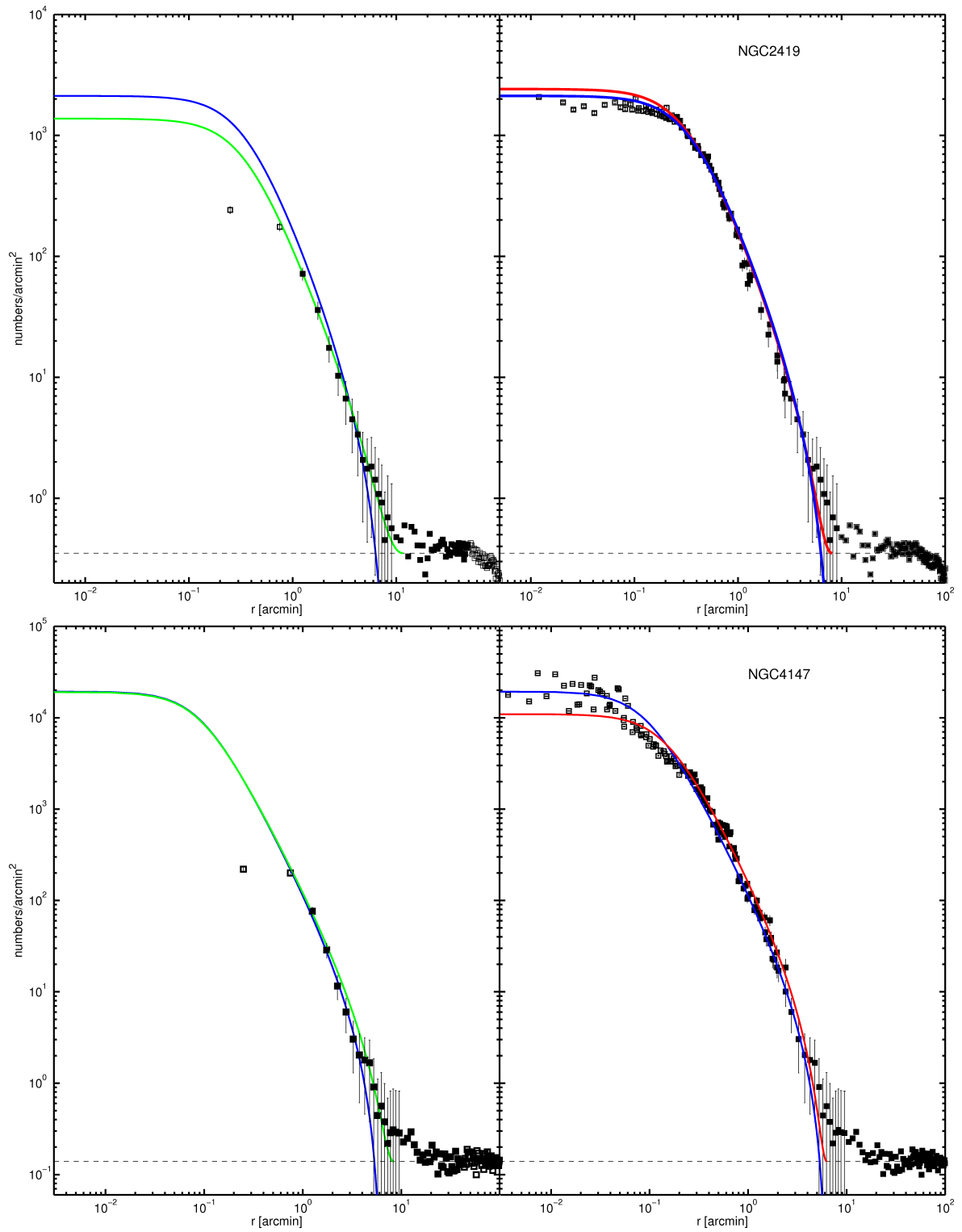
Figure 2.10: *Upper panel:* Number density profile for NGC 2419 from SDSS data (left) and the combined profile (right). In green we show the best fit to the SDSS profile. In red we show the best fit to the combined profile. The blue profile is based on the parameters published in M05. The dashed horizontal line is the average background level. *Lower panel:* Number density profile for NGC 4147. The colors are as in the upper panel.
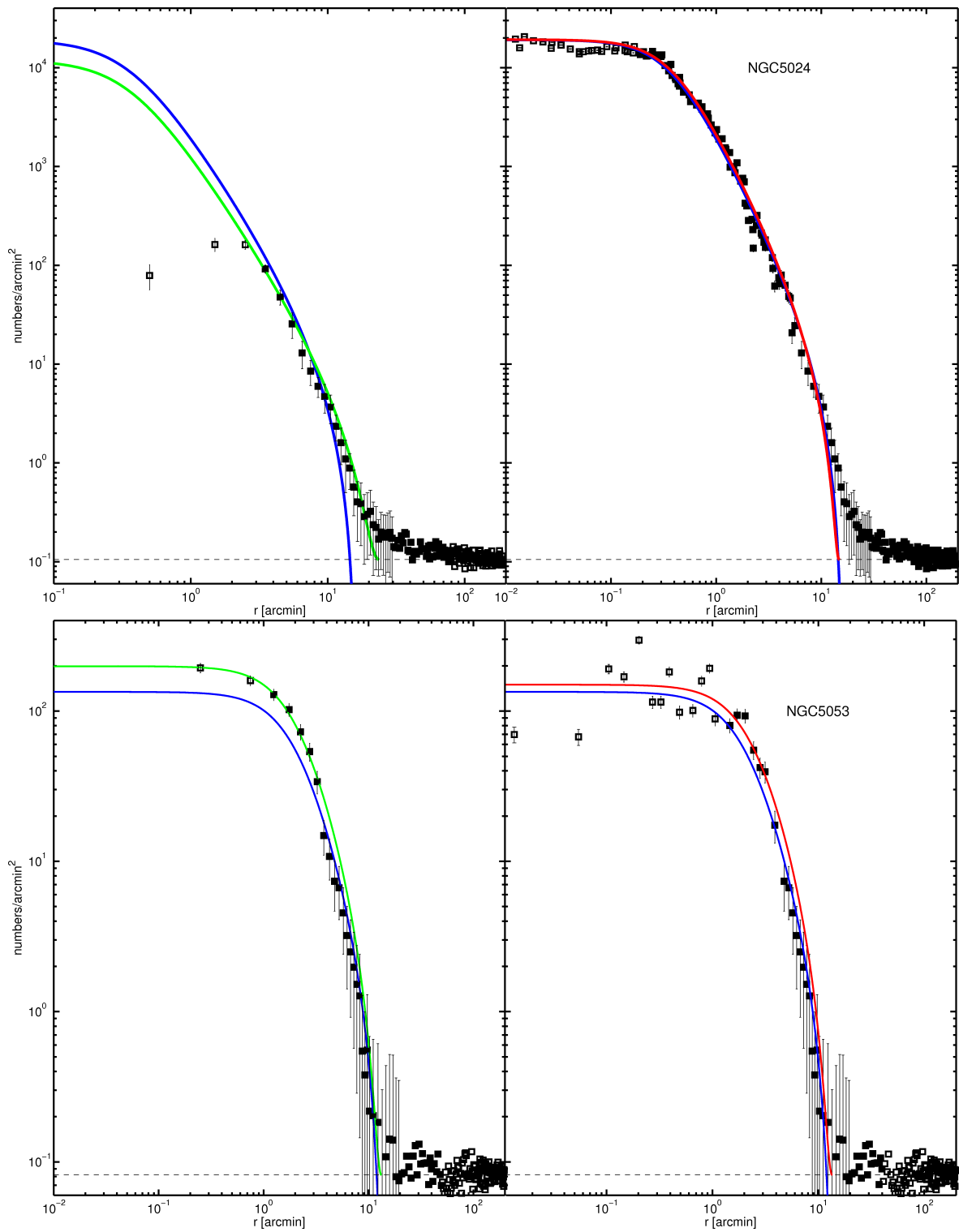
Figure 2.11: *Upper panel:* Number density profile for NGC 5024. *Lower panel:* Number density profile for NGC 5053. The colors are as in Figure 2.10.
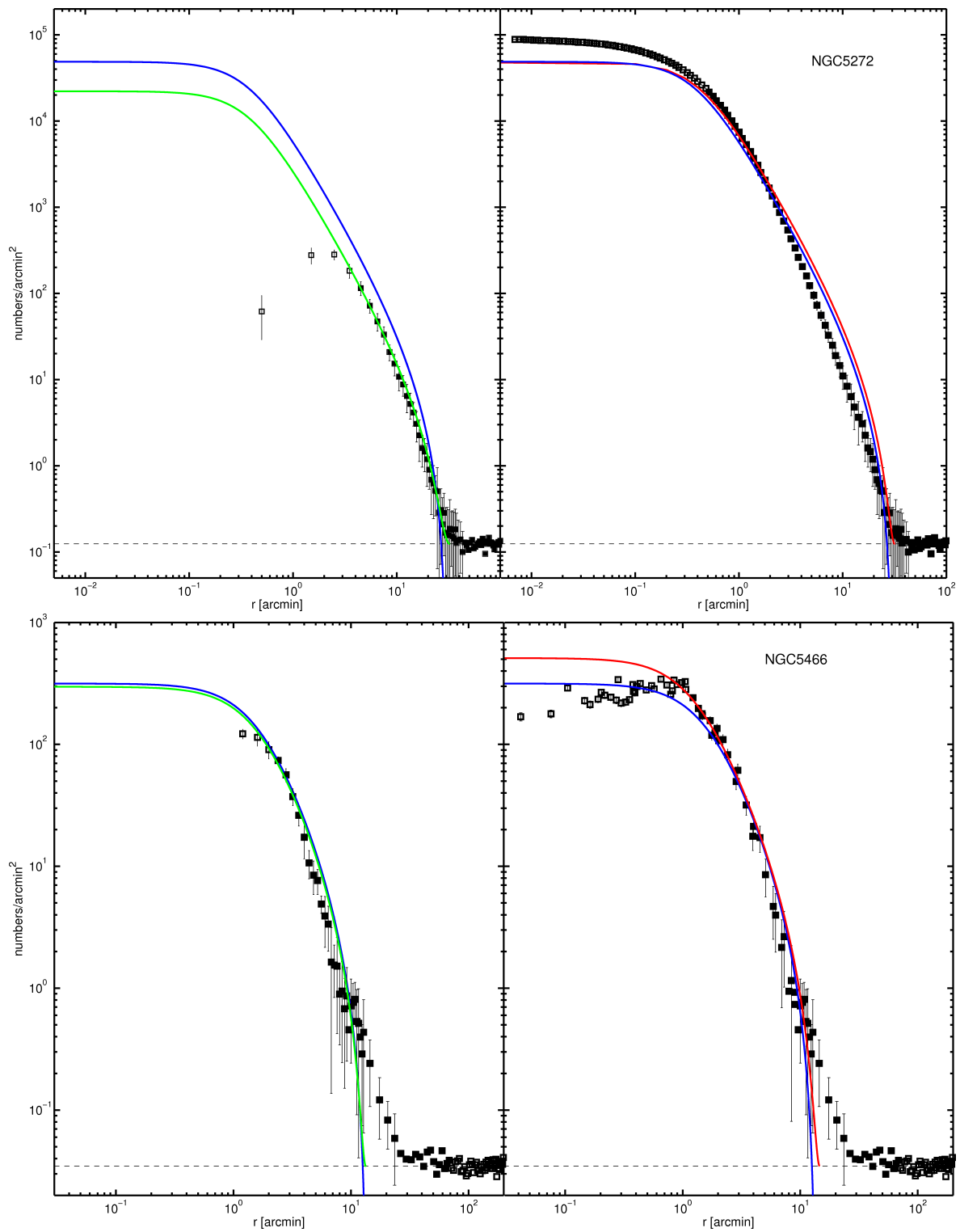
Figure 2.12: *Upper panel:* Number density profile for NGC 5272. *Lower panel:* Number density profile for NGC 5466. The colors are as in Figure 2.10.
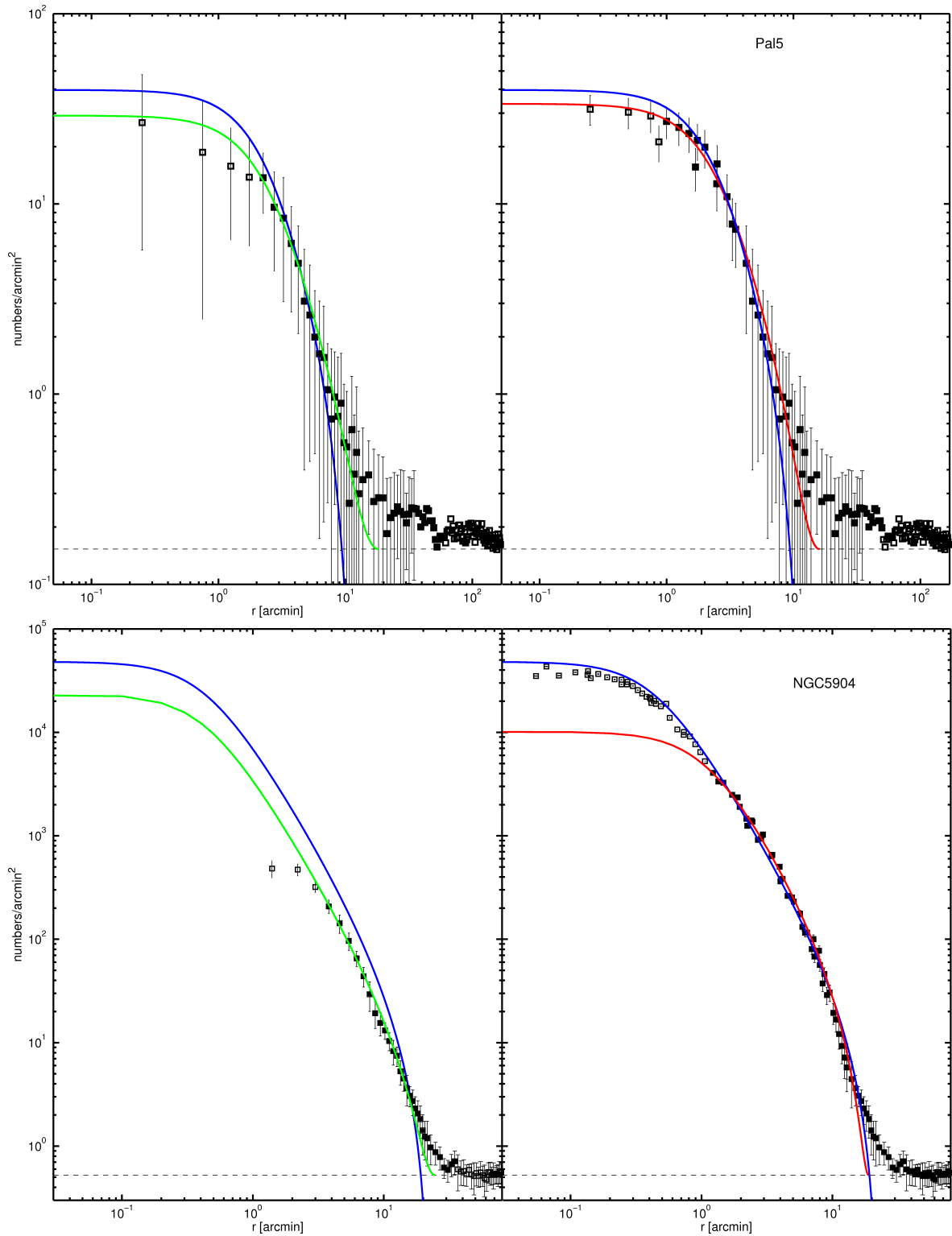
Figure 2.13: *Upper panel:* Number density profile for Pal 5. *Lower panel:* Number density profile for NGC 5904. The colors are as in Figure 2.10.
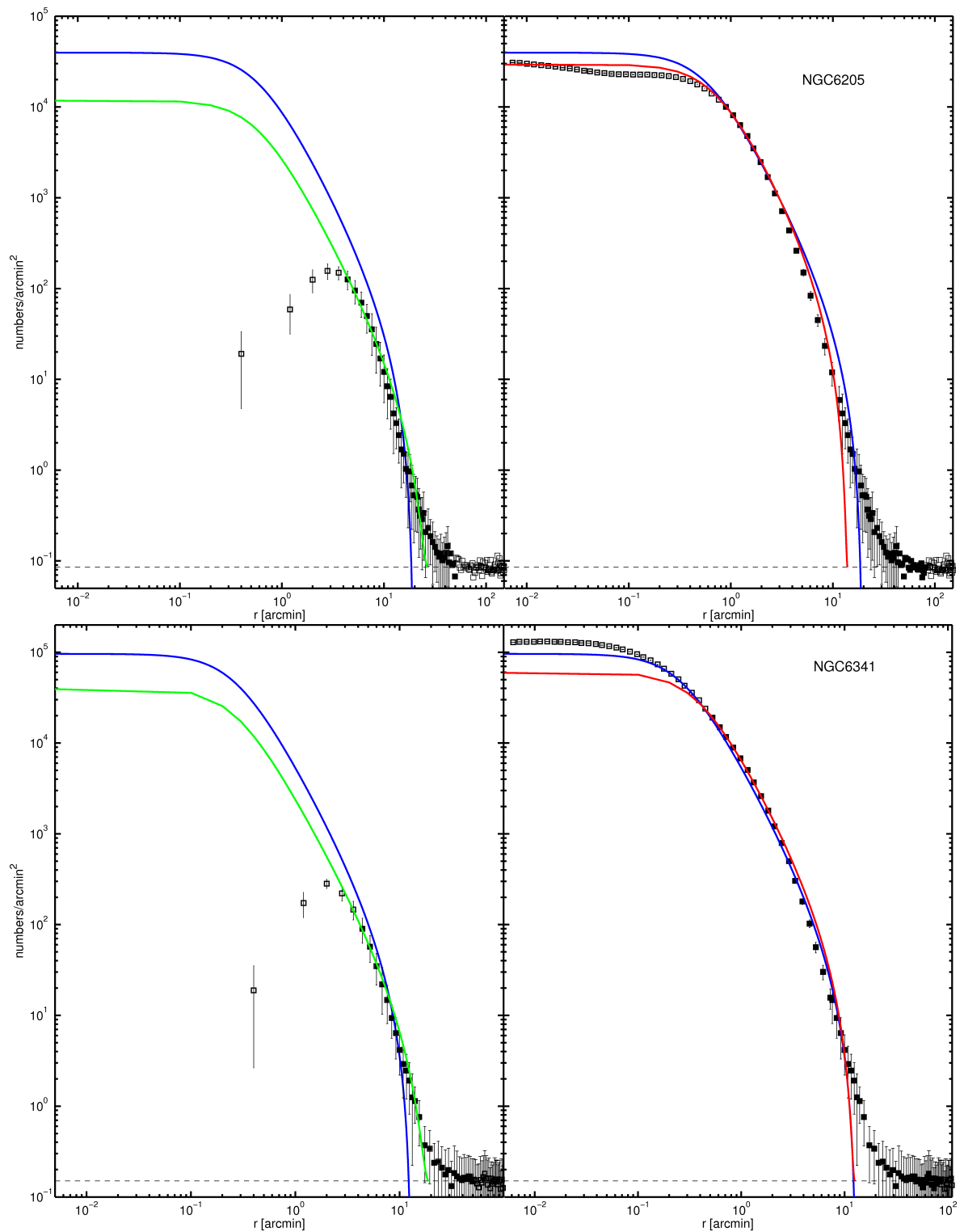
Figure 2.14: *Upper panel:* Number density profile for NGC 6205. *Lower panel:* Number density profile for NGC 6341. The colors are as in Figure 2.10.
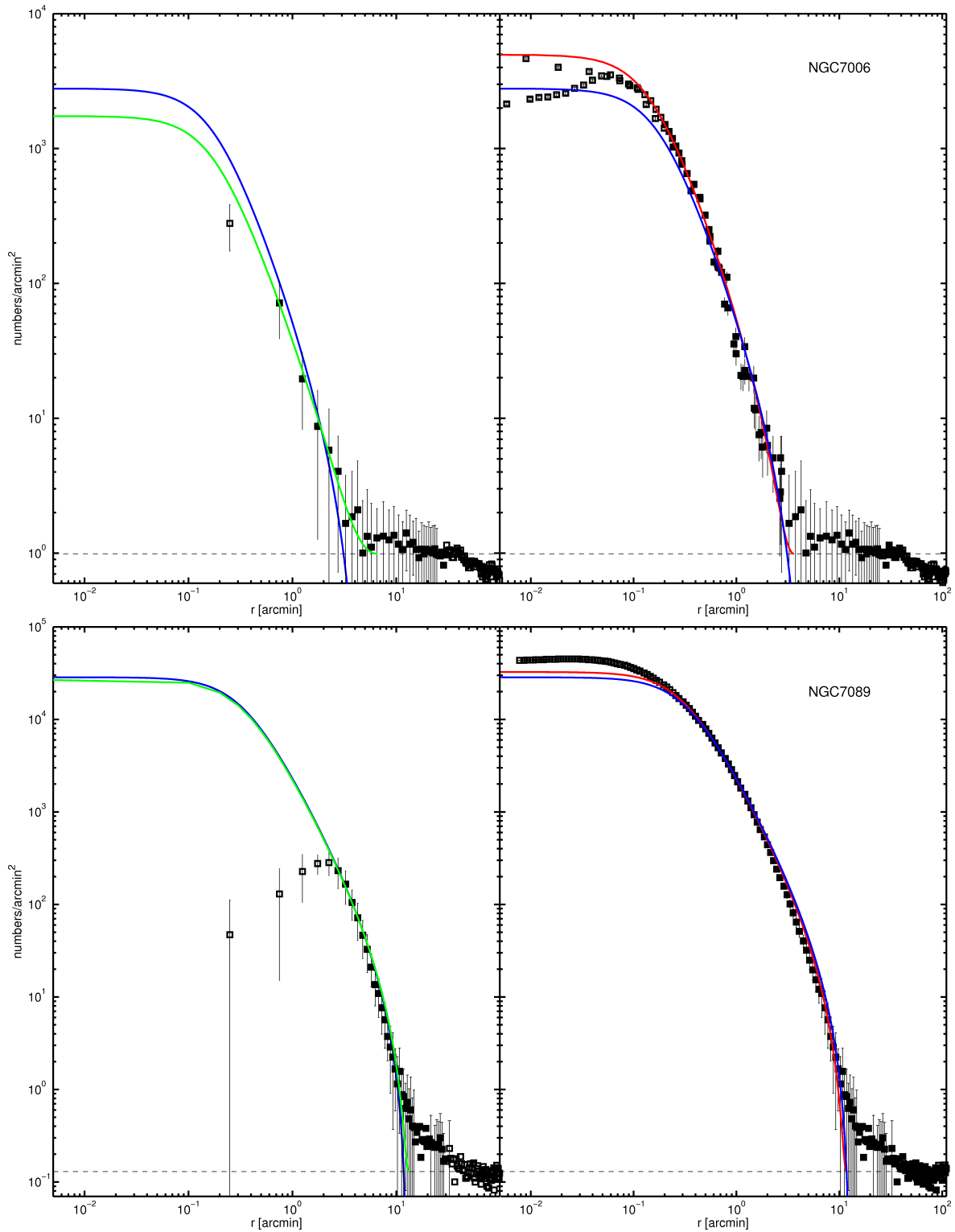
Figure 2.15: *Upper panel:* Number density profile for NGC 7006. *Lower panel:* Number density profile for NGC 7089. The colors are as in Figure 2.10.
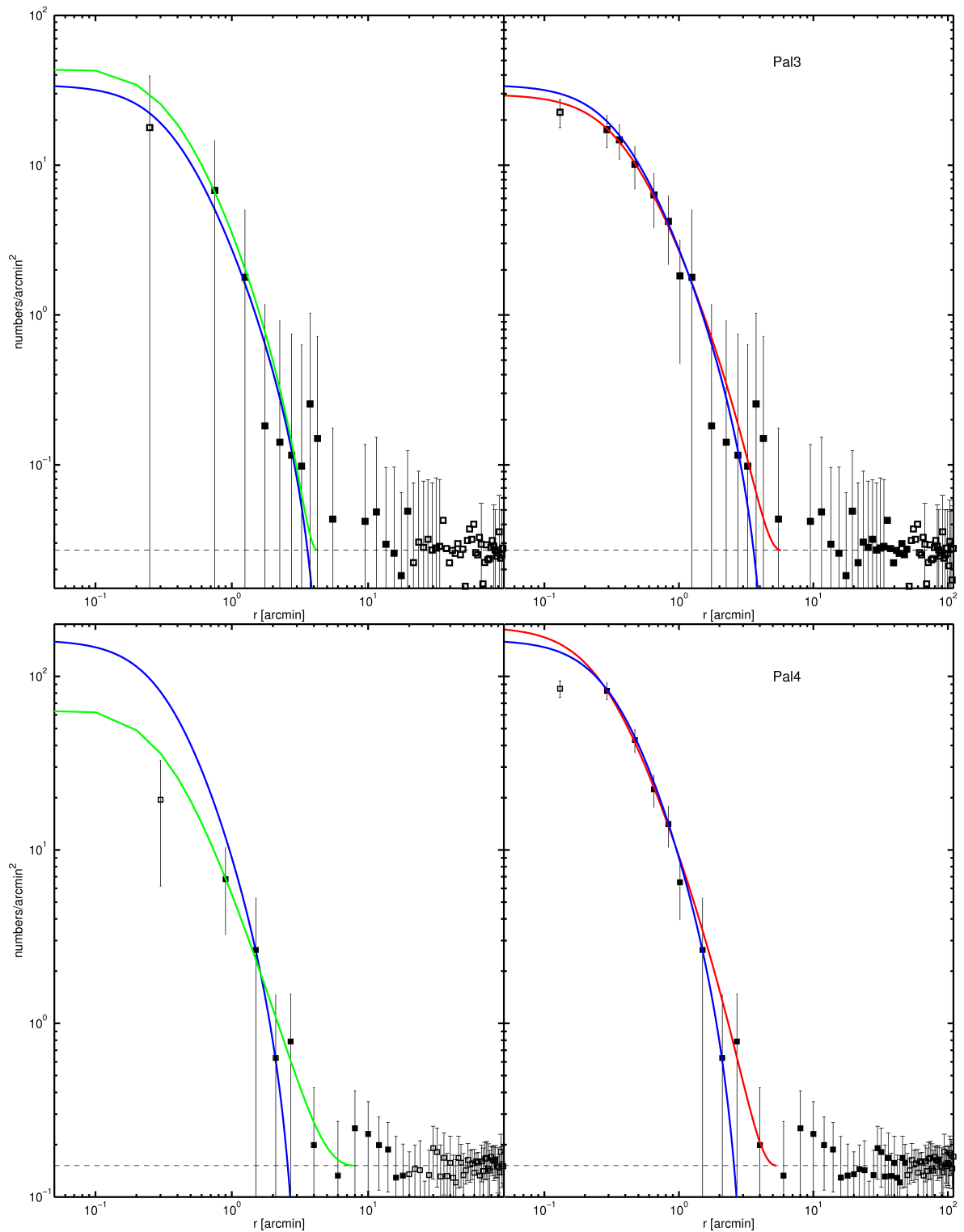
Figure 2.16: *Upper panel:* Number density profile for Pal 3. *Lower panel:* Number density profile for Pal 4. The colors are as in Figure 2.10.
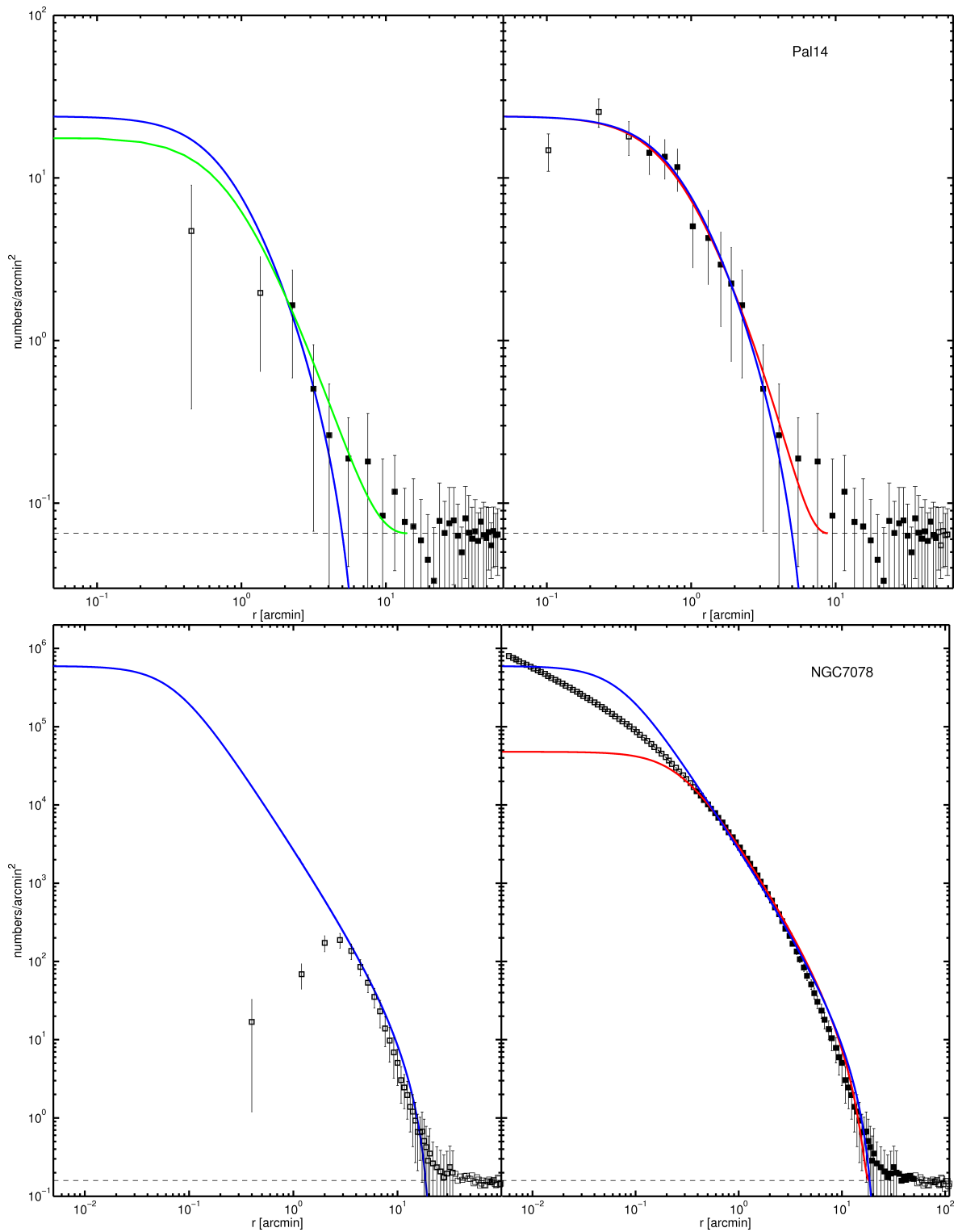
Figure 2.17: *Upper panel:* Number density profile for Pal 14. *Lower panel:* Number density profile for NGC 7078. The colors are as in Figure 2.10.
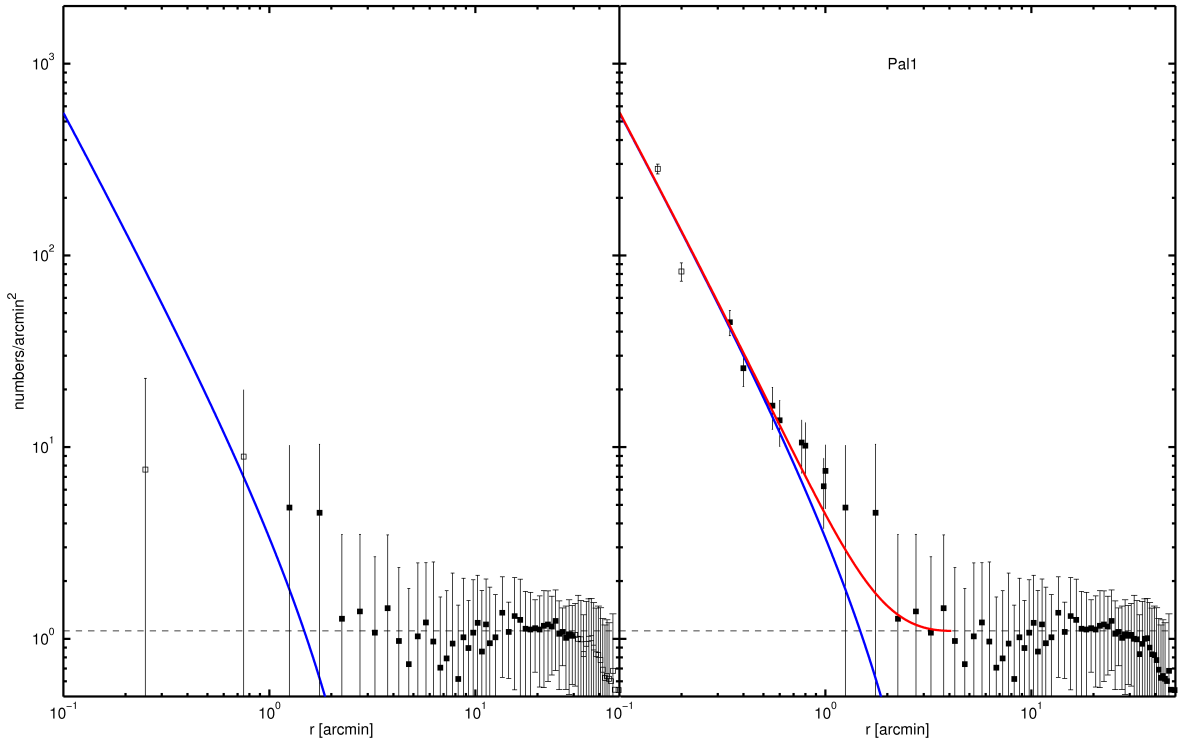
Figure 2.18: Number density profile for Pal 1. The colors are as in Figure 2.10.

2.5   2d structure for the individual globular clusters

In Section 2.3 we described how we selected our stellar sample for each cluster. Further we explained how we counted the (potential) cluster member stars on the sky. The distribution of cluster stars n_C was then smoothed with a Gaussian kernel of size 5×5 cells, corresponding to $15'$.

In Figure 2.19–2.34 we show the resulting contour maps. The top panels show the contour map of a large area centered on the cluster drawn in a Lambert conic projection. The lower panels show a zoom-in on the cluster. In this lower plot the covered area is not too big therefore we did not use any special projection to plot the data, but we corrected the coordinates as followed: $RA_{shown} = X_m + (RA - X_m) \cdot \cos(Y_m)$, where (X_m, Y_m) is the center of the cluster. In this way we take into account that (RA,Dec) are coordinates on a sphere. In all contour maps we plot iso-density lines at levels of

$$1, 2, 3, 5, 7, 8, 10, 20, 40, 60, 80, 100, 200, 400, 600, 800, 1000, 2000 \cdot \sigma_{bkg}$$

above the mean weighted background level n_{bkg}^w. The mean background was derived at least 2 tidal radii away from the cluster and if there were spurious areas, e.g., close neighboring clusters, overlapping SDSS scans, areas outside the SDSS scans, etc., these were not taken into account for its determination. σ_{bkg} denotes the standard deviation of the weighted density in the area, which was used to determine n_{bkg}^w.

In each contour map we draw

- as a solid arrow the direction to the Galactic center ($\alpha = 17^h 45^m 40.04^s$, $\delta = -29°0'28.1''$).
- the direction of the cluster's Galactic motion based on the proper motion from Dinescu et al. (1999) as the dash-dotted arrow.
- the cluster center as a light gray cross.
- as a red ellipse the tidal radius fitted to the combined profile.

- in green the tidal radius from the fit to the SDSS profile.
- as a blue ellipse is the tidal radius from McLaughlin & van der Marel (2005).
- the fields with An photometry by gray polygons.
- the edge of the survey in gray.

In all our contour maps East is to the left and North is up.

Expectations

In Table 2.1 we list the theoretically derived destruction rates due to evaporation ν_{evap} in column (9) and the total rate (incl. the destruction due to disk & bulge shocks) ν_{tot} in column (10) from GO97. The destruction rates are given in units of the inverse Hubble time ($t_{Hubble} = 10^{10}$yr) and defined as $\nu_{destr} = t_{Hubble}/t_{destr}$. I.e., a destruction rate of 1 corresponds to a destruction time of 10 Gyr, a destruction rate of 0.1 indicates a destruction time of 100 Gyr, a destruction rate of 10 results in a destruction time of 0.1 Gyr. From our sample, only NGC 5053, NGC 5466, Pal 1 and Pal 5 have total destruction rates larger than 1. They have the following destruction times: $t_{5053} = 7.2 \cdot 10^8$ yr, $t_{5466} = 3.3 \cdot 10^9$ yr, $t_{Pal1} = 4.4 \cdot 10^8$ yr, and $t_{Pal5} = 1.0 \cdot 10^9$ yr. These clusters are expected to be destroyed first. Therefore we also expect to see some sign of dissolution. For Pal 5 and NGC 5466 this has already been verified. We expect to see their known tidal tails as well. For NGC 5053 some sign of dissolution has also been found and we expect to verify these observations. Pal 1 was not included in any tidal tail search. It is known to be a very diffuse, maybe young (Sarajedini et al. 2007) cluster. It is not clear if it is a true GC.

The vital diagram in Figure 2.1 shows that almost all clusters are located inside of their appropriate *survival triangle*, hence they are likely to survive the next Hubble time. NGC 4147 is the exception. It is located in an area of the diagram, where relaxation processes are dominating the destruction. For the Palomar clusters (except Pal 1 and Pal 5) the shown *survival triangles* are not valid, as the clusters are too remote.

Therefore, we only expect to observe the known tidal tails of Pal 5, NGC 5466, the small features of NGC 5053 and NGC 6341. Also some sign of dissolution for NGC 4147 can be expected.

2.5.1   NGC 2419

NGC 2419 is a very bright, unusually large GCs located at a very large distance from the center of the Milky Way ($R_{MW} = 91.5$ kpc, H96). Previous studies of its surface brightness profile revealed some evidence for extra tidal stars (Bellazzini 2007, and references therein). In the upper panel of Figure 2.10 we show the number density profile. The fitted King profile to the combined profile results within the error in a same value for the tidal radius as the measurement by M05. We also observe an overabundance of stars compared to the fitted King model in the outer parts. As NGC 2419 is very remote, only the upper part of the red-giant branch and the horizontal branch are visible in the SDSS data. In the upper plot of Figure 2.19 we show the contour map of the entire area around NGC 2419. NGC 2419 is clearly detected as the highest peak several σ above the background level of $2.3 \cdot 10^{-2}$ stars arcmin^{-2}. Besides this evident overdensity other peaks exist at smaller levels. These features show sharp edges and a flat central plateau. There is no large tidal tail visible. The area north of NGC 2419 has an artificially increased background density. In this area a SEGUE stripe is overlapping with the original SDSS sky coverage, and we can still detect this area with an increased background density. Also the edge of the SDSS survey is observed south of NGC 2419. The lower plot of Figure 2.19 shows the resulting contour map zoomed in on the cluster. In the northeast we observed distorted contours. Comparable features might be visible on the cluster's southwestern side, but on larger scales no features connected to

NGC 2419 are observed. Casetti-Dinescu et al. (2009) speculated that NGC 2419 might be the nucleus of a (former) dwarf galaxy with the Virgo Stellar Stream being its tidal tail. With a tidal radius of 8.07 arcmin, we observe a large halo of extra tidal stars. But no large scale tidal feature is observed.

2.5.2 NGC 4147

From the position in the vital diagram (Figure 2.1) we expect to observe signs for the dissolution of NGC 4147. This cluster is currently about 18.7 kpc (Dinescu et al. 1999) away from the Galactic center, close to apogalacticon $R_{apo} = 25.5$ kpc. In the lower plot of Figure 2.10 we show its number density profile. We observe more stars in the cluster's outer parts as expected from the fitted King profile. In Figure 2.20 we plot the contour map of the cluster. In the upper plot we show the entire observed area on the sky around NGC 4147. NGC 4147 is identified as the highest density peak in the field. The large area plot reveals a variable background. We did not detect any large scale structure. The zoom-in in the lower panel reveals a very complex morphology. The 1σ contour appears to indicate S-shaped tidal arms extending over several tidal radii in southern and northern directions. Such a multiple arm morphology is predicted by Montuori et al. (2007) for clusters on elliptical orbits ($e_{4147} = 0.73$) close to apogalacticon. NGC 288 (Leon et al. 2000) and Willman I (Willman et al. 2006) have a similar complex morphology, showing three tidal arms. The tidal radius of 6.29 arcmin also reveals a halo of extra tidal stars confirming the findings by previous authors. Martínez Delgado et al. (2004) investigated the CMD of NGC 4147 and of a comparison field close by. They detected some hints for extra tidal cluster stars. NGC 4147 might be a former member of the Sagittarius dwarf galaxy (Bellazzini et al. 2003; Martínez Delgado et al. 2004). Bellazzini et al. (2003) found stars of the Sagittarius tidal arm in the vicinity of NGC 4147. They conclude that this cluster might be connected to the Sagittarius dwarf (Sgr dwarf). Recently, Law & Majewski (2010) investigated the association of MW GCs with the Sgr dwarf based on the authors' newest Sgr model. The authors conclude, in contrast to earlier studies (e.g., Bellazzini et al. 2003; Forbes & Bridges 2010), that NGC 4147's association with the Sgr dwarf is of relative low confidence. It is thus unclear whether the extended features we observe are a feature of the Sgr dwarf field population. In any case, these stars are located at a similar distance as the cluster.

2.5.3 NGC 5024 (M53)

NGC 5024 is, in projection on the sky, a very close neighbor of NGC 5053, although the two clusters are more than 1 kpc away from each other in the radial direction. NGC 5024 is currently located about 18.4 kpc from the Galactic center close to its perigalacticon $R_{peri} = 15.7$ kpc. The upper plot of Figure 2.11 shows its number density profile. The King model fitted to the combined profile reveals extra tidal stars. In Figure 2.21 we plot the contour map of the cluster. In the upper panel, the contour map of the entire observed area is shown. The cluster is clearly detected as the highest density peak. In the surrounding field mostly features up to 3σ above the mean of 0.6 stars arcmin^{-2} are observed. Southeast of NGC 5024 the close neighbor NGC 5053 is detected, but no connection between the two is observed in contrast to the findings of Chun et al. (2010). The black solid polygon shows the area observed by Chun et al. (2010). We find a strong (9σ) overdensity at $(198.2, 16.3)$. In Figure 2.22 this overdensity is not recognizable anymore. Therefore, we argue that it is an overdensity at the distance of NGC 5024. We found exactly one possible BHB/RR Lyrae star centered on the overdensity. It is still debated in the literature whether NGC 5024 is associated with the Sgr tidal stream (see Bellazzini et al. 2003b; Law & Majewski 2010). Our
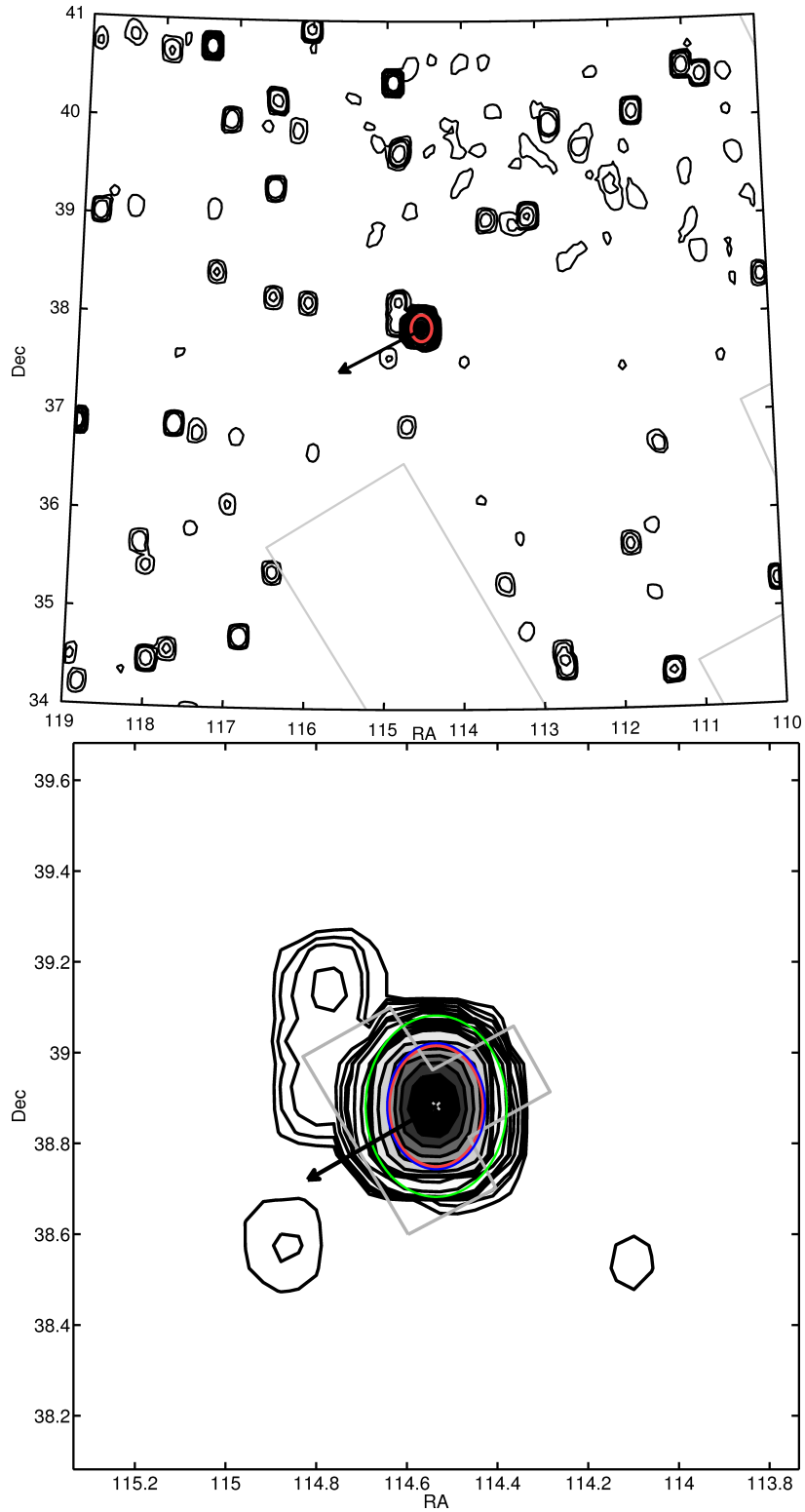
Figure 2.19: Contour plot of NGC 2419. *Upper panel:* A large area around NGC 2419 is shown. *Lower panel:* Zoom-in on NGC 2419. The red ellipse marks the tidal radius fitted to the combined number density profile. In green, we show the tidal radius fitted to the SDSS number density profile. The blue ellipse is the tidal radius from M05. The solid black arrow points in the direction of the Galactic center. The area outlined by the gray polygon marks the region with An et al. (2008) photometry. The contour lines are drawn at levels of $1, 2, 3, 5, 7, 8, 10, 20, 40, \ldots, 100, 200, 400, 600, 800, 1000, 2000 \cdot \sigma_{bkg}$ above n_{bkg}^{w}.
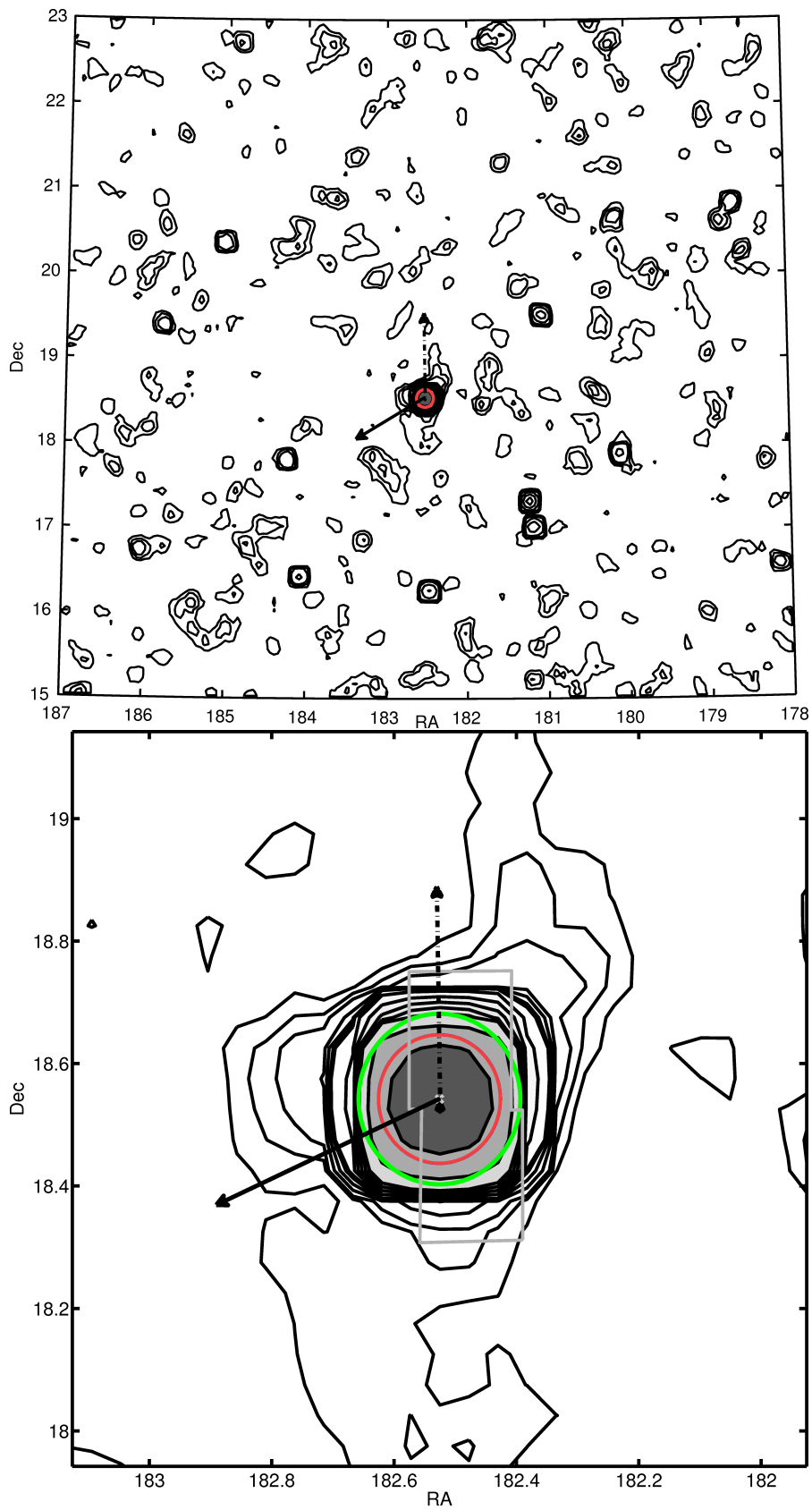
Figure 2.20: Same as Figure 2.19 for NGC 4147. The black solid arrow points toward the Galactic center. The black dashed arrow shows the direction of its Galactic motion based on the proper motions stated in Table 2.1.

data do not permit us to conclude whether the overdensity is related to NGC 5024 or the Sgr stream. We found no obvious large scale structure connected with NGC 5024. The zoom-in on NGC 5024 shows interesting features. The contours are spherical and smooth not only in the cluster center, but also in the pronounced extratidal halo. The 1σ contour is strongly influenced by the background. Chun et al. (2010) also observed NGC 5024 and NGC 5053. They detected a tidal-bridge like feature around the two GCs and tidal features that may be due to dynamical interaction between the two clusters. Their findings are in contrast to our observations.

2.5.4   NGC 5053

NGC 5053 located about 16.9 kpc from the Galactic center. Lauchner et al. (2006) studied the 2D distribution of NGC 5053 and detected extratidal features east and west of the cluster. NGC 5053 is believed to be a member of the Sgr dSph (Bellazzini et al. 2003b). In Figure 2.22 we show its contour map. In the large area contour map we see no pronounced large scale structure, but we definitely detect the GC and also random background noise up to 3σ above the mean of $4.1 \cdot 10^{-2}$ stars arcmin^{-2}. The high overdensity northeast of the cluster is NGC 5024. The right panel of Figure 2.22 is a zoom-in on NGC 5053. It reveals distorted contour lines. We observe a halo of extratidal stars. Towards the northeast and west the contours show a strong asymmetry. Similar features were observed by Lauchner et al. (2006). We see a one-armed tail-like extension toward the north-west. Such a structure is also seen to emerge from NGC 5024 (both in Figures 2.21 & 2.22). Our data do not permit us to tell whether these curious one-armed features are tidal tails. Law & Majewski (2010) classify NGC 5053 as moderately likely associated with the Sgr dwarf. Therefore, it is possible that we are looking at substructure in the Sgr dwarf field population. Forbes & Bridges (2010) discuss the possibility that NGC 5053 or NGC 5024 might be the remnant nucleus of a dwarf galaxy. The number density profile is shown in Figure 2.11. It is interesting to note that the density profile does not reveal a pronounced extratidal feature. Also Lehmann & Scholz (1997), on photographic plates, did not find any indications for tidal tails. Chun et al. (2010) observed NGC 5053 together with NGC 5024, and as stated earlier we do not reproduce their findings.

2.5.5   NGC 5272 (M3)

NGC 5272 is 11.5 kpc away from the Galactic center, located close to apogalacticon $R_{apo} = 13.7$ kpc. Compared to other clusters in our sample NGC 5272 has a low expected destruction rate. The upper panel of Figure 2.12 shows its number density profile. We are not able to find a King profile that traces the observed profile entirely. The profile with M05 parameters does not reproduce the slope of our combined profile. Our fitted profile shows a (too?) large extra tidal halo. In Figure 2.23 we show the contour map of this cluster. In the zoom-in plot we see that our determined tidal radius is definitely too small. The tidal radius from the SDSS profile and from M05 matches the observations better. But the number density profile with M05 parameters does not match the entire observed profile. The inner contours are smooth and round. On the other hand the outer contours up to 3σ show distortions. The extreme distortions of the lowest contour is likely to be induced by the background. There is no large scale tidal structure observed. The background shows random density peaks of up to 3σ above the mean of $4.45 \cdot 10^{-2}$ stars arcmin^{-2}. Leon et al. (2000) studied the 2d distribution of NGC 5272 and found extra tidal features correlated to dust emission. Our contours do not show any correlation with the dust. Also Grillmair & Johnson (2006) investigated the 2d-structure of NGC 5272 with SDSS and did not detect any tidal structure.
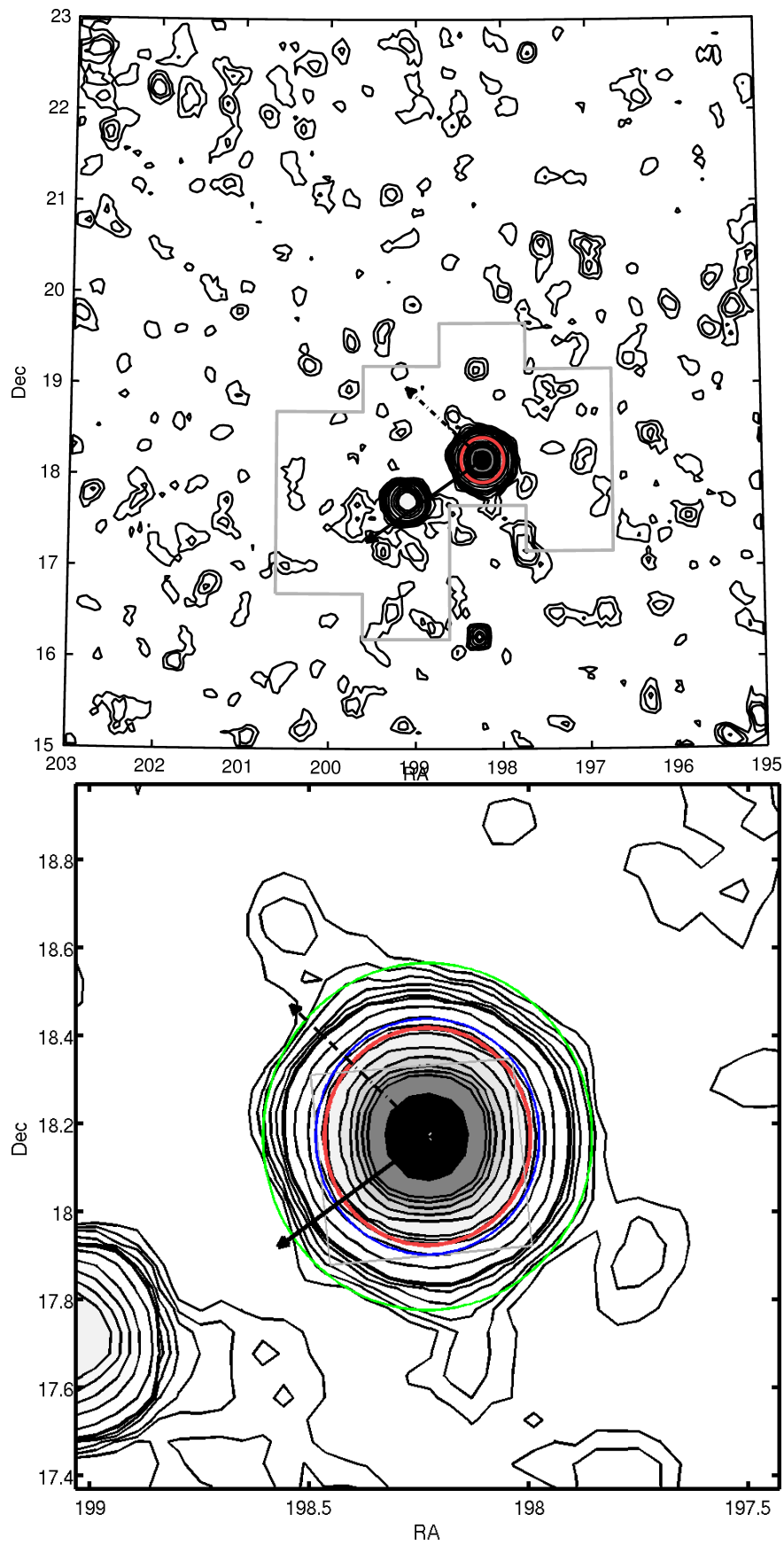
Figure 2.21: Same as Figure 2.20 for NGC 5024.
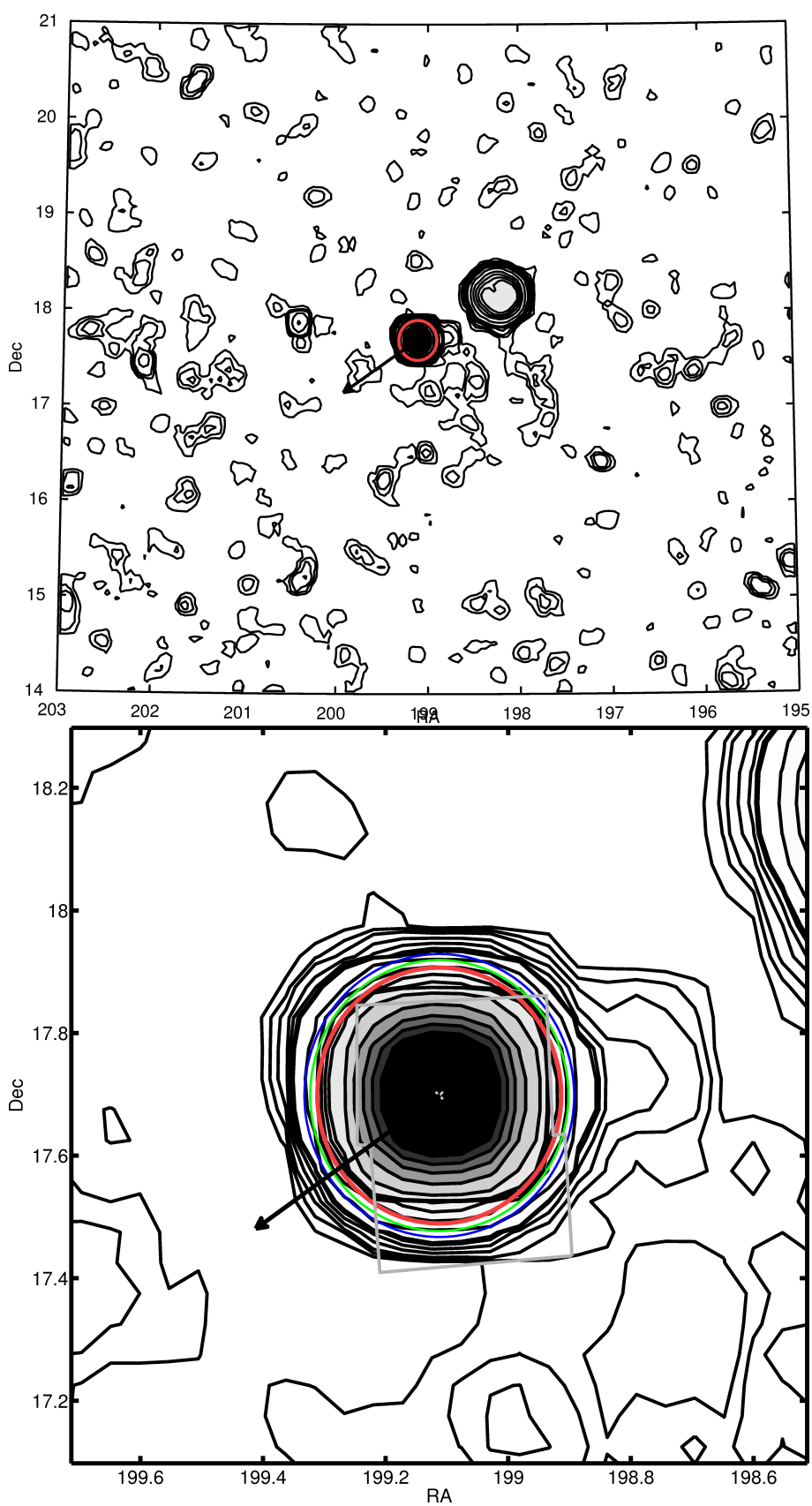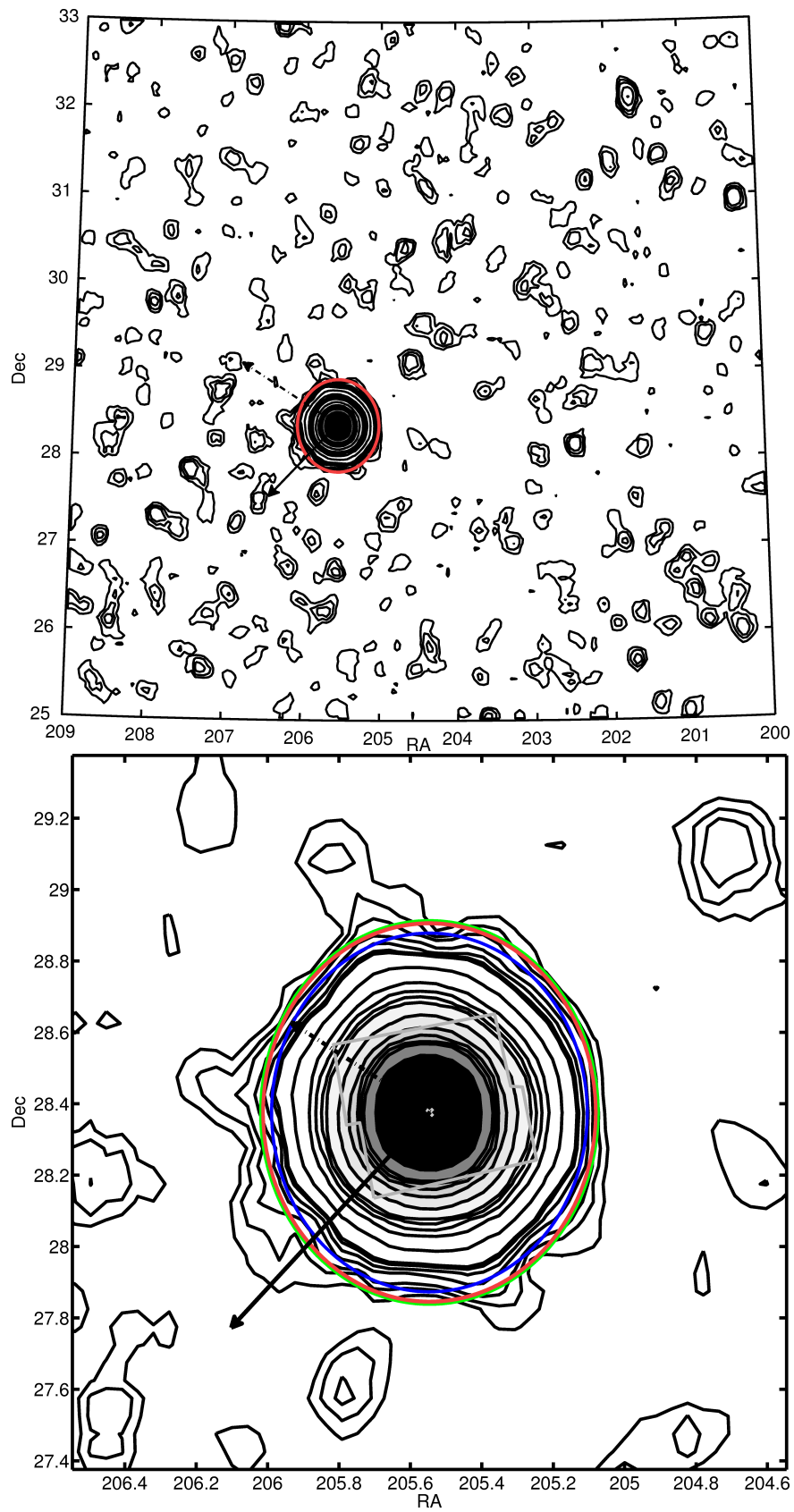
Figure 2.22: Same as Figure 2.20 for NGC 5053.

Figure 2.23: Same as Figure 2.20 for NGC 5272.

2.5.6   NGC 5466

Belokurov et al. (2006) studied the 2d distribution of NGC 5466 with SDSS data and detected a 4°-long tidal tail (see right panel in Figure 2.3). Grillmair & Johnson (2006) extended this tidal tail to 45°. We also detect the large extra tidal halo of NGC 5466. In Figure 2.24 (lower panel) we show the contour plot of the square degree around the cluster. The Northwest to Southeast extension of the tidal tail is clearly visible. The contour plot of the larger area also reveals the tidal tails close to the cluster. The long extensions are hard to distinguish. There are random foreground peaks of up to 5σ above the mean of $4.5 \cdot 10^{-2}$ stars arcmin^{-2}. This is also the case in the plots of Grillmair & Johnson (2006). NGC 5466 is currently at a distance of 15.8 kpc from the Galactic center, close to its perigalacticon $R_{peri} = 6.6$ kpc. The inner tidal tails are aligned with the cluster orbit as predicted by Montuori et al. (2007). Fellhauer et al. (2007) modeled the destruction of NGC 5466 and was able to reproduce the detected tidal tail. They further state that this cluster is mainly destroyed by tidal stripping at each perigalacticon, and that the destruction due to 2-body relaxation plays a minor role. This is in agreement with the destruction rates calculated by GO97.

2.5.7   Pal 5

Pal 5 is located 18.6 kpc from the Galactic center. Odenkirchen et al. (2003) studied the distribution of cluster stars with SDSS data and found tidal tails spanning 10° on the sky. Already Odenkirchen et al. (2001) and Rockosi et al. (2002) found Pal 5's tidal tails with SDSS data. Grillmair & Dionatos (2006) extended these tails to $\sim 20°$. Odenkirchen et al. (2002) measured the line-of-sight velocity dispersion of Pal 5 and concluded that the dispersion and the surface density profile are consistent with a King profile of $W_0 = 2.9$ and $r_t = 16.1'$, similar to the values found here. The disruption of Pal 5 was modeled in Dehnen et al. (2004) based on the initial observations of Odenkirchen et al. (2003). Vivas & Zinn (2006) studied RR Lyrae stars in the QUEST survey. They observed an overdensity of RR Lyrae stars in the vicinity of Pal 5. Some of these stars trace the cluster's tidal tails. Figure 2.13 shows the number density profile of Pal 5. The overabundance of member stars due to the tidal tails is clearly visible as a pronounced break in the profile. In Figure 2.25 we show the derived contour maps. In the large area view the tidal tails are clearly visible emanating from the cluster. In the zoom-in the $\mathcal{S}$-shape is observed as predicted by theory. The background harbors fluctuations several σ above the mean of $1.1 \cdot 10^{-1}$ stars arcmin^{-2}. Koch et al. (2004) show that the mass segregation in Pal 5 extends to its tidal tails, which contain predominantly low mass stars. Based on a kinematic study of the stars in the tails of Pal 5, Odenkirchen et al. (2009) suggest that the cluster's orbit is not exactly aligned with its tails.

2.5.8   NGC 5904 (M5)

NGC 5904 is currently 6.1 kpc away from the Galactic center, close to its perigalacticon $R_{peri} = 2.5$ kpc. I.e., potential tidal tails are aligned with the cluster's orbit. In the number density profile, shown in the lower panel of Figure 2.13, no change in slope is observed. The King profile of M5 traces the entire profile. In Figure 2.26 we show the contour map. The GC is detected as the highest density peak, while the background only shows contours at levels of 2σ above the mean of $1.2 \cdot 10^{-1}$ stars arcmin^{-2}. Also in this description the GC seems more or less undisturbed inside the tidal radius. The three lowest contours outside the tidal radius show distortions. The contours are elongated in the direction of motion possibly indicating weak evidence of tidal tails. Leon et al. (2000) has also studied the 2d distribution of this cluster before. They also observed round contours in the center and more boxy like contours
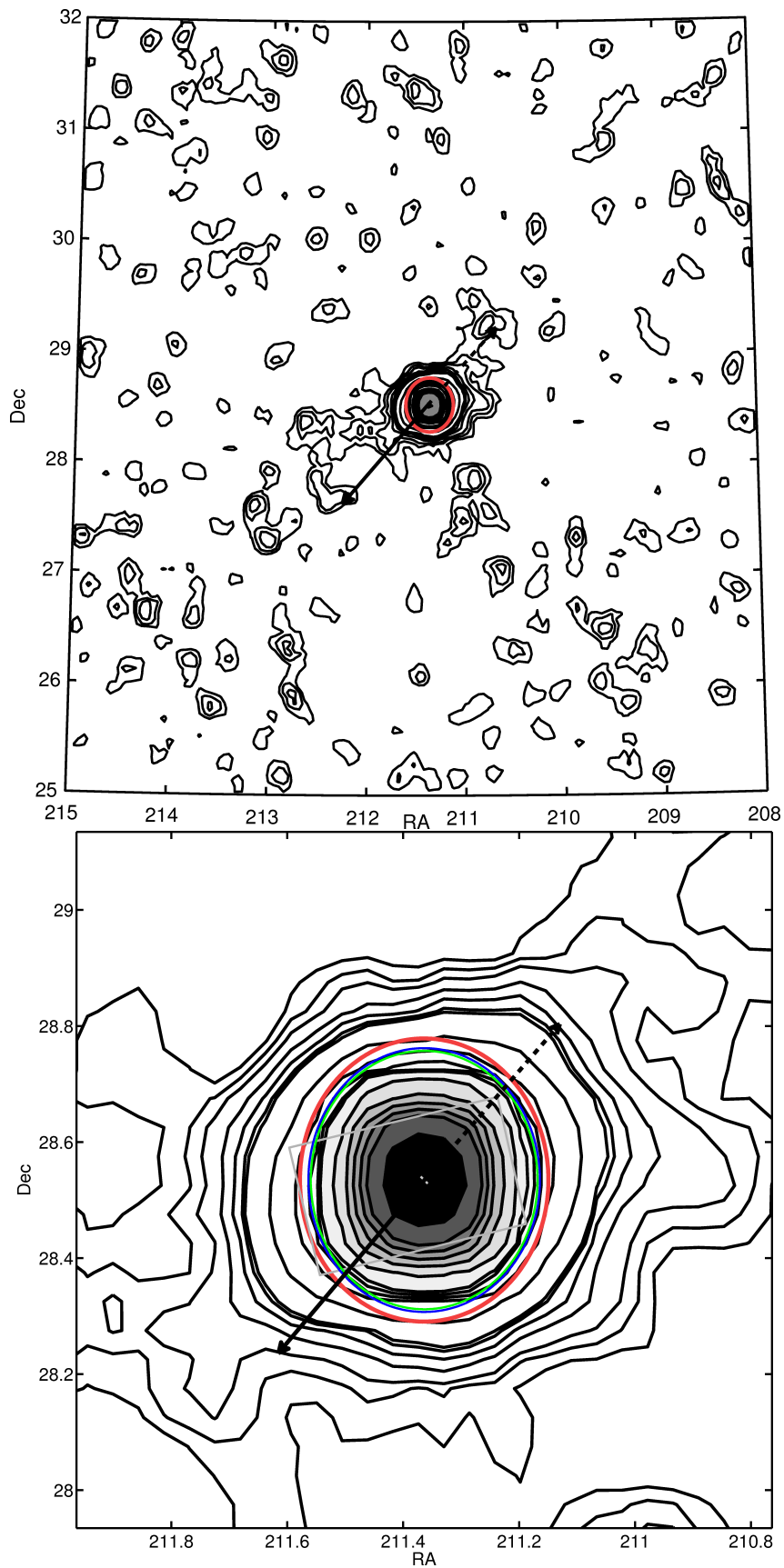
Figure 2.24: Same as Figure 2.20 for NGC 5466.
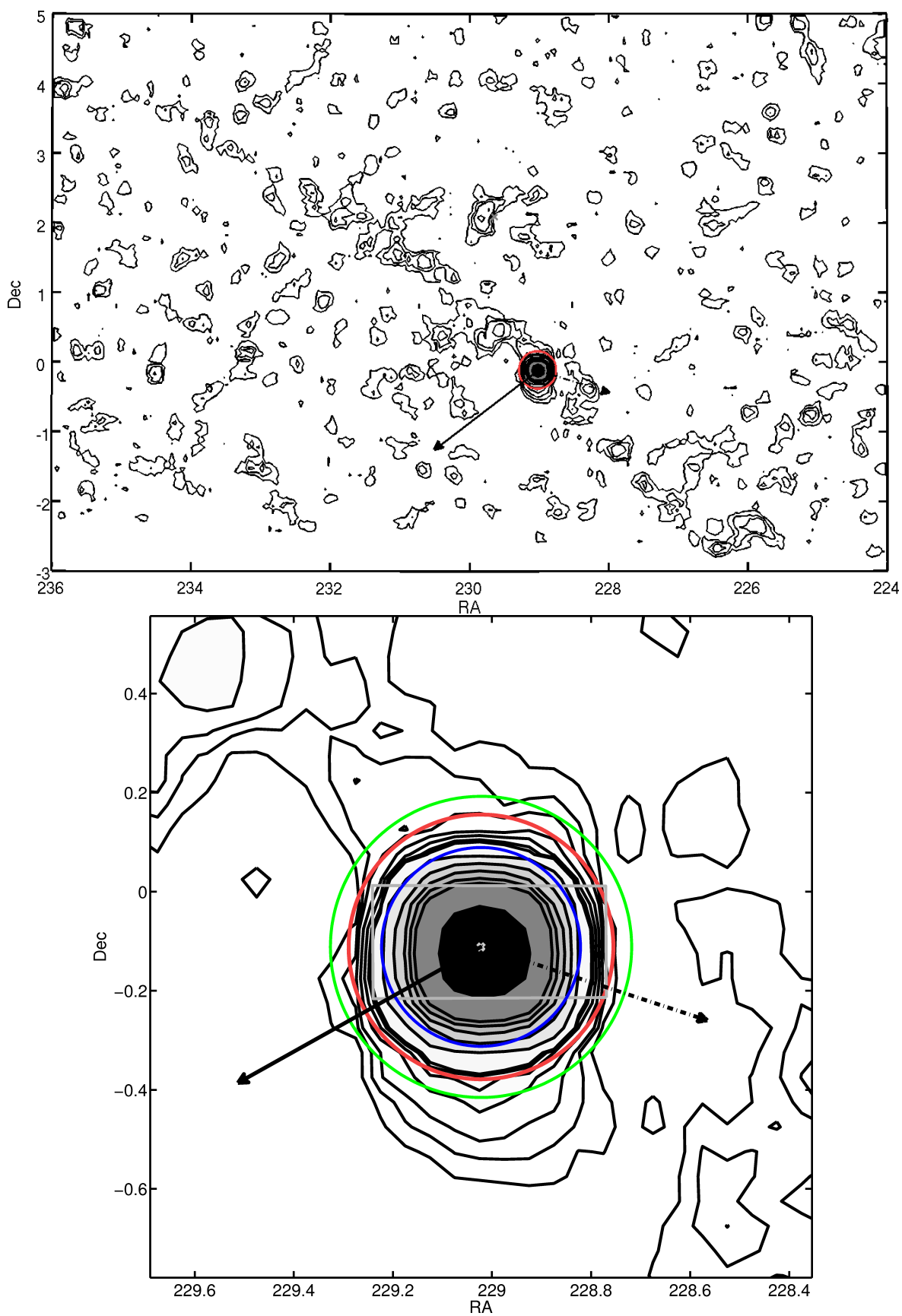
Figure 2.25: Same as Figure 2.20 for Pal 5.

at the outer parts. But in both cases no large extra tidal halo was observed. The destruction rate is dominated by internal processes (GO97). NGC 5904 is approaching perigalacticon, starting its crossing of the Galactic disk Odenkirchen et al. (1997).

2.5.9   NGC 6205 (M13)

NGC 6205 is currently 8.2 kpc from the Galactic center, close to its perigalacticon $R_{peri} = 5.0$ kpc. Thus, we can expect potential tidal tails to be aligned with the orbital path. In Figure 2.27 we show the resulting contour plot. the GC is detected as the highest density peak. The background shows contours only up to 2σ above the mean of $1.2 \cdot 10^{-1}$ stars arcmin^{-2}. The central contours are smooth. The contours in the outer regions of the cluster show distortions. The beginning of a characteristic $\mathcal{S}$-shape might be visible in the southeast in direction to the Galactic center. On the opposite side of the cluster such a tidal extension is hard to identify. Also further away from the cluster we see no extra tidal material. We detect a halo of extra tidal stars with a slight elongation in the direction of the proper motion. The number density profile in Figure 2.14 reveals an overabundance of stars around the tidal radius. Leon et al. (2000) studied the 2d distribution of NGC 6205 as well. They also detected disturbed contours in the southeast, corresponding to the feature visible in our data.

2.5.10   NGC 6341 (M92)

NGC 6341 is located 8.2 kpc away from the Sun, close to its apogalacticon $R_{apo} = 9.9$ kpc. In Figure 2.28 we show our derived contours of NGC 6341. In the upper panel the effect of missing data due to the edge of the SDSS in the Southeast corner is visible. Northeast of the cluster we detected a larger average background. A SEGUE stripe is overlapping with the traditional SDSS survey, artificially increasing the number of stars. We corrected for this. All stars in the area denoted by the dashed gray line were studied. If two stars were closer than $2''$ and similar in color and magnitude one of the stars was deleted from the sample. As seen in the contour map in this way we were able to reach almost the same background level as in any other area of our contour map. We clearly detect the GC as the main overdensity, no large scale tidal structure emanate from NGC 6341. The mean background level was determined in the area northeast and southwest of the cluster ignoring the spurious areas. The mean background is $9.6 \cdot 10^{-2}$ stars arcmin^{-2}. The zoom-in in the lower panel of the same figure reveals mostly smooth contours. Around the tidal radius the contours are distorted. The main distortion is in the direction of the stronger background. But also along a southwest to northeast axis we detect extra tidal material. The 2d structure of NGC 6341 has been studied before by Testa et al. (2000). They observed somewhat elongated contours in the same direction as we do. The number density profile in the lower panel of Figure 2.14 shows an overabundance of stars around the tidal radius.

2.5.11   NGC 7006

NGC 7006 is one of the most remote clusters in our sample with a distance to the Galactic center of $R_{MW} = 38.8$ kpc. The cluster is currently moving toward the Galactic plane and the Galactic center (Dinescu et al. 2001). It has not been included in any study on tidal tails searches so far. In Figure 2.29 we show its contour map. We clearly detect the GC as the highest overdensity. The 1σ-contour is very distorted and comparable to the background noise. The mean field background level is $1.2 \cdot 10^{-1}$ stars arcmin^{-2}. The 2σ and 3σ contours show some symmetric distortion. All higher contours are smooth, although the halo of extratidal stars for NGC 7006 is huge. For no other cluster in our sample we find
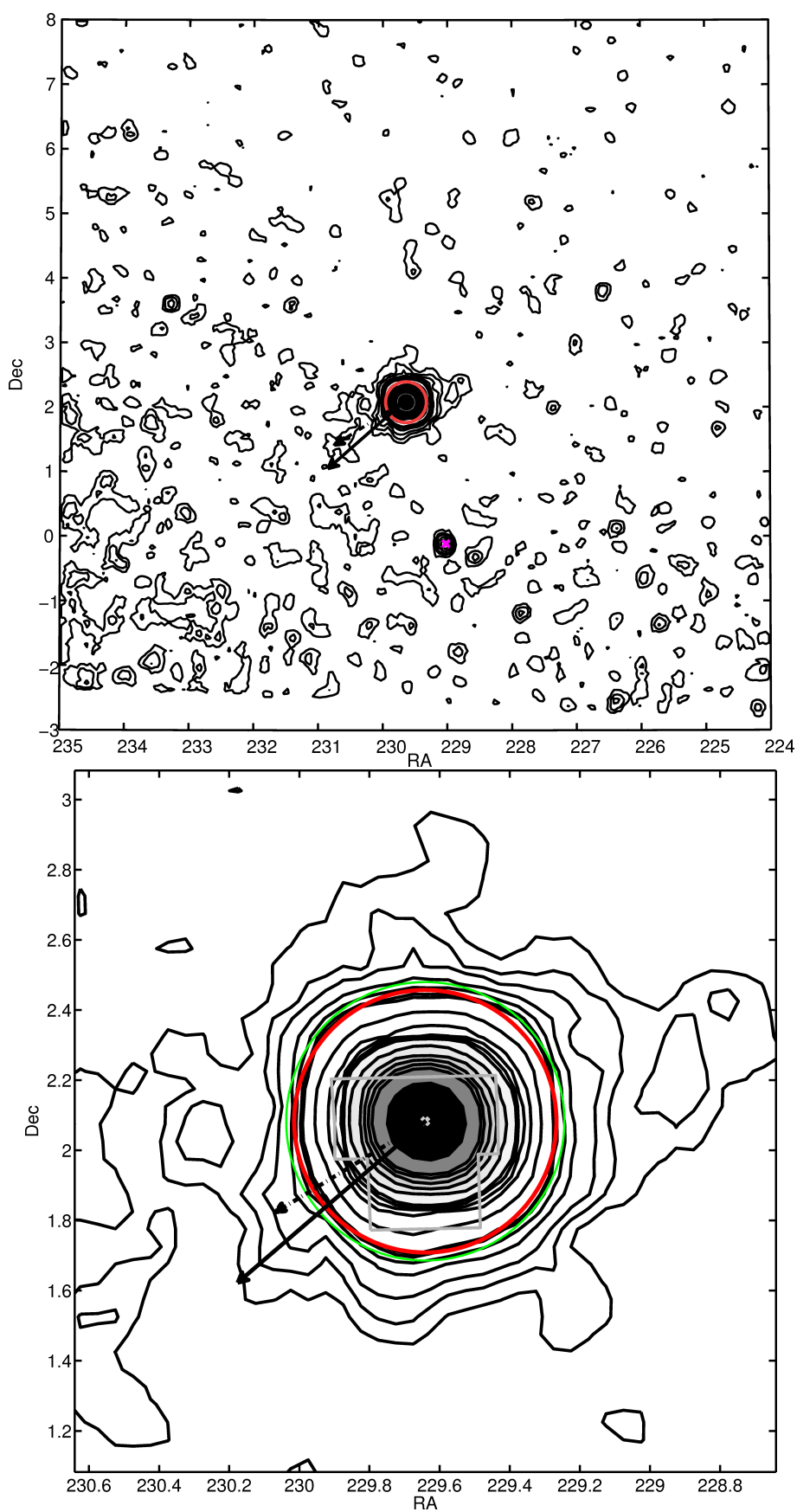
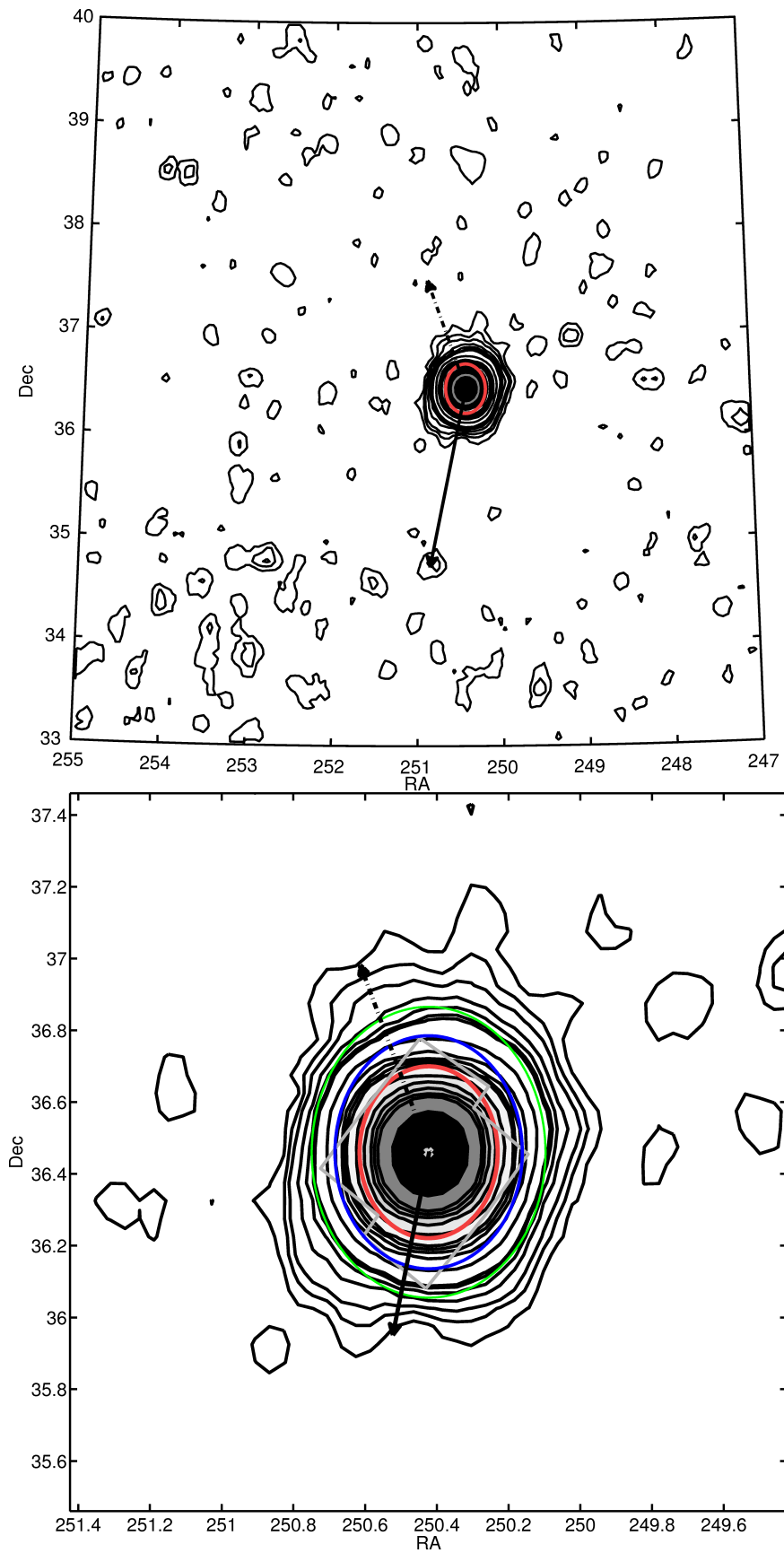Figure 2.26: Same as Figure 2.20 for NGC 5904.

Figure 2.27: Same as Figure 2.20 for NGC 6205.
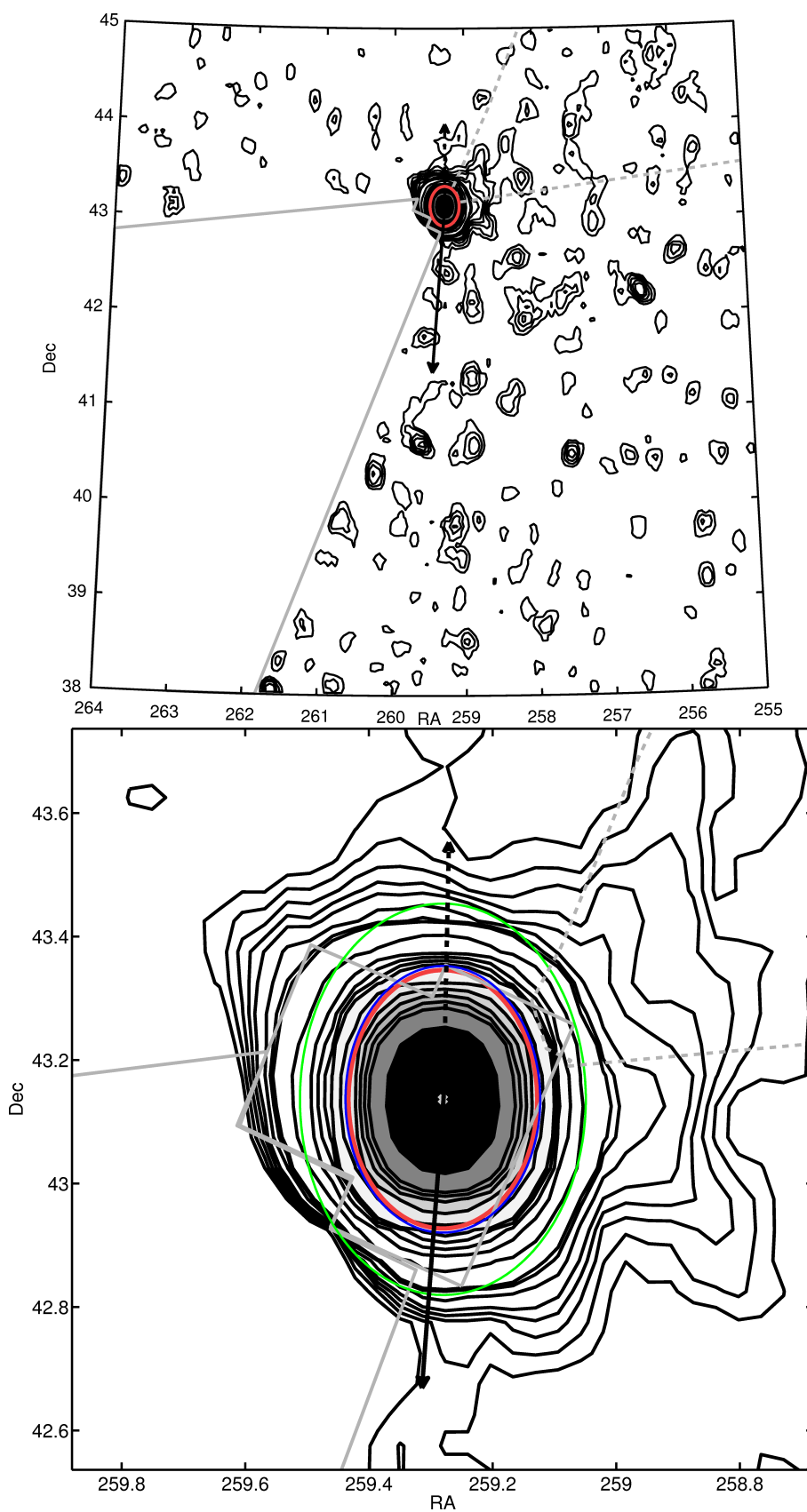
Figure 2.28: Same as Figure 2.20 for NGC 6341. The light dashed gray lines marks the area within which the field density is doubled.

such a large extratidal halo. In Figure 2.14 we show the number density profile. A clear overabundance of stars around the tidal radius is visible. The halo of extra tidal stars is also visible in the contour map. The destruction is dominated by internal mechanisms (GO97), which is expectable considering the cluster's current approach to the Galaxy.

2.5.12 NGC 7078 (M15)

NGC 7078 is currently located 9.8 kpc from the Galactic center, close to its apogalacticon $R_{apo} = 10.4$ kpc (Dinescu et al. 1999), i.e., we do not expect any correlation between the orbit and the (possible) tail's orientation. In Figure 2.30 we show the contour map.The GC is detected as the prominent overdensity. The field around the cluster is very smooth. It only shows contours up to 3σ above the mean of $3.0 \cdot 10^{-1}$ stars arcmin^{-2}, but not in any symmetric configuration around the cluster. No large scale structures are detected. The contours at the cluster center are undisturbed, but the contours at the tidal radius show some distortions. NGC 7078 is confined within its tidal radius. The lowest three contours show strong distortions. The cluster is at the edge of the survey, therefore the northern part of the contours is probably cut off. Grillmair et al. (1995) studied the 2d distribution of NGC 7078. They found an excess of cluster stars extending toward the southeast and a further density peak just north of the cluster. These features do not show up in our data. Instead, we confirm the features seen in the immediate surroundings of NGC 7078 that were also found by Chun et al. (2010). Owing to the borders of the SDSS survey, their northwestern feature is not covered by our data. On a larger scale, outside the field of view of Chun et al. (2010), we see extended low-density $(1-2\sigma)$ structures in roughly east-west direction. These are not aligned with the direction toward the Galactic center, but appear at an angle of approximately $20-30\,\mathrm{deg}$ (Figure 2.30), suspiciously aligned with the direction of the SDSS scan. While suggestive, deeper data are needed to confirm or rule out whether these are extended tidal tails. We observe a similar extratidal structure of the contour lines. Figure 2.17 shows the number density profile of NGC 7078. We detect a change in the profile's slope.

2.5.13 NGC 7089 (M2)

NGC 7089 is located 10.1 kpc from the Galactic center, close to perigalacticon $R_{peri} = 6.4$ kpc (Dinescu et al. 1999). I.e. a possible inner tidal tail is aligned with the orbital path of the cluster. In Figure 2.31 we show the contour plot of NGC 7089. The inner contours are smooth. The contours at and outside the tidal radius are distorted. The lowest contour is very extended, but comparable with background noise east of the cluster; therefore very likely an artifact. The mean background level is at $1.2 \cdot 10^{-1}$ stars arcmin^{-2}. No large scale features are detected. NGC 7089 shows an extratidal halo, which is a spherical structure. No $\mathcal{S}$-shape or elongation is observed. Also Grillmair et al. (1995) studied the 2D structure of NGC 7089. They found an excess of cluster stars extending along an E-W axis. In our contours only the 2σ-contours might show some elongation, but overall the halo is quite circular.
Dalessandro et al. (2009) derived a number density profile and also detected a slight excess of stars beyond the tidal radius compared to the best fit King model. Our number density profile is shown in the Figure 2.14. We detect a change in slope around the tidal radius as expected for a halo of extratidal stars.

2.5.14 Pal 1, Pal 3, Pal 4 & Pal 14

The Palomar clusters in our sample are five sparse objects plus the exceptional Pal 5 (see Section 2.5.7), which is also sparse but not remote as Pal 3, 4, and 14. In GO97s vital diagram
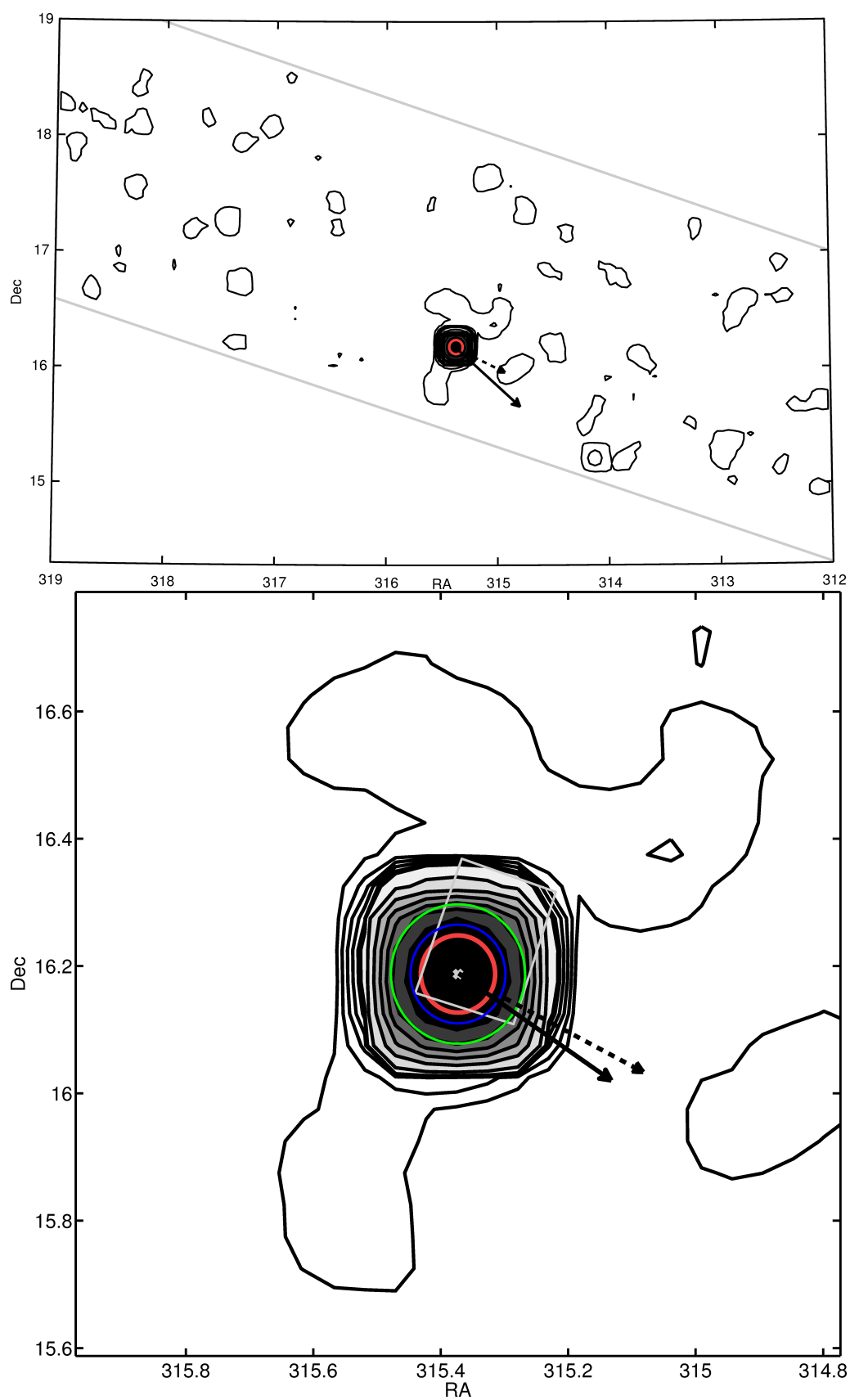
Figure 2.29: Same as Figure 2.20 for NGC 7006. The light gray line denotes the survey edge.
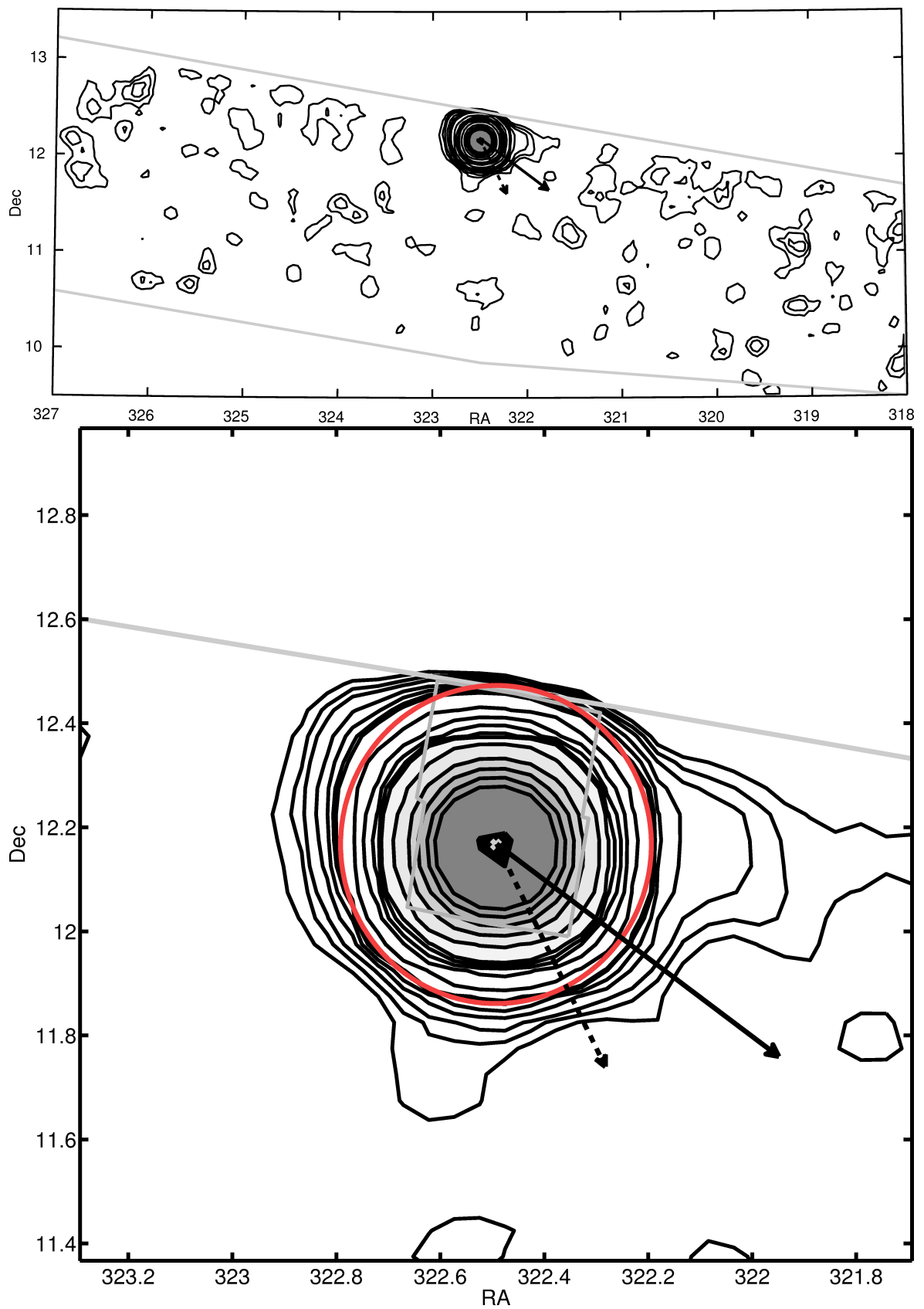
Figure 2.30: Same as Figure 2.20 for NGC 7078. The light gray line denotes the survey edge.
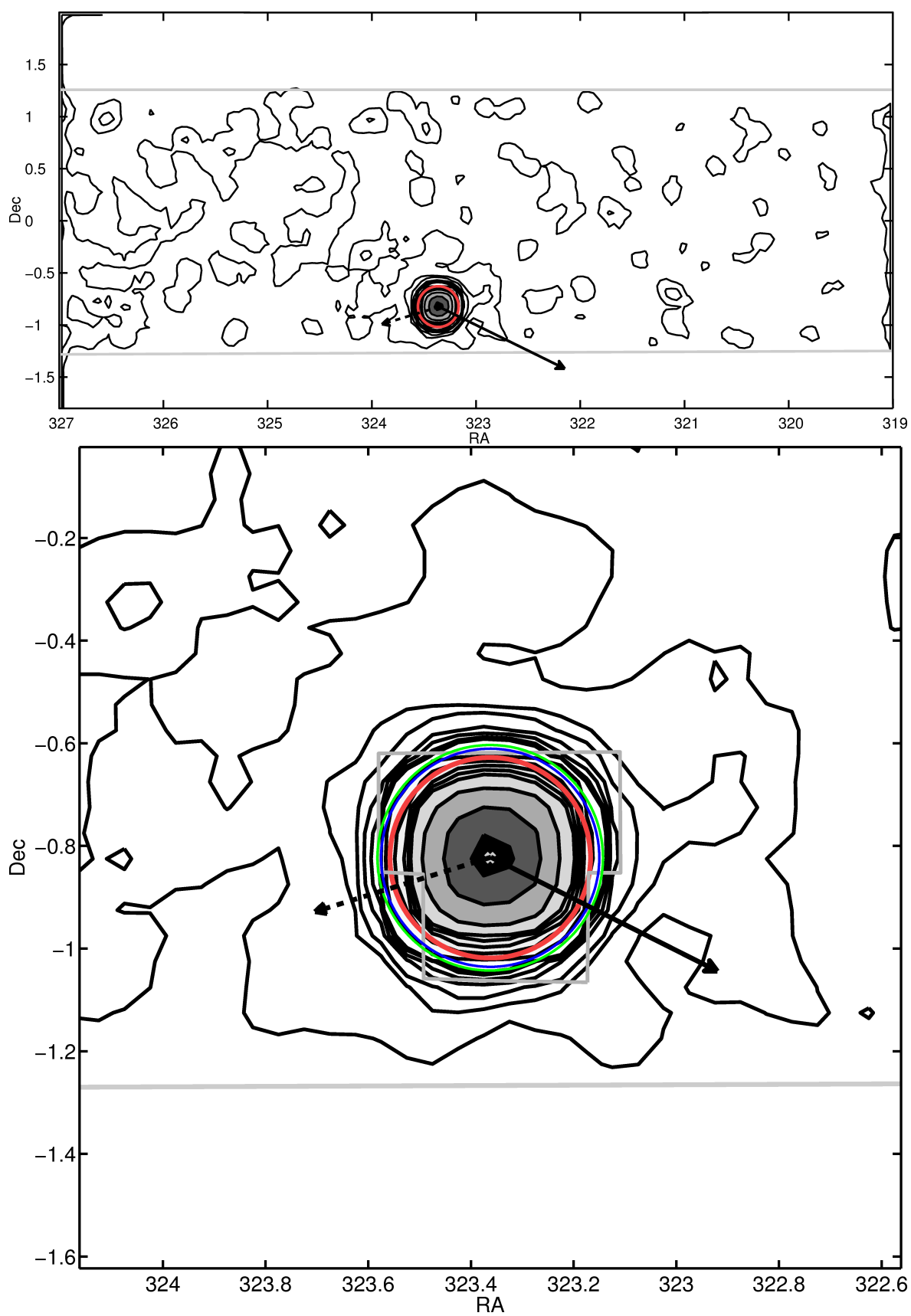
Figure 2.31: Same as Figure 2.20 for NGC 7089. The horizontal gray line marks the edge of the SDSS survey.
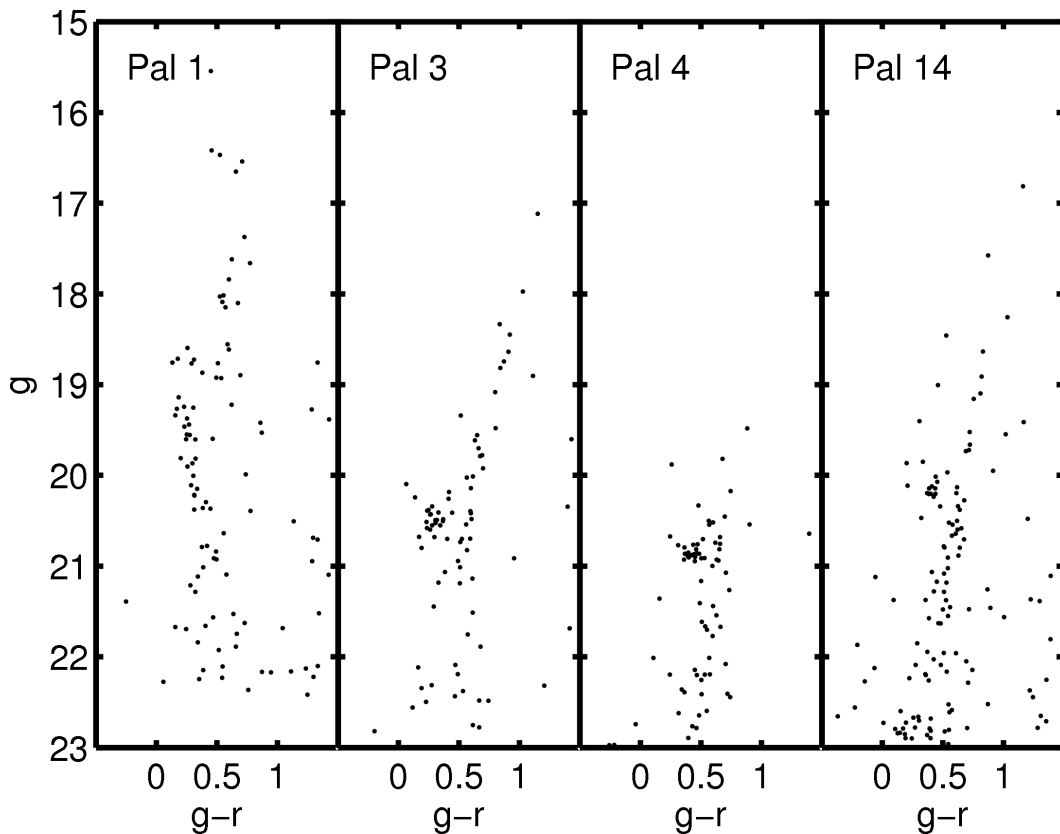
Figure 2.32: Color-magnitude diagrams of Pal 1, Pal 3, Pal 4, and Pal 14.

(Figure 2.1) the Palomar clusters are all found in a region where disk and bulge shocks are the main drivers of destruction. In Figure 2.32 we show the CMDs of the four sparse Palomar clusters. Comparing those to the CMD shown in Figure 2.6 it is easily seen that these clusters are very sparse. It is not straightforward to define characteristic features, e.g., a MS or an RGB and deriving a ridge line is not unambiguous. For these clusters, we therefore selected the stars fulfilling the following color and magnitude constraints: $0 < c_1 < 2$ (for Pal 1: $0 < c_1 < 1.5$) and for Pal 1: $15 < g < 22.5$, for Pal 3: $17 < g < 22.5$, for Pal 4: $19 < g < 22.5$, and for Pal 14: $17 < g < 22.5$. The selection in (c_2, g) was made identical as for the more populated clusters. As a result from the broader selection of stars we expect to see noisier contour plots.

Because the Palomar clusters are very sparse and remote they were not targets in many studies of their structure. Especially their large distance to the Sun made it very hard to measure proper motions for this sample. Only Pal 3 and Pal 5 are included in DG99. Figure 2.33 shows the large scale views of the contour maps for Pal 3, Pal 4, and Pal 14. In Figure 2.34 we show the zoomed in contour maps of the four Palomar clusters. In the following, we discuss the results for each Palomar cluster.

The average background for the four clusters is $n_{bkg}^{Pal1} = 3.9 \cdot 10^{-2}$ stars arcmin^{-2}, $n_{bkg}^{Pal3} = 6.8 \cdot 10^{-3}$ stars arcmin^{-2}, $n_{bkg}^{Pal4} = 1 \cdot 10^{-3}$ stars arcmin^{-2}, $n_{bkg}^{Pal14} = 1.5 \cdot 10^{-2}$ stars arcmin^{-2}. Pal 1 is not a typical GC. Its C-M diagram is quite unusual. It has a populated main sequence, but hardly any stars on the red giant branch and the horizontal branch. This feature was noticed before by Borissova & Spassova (1995), Rosenberg et al. (1998), and Sarajedini et al. (2007). It might be up to 8 Gyr younger(!) (Sarajedini et al. 2007) than a typical GC. Pal 1 might be a member of the Monoceros stream (Crane et al. 2003). It can still not be ruled

out that Pal 1 is misclassified as a GC. The contour map shown in Figure 2.34 is plotted in Galactic longitude and latitude, (l, b) due to the clusters high declination. Although Pal 1 has a high destruction rate (GO97), mainly driven by disk and bulge shocks, it does not show any distortions of its contours, but a large circular halo of extra tidal stars. In the field we see no density peaks. The number density profile is shown in Figure 2.18 and was already discussed in Section 2.4. In summary we can say that we detect an overdensity at the position of Pal 1.

Pal 3 is currently at a distance of $R_{MW} = 84.9$ kpc, very close to perigalacticon $R_{peri} = 82.5$ kpc. As this is the cluster's closest approach to the Galaxy we do not expect to see any large signs of dissolution due to tidal shocks. Also the destruction rates derived by GO97 are small. The cluster's contours look undisturbed and circular. Nevertheless, the background shows several pronounced overdensities. In the northwest of the cluster we observed an overdensity of stars at 5σ-level above the background. We observe a distortion of the contours towards the Galactic anti-center, but no corresponding feature towards the Galactic center. Generally, Pal 3 has a large extratidal halo which shows a sharp edge. The prominent overdensity at $(153.5, -1.5)$ is the Sextans dwarf spheroidal galaxy. The number density profile is shown in the upper panel of Figure 2.16. We note that owing to the sparseness of Pal 3's CMD and its large distance deeper data are needed to investigate options such as a connection with Sextans (see also discussions in Chapter 3).

The tidal features of Pal 4 are shown in the lower left panel of Figure 2.34. We discover a large halo of extra tidal stars, as well as a tidal tail stretching along towards the Galactic center, but only in one direction. The field around Pal 4 is showing strong overdensities of up to 10σ. These density peaks show steep edges and in the center broad plateaus. It is unclear where these features are coming from. Comparing these field peaks with the cluster's tidal tail, hardly any difference can be seen. An interesting structure of the contour lines is visible at the cluster's western edge.

Sohn et al. (2003) studied the 2d-morphology of Pal 3 and Pal 4 using CFH12K wide-field photometry. For Pal 3 they detect some extensions in the direction towards the Galactic center and anti-center which are not more prominent than 1σ over the background. For Pal 4 they see a tail extending to the northwest. In our data we do not observe such a feature. Pal 4 is the most distant cluster in our sample. Again, deeper data are needed to reveal the possible existence of tidal tails.

In the lower right panel of Figure 2.34 we show the contour map of Pal 14. Martínez Delgado et al. (2004) studied the CMD of Pal 14 and compared it to the CMD of a region outside the cluster. They detected some hints for extratidal stars in a region of the CMD. We see smooth central contours and an extratidal halo. The field background shows some overdensities of up to 5σ above the mean. The 1σ and 2σ contours show an elongated distortion, comparable to the field background contours. The extratidal halo is spherical with some asymmetry towards the southeast. Whether this indicates the beginning of sparsely populated tidal tails remains unclear. Also for this GC, deeper data would be desirable in order to confirm this or to rule it out.

2.6 Discussion

In the previous Section we showed the contour maps for all GCs in our sample. We detected the known tidal tails of Pal 5 and of NGC 5466. We only used stars in a given apparent magnitude range. The counted stars have to have "clean photometry", i.e., the bright limit is at $g \sim 14$ mag, and the photometric error should not be too big, i.e., the faint limit is set to $g = 22.5$ mag. The clusters in our sample are at various distances from the Sun. Therefore,
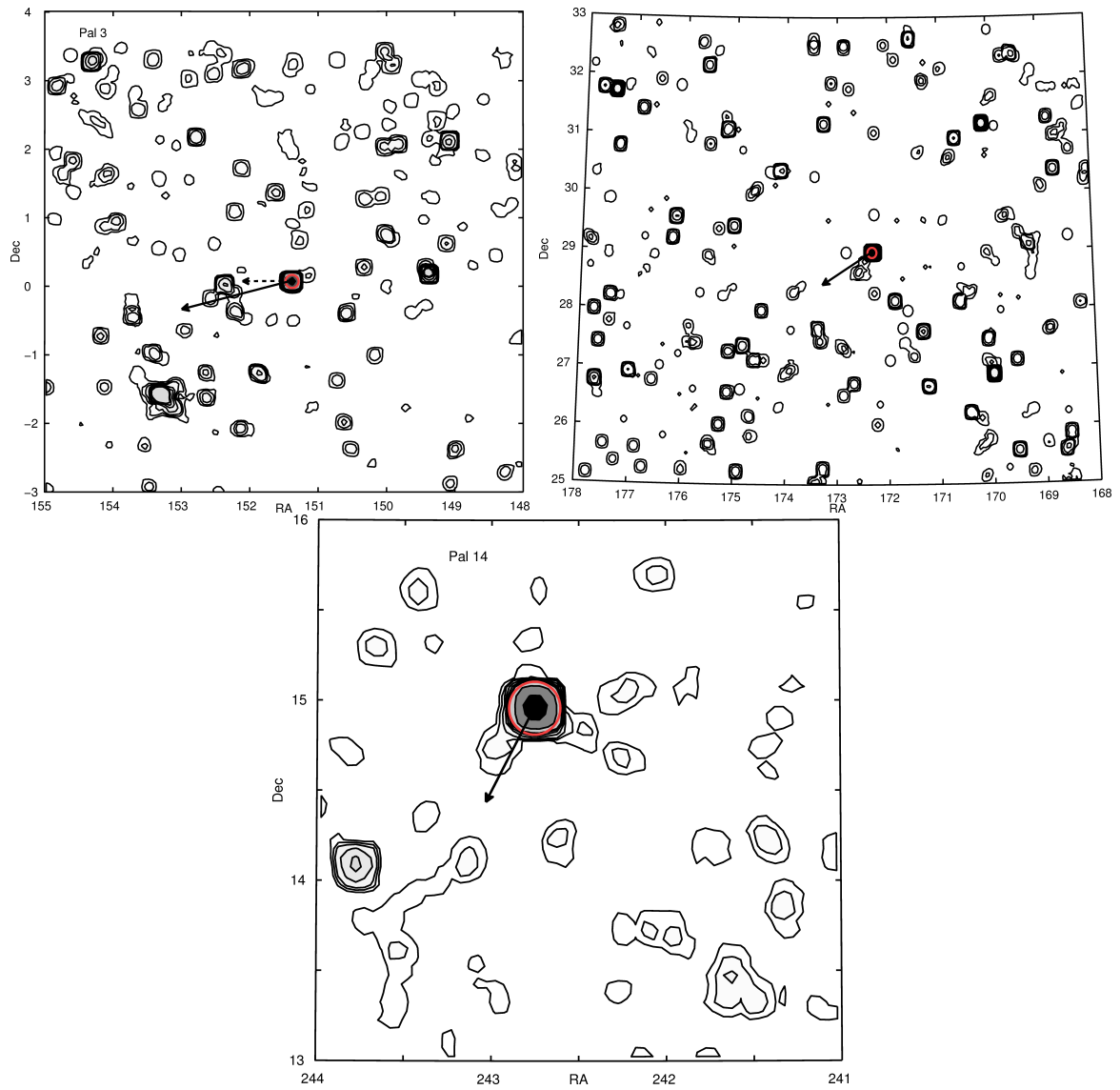
Figure 2.33: Contour maps of Pal 3, Pal 4, and Pal 14. The red ellipse is the tidal tail from the fit to the combined profile.
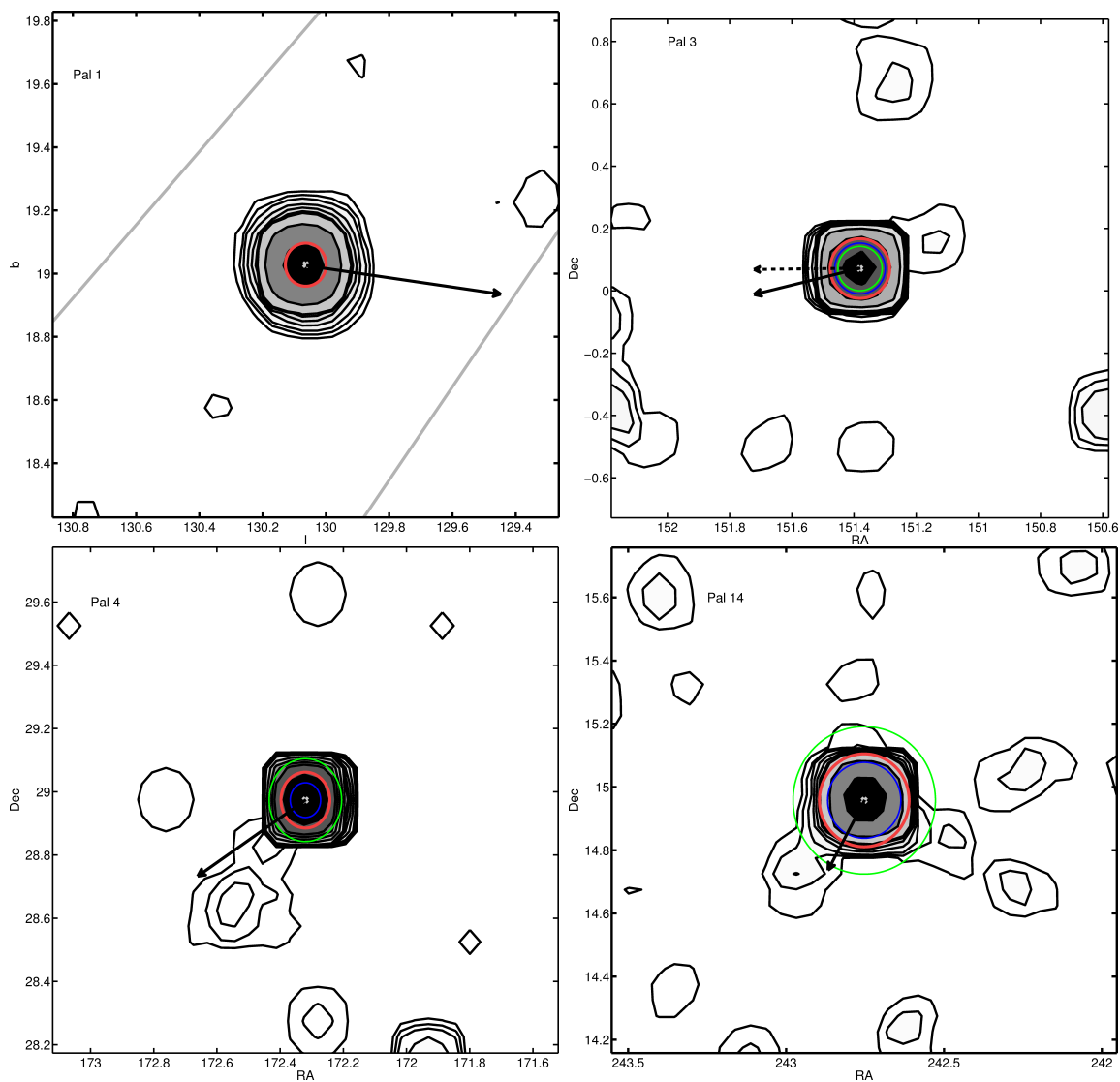
Figure 2.34: Zoomed in contour maps of Pal 1, Pal 3, Pal 4, and Pal 14. The contour map for Pal 1 is drawn in galactic coordinates (l, b), for all other clusters in equatorial coordinates (RA, Dec). The colors are the same as in Figure 2.20.

we did not trace identical stellar populations in each cluster. E.g., for the Palomar clusters (not Pal 1 & Pal 5) we only had stars available on the upper RGB ($\sim 17 < g < 22.5$), i.e., absolute magnitudes brighter than $-2.5 < M_g < 2.8$ mag. The same was the case for NGC 2419, $-2.6 < M_g < 2.9$ mag. The other clusters are close enough in order to also trace stars on the cluster's MS. For the closest cluster in our sample, NGC 5904, we observe stars down to $M_g = 8.12$ mag. I.e., we are tracing in some cases a wide range of stars and in other cases only the brightest, most massive ones.

From theoretical investigations and simulations (e.g., Baumgardt & Makino 2003) we know that preferentially stars of lower mass are lost. Therefore, tracing tidal structures with only upper RGB stars might not be very successful, not only because they are not preferentially lost, but also because they are less abundant than MS stars. Therefore, tracing tidal structures with only upper RGB stars may be difficult, as is the case for Pal 3, Pal 4, Pal 14 and NGC 2419 and this is exacerbated by the sparsely populated RGBs of the Palomar GCs. Nonetheless, we do find halos of extratidal stars as possible signs for some dissolution for all four clusters. But the field background is noisy and shows overdensities of more than 3σ.

2.6.1 Horizontal branch stars

The blue horizontal branch (BHB) and RR Lyrae stars are located at a position in the CMD where hardly any field stars are located. Therefore any BHB/RR Lyrae star found outside the cluster's tidal radius is with a high probability a former cluster member. For NGC 5466, Belokurov et al. (2006) found that the BHB/RR Lyrae stars also trace the tidal tails. For GCs which show no large tidal structures, but only distorted tidal contours the BHB/RR Lyrae stars are still inside the tidal radius. As an example: In NGC 6341, we found 194 BHB/RR Lyrae stars and only 20 are found outside the tidal radius. The remaining 174 BHB/RR Lyrae stars are all found within the innermost contour. For NGC 4147, for which we have found a complex multiple arm morphology, most BHB/RR Lyrae stars are within the innermost drawn contour, and 30% are found outside. The BHB stars do not trace the multiple arms. But the BHB/RR Lyrae stars in the field are mostly found in overdensities. E.g., at (181.2, 17) two overdensities of 9σ and 10σ, respectively are found. In the center of both a single BHB/RR Lyrae star is detected. At the same time, there are BHB stars that are not connected to any overdensity. The algorithm used to derive the density of cluster member stars gives high weights to BHB and RR Lyrae stars. Without spectroscopic information it is not possible to draw any reliable conclusion whether BHB/RR Lyrae stars connected to a prominent overdensity in the background are 'lost' cluster members. But the existence of BHB/RR Lyrae stars without any overdensity is supporting the hypothesis that the stars in those overdensities are more likely former member stars.

A similar connection between some of the cluster's BHB/RR Lyrae stars and overdensities in the field is observed for NGC 5024, NGC 5053, NGC 5466, NGC 5904, NGC 6205, and NGC 7006. Our current data do not permit us to conclude whether these overdensities are related to the GCs.

For some GCs in our sample a connection to the Sagittarius stream (e.g., Bellazzini et al. 2003b; Law & Majewski 2010; Forbes & Bridges 2010) or the Monoceros stream (Crane et al. 2003; Forbes & Bridges 2010) is discussed in the literature. It is possible that the detected extratidal structures and overdensities in the field of NGC 4147, NGC 5024, NGC 5053 and Pal 1 are features induced by the field populations of the disrupted dwarf galaxies. The data used here do not allow us to make a definite conclusion.

2.6.2 Comparing to theory

In Figure 2.1 we showed the *vital diagram* of GO97. The clusters within the drawn triangles will not be destroyed within the next Hubble time (= 10 Gyr). Only six of the clusters in our sample are found outside the triangles. For Pal 5, we already know it has tidal tails. For the remaining Palomar clusters we did not observe any large scale tidal structure. The outermost triangle is only appropriate for clusters with a current distance to the Galactic center smaller than 12 kpc. Pal 1 and Pal 5 are the closest with 17 kpc and 18.6 kpc, respectively. The other three Palomar clusters are currently at least 69 kpc away from the Milky Way. I.e., the vital diagram is in principle not valid for these clusters and we can not draw any conclusion from the theory regarding the observations. Or vice versa, we cannot confirm the theory with the observations. The remote location and the sparseness enhanced the contamination by field stars. At the same time the SDSS data only contain the red giant branch (except for Pal 1). Theory predicts that preferentially low mass stars are lost, as these are more likely found at the cluster's tidal boundary due to 2-body relaxation. Deeper data might reveal tidal structure. On the other hand these clusters are at very remote locations. For Pal 3 proper motion has been measured and DG99 calculated its orbit. They found a perigalactic distance of 82.5 kpc. The tidal interaction with the MW at such large distances is very small, if not negligible. Therefore only 2-body relaxation will contribute to the dissolution of this cluster. According to GO97 this is also the case for Pal 4 and Pal 14. Worth mentioning is that the destruction rate due to evaporation of Pal 14 is comparable to the same value for Pal 5. But in the case of Pal 5 the destruction due to the tidal shocks is 60 times stronger. For Pal 14 the effect of the tidal shocks is negligible. Pal 14 has the least pronounced halo of extra tidal stars of all Palomar clusters, but at the same time its contours have the most non-circular shape.

Pal 1 is once again a special case. It has a theoretically predicted large destruction rate (larger than Pal 5!). The contour map in the upper left panel of Figure 2.34 reveals some asymmetry, but no pronounced $\mathcal{S}$-shape or extended tidal tails. The number density profile is very busy and the fitted tidal radius is, compared to the 2d-distribution, too small. Applying this tidal radius Pal 1 has a large halo of extra tidal stars. No other GCs in our sample show such a pronounced halo. The large total destruction rate of $22.6/t_{hubble}$ translates in a destruction time of ~ 450 Myr. Pal 1 is only 3.6 kpc above the Galactic plane, but rather far out ($R_{MW} = 17$ kpc). The cluster's proper motion has not been measured. If it is almost dissolved, the observed contours do not show this. This cluster is and remains mysterious.

NGC 4147 is the sixth cluster outside the *survival triangles* in the vital diagram. With a current distance of 19.3 kpc the vital diagram is not suited as well. But as the cluster is located on the left edge of the triangles, where a common border to all triangles (regardless of the distance, they are derived for) exists, we expect that NGC 4147 is being dissolved by relaxation. The multiple tidal arm feature which we observe in Figure 2.20, confirms our expectation for dissolution. Such a "multiple arm" morphology was found by Montuori et al. (2007) for clusters on eccentric orbits approaching the apocenter. According to DG99 these conditions are all fulfilled by NGC 4147.

For the other clusters in our sample we naively did not expect any signs of tidal features, because these clusters are all located within the survival triangles. But at the same time we already know of three cluster in the sample, NGC 5466, NGC 5053, and NGC 6341, to have tidal features. For these three cluster we confirmed these known structures, even if the position in the vital diagram, we would not expect any strong signs of tidal destruction. Nevertheless, the total destruction rates for these three clusters are by far the largest (neglecting Pal 1). These clusters will be destroyed within the next Gyr.

For many GCs we detect a halo of extra tidal stars (see next Section). Although we do not

see any large scale tidal structure, we observe in almost all cases contours which are around the tidal radius not smooth and circular, but disturbed. The central contours are usually circular/elliptical and show no sign of interaction. NGC 5024 is a case, where all contours outside our fitted tidal radius (red ellipse in Figure 2.21) are distorted. We compare our contour map with simulated contour maps by Combes et al. (1999) in their Fig. 14. We find good agreement between our observations and their calculations of 2d-distributions, at various timestamps.

2.6.3   Halos of extra tidal stars

Not only the clusters for which we already expected extra tidal stars, but also most of the other clusters in our sample show a halo of stars outside the tidal boundary. Combes et al. (1999) simulated GCs in a tidal field and observed such a halo as well. The stars outside the tidal radius spread out in density like a power law. They also transformed their 3-dimensional simulations into a (observable) projection on the sky and derived the power law to be "r^{-3} or steeper". The observed extra tidal halos by Grillmair et al. (1995) and Leon et al. (2000) show only slopes of -1. Combes et al. (1999) argue that the discrepancy is a consequence of noisy background-foreground subtraction. In our sample especially for the Palomar clusters we see pronounced halos of extra tidal stars. Unfortunately their radial number density profiles are very noisy, due to the fact that the subtraction of field stars was not as accurate as for the other clusters. Therefore, also the pronounced halo of extra tidal stars might be heavily contaminated by field stars.

Grillmair et al. (1995) observed for clusters with tidal extensions a break in their number density profiles, becoming pure power laws at larger radii. We also see this effect in our sample, especially for those clusters which have a pronounced halo of extra tidal stars. For NGC 4147 we observe a nice break in the number density profile (see lower panel of Figure 2.10), resulting in a smoother transition between the cluster's declining profile and the flat background. The same is observed, i.e., for NGC 7089 (lower panel of Figure 2.15).

Leon et al. (2000) introduced Q_a^b as the slope of the number density profile between $a \times r_t$ and $b \times r_t$. They choose to compute the following three slopes: Q_1^3, Q_3^6, and Q_1^6. We applied the same method to the clusters in our sample and derived Q_1^3 and Q_3^6. In the profile shown in Figure 2.10-2.15 the remaining, flat background was not subtracted. To fit the power law slopes we first subtracted the background and then performed a least-squares fit between two radii. In Table 2.4 we list the resulting slopes for all clusters.

The theoretical prediction of slopes of "r^{-3} or steeper" is observed for many clusters in our sample for Q_1^3. Only NGC 4147, NGC 5053, Pal 4, and Pal 5 have a significantly flatter slope than predicted. The measurement for Pal 3 is affected by a large error. The fits for Q_3^6 show large errors or were in some cases not possible at all, due to the noisy background. For Pal 1, we did not perform any fit due to the strange shape of the number density profile. In general, the simulated halos of Combes et al. (1999) reproduce well the observed halos.

2.6.4   Ellipticity & $\mathcal{S}$-shape

Here, we study the shape and orientation of the contour lines presented in Section 2.5. In order to do this we fitted to all contours, which are centered on the GCs position, an ellipse. This least-squares fit resulted for each contour in a best fit ellipse with an ellipticity e, position angle P.A., a semi major and semi minor axis, and in central coordinates RA_e, Dec_e. Figures 2.35 and 2.36 show the results. In the left column the ellipticity e is shown for each contour at level σ, in the right column the position angle P.A[7] is shown for each contour

---

[7]P.A. quoted here are as follows: North - $0°$, East - $90°$.

Table 2.4: Power law slopes of the radial density profiles.

NGC	Name	$-Q_1^3$	$-Q_1^6$	$-Q_3^6$
2419		3.44 ± 0.75	3.32 ± 0.47	1.13 ± 2.4
4147		1.48 ± 0.24	1.70 ± 0.24	4.19 ± 0.32
5024	M 53	3.73 ± 0.35	3.69 ± 0.24	1.68 ± 1.28
5053		0.33 ± 1.05	2.35 ± 1.76	$\dots$
5272	M 3	0.94 ± 0.38	0.91 ± 0.16	$\dots$
5466		3.89 ± 0.46	1.52 ± 4.01	3.39 ± 0.75
5904	M 5	3.33 ± 3.72	3.33 ± 0.24	-0.70 ± 1.83
6205	M 13	3.28 ± 0.33	3.28 ± 0.20	1.65 ± 6.80
6341	M 92	3.65 ± 0.21	3.76 ± 0.21	3.76 ± 11.0
7006		3.38 ± 0.73	3.36 ± 0.51	1.23 ± 6.38
7078	M 15	2.88 ± 0.26	3.00 ± 0.21	$\dots$
7089	M 2	2.58 ± 0.21	2.65 ± 0.15	5.09 ± 2.58
	Pal 3	7.14 ± 10.58	7.16 ± 8.27	$\dots$
	Pal 4	1.47 ± 1.15	1.88 ± 0.77	$\dots$
	Pal 5	0.26 ± 0.42	1.33 ± 0.29	3.48 ± 2.95
	Pal 14	3.13 ± 2.96	3.46 ± 2.58	$\dots$

at level σ. The larger the σ of the contour the smaller the radii in the cluster. Our data are heavily affected by incompleteness in the central parts (at large σ) for almost all GCs. We observe in many cases (e.g., NGC 2419, NGC 7089, Pal 3) that the highest σ contour is more elliptical than the next lower contour. This is an artificial feature due to the low number of stars at these small radii.

Generally, the 1σ and 2σ contours are in almost all cases the most elliptical contours. This is not a surprise, these contours are the most affected by contamination by the field background. At the same time, these lowest contours are the first to be affected by tides. Nevertheless, there is a general trend that the contours in the outer parts are more elliptical than in the center. In some clusters we observe a trend in P.A.. E.g., for NGC 7006 we see a declining P.A. towards larger radii. At the same time the ellipticities are very small, i.e., the contour is essentially a circle. Therefore, it is hard to determine if the P.A. trend is real.

The average measured ellipticities for the GCs in our sample are very small. Our results are comparable to the measurements of White & Shawl (1987). In Table 2.5 we list in column (3) and (5) the mean ellipticity and mean position angle for the contours of level $5 - 600\sigma$. In columns (4) and (6) the standard deviation of the 12 data points are listed.

For some GCs the distribution of ellipticities is reproducing features which we have already encountered in the 2d-contour maps. Pal 5 and NGC 5466, where tidal tails are known, are discussed first. For both clusters we see contours getting more elliptical the further we go out in radius. The innermost contours are the least affected by the tidal field of the MW and therefore are not reshaped. In both cases we also observe a constant change in the position angle. Again, in good agreement with the observed $\mathcal{S}$-shape, which is typical for a tidal tail.

The complex morphology of the 2d-structure of NGC 4147 is reproduced in a complex distribution of ellipticity and P.A.. There is an overall trend, the three lowest σ contours are by far more elliptical than the others, although they do not look anything like an ellipse (see Figure 2.20). The contours around the tidal radius $(5 - 100\sigma)$ have a mean ellipticity of $e = 0.14 \pm 0.03$, whereas the three innermost contours are spherical, $e = 0.02 \pm 0.007$. For the position angle such a trend is hard to see. The $5 - 100\sigma$ contours have a mean P.A.

Table 2.5: Mean ellipticity and position angle.

NGC		e	σ_e*	P.A.	$\sigma_{P.A.}$*
2419		0.04	0.02	89.5	7.7
4147		0.11	0.06	101.9	18.7
5024	M 53	0.06	0.02	76.4	5.0
5053		0.10	0.02	81.2	1.8
5272	M 3	0.07	0.01	80.4	4.3
5466		0.14	0.09	96.1	11.1
5904	M 5	0.05	0.02	76.7	22.3
6205	M 13	0.13	0.02	95.8	4.5
6341	M 92	0.15	0.03	83.1	2.0
7006		0.02	0.01	97.5	21.6
7078	M 15	0.05	0.02	64.7	8.9
7089	M 2	0.04	0.01	115.5	22.7
	Pal 1	0.05	0.002	106.9	11.9
	Pal 3	0.03	0.02	75.3	8.3
	Pal 4	0.03	0.01	97.5	16.1
	Pal 5	0.11	0.08	90.5	8.6
	Pal 14	0.12	0.05	76.8	4.8

* σ_e and $\sigma_{P.A.}$ are not the error on the measurements, but the spread of the ellipticity and position angle, respectively, for the contours of level $5 - 600\sigma$.

of $97.6° \pm 13.7°$. Their orientation is not uniform. There is a slight trend representing an $\mathcal{S}$-shape (the P.A. is declining from 5σ inwards).

NGC 5053 revealed regular contours in Figure 2.22, but the lowest three contours show an asymmetry. At the same time, the ellipticity for the contours higher than 3σ is declining as expected, while the P.A. is on average constant for the same contours. Hence, no $\mathcal{S}$-shape is detected. This argues against the potential extra tidal features discussed above.

NGC 5904 is a very interesting case. The contours above 5σ in Figure 2.26 show a boxy shape, but inside the tidal radius the contours are elliptical without any asymmetry. The position angle for contours of level 20σ and above declines. The contour of level 20σ is the least elliptical of the entire cluster. This contour coincides with the tidal radius of 18.91 arcmin measured for the combined profile. The contours inside and outside are more elliptical and are oriented differently.

A special distribution of ellipticity is observed for NGC 6205: the contours get more elliptical for smaller radii. For NGC 6341 we detected a prominent extra tidal halo, and therefore expected to see some specialty in the distribution of ellipticity. This is not at all the case. There is only a slight trend for less ellipticity at smaller radii.

The Palomar clusters (except Pal 5) show flat distributions of ellipticity. Also for these clusters we observe for the lowest contours large ellipticities. Otherwise, these cluster seem to be undisturbed.

2.7 Summary

We investigated the large scale tidal structures of 17 GCs. We used a color-magnitude weighted counting algorithm to derive the distribution of probable member stars on the sky. For Pal 5 and NGC 5466 we re-detected the known extended tidal tails. For NGC 5053 and

Figure 2.35: *Left:* Ellipticity for each σ contour. The contours are those drawn in Figures 2.19-2.27. *Right:* Position angle for each σ contour, drawn in Figures 2.19-2.27.
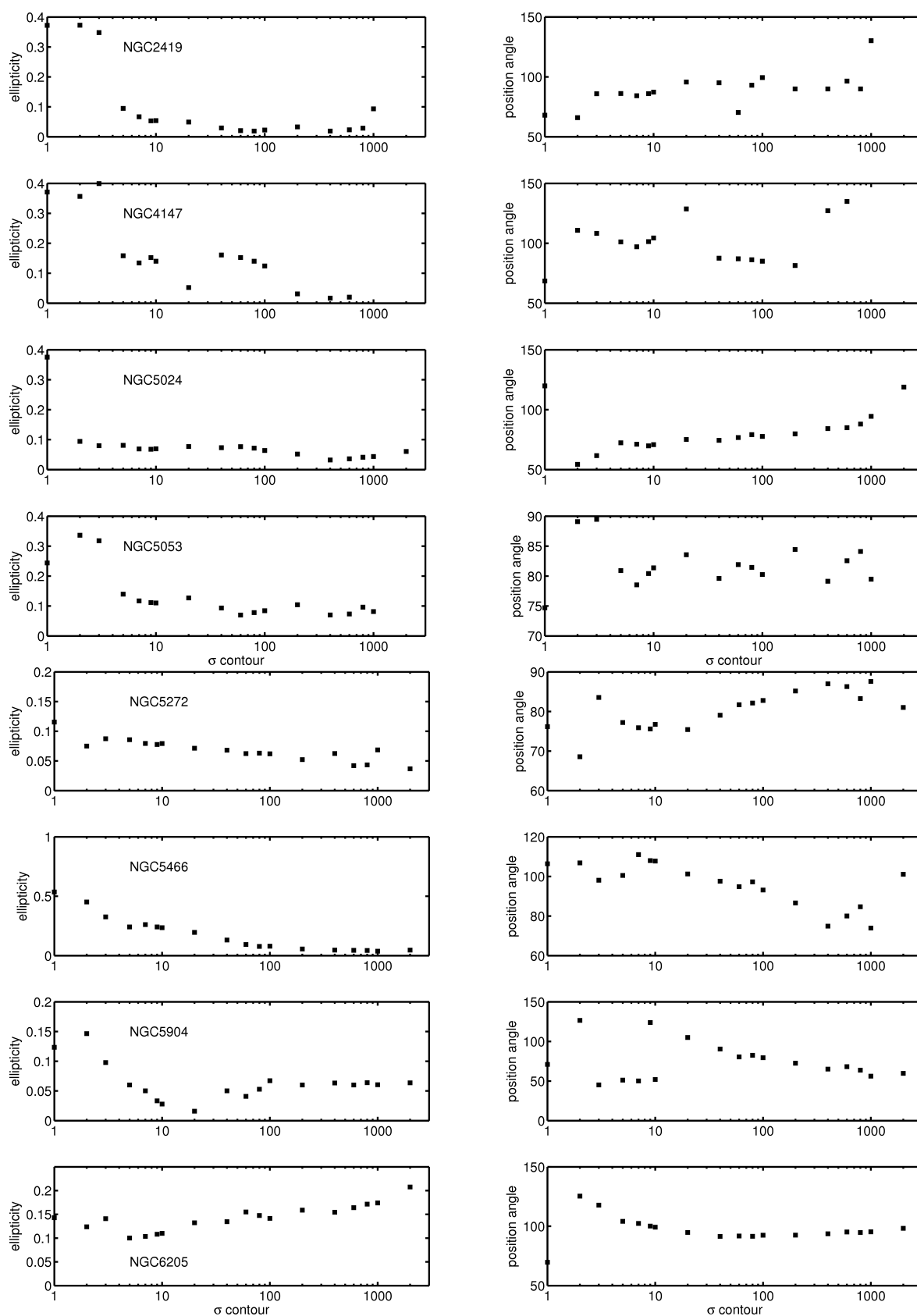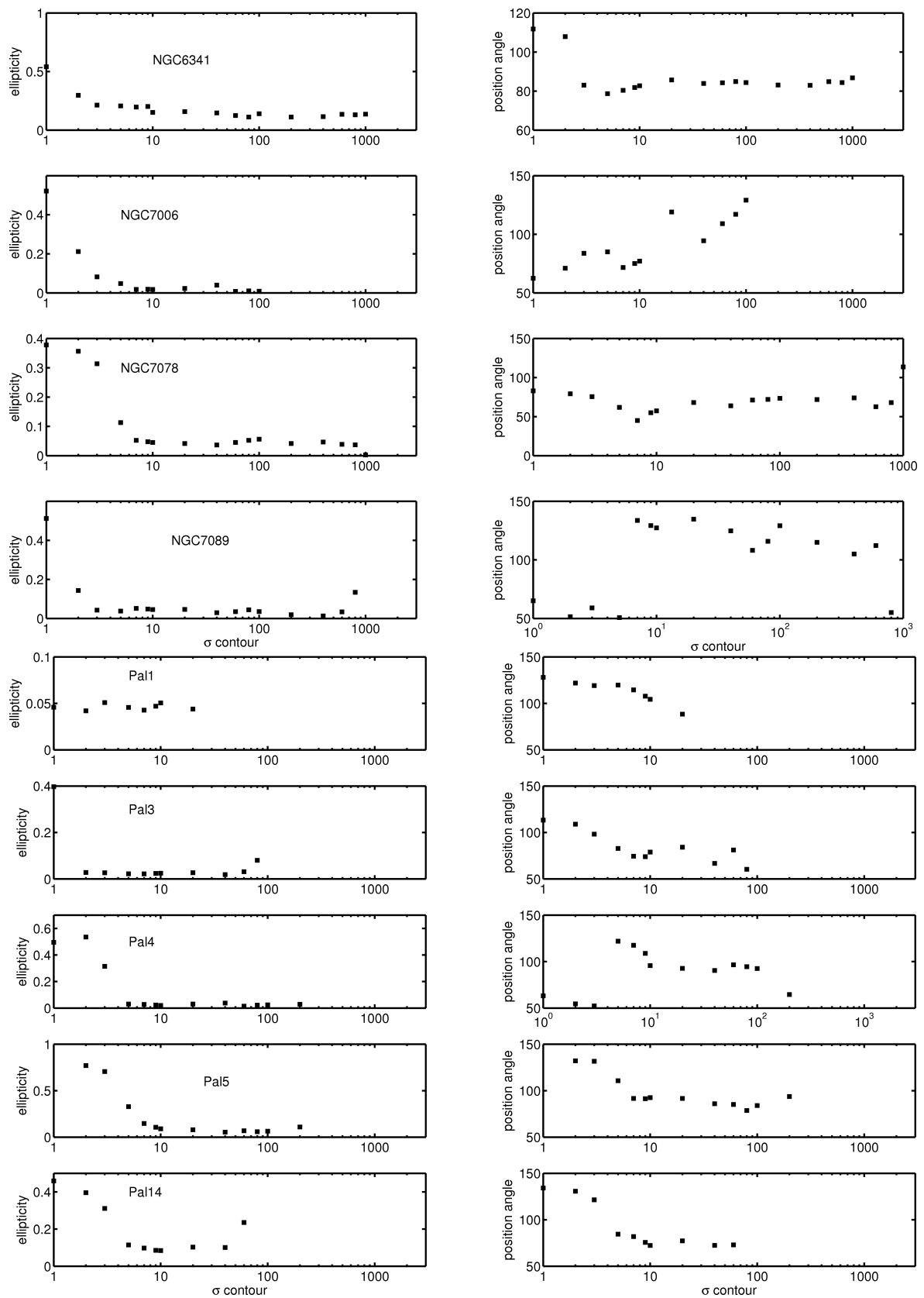
Figure 2.36: *Left:* Ellipticity for each σ contour. The contours are those drawn in Figures 2.28-2.34. *Right:* Position angle for each σ contour, drawn in Figures 2.28-2.34.

NGC 6341 we confirm the detection of extra tidal features by previous authors. We also detected for the first time multiple arm morphology around NGC 4147. The remaining GCs in our sample show in general a halo of extra tidal stars. The outer most contours are usually distorted and for some GCs we might even see the beginning of a characteristic $\mathcal{S}$-shape. But we did not observe any large scale features comparable to Pal 5.

We follow the distribution of stars brighter than $g \sim 22.5$ mag. As theoretical investigations have shown, GCs preferentially loose low mass stars. Therefore it is likely that our detection of no further extended tidal features is not a conclusive evidence against their existence. It is possible that the GCs have so far only lost stars fainter than our magnitude limit and are therefore just not detectable in our data. Also the lack of an obvious $\mathcal{S}$-shape in many of the GCs is not necessary due to its nonexistence, but might be a projection effect. The $\mathcal{S}$-shape is only visible if the orbit of the cluster is in the plane of the sky.

On the other hand, theoretical investigations on the destruction time scales of Galactic GCs do not predict large destruction rates for our sample. I.e., our discovery of no large scale tidal structures is in agreement with the theoretical predictions for our sample of clusters. An interesting exception is Pal 1, for which the theory predicts a fast dissolution, but we do not observe any large scale features.

Although, we have not detected any new large scale tidal features for the GCs in our sample we have detected for many clusters in our sample a halo of extra tidal stars. This is not only observable in the 2d-structure study but also as an excess of stars in number density profiles in the radial range around the tidal radius. This shows that real GCs are constantly surrounded by extra tidal stars as predicted by simulations. We have further investigated the distribution of ellipticity as a function of cluster radius and found for almost all clusters in our sample more elliptical contours in the outer parts.

The large area coverage with the SDSS data revealed for the first time the detailed structure of the outer parts of GCs. We were able to confirm the theoretical predictions dealing with GC dissolutions.

3

Tidal Structure of Dwarf Spheroidal Galaxies

We present a large scale study on the structure of three dwarf spheroidal (dSph) galaxies: Sextans, Leo II, and Ursa Minor. We use the *ugriz* photometry measured in the Sloan Digital Sky Survey (SDSS). We study for each dSph galaxy the distribution of potential member stars on an area of roughly $9° \times 9°$. We identify member stars according to their position in the color-magnitude diagram. To derive the distribution of stars on the sky, we applied a color-magnitude weighted counting algorithm. A similar algorithm has been used by Odenkirchen et al. (2001) to study the 2d-structure of the dSph Draco. We trace the structure of Ursa Minor with red giant branch and blue horizontal branch stars. Unfortunately Ursa Minor lies right at the edge of the SDSS survey, therefore only two thirds of its sky coverage is included in the SDSS. We detect the known off-center peaks in its surface density map. We also trace structures outside the nominal tidal radius. For Sextans, we trace the entire dSph. The main body is confined to an elliptical area much smaller than the tidal radius. The highest density peak is off-center. The distribution of stars on the red and blue horizontal branch are not identical. The blue horizontal branch stars are distributed in an elliptical area, which is roughly perpendicular to the dSph's main body. For Leo II, we trace the distribution of red giant branch stars. It shows an overall circular surface density distribution, the outermost iso-density curves have an asymmetry. For none of the three dSphs studied we detected large scale extra-tidal features. We also investigated the distribution of different populations. In the case of Sextans we observe a pronounced difference in the distribution of blue and red horizontal branch stars.

This work was done in collaboration with Eva K. Grebel.

3.1 Introduction

In cold dark matter (CDM) cosmology the dwarf spheroidal (dSph) galaxies are the lowest mass galaxies. They are the smallest stellar systems believed to be dominated by dark matter (DM). The prototype of a dSph galaxy is a low surface brightness clump of old stars, with little detectable gas and almost no sign of ongoing or recent star formation. The current standard theory for structure formation in the universe predicts that the collapse of DM halos proceeds in a "bottom-up" way, where smaller structures were build first and merged later into larger systems.

In the 20th-century, nine dSphs were known as satellite galaxies of the Milky Way (MW) (Grebel 1997; Mateo 1998). We will call these nine stellar objects "the classical dSphs". The discovery of new, very faint dwarf galaxies with low luminosities, $-7.9 \leq M_V \leq -3.8$, and surface brightnesses, $\mu_V > 27$ mag arcsec^{-2}, in the Local Group with the Sloan Digital Sky Survey (SDSS) (York et al. 2000; Abazajian et al. 2009) has nearly doubled the previously known population. Today, we know of 17 dSph companions of the Milky Way (Simon & Geha 2007, and references therein). The tidal structure of these ultra-faint dwarfs has been studied, usually, in their discovery papers (e.g., Belokurov et al. 2006, 2007). They are all extended and rather irregular in the outer parts. Only for Segue 1 (which might be a globular cluster and not a dSph galaxy (Martin et al. 2008; Geha et al. 2009)), probable tidal tails are observed in the SDSS data (Belokurov et al. (2007), but also see Martin et al. (2008)).

Although generally believed to be strongly DM dominated the mass-to-light ratio of dSph galaxies is still very uncertain. Different processes are discussed to explain the large measured velocity dispersions. Generally summarized the dSphs fall into one of two categories: *i)* dSph galaxies have high DM contents and are incommensurate with tidal stripping or *ii)* dSph galaxies have little DM and are highly prone to disruption by the Galactic tidal field. Muñoz et al. (2008) find that "tidal effects do not typically inflate central velocity dispersions". But these authors also hypothesize that "at least some dSphs might actually be well represented by tidally disrupting, mass-follows-light models". The discovery of extended tidal tails could support their hypothesis.

In this chapter we focus on the structure of three of the nine classical dSph galaxies. Although the ultra-faint dSphs were discovered by the SDSS, this catalog contains too few bright member stars to observe their morphology in detail. Therefore deeper data is needed for a detailed analysis of their structure. Five of the classical dSphs are included in the SDSS footprint, its large area coverage can reveal potential large scale tidal structures.

3.1.1 Previous observational studies

The structure of the classical dSph galaxies has been studied before. The first complete census was made by Irwin & Hatzidimitriou (1995) on the then known eight dSphs (Carina, Draco, Fornax, Leo I, Leo II, Sculptor, Sextans, & Ursa Minor) by using star counts on photographic plates. The structure of the ninth dSph, Sagittarius, was shown in its discovery paper (Ibata et al. 1994). It was later discovered to have extended tidal arms, wrapped around the MW several times (e.g., Majewski et al. 2003; Fellhauer et al. 2006). The five classical dSphs in the SDSS footprint (Draco, Leo I, Leo II, Sextans, & Ursa Minor) are all devoid of H I (Grcevich & Putman 2009). We will shortly discuss the already observed structure for these classical dSph galaxies in the SDSS footprint, see Table 3.1.

Leo I & Draco

Leo I is the most distant dSph in our sample, and simultaneously it is one of the most distant satellite galaxies of the MW. It had very likely only one encounter with a large Local Group galaxy (Peebles 1995), therefore no large tidal effect is expected to be observed. Smolčić et al. (2007) studied Leo I with SDSS data and derived the two-dimensional structure of the dSph galaxy. In Figure 3.1 (top left panel) we show their Fig. 10. They find no evidence for extra tidal structures down to a magnitude of $i = 22$ mag. Overall, Leo I shows smooth elliptical contours.

The 2d-structure of Draco was studied by Odenkirchen et al. (2001). They applied a CMD filtering method to SDSS data. In Figure 3.1 (top right panel) we show the contour map of Draco. No tidal tails were detected for stars brighter than $i = 21.7$ mag. In contrast the authors derived a larger tidal radius than previously measured, and extra tidal features were now located within the tidal boundary. Their derived total luminosity and mass-to-light ratio argues strongly for a highly DM dominated galaxy. Deeper studies by Ségall et al. (2007) confirmed the compact structure and detected no evidence for a tidal stream.

Leo II

Leo II is the second most distant classical dSph of the MW ($R_\odot \approx 233$ kpc). It had undergone little or even no interaction with the Galactic tidal field and its modest radial velocity ($v_r \approx 79.1$ km s^{-1} (Koch et al. 2007)) is consistent with an almost circular orbit that does not bring it close to the Galaxy. Radial velocity measurements and the flat velocity dispersion profile suggest that Leo II is dominated by DM (Koch et al. (2007), but also see Muñoz et al. (2008)). Coleman et al. (2007) studied the 2d-structure of Leo II with SDSS data: they used the same CMD filtering method based on a signal-to-noise ratio determination of the desired stars compared to the field population as Odenkirchen et al. (2001) for Draco. In Figure 3.1 (middle left panel) we show their results. Leo II showed some nonaxisymmetry, but they detected no significant evidence for extra tidal structures of stars brighter than $i = 21.3$ mag.

Ursa Minor

Ursa Minor contains only old stars with an age of about 13 Gyr, which formed in a single burst lasting less than 2 Gyr. The velocity dispersion profile is flat out to a radius of ~ 32 arcmin, where it drops sharply (Wilkinson et al. 2004). Depending on the assumed structural parameters the mass-to-light ratio varies considerably ($M/L = 12\ldots70$) (see Piatek et al. 2005, for a summary). The 2d-structure of Ursa Minor was studied by Palma et al. (2003). They derived the dSph's contour map by carefully choosing giant stars along the red giant branch and on the horizontal branch. The distribution of stars brighter than $M_0 = 20$ mag (Washington M pass band) is shown in Figure 3.1 (middle right panel). The isodensity map of Ursa Minor shows an interesting feature: two off-center peaks. The peak NE of the center is only statistically significant as a "shoulder" in the surface density profile, not as a peak. Kleyna et al. (2003) demonstrated the presence of a distinct subpopulation at the location of the shoulder NE of the center. Palma et al. (2003) report a visible $\mathcal{S}$-shape and detect extra tidal stars, but no large scale tidal tails. Piatek et al. (2005) derived the latest proper motion on astrometric measurements and concluded that Ursa Minor must contain DM to have a high probability of surviving for a Hubble time on their derived orbit.

Sextans

Sextans is the classical dSph with the lowest surface brightness ($\mu_0 = 26.2$ mag). It has only been discovered in 1990 by Irwin et al. (1990). For Sextans only Irwin & Hatzidimitriou (1995) have published a contour map (bottom panel in Figure 3.1) derived by star counts on photographic plates. Their derived surface density of stars is so low that the background noise dominates the map and it is hard to detect the dSph galaxy. Its large tidal radius of 160 arcmin makes it hard to observe the entire bound stellar population. Grebel et al. (2002) studied the 2d-structure with SDSS data. They detected population gradients and spatial disparity between blue and red horizontal branch stars. They also only detect a "compact" body of Sextans within ~ 50 arcmin, but a tidal radius of 160 arcmin.

3.1.2   Theoretical investigations

Muñoz et al. (2008) investigated to what extent Galactic tides are affecting dSph galaxies by modeling them as DM-dominated mass-follows-light systems. Although they tuned and compared their model to the Carina dSph, they still derive general conclusions valid for all dSph galaxies interacting with the MW. The Carina dSph was chosen as an existing galaxy to compare the simulations to, because its properties and its stellar populations are observed in great detail (Koch et al. 2006; Muñoz et al. 2006, and references therein). In their simulation they find for a dSph in tidal interaction tidal tails much further out than the observed tidal radius, and the bound core (containing still more than 10% of the initial mass) remains spherical with no tidally induced elongation. They further show that the pronounced $\mathcal{S}$-shape is only observable if the plane of the orbit is in the plane of the sky. The tidal tails are not a necessary discovery for a tidally disrupted dSph. The tails are very likely to have a low surface brightness which is probably not reached with the observations yet. But a halo of extra tidal stars, (more easily) observable in a number density profile, is a good indication for tidal interaction.

Peñarrubia et al. (2008) used N-body simulations to study the effects of tidal stripping on the structure of dSphs. They assumed the dSphs to be on eccentric orbits. They made predictions for the classical dSphs about how the surface brightness profile is affected by tidal interaction. They found that only systems in orbits where the tidal radius is comparable to the luminous radius of the dSph are significantly affected by tides. For Ursa Minor and especially for Sextans the tidal radii are far larger than the luminous, observed body of the dSphs. The authors therefore conclude that the observed structure of these dSph galaxies is not of tidal origin.

3.2   Data & counting algorithm

In the Section 2.2 we have introduced the Sloan Digital Sky Survey (SDSS) (York et al. 2000; Abazajian et al. 2009). The survey does not only provide photometry of stars in and around globular clusters, but also of dSph galaxies. In Table 3.1 we list the five classical dSph galaxies which are located in the SDSS DR7 footprint.

In Table 3.1 we list in row (1) and (2) the coordinates (RA, Dec). Row (3) contains the distance from the Sun. Rows (4) and (5) list the core and tidal radius of each dSph, respectively. Row (6) is the ellipticity. In Row (7) we list the position angle (P.A.)[1]. Rows (8) and (9) contain the dSph's proper motion.

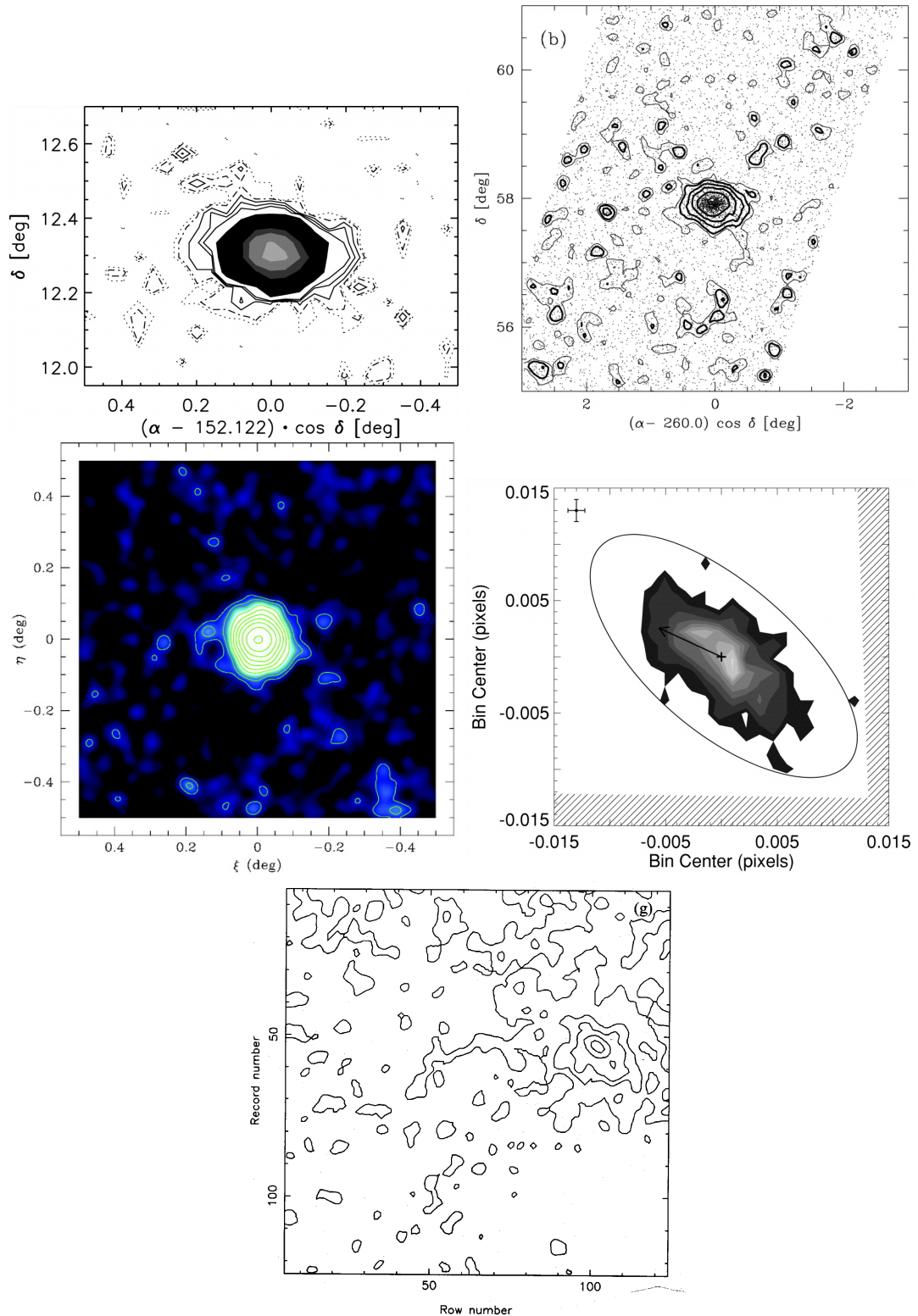[1]The orientation is such that $0°$ is North, $90°$ is to the East

Figure 3.1: Contour maps of Leo I (top left panel) from Smolčić et al. (2007, Fig. 10), Draco (top right panel) from Odenkirchen et al. (2001, Fig. 4), Leo II (middle left panel) from Coleman et al. (2007, Fig. 9), Ursa Minor (middle right panel) from Palma et al. (2003, Fig. 12), and Sextans (bottom panel) from Irwin & Hatzidimitriou (1995, Fig. 1).

Table 3.1: Dwarf spheroidal galaxies in the SDSS footprint

		Leo I	Sextans	Leo II	Ursa Minor	Draco
(1)	RA [hh mm ss]	10 08 29.4	10 13 03	11 13 28.8	15 09 11	17 20 13.2
(2)	Dec [° ′ ″]	12 18 48	-01 36 54	22 09 06.0	+67 12 54	57 54 54
(3)	$R_\odot$ [kpc]	254^{+16}_{-19}	95.2 ± 2.5	233 ± 15	76 ± 4	82 ± 6
(4)	r_c [′]	6.21 ± 0.95	16.6 ± 1.2	2.64 ± 0.19	15.8 ± 1.2	7.7 ± 0.2
(5)	r_t [′]	11.70 ± 0.87	160 ± 50	9.33 ± 0.47	50.6 ± 3.6	40.1 ± 0.9
(6)	e	0.3 ± 0.1	0.35 ± 0.05	0.11	0.56 ± 0.05	0.3 ± 0.02
(7)	P.A. [°]	-9.2 ± 5.7	56 ± 5	6.7 ± 0.9	53 ± 5	88 ± 3
(8)	μ_α [mas year^{-1}]	...	-0.26 ± 0.41	...	-0.5 ± 0.17	0.6 ± 0.4
(9)	μ_δ [mas year^{-1}]	...	0.1 ± 0.44	...	0.22 ± 0.16	1.1 ± 0.3
	References	1, 2	3, 4	5	3, 6	7, 8

References are: [1] Smolčić et al. (2007);   [2] Bellazzini et al. (2004);   [3] Mateo (1998);   [4] Lee et al. (2003);   [5] Coleman et al. (2007);   [6] Piatek et al. (2005);   [7] Odenkirchen et al. (2001);   [8] Scholz & Irwin (1994)

In Figure 2.4 we showed an Aitoff projection of the sky in right ascension and declination. The gray background shows the SDSS DR7 footprint. The blue dots are the dSph galaxies in the DR7 footprint. The blue crosses are the remaining classical dSph galaxies of the MW, not included in the SDSS footprint.

We downloaded all photometric data on point-sources from the DR7 database in areas of $\sim 9° \times 9°$ centered on the dSphs. We only used stars with "clean photometry"[2]. The observed magnitudes were corrected for extinction with the extinction values from Schlegel et al. (1998) listed in the SDSS database.

3.2.1   Color selection

To obtain the structure of the dSphs in our sample a crucial step is the removal of potential foreground contamination. To do this we divided the stars into a *cluster sample*[3] and a *field sample*. In the individual discussions on each dSph galaxy we mention the chosen radii for the definition of the two samples. We derive new, orthogonal color indices c_1 and c_2

$$
\begin{aligned}
c_1 &= k_1 \cdot (g - r) + k_2 \cdot (g - i) + k_3 \\
c_2 &= -k_2 \cdot (g - r) + k_1 \cdot (g - i) + k_4.
\end{aligned}
$$

We fitted a straight line $y = \tan(\alpha)x + b$ to the distribution of stars of the *cluster sample* in the color-color diagram $(g - r)$ *vs.* $(g - i)$. c_1 is the color index along the fitted line, c_2 perpendicular to it. We derived $k_1 = \cos(\alpha)$, $k_2 = \sin(\alpha)$, $k_3 = -b \cdot \sin(\alpha)$, and $k_4 = -b \cdot \cos(\alpha)$. In Figure 3.2 we show the color-magnitude diagrams (CMD) (c_1, g) for the three dSphs.

The CMD (c_1, g) of the *cluster sample* shows for all three dSphs a pronounced red giant branch (RGB). For Sextans we observe a prominent red horizontal branch (HB), and a less populated blue HB. Ursa Minor has a very pronounced blue HB. The contamination by foreground stars is large for the case of Sextans due to its position within the Galaxy.

The stars in the entire stellar catalog are now selected for the final catalog if they lie within 3σ of the dSph's ridge line in (c_1, g). The ridge line was derived by first selecting by eye in

---

[2]http://cas.sdss.org/astro/en/help/docs/algorithm.asp?key=flags

[3]We choose the term *cluster* as in Chapter 2, although the objects we are dealing with are not GCs but dSph galaxies.
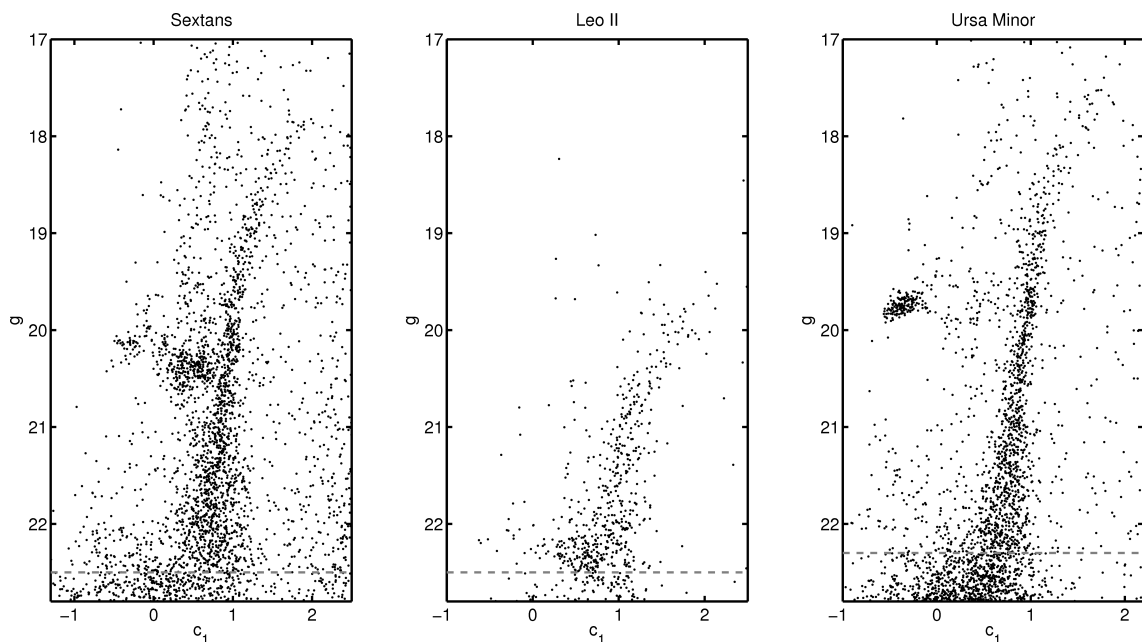
Figure 3.2: *Left panel:* CMD of Sextans. All stars within 30 arcmin are shown. *Middle panel:* CMD of Leo II. All stars within $2/3 \cdot r_t = 6$ arcmin are shown. *Right panel:* CMD of Ursa Minor. All stars within $2/3 \cdot r_t = 34$ arcmin are shown.

the CMD (c_1,g) an area around the dSphs RGB and HB containing the main population of member stars. Second, we derived the mean color in magnitude bins of height 0.2 mag for stars on the RGB. For stars on the HB we derived the mean magnitude in color bins of width 0.1 mag. We calculated the 3σ offsets and fitted 3rd-degree polynomials to these offsets. In (c_2,g) the scatter around the vertical mean is mainly due to photometric error, therefore it increases for increasing magnitudes. We selected stars within 2σ around the mean position. We also applied a faint limit, only stars brighter than the faint limit were chosen. The limits were chosen for each dSph separately. In Figure 3.2 we show the selection in the CMD (c_1,g) and the faint limit for each dSph. In this way we result in a catalog of stars which are explicitly chosen to have the same photometric properties as the dSph, but are located not only at the position of the galaxy but also in the wide field around it.

In Figure 3.3 we show the color-magnitude selection for Ursa Minor. In the left plot the CMD (c_1, g) and the selection criteria are shown. The black open circles are the stars selected at the end. In the right plot the CMD (c_2, g) is shown. We also show typical errors which are representative for all three dSphs.

3.2.2 Counting algorithm

The catalog of pre-selected stars is now used to derive the structure of the dSph. We use the color-magnitude weighted counting algorithm. The same algorithm was applied to Pal 5 for the discovery of its tidal tails (Odenkirchen et al. 2003). We explained the algorithm in detail in Section 2.3 to derive the 2d-structure of globular clusters. The resulting equations
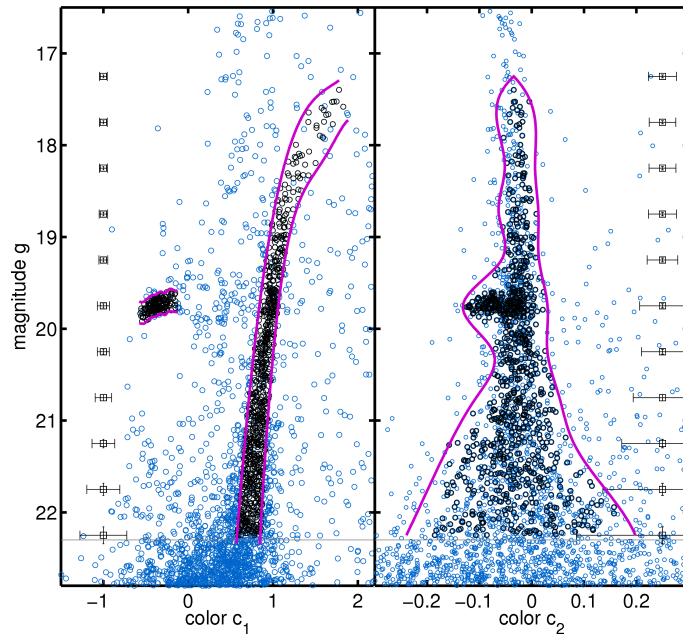
Figure 3.3: CMDs (c_1, g) *(left panel)* and (c_2, g) *(right panel)* of Ursa Minor's cluster sample. In blue we show all stars of the *cluster sample*. The black dots are the remaining stars in the *cluster sample* after the C-M selection. In red we show the borders within which we selected the stars. The gray line is at $g = 22.5$ mag.

are

$$n_C(k) = \frac{\sum_j n(j,k) \cdot \rho_C(j)/\rho_F(j) - n_F(k)}{\sum_j \rho_C^2(j)/\rho_F(j)} \qquad (3.1)$$

$$\sigma_{n_C}^2(k) = \frac{n_F(k)}{\sum_j \rho_C^2(j)/\rho_F(j)}, \qquad (3.2)$$

where n_C is the resulting number of member stars on the sky, $\sigma_{n_C}^2$ is a measure for the error on n_C. We introduce a grid on the sky with cells of 3×3 arcmin^2 labeled k and a second grid in C-M space with cells of 0.01×0.05 mag^2 labeled j. Each star in a given sky cell is weighted according to its position in the CMD by the factor $\rho_C(j)/\rho_F(j)$. ρ is the normalized distribution function in C-M space of the *field* and *cluster sample*, respectively. These weights are summed, corrected for a possible contamination of field stars $n_F(k)$, and divided by the factor $a = \sum_j \rho_C^2(j)/\rho_F(j)$. The contaminating field star population is derived from a least squares fit to the distribution of the *field sample* on the sky. The measure of the error was derived by assuming that outside the dSph's tidal radius the number of field stars is outnumbering the number of dSph member stars.

3.2.3 Contaminations

Dust

Dust along the line of sight might influence our photometric measurements. The magnitudes were all corrected for extinction as measured by Schlegel et al. (1998). We compared the observed structure with the measured extinction values. For Sextans we did not find any correlation between the derived 2d-structure of the dSph and the extinction values. In the field far away from Sextans we observed some correlation between "random" peaks in the

field density and higher extinction. For Ursa Minor and for Leo II we observe no correlation between the dSphs' morphology and the extinction due to dust. In Appendix A (Figure A.5), we show the derived contour maps plotted on top of the extinction maps for each dSph. The extinction maps show the mean extinction value from Schlegel et al. (1998).

Foreground stars, Quasars

The pre-selection of stars along the CMD features of each dSph galaxy in the color indices c_1 and c_2 ensured that we minimized the contamination by foreground stars. For all three dSph galaxies the resulting contour map showed an evident overdensity of stars at the position of the dSph. Comparing our results to previously published studies we observed similar structures. We have studied the number of potential quasar contaminants in Section 2.3.3 and saw that this source of contamination can be neglected.

3.3 2d-structure of dwarf spheroidals

In the following section we describe the contour maps for the three dSphs Sextans, Leo II, and Ursa Minor. In all contour maps we plot iso-density lines at levels of

$$1, 2, 3, 5, 7, 9, 10, 20, 40, 60, 80, 100, 200, 400, 600, 800, 1000, 2000 \cdot \sigma_{bkg}$$

above the mean weighted background level n_{bkg}^w. The mean background was derived at least 2 tidal radii away from the galaxies and if there were spurious areas, e.g., areas outside the SDSS scans, these were not taken into account for its determination. σ_{bkg} denotes the standard deviation of the weighted density in the area, which was used to determine n_{bkg}^w. For each dSph we show two plots. A large scale view which is shown in a Lambert projection for Sextans and Leo II, and in a Mercator projection for Ursa Minor. In the zoomed-in plot we did not use any specific projection, as the covered areas are not as large. But we corrected the coordinates as followed: $RA_{shown} = X_m + (RA - X_m) \cdot \cos(Y_m)$, where (X_m, Y_m) is the center of the cluster.

3.3.1 Sextans

To derive the distribution of member stars on the sky we defined the *cluster sample* to contain all stars in an ellipse, with P.A. and ellipticity as given in Table 3.1 and semi major axis of $30' \sim 2 \cdot r_c$. The *field sample* contains all stars outside an identical ellipse with a semi major axis of 100 arcmin. These radii were chosen, as the published tidal radius of 160 arcmin is definitely larger than the visible body of Sextans (in the SDSS). We tried different radii and these numbers resulted in the most robust results. From the *cluster sample* we derived the new color indices $c_1 = 0.64 \cdot (g - r) + 0.77 \cdot (g - i) - 0.05$ and $c_2 = 0.64 \cdot (g - i) - 0.77 \cdot (g - r) - 0.04$. The stars were then selected in (c_1, g) and (c_2, g). We only selected stars brighter than $g = 22.8$ mag. We then applied the color-magnitude weighted counting algorithm to derive the distribution of the selected stars on the sky. The resulting distribution of member stars was smoothed with a Gaussian kernel of width 15 arcmin.

In Figure 3.4, we show the resulting contour map of Sextans. The mean background level is $n_{bkg}^w = 2 \cdot 10^{-2}$ stars arcmin^{-2}. The contours of Sextans are of elliptical shape. The main detection of the dSph is within an ellipse with a semi major axis of ~ 40 arcmin. The inner-most contours do not show the elliptical shape. The highest density peak is off-center. The tidal radius is much larger than the luminous body of the dSph galaxy. The background is flat and shows only small random peaks of at most $5\sigma_{bkg}$.

Table 3.2: Ellipticity of Sextans' and Leo II's contours

σ_{bkg}	Sextans		Leo II	
	P.A.	e	P.A.	e
1	50.4	0.14	49.9	0.30
2	107.8	0.04	66.4	0.10
3	65.1	0.17	65.0	0.09
5	55.8	0.33	65.6	0.07
7	57.3	0.31	72.2	0.06
9	56.3	0.31	79.9	0.08
10	56.9	0.32	81.1	0.02
20	54.7	0.34	49.6	0.01
40	51.1	0.34	58.7	0.01
60	49.1	0.30	81.8	0.03
80	51.5	0.30	109.7	0.02
100	56.1	0.29	108.6	0.03
200	89.0	0.20	106.2	0.06
400	47.8	0.42	. . .	. . .
600	91.8	0.56	. . .	. . .

We determined the elliptical orientation of the contours at levels between 5 and 80σ. We used a Matlab routine to fit an ellipse to the contours in a least-square sense. We measured a mean P.A. of $54.2° \pm 3.2°$ and a mean ellipticity of $e = 0.32 \pm 0.02$, where the errors are the standard deviation for the eight measurements. In Table 3.2 we list the P.A. and ellipticity e for all contours centered on the central coordinates of Sextans in column (2) and (3). Especially the $1, 2, 400, and 600\sigma$-contours do not resemble ellipses. Hence, these values should be treated with care.

We derived the number density profile for Sextans. We counted the pre-selected stars in elliptical annuli with an ellipticity of 0.35 and a P.A. of $56°$ of width 2 arcmin within 100 arcmin and 5 arcmin outside. In the top panel of Figure 3.6 we show the resulting profile. The measured data points are corrected for the observed background of 0.1 stars arcmin^{-2}. The green line is the fit of a King profile (King 1962) to the observations, in blue we show the profile drawn with the tidal and core radius from Table 3.1. The profile shows a pronounced flat core, which is very likely steeper in reality as we did not correct for photometric incompleteness. Our resulting core and tidal radii are: $r_c = 15.4' \pm 0.9'$, $r_t = 157.3' \pm 44.3'$. Grebel et al. (2002) derived a surface brightness profile with SDSS data and derived $r_c = 16.75'$ and $r_t = 160'$. The two measurements are compatible within the errors.

3.3.2 Leo II

Leo II is one of the remotest dSphs of the MW. Therefore, the SDSS photometry only covers the upper part of the galaxy's red giant branch (see middle panel in Figure 3.2). To derive the structure of Leo II we defined the galaxy's *cluster sample* to contain all stars within $2/3 \cdot r_t$ and the *field sample* all stars outside $3/2 \cdot r_t$. We obtained two new color indices $c_1 = 0.646 \cdot (g - r) + 0.764 \cdot (g - i) - 0.095$ and $c_2 = 0.646 \cdot (g - i) - 0.764 \cdot (g - r) - 0.081$ from the *cluster sample*. The stars were selected in (c_1, g) and (c_2, g). We only selected stars brighter than $g = 22.7$ mag. The final distribution of stars on the sky was derived by applying the color-magnitude weighted counting algorithm and the calculated density distribution was smoothed with a Gaussian kernel of width of 15 arcmin.
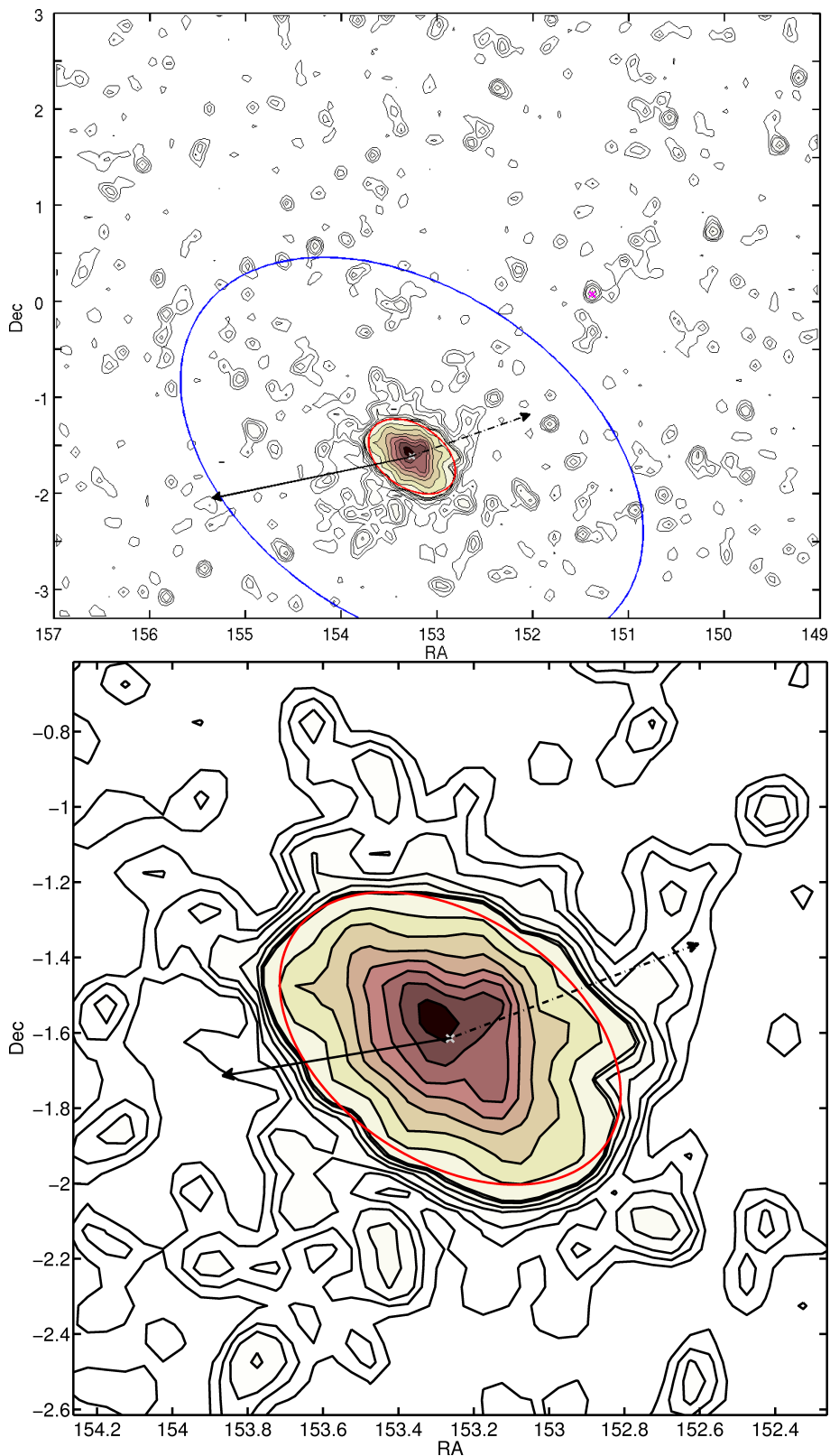
Figure 3.4: *Top panel:* Contour map in a wide-field view around Sextans dSph. *Lower panel:* Contour map of Sextans zoomed in. In both panels the red ellipse has a radius of 30 arcmin, in blue we show the tidal radius of 160 arcmin. The black solid arrow points towards the Galactic center, the dash-dotted arrow in direction of proper motion. The cross marks the position of Pal 3.

Figure 3.5: The contour plot of Leo II. A wide field view in the upper plot and a zoom-in in the lower plot. The green ellipse is the tidal boundary from this study. The blue ellipse is the tidal boundary from Coleman et al. (2007). The black arrow points towards the Galactic center.

In Figure 3.5 we present the contour map of Leo II, the top panel shows a wide field view in a Lambert projection around Leo II and the bottom panel a zoom-in on the dSph. The mean background level is $n_{bkg}^w = 3 \cdot 10^{-3}$ stars arcmin^{-2}. The wide field view revea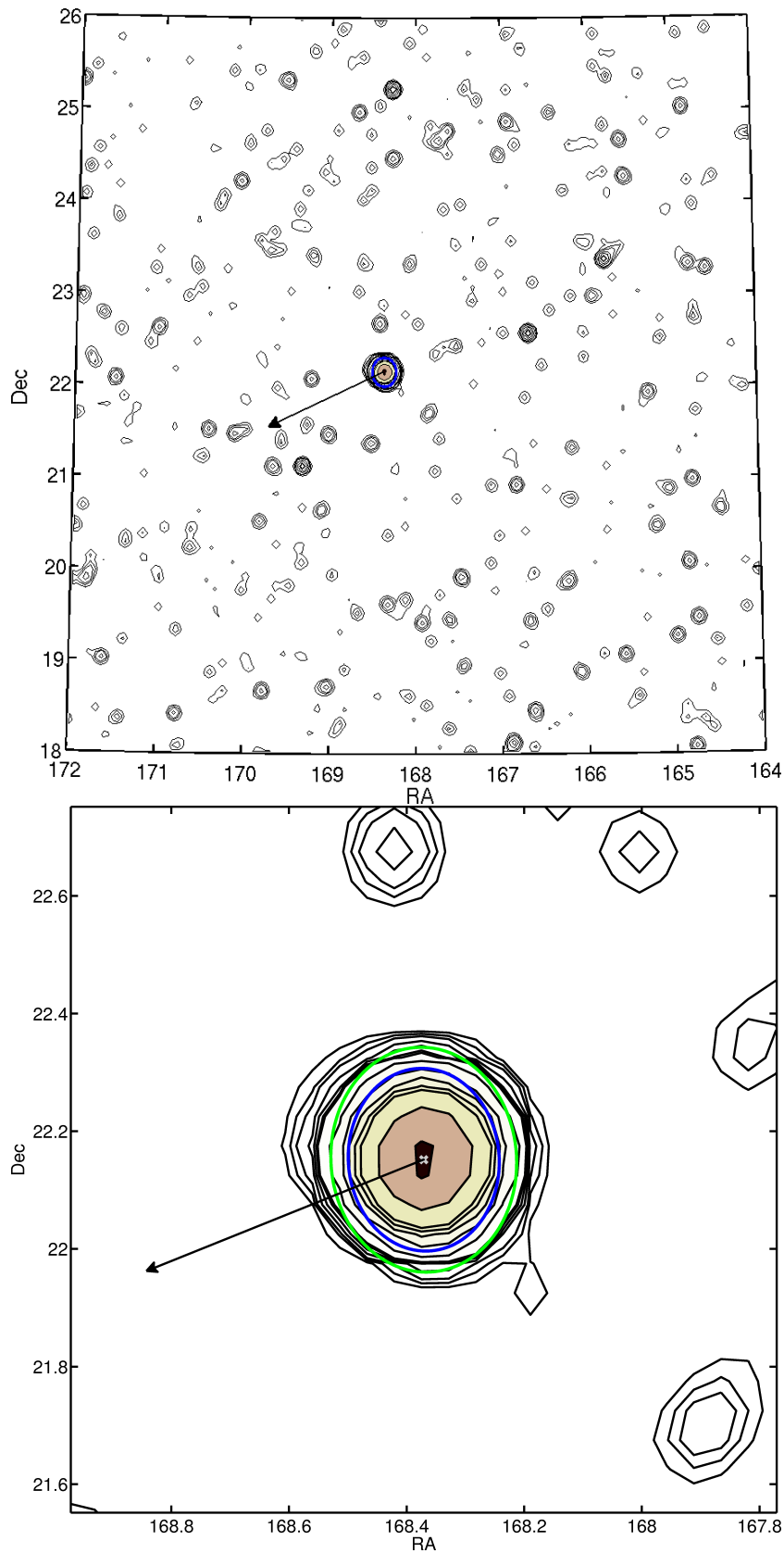ls no large scale tidal structure connected to Leo II. We observe random peaks in the background distribution, but these are all below $8\sigma_{bkg}$. The contours in the central parts of Leo II are round and undisturbed. The contours around the tidal radius are more elongated and show disturbed features. Comparing our contour map with the results of Coleman et al. (2007) in Figure 3.1 (middle left panel), we observe the same morphology. This is not a surprise as the two studies are using an almost identical approach.

We determined the elliptical orientation of the contours at levels between 2 and 80σ. We used a Matlab routine to fit an ellipse to the contours in a least-square sense in a identical way as we did for Sextans. The contours are very spherical. Therefore, the position angle scatters almost randomly. Hence, we did not derive a mean position angle and mean ellipticity. In Table 3.2 we list the P.A. and ellipticity e for all contours centered on the central coordinates of Sextans in column (4) and (5).

We derived a number density profile for Leo II. We divided the pre-selected stars in elliptical annuli with an ellipticity of 0.11 and a position angle of 6.7 deg. In the central part of Leo II the automatic photometry pipeline of SDSS fails, i.e., we only have a reliable profile outside of 3 arcmin. We fitted a King profile (King 1962) to the observed profile. We adopted the core radius of Coleman et al. (2007), $r_c = 2.64'$ and the observed background of 0.04 stars arcmin^{-2}. The resulting tidal radius is $r_t = 12.53 \pm 0.8'$. This value is larger than the value derived by Coleman et al. (2007). In the study of the number density profiles of GCs we already discovered the same effect. The tidal radii fitted only to the outer parts of the profile always resulted in a larger value. Because we have no measure of the photometric incompleteness, our number density profile cannot be corrected for this artificial effect. Therefore, the inner data points are too low compared to the outer points resulting in a less steep best fit King model and consequently in a larger tidal radius. In Figure 3.6 we show the number density profile. No excess of stars around the tidal radius is obvious. Comparing to the contour map in Figure 3.5 this is a confirmation of the only small extra tidal halo around Leo II.

3.3.3 Ursa Minor

For Ursa Minor we defined the *cluster sample* to contain all stars within an ellipse with semi major axis of $2/3 \cdot r_t$ and the *field sample* all stars outside $3/2 \cdot r_t$. The newly derived color indices are $c_1 = 0.56 \cdot (g-r) + 0.82 \cdot (g-i) - 0.03$ and $c_2 = 0.56 \cdot (g-i) - 0.82 \cdot (g-r) - 0.02$. The stars were selected in (c_1, g), (c_2, g) and with $g <= 22.3$. The final distribution of stars on the sky was derived by applying the color-magnitude weighted counting algorithm. Ursa Minor is right at the edge of the SDSS survey. The smoothing with a Gaussian kernel of width 15 arcmin results in contours outside the true observed area.

In Figure 3.7 we show the contour map of Ursa Minor. The top panel is a Mercator projection of a wider field centered on the dSph central coordinates. The bottom panel is a smaller area. The lower contours in both panels are drawn at the same level as for the two previous dSphs, but the higher contours are drawn at levels of $90, 110, 120, 130, 140 \cdot \sigma_{bkg}$ above the mean background of $n_{bkg}^w = 7 \cdot 10^{-3}$ stars arcmin^{-2}. In the "large area" view we clearly detect the dSph galaxy. The background is very smooth and shows only density peaks of $4 \cdot n_{bkg}^w$. In the area covered by our data, Ursa Minor has no large scale tidal feature. In the zoom-in, we detect two peaks of highest density. Both are located off-center. This has been seen by other authors before (e.g. Olszewski & Aaronson 1985; Irwin & Hatzidimitriou 1995; Palma et al. 2003, and references therein). Kleyna et al. (2003) investigated in detail the dynamics of the
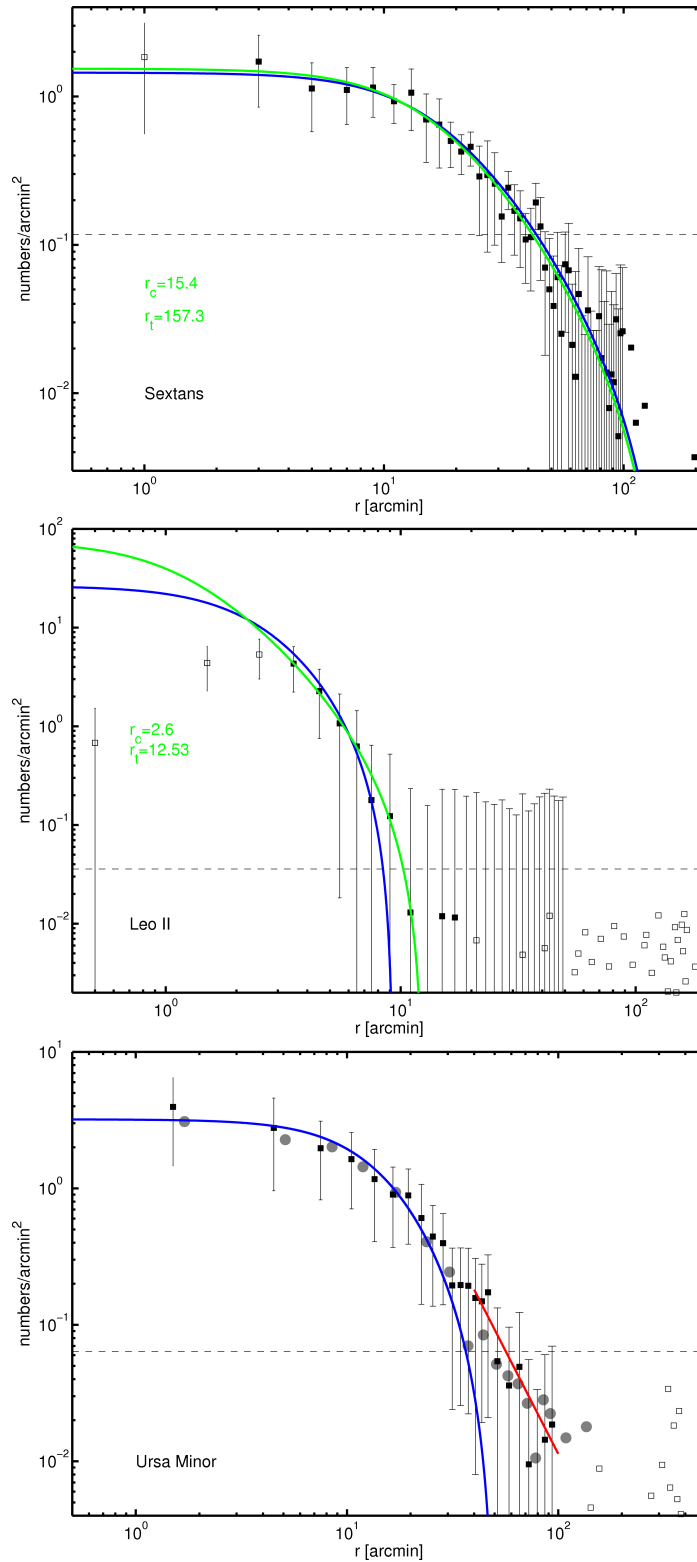
Figure 3.6: *Top panel:* Number density profile of Sextans. *Middle panel:* Number density profile of Leo II. *Bottom panel:* Number density profile of Ursa Minor. In blue we show the King profile with parameters adopted from Table 3.1. In green we show our fit to the data, the dashed horizontal line marks the measured background for each dSph. For Ursa Minor, in red we show a power law $r^{-\gamma}$ with $\gamma = 3.0$. The filled gray circles are data from Palma et al. (2003).

Figure 3.7: *Upper panel:* Contour map of Ursa Minor for the entire studied area. *Lower plot:* Contour map of the area around Ursa Minor. In both panels: The blue ellipse corresponds to a tidal radius of $50.6'$, at a position angle of $53\,\text{deg}$. The dash-dotted arrow points into the direction of proper motion, the solid arrow points towards the Galactic center. The gray line marks the edge of the SDSS footprint.

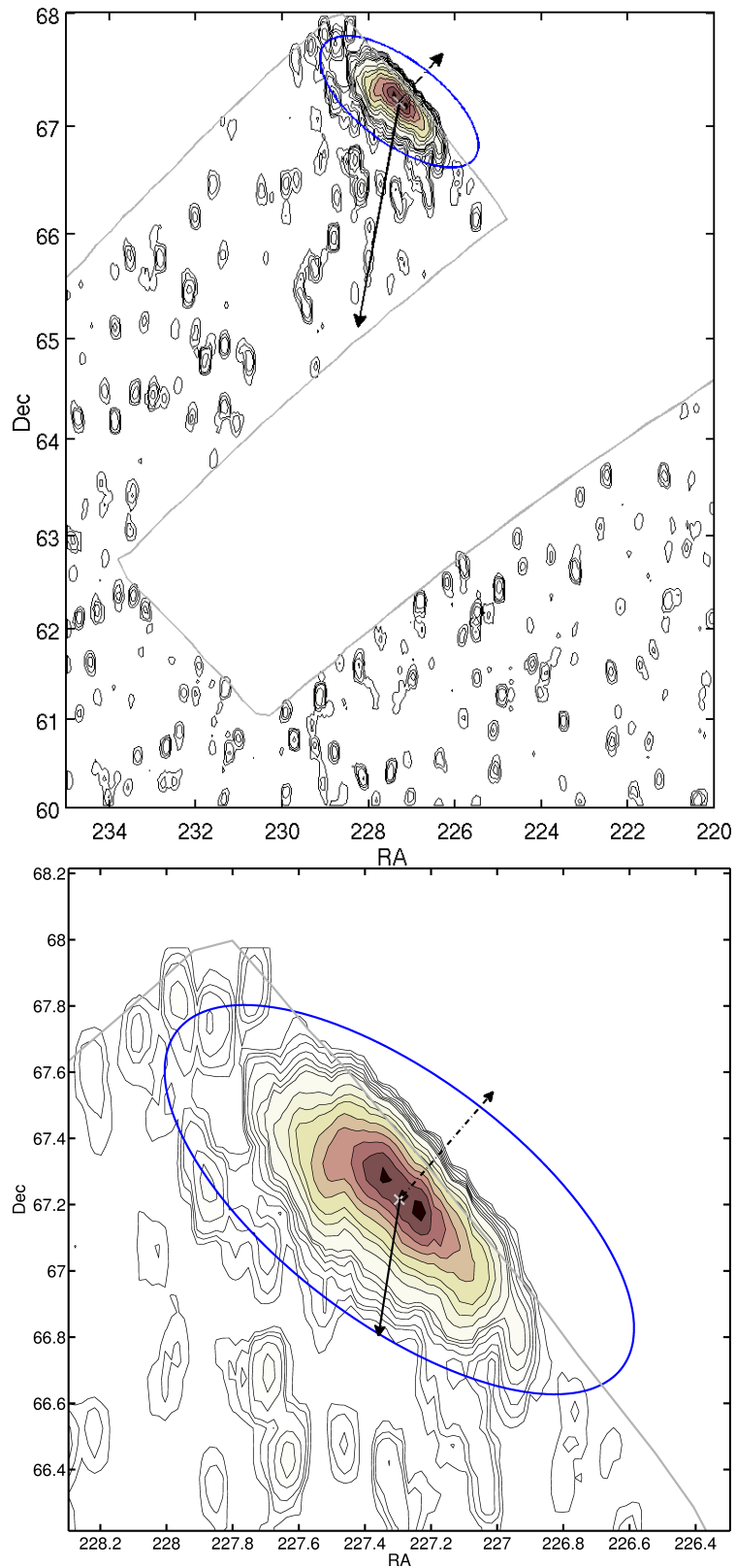density peak NE of the galaxy's center. They demonstrated that the stars around this second density peak are a kinematically cold sub-population. The properties of this sub-population are consistent with a disrupted stellar cluster on a orbit in the plane of the sky, if the DM halo of Ursa Minor is cored and not cusped.

We derived a number density profile for Ursa Minor (Figure 3.6). Because the dSph is at the edge of the survey, we only derived the profile for the southern half of the galaxy, i.e., we only counted stars South of the major axis of the blue ellipse in the lower plot of Figure 3.7. We counted these stars in elliptical, concentric annuli. Within 50 arcmin we chose annuli of width 3 arcmin, outside of 7 arcmin. To determine the error on our measurement, we divided each annulus into 25 segments and derived the standard deviation on the numbers in these segments as the error on our counted numbers. In Figure 3.6 we show the resulting profile in the lower panel. The squares are our observed profile minus the observed background of $n_{bkg} = 0.06$ stars arcmin^{-2}. The gray circles are the data points of the profile by Palma et al. (2003) shifted along the y-axis to match our absolute numbers. The King profile in blue is drawn with the parameters in Table 3.1. Outside of ~ 20 arcmin the observed profile deviates from the King profile. We did not find a King profile which fitted the observations. Already Palma et al. (2003) found a similar discrepancy. We fitted a power-law $r^{-\gamma}$ to the data points between 40 arcmin and 100 arcmin. We found a slope of $\gamma = 3.0 \pm 0.5$, similar to the slope of Palma et al. (2003) who also found $\gamma = 3$.

3.4 Discussion & summary

We have studied the structure of three dSph galaxies, Sextans, Leo II, and Ursa Minor, with data from the SDSS DR7. For each galaxy we downloaded all data on photometric point sources in an area of $\sim 9° \times 9°$ centered on the dSphs. To minimize the number of foreground stars contaminating our sample we calculated two new color indices c_1 and c_2 and selected only those stars which have the same color-magnitude signature as the dSphs. To derive the two-dimensional structure of the three galaxies we used a color-magnitude weighted counting algorithm to derive the density of (potential) member stars on the sky. Each of the three galaxies shows a unique morphology, although they all are classified as dSph galaxies.

3.4.1 Sextans

Walker et al. (2008) measured for the first time the proper motion of Sextans by using a perspective method (Kaplinghat & Strigari 2008), not astrometric measurements. The resulting value has a large error. The measurement implies that Sextans is currently receding from its perigalacticon, $R_{peri} = 66^{+17}_{-61}$ kpc, toward apogalacticon, $R_{apo} = 129^{+113}_{-33}$ kpc. Due to the large error the resulting orbital eccentricities range from 0.25 to 0.89. If the most likely proper motion is assumed, it is unlikely that Sextans is a member of a stream associated with other known objects in the MW halo (Walker et al. 2008). We observe, as for Ursa Minor, that Sextans is not elongated along the orbit. We determined the orientation and size of the elliptical contours for different radii (see Table 3.2). For contours at levels between 5σ and 100σ above the mean we find a constant ellipticity. The trend for a slowly rotating position angle is not very clear.

The tidal radius of Sextans is about 4 times larger than the observed spatial extent in Figure 3.4. Therefore, the interaction of the dSph with the MW does not leave any obvious traces in the galaxy's morphology (Peñarrubia et al. 2008).

We observe the highest density peak not in the center of Sextans but roughly 3 arcmin NE of the center. Kleyna et al. (2004) proposed to have identified a distinct cold subpopulation

in the center of Sextans. In our data we do not detect any special feature at the center. Walker et al. (2006) identified 294 probable member stars of Sextans and derived the velocity dispersion profile. The profile remains flat out to $\sim 30'$. They further detected a cold substructure population roughly $15'$ north of the dSph's center, but did not confirm the detection of Kleyna et al. (2004). This newer substructure does not coincide with the highest density peak which we observe very close to the center. We examined the color and magnitude of the stars within the second innermost contour. The stars are all spread over the observed CMD, including one BHB star and several red HB stars.

Horizontal branch populations

Sextans is the only dSph in our sample which has a pronounced red and blue horizontal branch (see Figure 3.2 left panel). Harbeck et al. (2001) observed a population gradient in several Local Group dSphs, including Sextans. The red HB stars are more concentrated than the blue HB stars. We investigated the distribution of red and blue horizontal branch (HB) stars, respectively. We selected the red and blue HB stars in the selection boxes drawn in the left panel of Figure 3.2. Further we selected the stars to fulfill the color & magnitude constraints in (c_2, g). The contamination due to field stars for the red HB is much larger than for the blue HB. Ratnatunga & Bahcall (1985) estimated the foreground contamination at the location of Pal 3, which is very close to Sextans, to be ~ 9.4 stars arcmin^{-2} with magnitudes within one magnitude of Sextans' red HB.

In Figure 3.8, we show the distribution of the red and blue HB stars respectively. The distributions are normalized to their highest density peaks and the contours are drawn at levels of $0.1, 0.2, \ldots, 0.9, 1$ in both figures. Both distributions have their central peak not at the center of the dSph. The central peak of the red HB population located at the highest density peak of the general distribution. The central peak of the blue HB is at a totally different location. The blue HB stars are distributed around their center in an elliptical shape. The position angle is roughly $90°$ off of the general elliptical distribution.

In the lower panel of Figure 3.8 we show the radial density profiles for the red and the blue HB population, respectively. Although, the red HB population is much more contaminated by foreground stars, this population is more centrally concentrated than the blue HB population. For the red HB population the "flat" background is visible outside of 200 arcmin.

Connection to Pal 3?

The remote globular cluster Pal 3 is located on the sky only $2.5°$ NW of Sextans. Sextans was detected in the contour map of Pal 3 (see Figure 2.34, upper right panel). Pal 3 was also detected in the contour map of Sextans (the magenta cross in Figure 3.4. The two MW satellites have a comparable distance to the Sun, $R_{Pal\ 3} = 92.7$ kpc and $R_{Sextans} = 95.2 \pm 2.5$ kpc. A connection between the two might exist. The large errors on the proper motions of the two does not prohibit a connection. The density map of Sextans red HB stars shows a clear overdensity at the position of Pal 3. Comparing the CMDs (c_1, g) of Pal 3 and Sextans we see that the two red HBs coincide and the red giant branches are partially overlapping. But the heliocentric radial velocities are very different: for Sextans $v_r = 225.8 \pm 0.5$ km s^{-1} (Walker et al. 2006) and for Pal 3 $v_r = 83.4 \pm 8.4$ km s^{-1} (Dinescu et al. 1999). We conclude that there is no connection between Sextans and Pal 3.

3.4.2 Leo II

For Leo II, one of the remotest satellite galaxies of the MW, we found smooth contours and a halo of extra tidal stars, but no large scale tidal structure. We observed stars outside the
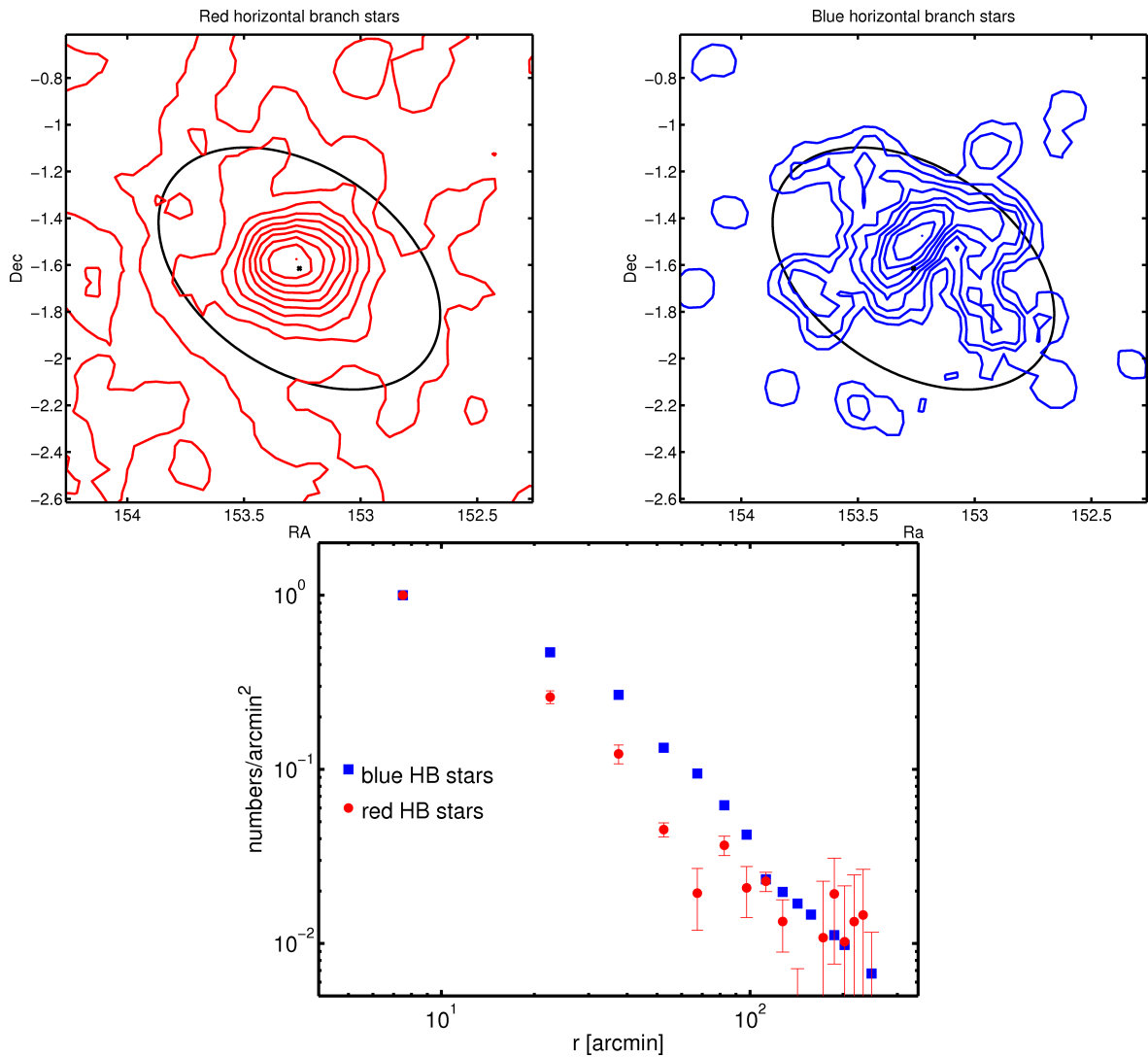
Figure 3.8: Comparison of red and blue HB stars of Sextans. *top panels:* 2d-distribution of red (left) and blue (right) HB stars. In black we draw the ellipse with a semi major axis corresponding to the core radius. The black cross marks the center. See text for level of contours. *bottom panels:* Radial profiles from counts in elliptical annuli.

nominal tidal radius. Komiyama et al. (2007) detected a substructure roughly 11 arcmin east of the center of Leo II. We do not observe any plateau or additional density peak, as our data is not as deep as the data of Komiyama et al. (2007). But our derived contours show a disturbed shape towards this substructure, which is not found on the opposite side of Leo II. Coleman et al. (2007) observed a density peak at this position.

Leo II has had little interaction with the Galactic potential (Koch et al. 2007; Coleman et al. 2007) and its modest radial velocity is consistent with a circular orbit which does not bring it close to the MW. The number density profile shows no deviation from a King profile as we would expect if tides had influenced the galaxy (Peñarrubia et al. 2008). The non-detection of large scale tidal features supports the idea that Leo II has spent most of its time at such remote distances.
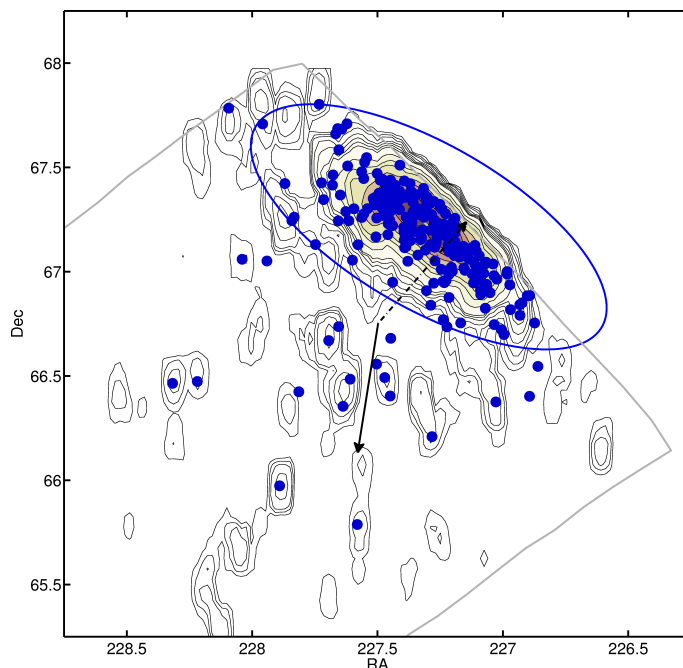
Figure 3.9: Distribution of blue horizontal branch stars of Ursa Minor as blue filled circles. The contour map is the same as in the lower panel of Figure 3.7.

3.4.3 Ursa Minor

Ursa Minor is right at the edge of the SDSS survey area. We revealed a very complex structure, including two off-center density peaks. The tidal radius of Ursa Minor is larger than the observed spatial extent. We also detect peaks of high density outside of the tidal radius. The origin of the disturbed morphology remains unknown, as the interaction of the dSph with the MW is unlikely to induce these features because the tidal radius is larger than the observed main body of the galaxy (Peñarrubia et al. 2008). On the other hand, the lack of detected tidal tails does not necessary mean no tidal disruption. Muñoz et al. (2008) shows with their N-body simulation of Carina that the simulated tidal tails are much fainter than an observer is able to detect today.

Ursa Minor has the greatest flattening of all classical dSphs (not considering Sagittarius). We reproduced the overall elliptical shape, but due to the galaxy's unfortunate location in the SDSS footprint were not able to re-measure the ellipticity. We also see that Ursa Minor is not elongated along its orbit.

Horizontal branch stars

In Figure 3.9 we show the same plot as in Figure 3.7 in the lower panel overplotting the blue horizontal branch (BHB) stars of Ursa Minor as light blue crosses. Most of the high density peaks are correlated to such a BHB star. Generally only few foreground stars are contaminating the population of BHB stars in a CMD. There are also BHB stars not correlated to any density peak. Might these be field star contaminants? And might the density peaks correlated to a BHB star be tidally stripped material of Ursa Minor?

Only with the photometric data it is not possible to answer these questions. Extra tidal stars of Ursa Minor have been detected by Muñoz et al. (2005). They found member stars at least 210′ away from Ursa Minor. The membership was determined in a combination of position in the CMD and radial velocity measurements. If a star at this radius was bound to
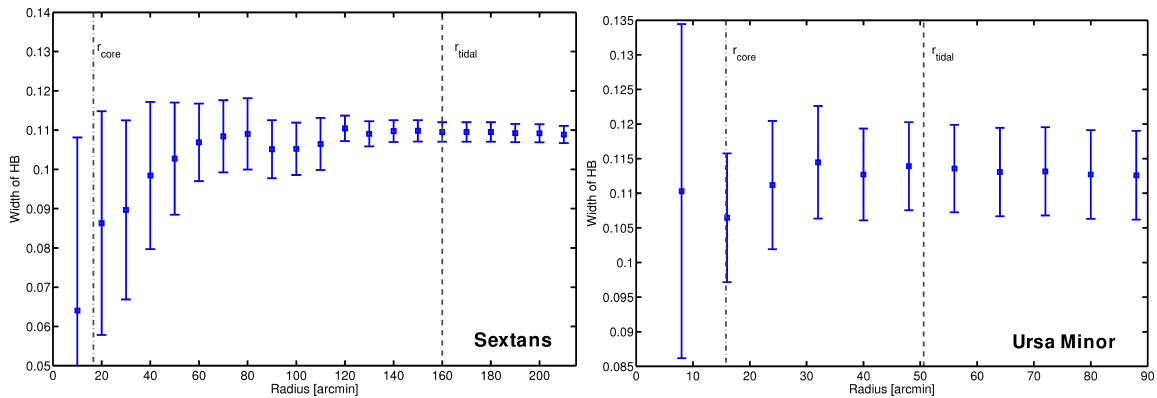
Figure 3.10: Width of the horizontal branch as a function of radius for Sextans (left panel) and Ursa Minor (right panel). The dash-dotted line denotes the core radius, the dashed line the tidal radius. See text for details.

the dSph galaxy it would imply a mass-to-light ratio $(M/L)_{tot} > 900(M/L)_\odot$. This unlikely value led the authors to the conclusion that they have found at least one unbound member star of Ursa Minor. Unfortunately, the SDSS sky coverage does not include the location of this unbound member star.

3.4.4 Width of the blue horizontal branch of Sextans & Ursa Minor

To determine the width of the blue HB (BHB) of Sextans & Ursa Minor we applied the same method as used in Klessen et al. (2003) in the case of Draco. We determined the average over the standard deviations σ_g of HB star candidates in color bins of width $\Delta(g-i) = 0.05$ mag including all BHB stars within a certain distance from the dSph's center. In Figure 3.2 the selection boxes for the BHB stars are shown. For Sextans, we used the BHB stars in ellipses at an interval of 10 arcmin, for Ursa Minor in ellipses spaced by 8 arcmin. In Table 3.3 for Ursa Minor and Table 3.4 for Sextans we list in column (1) the semi major axis of the ellipse, in the second column the measured average width of the HB, in the third column we list the spread of the width and in column four we list the number of stars used to measure the width. In Figure 3.10 we show the results for Sextans in the left plot and for Ursa Minor in the right plot. The radius shown is equal to the semi major axis of the ellipse within which the stars were chosen to determine the HB thickness.

The innermost point for Sextans only includes 6 stars, this data point should not be taken into account for the discussion. Outside of 120 arcmin we see a constant width of the BHB. Within the inner 60 arcmin we see an increase of the HB thickness. But there large errors for the three innermost points, hence, the increase is not as significant as it initially seems. The difference between the data point at $r = 20$ arcmin and $r = 80$ arcmin is 0.023 mag. The average photometric error for stars on the BHB is $\sigma = 0.029$ mag. The two numbers are comparable. Only a detailed model of Sextans, like Klessen et al. (2003) did for Draco, can give more clues to the possible distance spread along the line of sight.

For Ursa Minor we observe similar trends. We detect an increasing width, but the difference between the data point at $r = 16$ arcmin and $r = 48$ arcmin is much smaller, and the average photometric error, $\sigma = 0.048$ mag, is roughly eight times larger. Therefore, we conclude for Ursa Minor that it has no distance spread along the line-of-sight.

Table 3.3: Width of the BHB of Ursa Minor

radius	width [mag]	σ_{width} [mag]	# of Stars
(1)	(2)	(3)	(4)
8′	0.110	0.024	32
16′	0.107	0.009	106
24′	0.111	0.009	148
32′	0.115	0.008	172
40′	0.113	0.007	183
48′	0.114	0.006	197
56′	0.114	0.006	202
64′	0.113	0.006	204
72′	0.113	0.006	205
80′	0.113	0.006	207
88′	0.113	0.006	210

Table 3.4: Width of the BHB of Sextans

radius	width [mag]	σ_{width} [mag]	# of Stars
(1)	(2)	(3)	(4)
10′	0.064	0.044	6
20′	0.086	0.029	21
30′	0.090	0.023	35
40′	0.098	0.019	51
50′	0.103	0.014	65
60′	0.107	0.010	75
70′	0.108	0.009	80
80′	0.109	0.009	87
90′	0.105	0.007	93
100′	0.105	0.007	97
110′	0.107	0.007	100
120′	0.110	0.003	104
130′	0.109	0.003	107
140′	0.110	0.003	109
150′	0.110	0.003	110
160′	0.110	0.003	112
170′	0.110	0.003	112
180′	0.110	0.003	112
190′	0.109	0.002	113
200′	0.109	0.002	114
210′	0.109	0.002	115

3.4.5   Summary

We did not detect for any of our three dSph galaxies large scale extra tidal structures or a prominent $\mathcal{S}$-shape as a sign of ongoing tidal destruction. For Ursa Minor, for which an $\mathcal{S}$-shape was observed before, we could not verify this observation, due to the impractical location in the SDSS footprint. According to Muñoz et al. (2008) the non-detection of an $\mathcal{S}$-shape does not rule out tidal interaction as the $\mathcal{S}$-shape is only observable in the plane of the orbit. It must not be true that the plane of the sky and the plane of the orbit coincide. Also large scale tidal features might just not be observable with our data, as these are usually of low surface density or surface brightness. Our data only includes stars brighter than $g \approx 22$ mag, i.e., the dSph's red giant branches. On the other hand Sextans does not fill out its tidal radius, strongly supporting the idea that it is not influenced by the tides of the MW. For Ursa Minor, which does not fill its tidal radius fully either, extra tidal stars are already claimed to have been found. The case of Leo II is on first sight, due to its remote distance (and probably circular orbit) clear, supporting no tidal interaction. But we have found, as well as previous authors, some hints for extra tidal stars.

Definitely deeper data, covering large areas around the dSphs as well as kinematic follow-up confirmation can help solving some of the mystery of the interaction between the dSphs and the MW.

Further, we have investigated the possibility if Sextans or Ursa Minor might be unbound remnants of tidally disrupted dwarf galaxies Kroupa (1997); Klessen & Kroupa (1998) by measuring the width of the blue HB. For Ursa Minor the HB thickness is increasing, but the photometric error is larger than the increase. Therefore, we cannot rule out a "tidal scenario" for Ursa Minor. For Sextans, the increase is much larger and of about the same magnitude as the photometric error. A large line-of-sight extension cannot be ruled out.

4

Testing MOND in Palomar 14

We use the distant outer halo globular cluster Palomar 14 as a test case for classical vs. modified Newtonian dynamics (MOND). Previous theoretical calculations have shown that the line-of-sight velocity dispersion predicted by these theories can differ by up to a factor of three for such sparse, remote clusters like Pal 14. We determine the line-of-sight velocity dispersion of Palomar 14 by measuring radial velocities of 17 red giant cluster members obtained using the Very Large Telescope (VLT) and Keck telescope. The systemic velocity of Palomar 14 is (72.28 ± 0.12) km s^{-1}. The derived velocity dispersion of (0.38 ± 0.12) km s^{-1} of the 16 definite member stars is in agreement with the theoretical prediction for the classical Newtonian case according to Baumgardt et al. (2005). In order to exclude the possibility that a peculiar mass function might have influenced our measurements, we derived the cluster's main sequence mass function down to 0.53 $M_\odot$ using archival images obtained with the Hubble Space Telescope. We found a mass function slope of $\alpha = 1.27 \pm 0.44$, which is, compared to the canonical mass function, a significantly shallower slope. The derived lower limit on the cluster's mass is higher than the theoretically predicted mass in case of MOND. Our data are consistent with a central density of $\rho_0 = 0.1$ $M_\odot pc^{-3}$. We need no dark matter in Palomar 14. If the cluster is on a circular orbit, our spectroscopic and photometric results argue against MOND, unless this cluster experienced significant mass loss.

4.1 Introduction

Is classical Newtonian dynamics valid on all scales? On Earth classical Newtonian dynamics describes all non-relativistic phenomena very well. With the exploration and study of the Universe, we can explore low acceleration regimes that cannot be studied in our backyard and we observe deviations from the expected classical Newtonian behavior. E.g. the rotation curves of spiral galaxies do not show the classically expected Keplerian fall-off, but stay flat in the outer parts of these galaxies (Sofue & Rubin 2001). These flat rotation curves are commonly explained by introducing dark matter (DM). In the outer parts of the galaxies, DM is more abundant than regular baryonic matter and the gravitational effect of the DM on the baryons results in a flat rotation curve (Rubin et al. 1982). A major problem DM theory has encountered recently is the discovery that young tidal-dwarf galaxies also have rotation curves that imply a significant invisible matter component although they cannot be dominated by non-baryonic DM suggesting a non-classical physical solution (Gentile et al. 2007).

An alternative theory to DM is modified Newtonian dynamics (MOND; Milgrom 1983a,b; Bekenstein & Milgrom 1984). In MOND, the flat rotation curves of galaxies can be fitted without any assumption of unseen matter. According to MOND, Newtonian dynamics breaks down for accelerations lower than $a_0 \simeq 1 \times 10^{-8}$ cm s^{-2} (Begeman et al. 1991; Sanders & McGaugh 2002). The acceleration $\boldsymbol{a}$ in MONDian dynamics is given by the (heuristic) equation:

$$\mu \left(\frac{|\boldsymbol{a}|}{a_0} \right) \boldsymbol{a} = \boldsymbol{a}_N, \qquad (4.1)$$

where $\mu(x)$ is an arbitrary function with the following limits:

$$\mu(x) = \begin{cases} x & \text{if} \quad x \ll 1 \\ 1 & \text{if} \quad x \gg 1. \end{cases} \qquad (4.2)$$

Here, $\boldsymbol{a}_N$ is the standard Newtonian acceleration and a_0 is the acceleration limit below which MOND is applicable.

It has been claimed that MOND has difficulties explaining the merging of galaxy clusters, where the baryonic matter is clearly separated from the gravitational mass, as found by gravitational lensing (Clowe et al. 2006). However, Angus et al. (2006, 2007) demonstrated that such systems are consistent with MOND, but do require the existence of some hot dark matter.

Baumgardt et al. (2005, BGK05) proposed to use distant, outer halo globular clusters (GCs) to distinguish between classical and modified Newtonian dynamics. They calculated the line-of-sight velocity dispersion for 8 Galactic GCs in classical and in modified Newtonian dynamics. For these GCs the external acceleration due to the Milky Way and the internal acceleration due to the stars themselves are significantly below the critical limit of a_0. The expected velocity dispersions in case of MOND exceed those expected in the classical Newtonian case by up to a factor of three (see Table 1 in BGK05).

Palomar 14 (Pal 14) is a diffuse GC in the outer halo of our Galaxy. Pal 14's sparseness, faintness, and large distance to the Sun makes it a difficult observational target, and therefore it did not receive much attention. The first radial velocity for a Pal 14 member star was measured by Hartwick & Sargent (1978) resulting in 81 ± 3 km s^{-1}. Armandroff et al. (1992), based on radial velocity measurements for two stars, reported a systemic velocity of 72 ± 3 km s^{-1}. The deepest ground-based color-magnitude diagram (CMD) of Pal 14 was published by Sarajedini (1997). He concluded that Pal 14 is 3-4 Gyr younger than halo GCs with a similar metallicity. Hilker (2006, H06) published photometric data on three GCs from

the BGK05 sample: AM 1, Pal 3, and Pal 14. H06 confirmed Pal 14's youth of ~ 10 Gyr. The data from his study are used here to obtain targets for our spectroscopic observations. Dotter et al. (2008) published a photometric study of Pal 14 based on archival data obtained with the Wide Field Planetary Camera 2 on board the Hubble Space Telescope. The authors confirm Pal 14's relative youth. Here the same data are used to obtain the cluster's mass function.

This paper is the second in a series that investigates theoretically and observationally the dynamics of distant star clusters. In the first paper (Haghi et al. 2009, HBK09), we derived theoretical models for pressure-supported stellar systems in general and made predictions for the outer-halo globular cluster Pal 14. In the current paper, we present a spectroscopic and photometric study of Pal 14, as a test case for the validity of MOND. I.e. we are measuring the velocity dispersion of Pal 14 in order to compare the measured value to the predicted values made for MOND and classical dynamics by HBK09. Further, we are determining the mass function of Pal 14 in order to infer the cluster's mass. The derived mass and velocity dispersion are then compared to the predictions made by HBK09 for Pal 14 on a circular orbit in MOND.

The Chapter is organized as follows: In Section 4.2 we describe the observational material. In Sections 4.3 & 4.4 we present stellar radial velocities, the color-magnitude diagram and the mass function of Pal 14. In Section 4.5 we discuss the effects of our result for MOND and classical Newtonian gravity. The last Section concludes the paper with a summary.

4.2 Observations and data reduction

To distinguish between MOND and classical Newtonian dynamics we used two different kinds of observations. In order to measure Pal 14's velocity dispersion we obtained high-resolution spectra of red giant candidates towards Pal 14 with the Ultraviolet-Visual Echelle Spectrograph (UVES; Dekker et al. 2000) at the Very Large Telescope (VLT) of the European Southern Observatory (ESO) in Chile and with the High Resolution Echelle Spectrograph on the Keck I telescope. To be able to measure the cluster's mass function we used imaging data from the Hubble Space Telescope archive. In the following subsections we describe the reduction process of our observational data.

4.2.1 Spectroscopy with UVES

The photometry published by H06 shows the red giant branch and horizontal branch of Pal 14. Based on this photometry, we selected 16 of the 17 brightest red giants of Pal 14 for spectroscopy with UVES at the VLT. Our target stars cover the magnitude range V = 17.3 - 19.6 mag, which includes the brightest red giant of Pal 14 and goes down to the limit of faint stars observable with UVES. Figure 4.1 shows Pal 14's color-magnitude diagram. 15 of our targeted stars are probable red giants and one of the targets may be an AGB or evolved horizontal branch star. The significance of this different evolutionary state will be discussed in Section 4.3.1.

The spatial distribution of our spectroscopic targets is shown in Figure 4.2. The targeted stars lie mainly within two core radii with two stars in the cluster's outer region.

We used the Besançon Galaxy model (Robin et al. 2003) to estimate the number of foreground stars in our sample. We extracted stars towards Pal 14 in an area on the sky covering $\sim 20 r_h$, where $r_h = 1.28'$ is the half-light radius of Pal 14 (H06). The area covered with our sample stars is $\sim 2 r_h$. We selected only those stars located in the gray curves shown in Figure 4.1 and having apparent magnitudes V < 20 mag, and colors (B-V) > 0.65 mag. The resulting
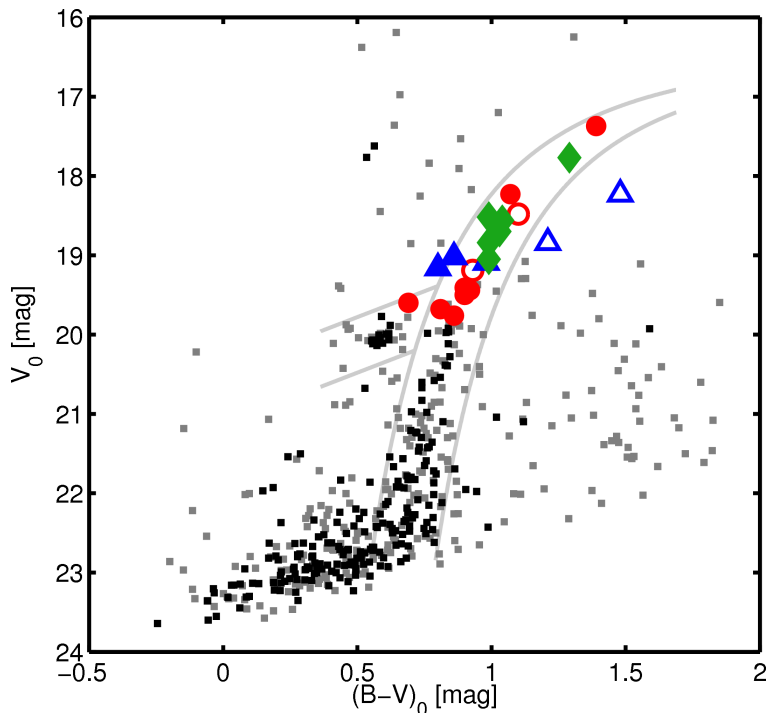
Figure 4.1: Color-magnitude diagram of Pal 14 from Hilker (2006). The observed targets for the radial velocity measurements with UVES are drawn as filled and open (red) circles. The open circles denote stars that were subsequently found to be the non-members (according to their radial velocity). The (blue) filled and open triangles are the stars observed with HIRES, the open triangles are the non-members. The (green) diamonds are the stars observed with UVES and HIRES. Dark grey dots are stars within 1 half light radius of Pal 14.

number of foreground contaminants in the actual area covered predicted by the model is ~ 1. UVES was used in its RED 580nm setting covering the wavelength ranges 476 - 577 nm (in the lower chip) and 584 - 648 nm (in the upper chip). We divided the 16 target stars into three setups according to their brightness: the *bright* setup, containing the five brightest stars in the magnitude range $m_V = 17.37$ - 18.52, was observed for 4×60 min in total. The *medium* setup with the four next fainter stars ($m_V = 18.56$ - 19.05) was observed for 6×60 min in total The *faint* setup, which included the seven least luminous stars ($m_V = 19.19$ - 19.76), was observed for 11×60 min in total. The observations were carried out in service mode within two observation periods, between May 30, 2006, and March 27, 2007. The pipeline reduced spectra ($R = 60\,000$) were used for the subsequent analysis.

The zero points in the reduced spectra were not identical. The sky emission lines in the single 1h-exposures were shifted with respect to each other. To correct for this we shifted the spectra to a common position of the sky emission lines. As a sky zero point location we used the sky lines in one of our own observed sky spectra, which we defined as reference spectrum. The resulting, shifted science exposures were further corrected for the heliocentric velocity shift. Finally all the shifted single 1h-exposure spectra were co-added for each star. In this way we get for the brightest star a $S/N = 16$ and for the faintest star $S/N = 4$.

4.2.2 Spectroscopy with HIRES

Within a program to study the internal kinematics of outer halo GCs (for details of the program see Côté et al. 2002) spectra for 11 candidate red giants in the direction of Pal 14
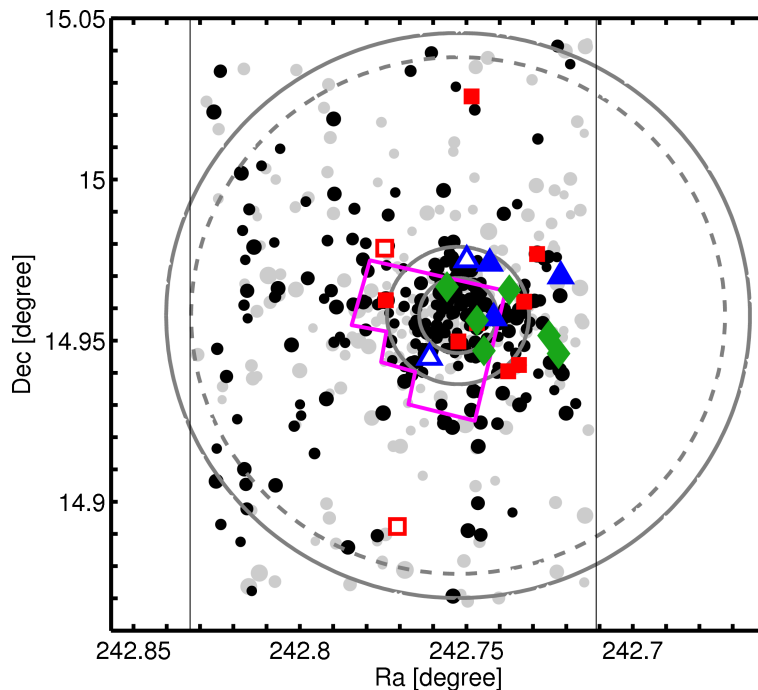
Figure 4.2: Spatial distribution of the spectroscopically observed Pal 14 stars. The observed targets for the radial velocity measurements with UVES are drawn as (red) filled and open circles. The two open squares mark the non-members (according to their radial velocity). The (blue) open and filled triangles are the stars observed with HIRES. The open triangles are the non-members. The (green) diamonds are the stars observed with UVES and HIRES. Dark grey dots are probable member stars according to their position in the CMD (see Figure 4.1). The grey concentric, solid circles are from inside out the core radius, the half-light radius and the tidal radius (H06); the dashed circle is the tidal radius calculated by BGK05. The (magenta) area is the HST/WFPC2 coverage.

were obtained using the High Resolution Echelle Spectrograph (HIRES; Vogt et al. 1994) mounted on the Keck I telescope. The spectra, which were collected during a single night in May 1998, have a resolution of R = 45 000 (for the 0.866″ entrance slit) and cover the wavelength range between 506 - 530 nm. The program stars were selected from CMDs published by Harris & van den Bergh (1984) and Holland & Harris (1992). The exposure times were adjusted on a star-to-star basis, varying between 900s and 2400s with a median value of 1800s. The spectra were reduced entirely within the IRAF[1] environment, in a manner identical to that described in Côté et al. (2002).

4.2.3 Radial velocity

To measure the radial velocity of our targeted stars we cross-correlated our final UVES and HIRES spectra with two high-resolution spectra of the UVES Paranal Observatory Project (UVES POP; Bagnulo et al. 2003): HD37811 (a G7 red giant) and HD45415 (a G9 red giant). The cross-correlation was done with the IRAF task *fxcor*. The heliocentric radial velocities of our two standard stars are: $v_{HD37811} = (-4.68\pm0.11)$ km s^{-1}, $v_{HD45415} = (52.70\pm0.04)$ km s^{-1}

---

[1]IRAF is distributed by the National Optical Astronomy Observatory, which is operated by the Association of Universities for Research in Astronomy, Inc., under cooperative agreement with the National Science Foundation.

(C. Melo 2007, private communication).

We determined the velocity shift of our sample stars relative to each of the two UVES POP stars. The UVES camera consists of two CCDs. For each pair of a UVES science target star and of a UVES POP star, we determined two radial velocities, one for the upper UVES chip and one for the lower UVES chip. These two velocities are averaged to a final velocity relative to the UVES POP star. Comparing the relative velocities measured for the two UVES POP stars, we find a mean difference of 0.1 km s^{-1}. Within the errors the two velocities are equal. The UVES science stars' radial velocity is the mean of the two velocities weighted by the Tonry-Davis R value (Tonry & Davis 1979) determined by *fxcor*.

For the HIRES sample, we determined the velocity of each science star relative to both UVES POP stars. Comparing the two relative velocities we find a mean difference of 0.07 km s^{-1}. The HIRES stars' radial velocity is the mean of these two measured velocities weighted by the Tonry-Davis R value.

For 6 stars we have both UVES and HIRES spectra. To determine a common zero point of the two different samples we compared the measured velocities for these 6 stars. A mean velocity shift of $\Delta v = 0.64$ km s^{-1} was found. The shift is probably due to a different instrumental zero point. The final HIRES velocities are corrected for this shift. The shift can also be due to binarity or stellar variability. For two of the six stars we also have UVES measurements at two epochs, within the errors the velocities agree very well. Short-period binarity and variability can be excluded for these two stars. The error of the HIRES measurements for the five fainter stars is comparable to the mean shift. Five stars have a positive velocity shift and only one a negative. If all stars were binaries we would not expect a clear spread around a positive shift.

The final radial velocity for the 6 stars, with UVES and HIRES spectra, is the weighted mean of the measured velocities. For the remaining 15 stars we only have measurements of one instrument, therefore this velocity is taken as the final radial velocity of the star.

4.2.4 Photometry

We used imaging data obtained with the Hubble Space Telescope/Wide Field Planetary Camera 2 (HST/WFPC2) from the HST archive to obtain a deep CMD of Pal 14. The data were obtained as part of the proposal GO-6512 (PI: Hesser). The same data were used by Dotter et al. (2008). The WFPC2 images cover the entire area within the cluster's core radius (H06), about 67% of the area within the nominal half-light radius (H06), and only 7% of the area within the tidal radius (H06) (see Figure 4.2). The pipeline-reduced FITS files were run through multidrizzle/tweakshifts (Koekemoer et al. 2002) to refine the image registration. All further processing was done on the original files together with the refined shifts, using the WFPC2 photometry package HSTphot (Dolphin 2000) and following the strategy outlined in the HSTphot User's Guide for preprocessing, photometry and artificial star tests. As in each subset of well aligned images in the same filter, the exposure times differed significantly, no co-adding was done. In Figure 4.3 we show the CMD of all stars brighter than 28th mag detected by HSTphot with the following selections: the HSTphot sharpness parameter ($|sharpness| < 0.2$), HSTphot type parameter ($type < 3$, i.e. the star is either a single star or a possible unresolved binary), and magnitude errors $\sigma_{mag} < 0.2$ mag.

To determine the photometric errors we inserted artificial stars with known magnitudes. The deviations of the subsequently measured magnitudes to the inserted values let us determine the photometric errors shown in Figure 4.3.
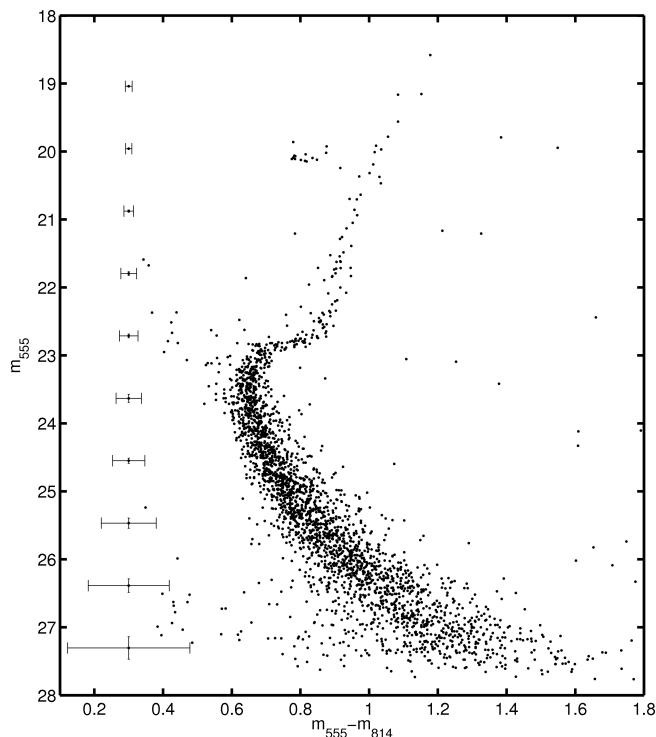
Figure 4.3: Color-magnitude diagram of Pal 14. We show the remaining stars after applying selections in the HSTphot parameters: sharpness, magnitude errors, and type. The CMD contains 2752 stars.

4.2.5 Completeness

For a detailed analysis of the stars in Pal 14, we performed radius-dependent artificial star tests within HSTphot to determine the completeness of the observations. For the artificial star experiment we added ~160 000 stars onto the image. For 7 annuli of a width of 0.3 arcmin we counted the number of artificial stars retrieved from the image with a magnitude not more than 0.2 mag different from the input value. In Figure 4.4 we show the seven completeness profiles (gray curves), which essentially fall on top of each other. Therefore, no radial dependence is observed, which is mainly due to the low density of Pal 14. The profile of the outermost annulus (solid line with squares) shows a decline at slightly brighter magnitudes. This is an artificial effect. The number of stars in this annulus is only 10% of the average number of stars in the other annulii. We used an averaged completeness profile in our analysis, shown as the black line. The 50% completeness limit is reached at $m_{555} = 27.21$ mag.

4.3 Spectroscopic results

4.3.1 Individual stellar radial velocities

In Table 4.1, we list the measured heliocentric radial velocities ($v(UVES)$ and $v(HIRES)$) and their errors ($\sigma_{v(UVES)}$ and $\sigma_{v(HIRES)}$) for the 21 stars in our sample. The listed velocities v_{rad} are the weighted mean of the UVES and the HIRES observations. The listed errors are the propagated errors, weighted by the Tonry-Davis R value from the cross-correlations. Star 4, Star 10, HV051 and HV086 all have significantly different velocities than the majority of the

Table 4.1: Heliocentric radial velocities of our sample stars.

Star[a]	Star[b]	$\alpha(2000)$ hh:mm:ss.ss	$\delta(2000)$ °:′:″	m_V mag	$B-V$ mag	$v(UVES)$ km s^{-1}	$\sigma_{v(UVES)}$ km s^{-1}	$v(HIRES)$ km s^{-1}	$\sigma_{v(HIRES)}$ km s^{-1}	v_{rad} km s^{-1}	$\sigma_{v_{rad}}$ km s^{-1}	m?
1		16:11:05.81	14:57:45.1	17.37	1.39	72.53	0.07	...	...	72.53	0.07	Y
2	HV025	16:10:58.73	14:56:48.7	17.77	1.29	72.76	0.09	71.49	0.30	72.47	0.14	Y
3	HV051	16:10:54.90	14:58:36.7	18.23	1.07	71.75	0.14	...	...	71.75	0.14	Y
		16:10:59.98	14:58:30.1	18.23	1.48	...	...	-73.77	1.17	...	...	N
4		16:11:04.98	14:53:32.3	18.48	1.10	-32.14	0.16	...	...	...	...	N
5	HV007	16:10:59.24	14:57:22.5	18.52	0.99	71.68	0.18	73.23	0.53	72.21	0.30	Y
6	HH244	16:10:53.36	14:56:45.4	18.56	1.04	72.58	0.18	72.79	0.46	72.65	0.27	Y
7	HH201	16:10:54.04	14:57:05.6	18.70	1.03	72.62	0.18	72.68	0.49	72.64	0.27	Y
8	HV043	16:10:56.90	14:57:56.5	18.84	0.99	71.56	0.21	70.97	0.47	71.38	0.31	Y
	HV086	16:11:02.66	14:56:41.1	18.84	1.21	...	...	-155.31	0.85	...	...	N
	HV055	16:10:58.31	14:58:26.2	19.02	0.86	...	...	73.62	0.89	73.62	0.89	Y
9	HV104	16:11:01.40	14:57:60.0	19.05	0.99	73.49	0.21	73.53	0.91	73.50	0.43	Y
	HH042	16:10:53.20	14:58:12.0	19.09	0.98	...	...	71.94	0.35	71.94	0.35	Y
	HV004	16:10:58.03	14:57:25.1	19.16	0.80	...	...	73.23	0.56	73.23	0.56	Y
10		16:11:05.89	14:58:43.2	19.19	0.93	50.44	0.19	...	...	...	...	N
12	HV074	16:10:56.21	14:56:32.7	19.41	0.90	71.83	0.23	...	...	71.83	0.23	Y
13	HV075	16:10:56.98	14:56:25.8	19.44	0.92	72.33	0.41	...	...	72.33	0.41	Y
14	HV006	16:10:59.24	14:57:19.7	19.50	0.90	71.80	0.27	...	...	71.80	0.27	Y
15	HV042	16:10:55.84	14:57:43.4	19.60	0.69	69.99	0.38	...	...	69.99	0.38	Y?
16		16:10:59.62	15:01:32.9	19.68	0.81	72.14	0.43	...	...	72.14	0.43	Y
17	HV021	16:11:00.58	14:56:59.1	19.76	0.86	72.39	0.32	...	...	72.39	0.32	Y

[a] Identification from Hilker (2006);   [b] Identification from Harris & van den Bergh (1984) and Holland & Harris (1992)
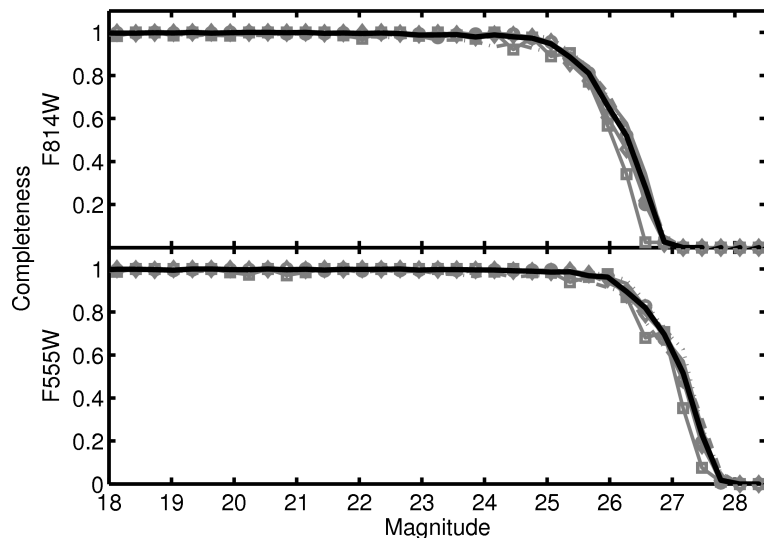
Figure 4.4: Completeness for the two filters F555W (lower plot) and F814W (upper plot). For each filter the completeness profile for seven annuli of width 0.3 arcmin are plotted as gray lines with different symbols, the black line is the overall completeness used in the data analysis.

Table 4.2: Radial velocity and velocity dispersion of Pal 14.

INSTRUMENT	VELOCITY $km\ s^{-1}$	ERROR$_V$ $km\ s^{-1}$	DISPERSION $km\ s^{-1}$	ERROR$_D$ $km\ s^{-1}$
UVES[a]	72.28 (72.12)	0.15 (0.20)	0.50 (0.70)	0.11 (0.15)
HIRES	72.46	0.29	0.66	0.26
combined[a]	72.28 (72.19)	0.12 (0.18)	0.38 (0.64)	0.12 (0.15)

[a] The first value is without the measurement of Star 15. The value in parentheses includes the measurement of Star 15.

measured stars which are centered around ~ 72.2 km s^{-1}: $v_{Star4} = (-32.14 \pm 0.16)$ km s^{-1}, $v_{Star10} = (50.44 \pm 0.18)$ km s^{-1}, $v_{HV051} = (-74.41 \pm 1.17)$ km s^{-1} and $v_{HV086} = (-155.95 \pm 0.85)$ km s^{-1}. These four stars are categorized as non-members (open circles and triangles in Figures 4.1 & 4.2). The remaining 17 stars are considered to be members of Pal 14 (see last column in Table 4.1). The measured velocity of Star 15 is more than 3σ away from the mean of the other member stars. Therefore, we present all our results including and excluding Star 15.

4.3.2 The systemic velocity and the velocity dispersion

First, we determined the mean velocity and the global velocity dispersion for the two different measurement sets, respectively. We used the maximization method described in Pryor & Meylan (1993). The mean velocity for the HIRES measurements is (72.46 ± 0.29) km s^{-1} and the velocity dispersion (0.66 ± 0.26) km s^{-1}. For the UVES measurements we find a mean velocity of (72.28 ± 0.15) km s^{-1} and a velocity dispersion of (0.50 ± 0.11) km s^{-1} if we exclude Star 15. Including Star 15, we find (72.12 ± 0.20) km s^{-1} and (0.70 ± 0.15) km s^{-1}. The measurements of the two samples agree very well.

Second, to determine the overall mean velocity and the global dispersion for all stars we also used the maximization method of Pryor & Meylan (1993). Including Star 15, we measured
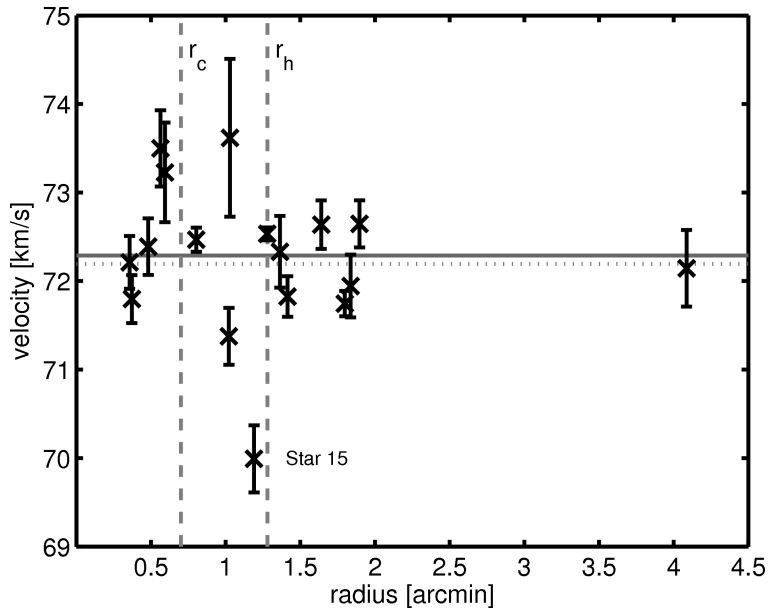
Figure 4.5: Radial distribution of stars with velocity measurements in Table 4.1. Black crosses indicate the 17 member stars of our sample of Pal 14. Star 15, for which the measured velocity is suspicious, is labeled. The horizontal solid line marks Pal 14's global radial velocity without Star 15, and the dotted line the radial velocity including Star 15. Further the core and half-light radii are indicated by dashed grey lines for an easier comparison with Figure 4.11.

a mean heliocentric radial velocity for Pal 14 of (72.19 ± 0.18) km s^{-1}, excluding Star 15, (72.28 ± 0.12) km s^{-1}. Within the error bars the two values agree. Our results confirm the earlier measurements by Armandroff et al. (1992).

Figure 4.5 shows the radial profile of our measured velocities (Star 15 is labeled). The cluster's mean velocity (for both cases) is marked by the solid (without Star 15) and dotted (with Star 15) horizontal line. In Table 4.2 we summarize the radial velocity and velocity dispersion measurements for the two instruments and for the combined stellar sample.

The global line-of-sight velocity dispersion for Pal 14 with Star 15 included is (0.64 ± 0.15) km s^{-1} with 99% confidence limits of 0.41 km s^{-1} and 1.10 km s^{-1}. Without Star 15, the line-of-sight velocity dispersion is (0.38 ± 0.12) km s^{-1} with 99% confidence limits of 0.26 km s^{-1} and 0.67 km s^{-1}. Within the errors the two values would agree. The theoretical prediction for the velocity dispersion of BGK05, for which a $M/L = 2$ was assumed, is $\sigma_{MOND} = 1.27$ km s^{-1} and $\sigma_{Newton} = 0.52$ km s^{-1}. For both cases, when Star 15 is included or excluded, our results are more consistent with the classical Newtonian prediction, while the MONDian prediction is outside the 99% confidence limits.

As described above the measured velocity of Star 15 seems to be deviant. There are several possible explanations for this discrepant velocity of Star 15:

1. Star 15 is a normal member of Pal 14. We performed a Monte Carlo simulation in order to evaluate how likely the measured radial velocity profile is. In the Monte Carlo simulation we randomly drew velocities from a Gaussian distribution, which was newly initialized for each draw by calculating the mean velocity and standard deviation of our measured radial velocities randomly convolved with their errors. The radial distributions of all draws were added. We performed a KS-test of the simulated velocity distribution with the distribution of the actually measured velocity. The KS-test re-

vealed a $< 1\%$ probability that the distribution that includes Star 15 comes from a Gaussian distribution, whereas the probability was $\sim 50\%$ that the distribution without Star 15 is Gaussian. This argues against Star 15's membership in Pal 14.

2. Star 15 is not a red giant, but more likely an evolved horizontal branch (HB) star or an AGB star judging from its position in the CMD (see Figure 4.1). The used templates of a G7 (HD37811) and a G9 (HD45415) red giant may not be appropriate for Star 15.

3. Star 15 could be a binary. For our faint UVES sample (Stars 10-17) we have observations at two epochs: June, 2006 and March, 2007. Theoretically this allows us to measure a possible change in velocity due to binarity. The faintness and the therefore low S/N of Star 15's spectra does not allow us to accurately measure the individual radial velocity for both epochs. The two measured velocities are $v_{2006} = (70.64 \pm 0.63)$ km s^{-1} and $v_{2007} = (69.13 \pm 0.75)$ km s^{-1}. Within the errors the two velocities are the same. Nonetheless, this does not allow us to exclude long-period binarity.

4. A further cause for the large offset of Star 15's velocity could be strong atmospheric variability, which can occur among AGB stars. However, from its position in the CMD, Star 15 would be an early-AGB star. In this early phase, AGB stars are not yet pulsating very strongly (Habing & Olofsson 2003). With essentially only one observing epoch it is impossible to know about the star's variability.

5. Another option might be that Star 15 is not a member of Pal 14. We computed a model velocity distribution of stars which are located within the light gray curves shown in Figure 4.1 using the Besançon Galaxy model (Robin et al. 2003) as described in Section 4.2.1. The expected velocity distribution, for stars with radial velocities > -160 km s^{-1}, is shown in Figure 4.6. The number of stars in each bin is scaled to an area of $\sim 2r_h$, in order to reproduce the actually observed area. We expect about 9 stars to fulfill the photometric constraints. 0.5 stars have a radial velocity between 50 km s^{-1} and 75 km s^{-1}. Therefore, Star 15 could be a foreground contaminant.

4.4 Photometric results

In order to make predictions for the velocity dispersion in Newtonian and MONDian dynamics, we first have to determine the mass of Pal 14. The measured low velocity dispersion is in excellent agreement with the theoretical prediction of classical Newtonian dynamics, and a very strong indicator against MOND. The theoretical calculations by HBK09 show the dependence of velocity dispersion and mass (see Figure 8 in HBK09) for classical dynamics and MOND. For a given velocity dispersion the necessary mass is always smaller in MOND than in classical dynamics. Our derived low velocity dispersion is explainable in MOND if we find a low total mass for Pal 14. To constrain the mass in Pal 14, we analyzed Pal 14's CMD and main sequence mass function.

4.4.1 Color-magnitude diagram

Figure 4.3 shows the HST CMD of Pal 14 with the remaining stars after the HSTphot parameter cuts (see Section 4.2.4 for details). The CMD reaches ~ 4 mag below the main sequence turnoff, m$_{MSTO} = 23.63 \pm 0.01$ mag, which allows us to theoretically determine the cluster's mass function down to ~ 0.49 $M_\odot$ (see Section 4.4.4). The CMD shows a well-populated main sequence (MS), subgiant branch, red giant branch, red horizontal branch
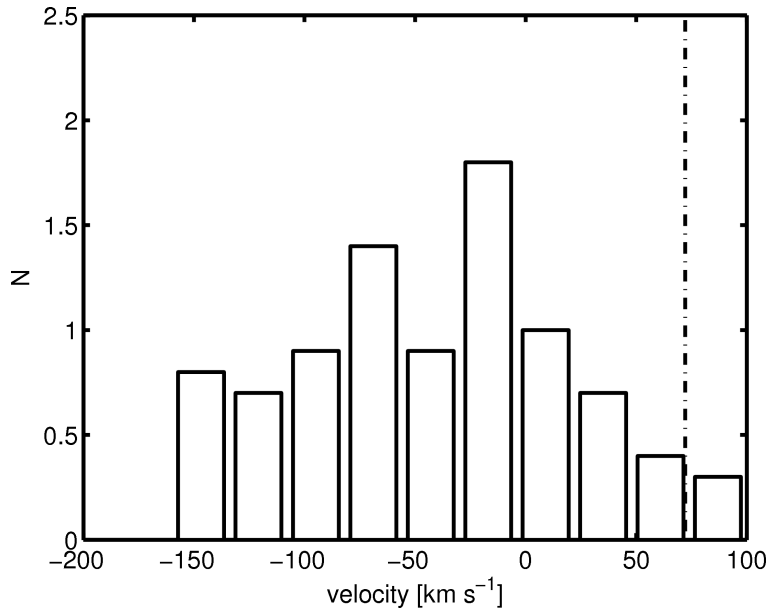
Figure 4.6: Expected velocity distribution based on the Besançon Galaxy model. Only stars that lie within the grey area in Figure 4.1 and that have a radial velocity larger than -160 km s^{-1} are counted (see text for more details). The dash-dotted, vertical line marks the systemic velocity of Pal 14, ~ 72.2 km s^{-1}.
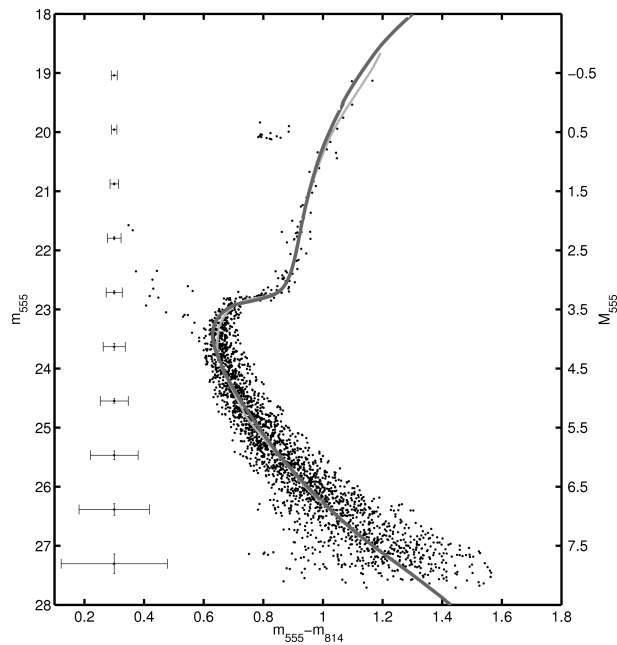

Figure 4.7: Color-magnitude diagram of our final sample of Pal 14 stars from WFPC2. The light gray line shows the derived cluster ridgeline, the dark gray line is the best fitted α-enhanced, $[\alpha/\text{Fe}]=+0.2$, Dartmouth isochrone with an age of 11.5 Gyr, E(m$_{555}$-m$_{814}$) = 0.063, and $(m - M)_{555} = 19.45$ mag.

(HB), and some probable blue straggler stars. The presence of a red HB and its implications were discussed in Sarajedini (1997) and Dotter et al. (2008). As expected there is only little field star contamination of Milky Way stars due to the moderately high Galactic latitude of Pal 14 and due to the small field of view of WFPC2. Judging from the TRILEGAL Galaxy Model (Girardi et al. 2005), the number of contaminating foreground stars on our WFPC2 image in the CMD-area covered by Pal 14 is ~ 2. The width of the main sequence which we observe is due to a combination of the photometric errors and binary stars.

For our further analysis of Pal 14, we applied a stricter selection of our stellar sample. We determined the cluster's fiducial ridgeline (see Figure 4.7, the light gray line). The ridgeline reproduces the mean location of the stellar distribution in the CMD. To derive the cluster's ridgeline we adopted the method described in Glatt et al. (2008a). We selected all stars within 2σ of the ridgeline and added the blue stragglers and the HB stars for our final sample. The $2\,500$ stars in our final sample are plotted in Figure 4.7.

4.4.2 Age & distance

Pal 14 is known to be younger than typical halo GCs (Sarajedini 1997; Hilker 2006; Dotter et al. 2008) at its metallicity. We derived Pal 14's age via isochrone fitting. We used the Dartmouth isochrones (Dotter et al. 2007), which have been shown to reproduce the location of the MS, subgiant branch, and red giant branch very well (Glatt et al. 2008b). We adopted the published spectroscopically determined metallicity of [Fe/H] = -1.50 (Harris 1996). Distance and reddening were treated as free parameters. A large number of isochrones was fitted using different combinations of age, distance, and reddening. We selected by trial-and-error the isochrone that best matched the above derived ridgeline.

With an α-enhanced isochrone, $[\alpha/\mathrm{Fe}] = +0.2$, our best fit yields an age of (11.5±0.5) Gyr, a reddening of $\mathrm{E}(m_{555} - m_{814}) = 0.063$ (corresponding to $\mathrm{E(B-V)} = \mathrm{E}(m_{555} - m_{814})/1.2 = 0.05$ (Holtzman et al. 1995)), and an extinction corrected distance modulus of $(m - M)_{555,0} = 19.25$ mag. Sarajedini (1997) stated the age of Pal 14 is 3-4 Gyr younger than the age of similar halo GCs, H06 derived an age of 10 Gyr and Dotter et al. (2008) determined an age of 10.5 Gyr via α-enhanced isochrone fitting. An α-enhancement is found for many of the Milky Way GCs (see, e.g. Carney 1996). Our new age determination reduces the offset to other halo GCs slightly.

From our CMD and the isochrone fit, we find a dereddened distance to Pal 14 of (71±1.3) kpc, which places Pal 14 a bit closer to the Sun than previously thought. In comparison, H06 derived a distance to Pal 14 of 74.7 kpc. Dotter et al. (2008) derived an even larger distance of 79 kpc.

4.4.3 Luminosity function

The cluster's MS luminosity function was derived by counting the number of stars, fainter than the MS turnoff at $\mathrm{m}_{MSTO,0} = 23.44\pm0.01$ mag, in 0.5 mag wide bins separated by 0.1 mag along the dereddened m_{555} axis.

Furthermore, the WFPC2 images do not cover the entire projected spatial extension of the cluster on the sky. Our data cover the entire area within the cluster's core radius (H06), about 67% of the area within the nominal half-light radius (H06), and only 7% of the area within the tidal radius (H06). The correction for the missing coverage within the half-light radius was done as follows. We derived the luminosity function for the stars within the annulus between the half-light and the core radius ($n_{annulus}$). We then corrected each magnitude bin of the entire distribution proportionally to the distribution of stars within the covered
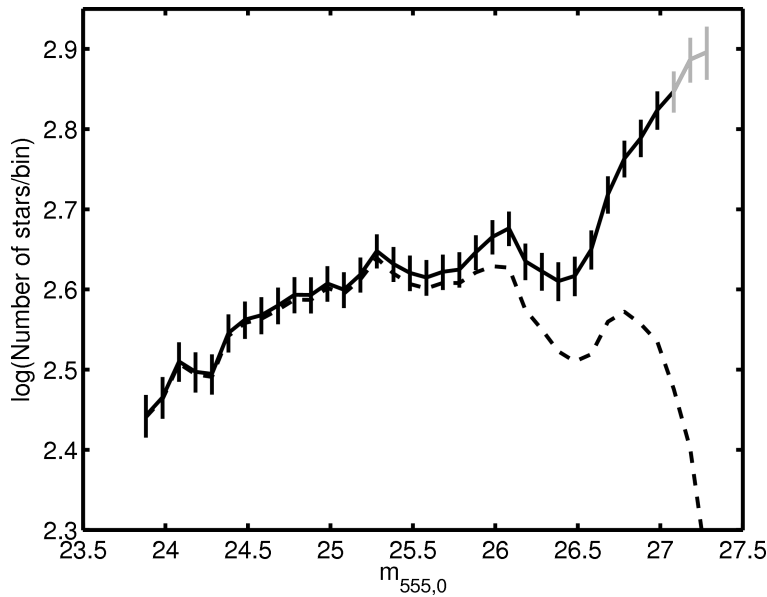
Figure 4.8: Luminosity function of Pal 14's MS. The dashed line is the number of observed stars corrected for the missing area coverage The solid line is the number of stars after the correction for photometric incompleteness (the grey dots mark points with a completeness $<50\%$). The horizontal bars are the $N^{1/2}$ errors.

annulus:

$$N_{area} \quad = \quad N_{obs} + n_{annulus}(\frac{A_{annulus}}{A_{covered}} - 1), \qquad \boxed{4.3}$$

where $A_{covered}$ is the area of the annulus covered by the WFPC2 image, and $A_{annulus}$ the area of the annulus itself. The final correction was done for the photometric incompleteness (see Figure 4.4 and Section 4.2.5). We did not correct for potential foreground contaminants. The TRILEGAL Galaxy model only predicts a very small number of stars on our main sequence. In Figure 4.8 we show the resulting luminosity function of Pal 14. The solid line shows the final number of stars per 0.5 mag bin. The errors are given as $N^{1/2}$.
Dotter et al. (2008) report an unusual flat luminosity function for Pal 14 between V $=23$ mag and 28 mag. Their data was not corrected for incompleteness. Our MS luminosity function shows the same flat behavior, correcting for incompleteness does not change the slope dramatically.

4.4.4   Mass function

The function $dN/dm \propto m^{-\alpha}$ describes the number of stars in the mass interval $[m, m+dm]$. We obtained such a mass function for Pal 14's MS. The upper boundary of the MS is at the turnoff, $m_{MSTO,0} = 23.44 \pm 0.01$ mag. Using the masses given by the 11.5 Gyr isochrone by Dotter et al. (2007), we have stellar masses on the MS covered by our photometry between $0.49\ M_{\odot}$ and $0.79\ M_{\odot}$. We binned the masses linearly into 10 bins of equal width of 0.03 $M_{\odot}$. In Table 4.3, we list the center of the mass bins in the first column, and the number of observed stars (N_{obs}) for each bin in the second column.
We corrected the number of stars per mass bin for the same effects as in the case for the luminosity function. First, the observed number of stars per mass bin was corrected for the missing area coverage in the same way as described above (Table 4.3, column 3). Second,

Table 4.3: Mass function of Pal 14.

BIN CENTER $\mathcal{M}_\odot$	N_{obs}	$N_{corrected}$	N_f	σ_{N_f}	COMPLETENESS
0.51	114	152	706	59	0.21
0.54	249	330	542	30	0.61
0.57	196	255	316	20	0.81
0.60	258	328	372	21	0.91
0.63	201	274	282	17	0.97
0.66	226	306	311	18	0.98
0.69	219	282	286	17	0.99
0.72	212	271	273	17	0.99
0.75	213	268	270	17	0.99
0.78	225	301	302	18	1.00
0.81	289	366	367	20	1.00

Column 1 lists the center of our mass bins, column 2 the number of observed stars per bin, column 3 the number of stars per bin after correcting for the missing area coverage, column 4 contains the final number of stars per bin after correcting for completeness, column 6 lists the propagated error on the final number of stars per bin, and column 7 lists the average completeness value for the mass bin. (The numbers in columns 3,4, and 5 are rounded to the nearest integer.)

the mean of the stars' incompleteness was used as a correction factor. The corrected number of stars per mass bin is listed in Table 4.3, column 4. To fit a slope to our data we only considered data with a completeness factor > 0.50 (see last column in Table 4.3). This restriction leads to a MS mass function covering the range from 0.525 $M_\odot$ to 0.79 $M_\odot$. We fitted a slope to our data points in $log(number)$ vs $log(mass)$ space. In Figure 4.9 we plot the resulting mass function and the fitted slope of $\alpha = 1.27 \pm 0.44$ as the gray line. Dotter et al. (2008) find a similar mass function slope of $\alpha \approx 1.2$. The canonical Kroupa IMF (Kroupa 2001) in this notation is 2.35 for the given mass range. In Figure 4.9, the observed mass function is shown as the dash-dotted line. The dotted line is the mass function after the area corrections. The solid line denotes the completeness corrected number of stars.

Compared to the canonical slope of 2.35 Pal 14's mass function is flatter in the given mass range. De Marchi et al. (2007) compiled the mass function slope in the stellar mass range 0.3 to 0.8 $M_\odot$ for 20 Galactic GCs of different sizes, concentrations, positions in the Galaxy, etc. Pal 14 has a (measured) concentration of c = 0.85 (H06). Clusters with a similar concentration span a mass function slope range of $\alpha = -0.9 \dots 1.3$ (see Figure 1 in De Marchi et al. (2007)). The derived slope is comparable with the slope of similar clusters. E.g., NGC 6809 has a concentration of 0.76 and a mass function slope of 1.3. This slope was derived around the cluster's half-light radius, where the impact of mass segregation is negligible (Paresce & De Marchi 2000). For Pal 14 we see an increasing number of stars per unit mass down to 0.525 $M_\odot$. A sudden decrease below this low-mass limit would be a unique case as no Galactic GC is known to show an initial rise followed by a decrease.

In principle there are two reasons for such a depleted mass function: Either Pal 14 did form with only few low-mass stars, or the cluster is mass segregated and lost most of its low-mass stars through interaction with the Galactic tidal field. The small area covered by the WFPC2 image does not allow us to estimate the amount of mass segregation. In an upcoming paper we will discuss the issue of mass segregation in Pal 14 based on imaging data we obtained at the VLT.

4.4.5   Total mass & mass-to-light ratio

To estimate the mass of Pal 14 we corrected for the missing area within the half-light radius. We measured an observed mass for Pal 14's main sequence $\mathcal{M}_{ms,obs} = (1\,340 \pm 50)\ M_\odot$ (above the 50% completeness limit). The errors are propagated from the measured photometry. Taking into account the stars brighter than the MS turn off, correcting for the missing area within the half-light radius and the completeness we get $\mathcal{M}_{cor} = (2\,200 \pm 90)\ M_\odot$ within the mass range $0.525\ M_\odot$ to $0.83\ M_\odot$. If we extrapolate by assuming that the measured slope of $\alpha = 1.27$ holds down to $0.5\ M_\odot$ and assume a Kroupa-like mass function, $\alpha = 1.3$ for masses between $0.1\ M_\odot$ and $0.5\ M_\odot$, we have a total mass within the half-light radius for Pal 14 of $\mathcal{M}_{tot,hl} = (6\,020 \pm 500)\ M_\odot$.

The slope of the mass function for stars with masses $< 0.5\ M_\odot$ is still under debate (Kroupa 2002; Elmegreen 2009). Pal 14 is very far from the Milky Way. It may have an eccentric orbit that would bring it much closer to the Milky Way at perigalacticon possibly leading to strong tidal interaction and to an enhanced loss of very low-mass stars. Richer et al. (2004, 2008) studied the main sequence mass function of the GCs NGC 6397 and M 4 down to the hydrogen-burning limit. In the cluster cores they found mass function slopes of $\alpha = -0.7$, these cluster centers lack low-mass stars. Therefore, we also calculated the mass in Pal 14 for a mass function with a linearly declining slope for masses $< 0.5\ M_\odot$ towards less massive stars ($\alpha = -1.0$). In that case the lower limit for the total mass within the half-light radius of Pal 14 is $\mathcal{M}_{tot,hl} = (2\,930 \pm 130)\ M_\odot$.

If we assume that light traces mass, then the half-light radius will also be the half-mass radius. Therefore we double the above numbers to estimate the total mass of Pal 14. The extrapolation with a Kroupa-like IMF for stellar masses between $0.1\ M_\odot$ and $0.5\ M_\odot$ yields a total mass of Pal 14 of $\mathcal{M}_{tot} \approx 12\,040\ M_\odot$. With the declining mass function for masses $< 0.5\ M_\odot$, we get a total mass of $\mathcal{M}_{tot} \approx 5\,860\ M_\odot$. Considering stellar remnants will increase the mass further.

Using the total mass of Pal 14, we derive the mass-to-light ratio. The extrapolation with the Kroupa-like mass function yields $M/L = (2.2 \pm 0.4)\ M_\odot/L_\odot$. The extrapolation with the declining mass function gives $M/L = (1.1 \pm 0.1)\ M_\odot/L_\odot$.

4.5   Discussion

4.5.1   MOND?

In HBK09, we calculated the global line-of-sight velocity dispersion of isolated and non-isolated stellar systems in MOND for circular orbits. For details on the simulation see HBK09. In Figure 4.10, we plot the two curves from these calculations showing the global line-of-sight velocity dispersion as a function of stellar mass for the classical (open squares) and the modified Newtonian case (open circles). For a given total mass the velocity dispersion in the MONDian case is larger than in the classical theory. In our case, we observed a line-of-sight velocity dispersion (shown as the horizontal lines) and derived the cluster's mass (shown as the vertical lines).

We measured a line-of-sight velocity dispersion of (0.38 ± 0.12) km s^{-1}, not including Star 15. For such a low dispersion, the theoretically predicted mass in MOND is $950^{+600}_{-400}\ M_\odot$, and in classical dynamics $8\,200^{+6000}_{-4000}\ M_\odot$. We have observed a lower limit of $(2\,200 \pm 90)\ M_\odot$ (marked in Figure 4.10 by the vertical line labeled *observed*) considering only the area within the half-light radius of Pal 14. Already the lower limit excludes the MONDian case, as we have observed more stellar mass than MOND predicts and the stars outside the cluster's half-light radius are not considered yet. The total mass of $\sim 12\,000\ M_\odot$ (in Figure 4.10 vertical
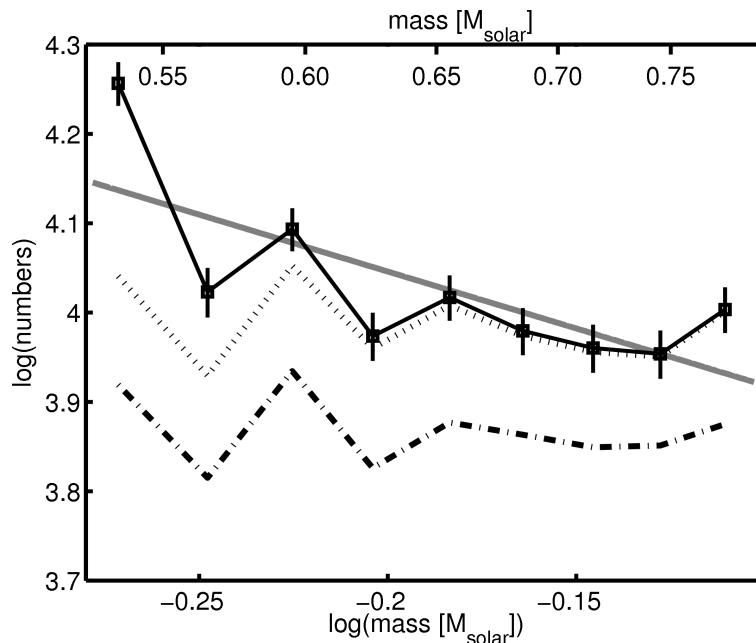
Figure 4.9: Mass function of Pal 14. The lowest (dash-dotted) line is the observed mass function for stars with masses between 0.49 $M_\odot$ and 0.80 $M_\odot$. The dotted line shows the mass function after correcting the number of stars per bin for the missing area coverage of the WFPC2 data. The top line also includes the correction for the photometric completeness. In gray the fitted slope $\alpha = 1.27 \pm 0.44$ is shown.

line marked *extrapolated ($\alpha = 1.3$)*) is several times larger than the MONDian prediction. A declining extrapolation at the low-mass end down to 0.1 $M_\odot$ gives a total mass of Pal 14 of 5 860 $M_\odot$ (in Figure 4.10 vertical line marked *extrapolated ($\alpha = -1$)*), which is also clearly higher than the MONDian prediction. The resulting dynamical mass-to-light ratio for the classical Newtonian case is $M/L_{dyn} = (1.48^{+1.00}_{-0.70})$ $M_\odot/L_\odot$.

If we include the measured velocity of Star 15, we find a line-of-sight velocity dispersion of (0.64 ± 0.15) km s^{-1}. According to the theoretical calculation of HBK09 the cluster mass in MOND would be $2\,600^{+1400}_{-1200}$ $M_\odot$, and in classical dynamics $24\,000^{+11000}_{-10000}$ $M_\odot$. In this case, the extrapolated mass is still larger than the predicted mass in MOND. Also, for the declining mass function for masses < 0.5 $M_\odot$ the total mass is larger than the MONDian prediction.

Although the measured low velocity dispersion is an indication of whether MOND or classical Newtonian dynamics is correct, one can think of a scenario in which the cluster would be governed by MOND but shows at the same time a velocity dispersion consistent with the classically derived (low) value. In MOND the gravitational force is effectively stronger than in classical dynamics. The stars in a GC which resides in the MOND regime therefore acquire a higher internal velocity, thus leading to a shorter dynamical time and a faster relaxation time for the cluster (Ciotti & Binney 2004; Zhao 2005). Therefore, already after only a couple of orbits around the Galaxy, Pal 14 would have lost a large fraction of its low-mass stars and stellar remnants, leaving the cluster enriched in stars around the main sequence turnoff and on the red giant branch. In one of Pal 14's perigalactica (if it is on an eccentric orbit), the cluster would become partially unbound and would expand, while it still resides in the classical Newtonian environment close to the Galaxy. The unbound cluster, then, would move further outward on its orbit and would eventually drift into the MONDian regime in the Galaxy's outskirts. As MOND is 'stickier' than classical Newtonian dynamics, the
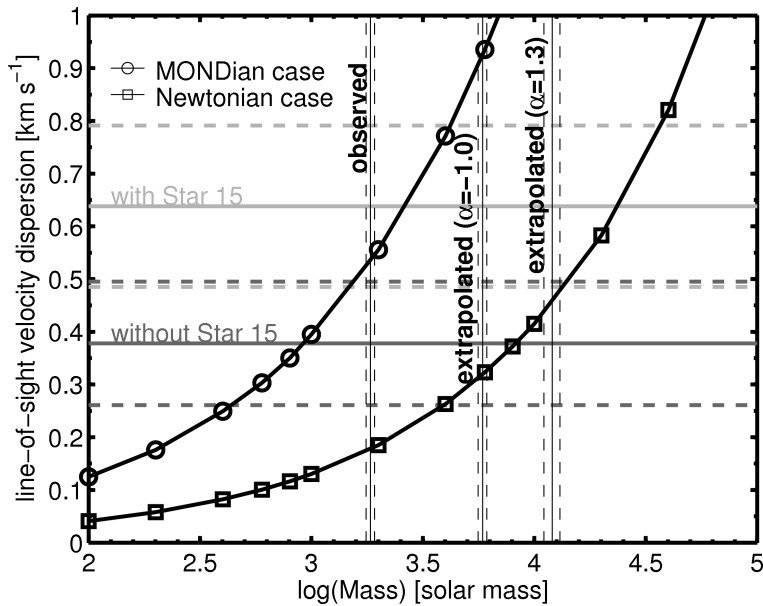
Figure 4.10: Theoretically predicted velocity dispersion as a function of mass. The two black curves are the predictions in MONDian dynamics (open circles) and in classical Newtonian dynamics (open squares). The observed velocity dispersions (and the errors) are drawn as the two horizontal lines, the light gray without Star 15, dark gray with Star 15. The vertical lines mark the observed lower mass limit and the two extrapolated lower mass limits.

stars are bound more strongly again. As a consequence, an observer may measure a low velocity dispersion, similar to the value derived in classical dynamics. At the same time, the cluster's mass is small. For such a scenario to be valid, the cluster would have to be strongly effected by tidal forces, but should not move too far in to be completely destroyed. Detailed simulations on the influence of radial orbits on the velocity dispersion in MOND are necessary. Unfortunately no proper motion is available for Pal 14 in order to make any constraints on its orbit.

MOND is not the only modification of classical Newtonian dynamics. One other possible theory is modified gravity (MOG; Moffat 2005; Moffat & Toth 2008). MOG explains/predicts galaxy rotation curves, galaxy cluster masses, etc. and at the same time produces predictions consistent with classical dynamics for smaller systems, e.g. GCs. MOG predicts little or no observable deviation from classical Newtonian gravity for GCs with masses of a few times $10^6 \, M_\odot$ (Moffat & Toth 2008). Our result is consistent with the classical prediction and can, therefore, neither support nor contradict MOG.

Recently Bruneton et al. (2009) proposed an extension of MOND which predicts a return to Newtonian dynamics (plus possibly DM in the form of a massive scalar field) in low medium-density (i.e. low gas density) environments. Newtonian GCs could be compatible with such an extension of MOND, although the question would then be what distinguishes DM-free GCs from DM-dominated dSph galaxies.

4.5.2   Velocity dispersion profile and dark matter

It is widely believed that globular clusters contain no dark matter (e.g., Moore 1996). Their dynamical masses closely match the values from population synthesis (McLaughlin & van der Marel 2005). The velocity dispersion profile of GCs should, therefore, show a Keplerian fall-off. Scarpa et al. (2007) studied velocity dispersion profiles of six GCs in the Galaxy. For
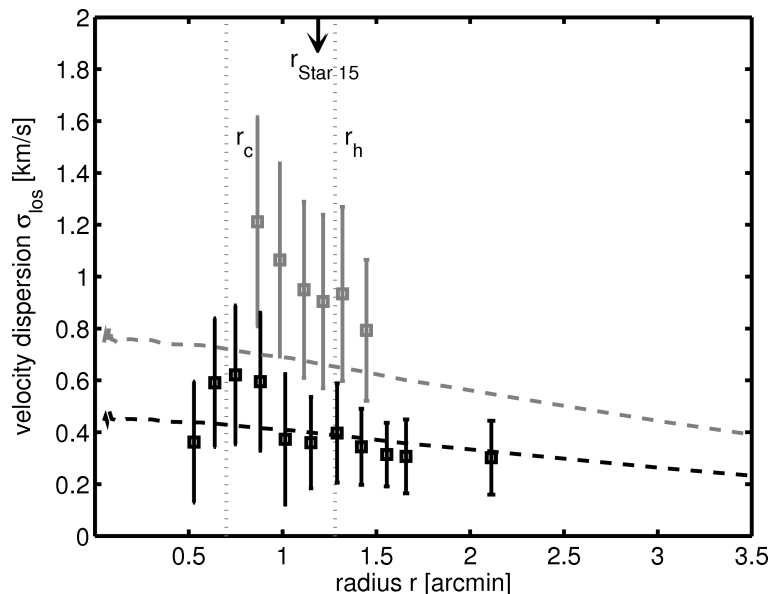
Figure 4.11: The velocity dispersion profile of Pal 14 using running bins with six stars in each bin. The black squares denote the velocity dispersion without Star 15. The gray squares denote these bins where Star 15 was included. The black and gray dashed curves are the theoretical dispersion profiles if Star 15 was included and excluded, respectively. The vertical, dotted lines are the core and half-light radii (H06), respectively. The arrow at the top of the plot marks the radial distance of Star 15 from the cluster center.

the five high-concentration clusters in their study (ωCen, NGC 6171, NGC 6341, NGC 7078, NGC 7099) they found the predicted fall-off in the inner parts of the clusters, but also an unexpected flattening in the outer parts. On the other hand, for the low-concentration cluster NGC 288 they found a more or less flat dispersion profile. For the high-concentration clusters, the profiles always flatten at a radius where the acceleration is around the MONDian limit of a_0 for a mass-to-light ratio of 1. To draw any conclusion about MOND from this is rather difficult, as the discussed clusters' total accelerations are not below a_0 and therefore the effect of MOND is tiny or even not existent; the clusters are all too close to the Galactic center.

All our stars but one are located within $2.5'$ of the center of Pal 14. We derived the line-of-sight velocity dispersion profile with running radial bins, each bin containing six stars. Figure 4.11 shows the resulting velocity dispersion profile. Between $1'$ and $1.5'$ we derived the velocity dispersion either including Star 15 or excluding Star 15. The lower black squares are the case where Star 15 was not included, the upper gray squares the case including Star 15's velocity. For the case excluding Star 15, we can see (within the errors) a slightly declining velocity dispersion profile. The dashed curves in Figure 4.11 are the theoretically calculated profiles of HBK09. If we compare our dispersion profile to the theoretical predictions we see a slow fall-off towards outer radii for both. We have observed velocity measurements in the inner $2.5'$ (~ 50 pc ~ 3.6 core radii). On the other hand, Scarpa et al. (2007) showed the velocity dispersion profile of NGC 288, another sparse GC with a concentration of c = 0.96 (Harris 1996). They describe the profile to be flat out to 4.5 core radii. In order to improve the significance of the comparison of the theoretical prediction and the observational data for Pal 14 as well as of the comparison with similar clusters, spectroscopic data out to larger radii are needed for Pal 14.

We treat this GC the same way as dwarf spheroidal (dSph) galaxies in Madau et al. (2008) to calculate the central density, using $\rho_0 = 166\eta\sigma^2/r_c^2 \; M_\odot pc^{-3}$, setting $\eta = 1$, $r_c = 0.7' =$

14.5 pc, and $\sigma = 0.38 \pm 0.12$ km s^{-1}. We find a central density of $\rho_0 = 0.1 \pm 0.07$ $M_\odot pc^{-3}$. A value which is very similar to values found for dSph galaxies (see e.g. Table 1 in Madau et al. (2008)). On the other hand, if we derive the density within the half-light radius from our mass estimate $\mathcal{M}_{tot,hl} = (6\,020 \pm 500)$ $M_\odot$ and $r_h = 1.28' = 26$ pc, we find $\rho = 0.08 \pm 0.01$ $M_\odot pc^{-3}$. Within the errors the two values agree. We do not need to assume DM for Pal 14.

4.6 Summary

Modified Newtonian dynamics has proven to be quite successful on galactic and also on intergalactic scales (Sanders & McGaugh 2002). However, not only galaxy size objects must be correctly explained by MOND. Objects with similar low accelerations, for which there is no need for additional, unseen matter such as GCs must be described correctly by this modified theory, as well. Hence, we have studied the outer halo GC Pal 14 to test whether modified or classical Newtonian dynamics applies. Pal 14 has an internal and external acceleration that are both significantly smaller than a_0. Also, the total acceleration of stars in Pal 14 is still significantly smaller than a_0 and therefore, Pal 14 is an excellent test object for the two theories.

We determined the radial velocities of 17 giant stars in Pal 14. Using the measurements of all 17 giants, we confirmed the cluster's mean radial velocity of (72.19 ± 0.18) km s^{-1} and measured a global line-of-sight velocity dispersion of (0.64 ± 0.15) km s^{-1} (see Section 4.3 for details). Excluding Star 15, we find a similar systemic velocity of Pal 14 of (72.28 ± 0.12) km s^{-1} and a lower velocity dispersion of (0.38 ± 0.12) km s^{-1}. These velocity dispersions lead to dynamical masses of 950^{+600}_{-400} $M_\odot$ in modified dynamics, and $8\,200^{+6000}_{-4000}$ $M_\odot$ in classical dynamics for the case without Star 15. In the case including Star 15 we expect total masses of Pal 14 of $2\,600^{+1400}_{-1200}$ $M_\odot$ in MOND, and $24\,000^{+11000}_{-10000}$ $M_\odot$ in classical dynamics.

The mass function of Pal 14 has a slope of $\alpha = 1.27 \pm 0.44$ in the mass range $0.53 M_\odot$ to $0.78 M_\odot$ and is thus flatter than the canonical mass function. This is consistent with the cluster being formed mass segregated with a normal (canonical) IMF but suffering major mass loss through gas expulsion (Marks et al. 2008). The HST image covers only 7% of the area within the cluster's tidal radius, but more than 2/3 of the area within the half-light radius. The observed total mass within the half-light radius with an extrapolation to lower masses with a Kroupa-like mass function is $\sim 6\,020$ $M_\odot$. If we extrapolate with a linearly declinig slope for masses $< 0.5 M_\odot$, we get a total mass within the half-light radius of $\sim 2\,930$ $M_\odot$. In both cases, these values are lower limits. By doubling the numbers to get a rough estimate of the total mass of Pal 14, we get numbers that are substantially higher than the predictions made by HBK09 for MOND. Hence, the cluster's current stellar content is an indication against MONDian dynamics, unless the cluster is on an eccentric orbit.

If Pal 14 is on a circular orbit, MOND cannot explain the low velocity dispersion and the measured mass simultaneously. If Pal 14 is on an eccentric orbit, the low velocity dispersion may still be a problem for MOND, but the measured mass function slope, being flatter than the canonical value, does not allow us to draw a definite conclusion. With the sample of BGK05 and the theoretical predictions of BGK05 and HBK09 we have a basis for extending the study to other outer halo, low-mass Galactic GCs to further refine and improve the tests of gravitational theory.

A

Extinction in the Fields around the Satellites

On the following pages we show the distribution of dust in the areas around the globular clusters (GCs) in our sample (Figure A.1-A.4). In Figure A.5 we show the identical plots for the areas around the dwarf spheroidal (dSph) galaxies. The extinction values are given in the SDSS database and are taken from Schlegel et al. (1998). In all five Figures the contours are the same as in Chapter 2 and 3. The background is the mean of the extinction values in the five filters *ugriz* as listed in the SDSS database. The values of the color scale are indicated for each satellite in the colorbar drawn on the left side of each field. For some cases no SDSS photometry was available for the crowded regions of GCs. In those cases we interpolated the given extinction values over the missing area. The mean values should only be used to guide the eye.

Figure A.1: Extinction maps of NGC 2419, NGC 4147, NGC 5024, and NGC 5053.
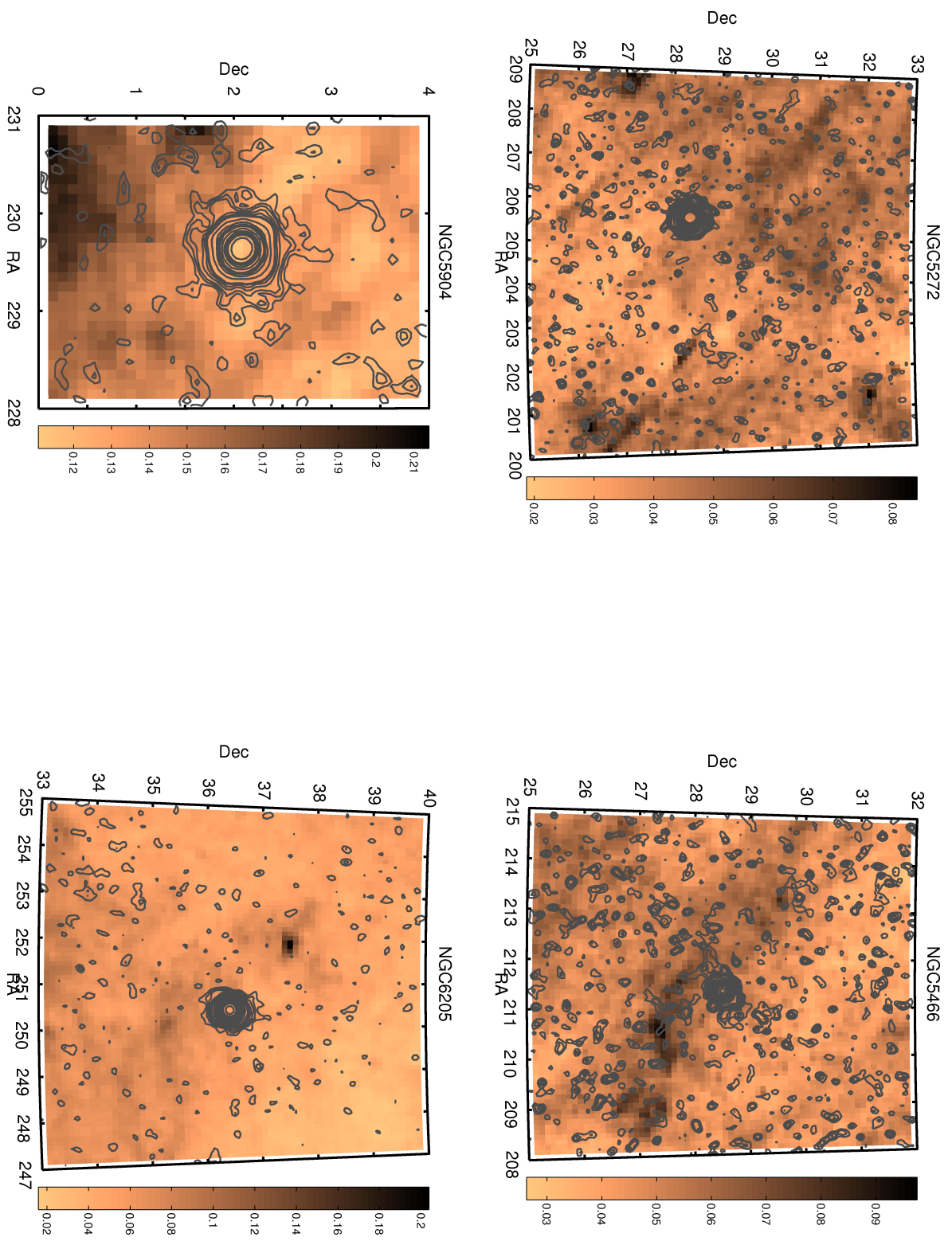
Figure A.2: Extinction maps of NGC 5272, NGC 5466, NGC 5904, and NGC 6205.

Figure A.3: Extinction maps of NGC 6341, NGC 7006, NGC 7078, and NGC 7089.
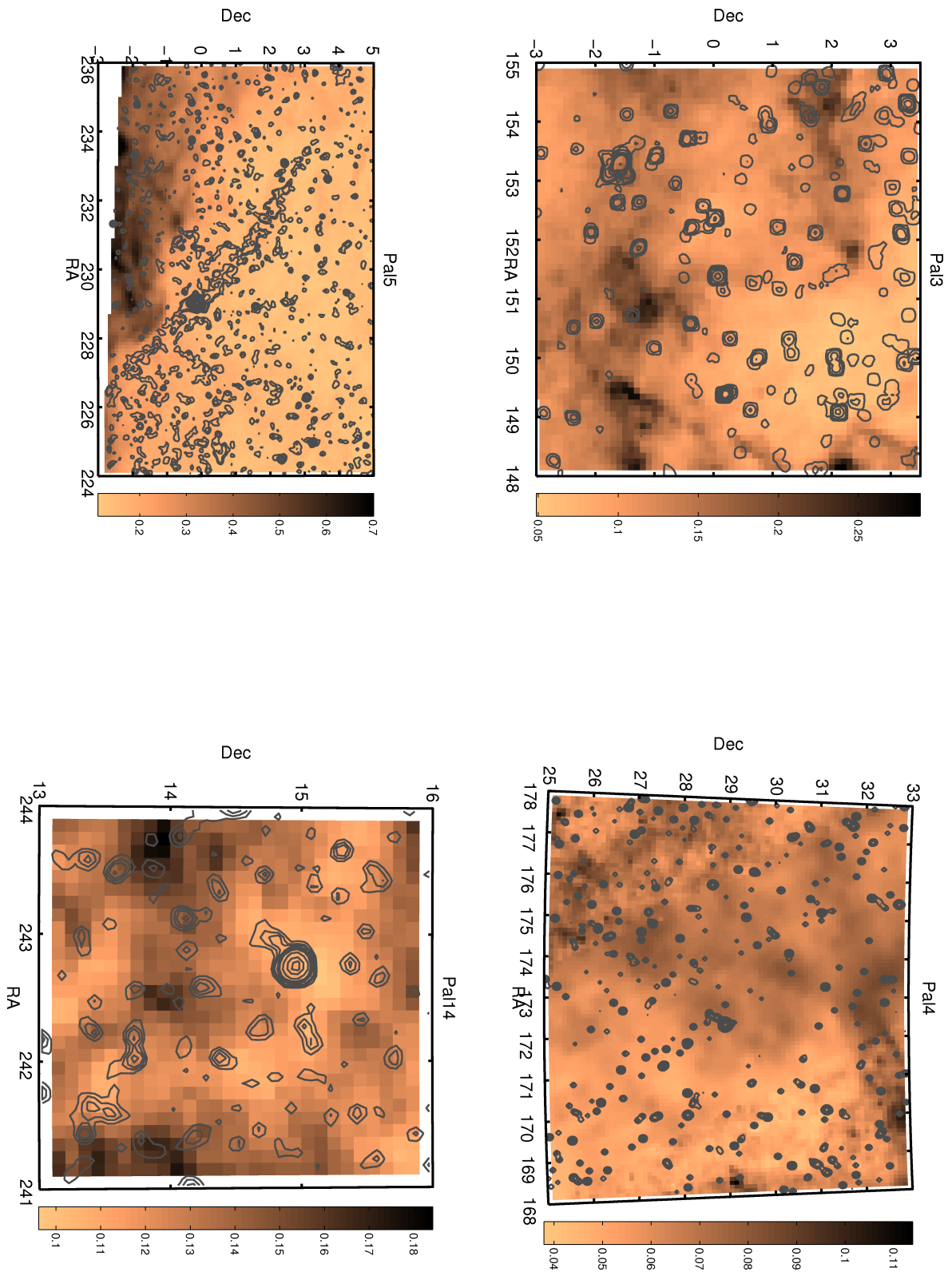
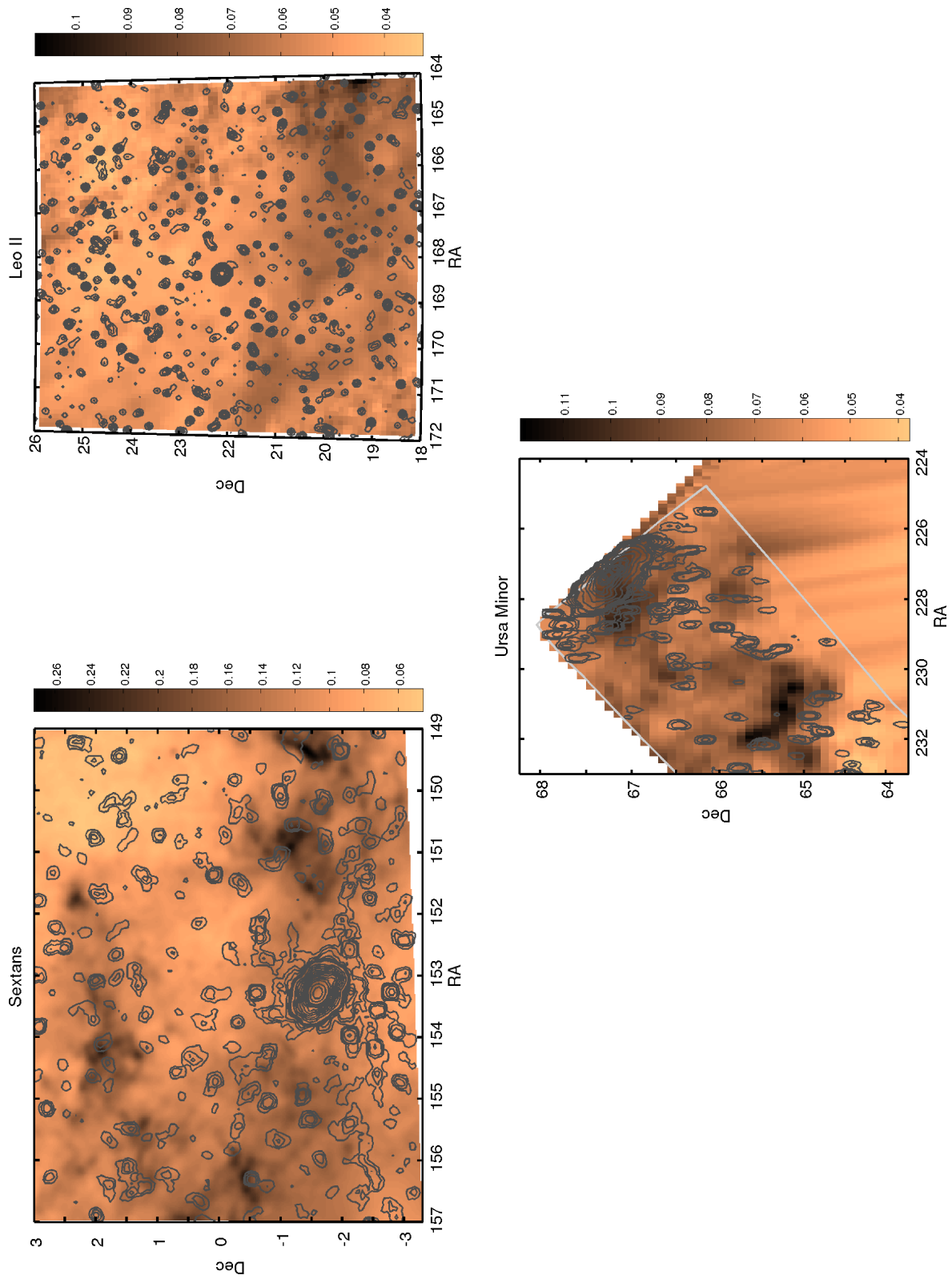Figure A.4: Extinction maps of Pal 3, Pal 4, Pal 5, and Pal 14.

Figure A.5: Extinction maps of Sextans, Leo II, and Ursa Minor.

Bibliography

Abazajian, K., et al. 2009, ApJS, 182, 543

Adelman-McCarthy, J. K., et al. 2008, ApJS, 175 297

Allen, C., Moreno, E., & Pichardo, B. 2006, ApJ, 652, 1150

An, D., et al. 2008, ApJS, 179, 326

Angus, G. W., Famaey, B., & Zhao, H. S. 2006, MNRAS, 371, 138

Angus, G. W., Shan, H. Y., Zhao, H. S., & Famaey, B. 2007, ApJ, 654, L13

Aaronson, M., et al. 1982, ApJS, 50, 241

Armandroff, T. E., Da Costa, G. S., & Zinn, R. 1992, AJ, 104, 164

Bagnulo, S., Jehin, E., Ledoux, C., Cabanac, R., Melo, C., Gilmozzi, R., & The ESO Paranal
    Science Operations Team 2003, The Messenger, 114, 10

Barmby, P., Boyer, M. L., Woodward, C. E., Gehrz, R. D., van Loon, J. T., Fazio, G. G.,
    Marengo, M., & Polomski, E. 2009, AJ, 137, 207

Baumgardt, H., & Makino, J. 2003, MNRAS, 340, 227

Baumgardt, H., Grebel, E. K., & Kroupa, P. 2005, MNRAS, 359, L1 [BGK05]

Baumgardt, H., & Kroupa, P. 2007, MNRAS, 380, 1589

Begeman, K. G., Broeils, A. H., & Sanders, R. H. 1991, MNRAS, 249, 523

Bertone, G., Hooper, D., & Silk, J. 2005, Phys. Rep., 405, 279

Bekenstein, J., & Milgrom, M. 1984, ApJ, 286, 7

Bekenstein, J. D. 2004, Physical Review D, 70, 083509

Bekenstein, J. 2006, Contemporary Physics, 47, 387

Bekenstein, J. D. 2009, arXiv:0901.1524

Bekki, K., & Freeman, K. C. 2003, MNRAS, 346, L11

Bellazzini, M., Ibata, R., Ferraro, F. R., & Testa, V. 2003, A&A, 405, 577

Bellazzini, M., Ferraro, F. R., & Ibata, R. 2003, AJ, 125, 188

Bellazzini, M., Gennari, N., Ferraro, F. R., & Sollima, A. 2004, MNRAS, 354, 708

Bellazzini, M. 2007, A&A, 473, 171

Belokurov, V., et al. 2006, ApJ, 642, L137

Belokurov, V., et al. 2006, ApJ, 647, L111

Belokurov, V., Evans, N. W., Irwin, M. J., Hewett, P. C., & Wilkinson, M. I. 2006, ApJ, 637,
    L29

Belokurov, V., et al. 2007, ApJ, 654, 897

Bizyaev, D., et al. 2006, AJ, 131, 1784

Borissova, J., & Spassova, N. 1995, A&AS, 110, 1

Brodie, J. P., & Strader, J. 2006, ARA&A, 44, 193

Bruneton, J.-P., Liberati, S., Sindoni, L., & Famaey, B. 2009, Journal of Cosmology and Astro-Particle Physics, 3, 21

Capuzzo Dolcetta, R., Di Matteo, P., & Miocchi, P. 2005, AJ, 129, 1906

Carney, B. W. 1996, PASP, 108, 900

Carney, B. W., Latham, D. W., Stefanik, R. P., Laird, J. B., & Morse, J. A. 2003, AJ, 125, 293

Carraro, G. 2009, AJ, 137, 3809

Casetti-Dinescu, D. I., Girard, T. M., Majewski, S. R., Vivas, A. K., Wilhelm, R., Carlin, J. L., Beers, T. C., & van Altena, W. F. 2009, ApJ, 701, L29

Ciotti, L., & Binney, J. 2004, MNRAS, 351, 285

Chen, D.-M. 2008, Journal of Cosmology and Astro-Particle Physics, 1, 6

Chun, S.-H., et al. 2010, AJ, 139, 606

Clowe, D., Bradač, M., Gonzalez, A. H., Markevitch, M., Randall, S. W., Jones, C., & Zaritsky, D. 2006, ApJ, 648, L109

Coleman, M. G., Jordi, K., Rix, H.-W., Grebel, E. K., & Koch, A. 2007, AJ, 134, 1938

Combes, F., Leon, S., & Meylan, G. 1999, A&A, 352, 149

Côté, P., Djorgovski, S. G., Meylan, G., Castro, S., & McCarthy, J. K. 2002, ApJ, 574, 783

Crane, J. D., Majewski, S. R., Rocha-Pinto, H. J., Frinchaboy, P. M., Skrutskie, M. F., & Law, D. R. 2003, ApJ, 594, L119

Da Costa, G. S., & Armandroff, T. E. 1995, AJ, 109, 2533

Dalessandro, E., Beccari, G., Lanzoni, B., Ferraro, F. R., Schiavon, R., & Rood, R. T. 2009, ApJS, 182, 509

Dehnen, W., Odenkirchen, M., Grebel, E. K., & Rix, H.-W. 2004, AJ, 127, 2753

Dekker, H., D'Odorico, S., Kaufer, A., Delabre, B., & Kotzlowski, H. 2000, Proc. SPIE, 4008, 534

De Marchi, G., Paresce, F., & Pulone, L. 2007, ApJ, 656, L65

Dinescu, D. I., Girard, T. M., & van Altena, W. F. 1999, AJ, 117, 1792

Dinescu, D. I., Majewski, S. R., Girard, T. M., & Cudworth, K. M. 2001, AJ, 122, 1916

Dolphin, A. E. 2000, PASP, 112, 1383

Dotter, A., Chaboyer, B., Jevremović, D., Baron, E., Ferguson, J. W., Sarajedini, A., & Anderson, J. 2007, AJ, 134, 376

Dotter, A., Sarajedini, A., & Yang, S.-C. 2008, AJ, 136, 1407

Einstein, A. 1916, Annalen der Physik, 354, 769

Elmegreen, B. G. 2009, Proc. 4th Spitzer Science Center Conf.: The Evolving ISM in the Milky Way and Nearby Galaxies, ed. K. Sheth et al., E14, http://ssc.spitzer.caltech.edu/mtgs/ismevolv

Feix, M., Fedeli, C., & Bartelmann, M. 2008, A&A, 480, 313

Fellhauer, M., et al. 2006, ApJ, 651, 167

Fellhauer, M., Evans, N. W., Belokurov, V., Wilkinson, M. I., & Gilmore, G. 2007, MNRAS, 380, 749

Fleck, J.-J., & Kuhn, J. R. 2003, ApJ, 592, 147

Forbes, D. A., & Bridges, T. 2010, MNRAS, 404, 1203

Fukugita, M., Ichikawa, T., Gunn, J. E., Doi, M., Shimasaku, K., & Schneider, D. P. 1996, AJ, 111, 1748

Fukushige, T., & Heggie, D. C. 2000, MNRAS, 318, 753

Geha, M., Willman, B., Simon, J. D., Strigari, L. E., Kirby, E. N., Law, D. R., & Strader, J. 2009, ApJ, 692, 1464

Gentile, G., Famaey, B., Combes, F., Kroupa, P., Zhao, H. S., & Tiret, O. 2007, A&A, 472, L25

Geyer, M. P., & Burkert, A. 2001, MNRAS, 323, 988

Girardi, L., Groenewegen, M. A. T., Hatziminaoglou, E., & da Costa, L. 2005, A&A, 436, 895

Gnedin, O. Y., & Ostriker, J. P. 1997, ApJ, 474, 223

Glatt, K., et al. 2008a, AJ, 135, 1106

Glatt, K., et al. 2008b, AJ, 136, 1703

Grcevich, J., & Putman, M. E. 2009, ApJ, 696, 385

Grebel, E. K. 1997, Reviews in Modern Astronomy, 10, 29

Grebel, E. K., Odenkirchen, M., & Harbeck, D. 2002, Bulletin of the American Astronomical Society, 34, 717 009, ApJ, 696, 385

Grebel, E. K., & Gallagher, J. S., III 2004, ApJ, 610, L89

Grillmair, C. J., Freeman, K. C., Irwin, M., & Quinn, P. J. 1995, AJ, 109, 2553

Grillmair, C. J., & Dionatos, O. 2006, ApJ, 641, L37

Grillmair, C. J., & Johnson, R. 2006, ApJ, 639, L17

Gunn, J. E., et al. 1998, AJ, 116, 3040

BIBLIOGRAPHY

Gunn, J.E., Siegmund, W.A., Mannery, E.J., Owen, R.E., et al. 2006, AJ, 131

Habing, H. J., & Olofsson, H. 2003, Asymptotic giant branch stars, by Harm J. Habing and Hans Olofsson. Astronomy and Astrophysics Library, New York, Berlin: Springer, 2003, 31

Haghi, H., Baumgardt, H., Kroupa, P., Grebel, E. K., Hilker, M., & Jordi, K. 2009, MNRAS, 395, 1549 [HBK09]

Harbeck, D., et al. 2001, AJ, 122, 3092

Harris, W. E., & van den Bergh, S. 1984, AJ, 89, 1816

Harris, W. E. 1996, AJ, 112, 1487

Harris, W. E. 2001, Saas-Fee Advanced Course 28: Star Clusters, 223

Hartwick, F. D. A., & Sargent, W. L. W. 1978, ApJ, 221, 512

Heggie, D., & Hut, P. 2003, The Gravitational Million-Body Problem: A Multidisciplinary Approach to Star Cluster Dynamics, by Douglas Heggie and Piet Hut. Cambridge University Press, 2003, 372 pp.,

Hilker, M. 2006, A&A, 448, 171

Hinshaw, G., et al. 2009, ApJS, 180, 225

Hodge, P. W. 1961, AJ, 66, 83

Hogg, D.W., Finkbeiner, D.P., Schlegel, D.J., and Gunn, J.E. 2001, AJ, 122, 2129

Holland, S., & Harris, W. E. 1992, AJ, 103, 131

Holtzman, J. A., Burrows, C. J., Casertano, S., Hester, J. J., Trauger, J. T., Watson, A. M., & Worthey, G. 1995, PASP, 107, 1065

Ibata, R. A., Gilmore, G., & Irwin, M. J. 1994, Nature, 370, 194

Inman, R. T., & Carney, B. W. 1987, AJ, 93, 1166

Irwin, M. J., Bunclark, P. S., Bridgeland, M. T., & McMahon, R. G. 1990, MNRAS, 244, 16P

Irwin, M., & Hatzidimitriou, D. 1995, MNRAS, 277, 1354

Ivanov, V. D., Kurtev, R., & Borissova, J. 2005, A&A, 442, 195

Ivezic, Z., Lupton, R.H., Schlegel, D., et al. 2004, AN, 325, 583

Kaplinghat, M., & Strigari, L. E. 2008, ApJ, 682, L93

King, I. 1962, AJ, 67,471

King, I. R. 1966, AJ, 71, 64

Kiss, L. L., Székely, P., Bedding, T. R., Bakos, G. Á., & Lewis, G. F. 2007, ApJ, 659, L129

Klessen, R. S., & Kropua, P. 1998, ApJ, 498, 143

Klessen, R. S., & Zhao, H. 2002, ApJ, 566, 838

Klessen, R. S., Grebel, E. K., & Harbeck, D. 2003, ApJ, 589, 798

Kleyna, J., Wilkinson, M. I., Evans, N. W., Gilmore, G., & Frayn, C. 2002, MNRAS, 330, 792

Kleyna, J. T., Wilkinson, M. I., Gilmore, G., & Evans, N. W. 2003, ApJ, 588, L21

Kleyna, J. T., Wilkinson, M. I., Evans, N. W., & Gilmore, G. 2004, MNRAS, 354, L66

Koch, A., Grebel, E. K., Odenkirchen, M., Martínez-Delgado, D., & Caldwell, J. A. R. 2004, AJ, 128, 2274

Koch, A., Grebel, E. K., Kleyna, J. T., Wilkinson, M. I., Harbeck, D. R., Gilmore, G. F., Wyse, R. F. G. & Evans, N. W. 2006, AJ, 133, 270

Koch, A., Kleyna, J. T., Wilkinson, M. I., Grebel, E. K., Gilmore, G. F., Evans, N. W., Wyse, R. F. G., & Harbeck, D. R. 2007, AJ, 134, 566

Koekemoer, A. M., Fruchter, A. S., Hook, R. N., & Hack, W. 2002, The 2002 HST Calibration Workshop : Hubble after the Installation of the ACS and the NICMOS Cooling System, S. Arribas, A. Koekemoer, & B. Whitmore. Baltimore, MD: Space Telescope Science Institute, p.337

Komatsu, E., et al. 2009, ApJS, 180, 330

Komiyama, Y., et al. 2007, AJ, 134, 835

Kowalski, M., et al. 2008, ApJ, 686, 749

Kroupa, P. 1997, New Astronomy, 2, 139

Kroupa, P. 2001, MNRAS, 322, 231

Kroupa, P. 2002, Science, 295, 82

Küpper, A. H. W., MacLeod, A., & Heggie, D. C. 2008, MNRAS, 387, 1248

Kurtev, R., Ivanov, V. D., Borissova, J., & Ortolani, S. 2008, A&A, 489, 583

Lauchner, A., Powell, W. L. J., & Wilhelm, R. 2006, ApJ, 651, L33

Law, D. R., & Majewski, S. R. 2010, arXiv:1005.5390

Lee, M. G., et al. 2003, AJ, 126, 2840

Lehmann, I., & Scholz, R.-D. 1997, A&A, 320, 776

Leon, S., Meylan, G., & Combes, F. 2000, A&A, 359, 907

Lupton, R. H., Ivezic, Z., Gunn, J. E., Knapp, G., Strauss, M. A., & Yasuda, N. 2002, Proc. SPIE, 4836, 350

Madau, P., Diemand, J., & Kuhlen, M. 2008, ApJ, 679, 1260

Majewski, S. R., & Cudworth, K. M. 1993, PASP, 105, 987

Majewski, S. R., Skrutskie, M. F., Weinberg, M. D., & Ostheimer, J. C. 2003, ApJ, 599, 1082

Marín-Franch, A., et al. 2009, ApJ, 694, 1498

Marks, M., Kroupa, P., & Baumgardt, H. 2008, MNRAS, 386, 2047

Martin, N. F., de Jong, J. T. A, & Rix, H. W. 2008, ApJ, 684, 1075

Martínez-Delgado, D., Alonso-García, J., Aparicio, A., & Gómez-Flechoso, M. A. 2001, ApJ, 549, L63

Martínez Delgado, D., Dinescu, D. I., Zinn, R., Tutsoff, A., Côté, P.,& Boyarchuck, A. 2004, Satellites and Tidal Streams, 327, 255

Mateo, M. L. 1998, ARA&A, 36, 435

McLaughlin, D. E., & van der Marel, R. P. 2005, ApJS, 161, 304

Mighell, K. J., & Burke, C. J. 1999, AJ, 118, 366

Milgrom, M. 1983, ApJ, 270, 365

Milgrom, M. 1983, ApJ, 270, 371

Moffat, J. W. 2005, Journal of Cosmology and Astro-Particle Physics, 5, 3

Moffat, J. W., & Toth, V. T. 2008, ApJ, 680, 1158 Aaronson, M., & Peterson, R. C. 1986, ApJ, 302, L45

Montuori, M., Capuzzo-Dolcetta, R., Di Matteo, P., Lepinette, A., & Miocchi, P. 2007, ApJ, 659, 1212

Moore, B. 1996, ApJ, 461, L13

Muñoz, R. R., et al. 2005, ApJ, 631, L137

Muñoz, R. R., et al. 2006, ApJ, 649, 201

Muñoz, R. R., Majewski, S. R., & Johnston, K. V. 2008, ApJ, 679, 346

Noyola, E., & Gebhardt, K. 2006, AJ, 132, 447

Odenkirchen, M., Brosche, P., Geffert, M., & Tucholke, H.-J. 1997, New Astronomy, 2, 477

Odenkirchen, M., et al. 2001, AJ, 122, 2538

Odenkirchen, M., et al. 2001, ApJ, 548, L165

Odenkirchen, M., Grebel, E. K., Dehnen, W., Rix, H.-W., & Cudworth, K. M. 2002, AJ, 124, 1497

Odenkirchen, M., et al. 2003, AJ, 126, 2385

Odenkirchen, M., Grebel, E. K., Kayser, A., Rix, H.-W., & Dehnen, W. 2009, AJ, 137, 3378

Olszewski, E. W., & Aaronson, M. 1985, AJ, 90, 2221

Palma, C., Majewski, S. R., Siegel, M. H., Patterson, R. J., Ostheimer, J. C., & Link, R. 2003, AJ, 125, 1352

Paresce, F., & De Marchi, G. 2000, ApJ, 534, 870

Peebles, P. J. E. 1995, ApJ, 119, 52

Peñarrubia, J., Navarro, J. F., & McConnachie, A. W. 2008, ApJ, 673, 226

Peñarrubia, J., Navarro, J. F., McConnachie, A. W., & Martin, N. F. 2008, arXiv:0811.1579

Percival, W. J., Cole, S., Eisenstein, D. J., Nichol, R. C., Peacock, J. A., Pope, A. C., & Szalay, A. S. 2007, MNRAS, 381, 1053

Piatek, S., Pryor, C., Bristow, P., Olszewski, E. W., Harris, H. C., Mateo, M., Minniti, D., & Tinney, C. G. 2005, AJ, 130, 95

Pier, J.R., Munn, J.A., Hindsley, R.B., Hennessy, G.S., Kent, S.M., Lupton, R.H., and Ivezic, Z. 2003, AJ, 125, 1559

Piotto, G. 2009, arXiv:0902.1422

Praagman, A. K., Hurley, J. R., & Power, C. 2009, arXiv:0905.1593

Pryor, C., & Meylan, G. 1993, Structure and Dynamics of Globular Clusters, 50, 357

Ratnatunga, K. U., & Bahcall, J. N. 1985, ApJS, 59, 63

Richer, H. B., et al. 2004, AJ, 127, 2771

Richer, H. B., et al. 2008, AJ, 135, 2141

Robin, A. C., Reylé, C., Derrière, S., & Picaud, S. 2003, A&A, 409, 523

Rockosi, C. M., et al. 2002, AJ, 124, 349

Rosenberg, A., Saviane, I., Piotto, G., Aparicio, A., & Zaggia, S. R. 1998, AJ, 115, 648

Rubin, V. C., Thonnard, N. T., & Ford, W. K., Jr. 1982, AJ, 87, 477

Salpeter, E. E. 1955, ApJ, 121, 161

Sanders, R. H., & McGaugh, S. S. 2002, ARA&A, 40, 263

Sarajedini, A. 1997, AJ, 113, 682

Sarajedini, A., et al. 2007, AJ, 133, 1658

Scarpa, R., Marconi, G., Gilmozzi, R., & Carraro, G. 2007, The Messenger, 128, 41

Scholz, R.-D., Irwin, M., Odenkirchen, M., & Meusinger, H. 1998, A&A, 333, 531

Schlegel, D. J., Finkbeiner, D. P., & Davis, M. 1998, ApJ, 500, 525

Schneider, D. P., et al. 2007, AJ, 134, 102

Scholz, R.-D., & Irwin, M. J. 1994, Astronomy from Wide-Field Imaging, 161, 535

Ségall, M., Ibata, R. A., Irwin, M. J., Martin, N. F., & Chapman, S. 2007, MNRAS, 375, 831

Simon, J. D., & Geha, M. 2007, ApJ, 670, 313

Smecker-Hane, T. A., Stetson, P. B., Hesser, J. E., & Vandenberg, D. A. 1996, From Stars to Galaxies: the Impact of Stellar Physics on Galaxy Evolution, 98, 328

Smith, J.A., Tucker, D.L., Kent, S.M., et al. 2002, AJ, 123, 2121

Smolčić, V., Zucker, D. B., Bell, E. F., Coleman, M. G., Rix, H. W., Schinnerer, E., Ivezić, Ž., & Kniazev, A. 2007, AJ, 134, 1901

Sofue, Y., & Rubin, V. 2001, ARA&A, 39, 137

Sohn, Y.-J., et al. 2003, AJ, 126, 803

Spitzer, L. 1987, Princeton,NJ, Princeton University Press, 1987, 191 p.,

Taoso, M., Bertone, G., & Masiero, A. 2008, Journal of Cosmology and Astro-Particle Physics, 3, 22

Testa, V., Zaggia, S. R., Andreon, S., Longo, G., Scaramella, R., Djorgovski, S. G., & de Carvalho, R. 2000, A&A, 356, 127

Tonry, J., & Davis, M. 1979, AJ, 84, 1511

Trager, S. C., King, I. R., & Djorgovski, S. 1995, AJ, 109, 218

Tucker, D., Kent, S., Richmond, M.W., et al. 2006, AN, 327, 821

Tully, R. B., & Fisher, J. R. 1977, A&A, 54, 661

van den Bergh, S. 1993, Structure and Dynamics of Globular Clusters, 50, 1

van den Bergh, S. 1999, A&A Rev., 9, 273

Vesperini, E., & Heggie, D. C. 1997, MNRAS, 289, 898

Vivas, A. K., & Zinn, R. 2006, AJ, 132, 714

Vogt, S. S., et al. 1994, Proc. SPIE, 2198, 362

Walker, M. G., Mateo, M., Olszewski, E. W., Pal, J. K., Sen, B., & Woodroofe, M. 2006, ApJ, 642, L41

Walker, M. G., Mateo, M., & Olszewski, E. W. 2008, ApJ, 688, L75

Willman, B., et al. 2006, arXiv:astro-ph/0603486

Wilkinson, M. I., Kleyna, J. T., Evans, N. W., Gilmore, G. F., Irwin, M. J., & Grebel, E. K. 2004, ApJ, 611, L21

White, R. E., & Shawl, S. J. 1987, ApJ, 317, 246

Xue, X. X., et al. 2008, ApJ, 684, 1143

York, D.G., Adelman, J., Anderson, J.E., et al. 2000, AJ, 120, 1579

Zhao, H. 2005, IAU Colloq. 198: Near-fields cosmology with dwarf elliptical galaxies, ed. H. Jerien & B. Binggeli (Cambridge Univ. Press) 189

Zinn, R. 1985, ApJ, 293, 424

Zwicky, F. 1933, Helvetica Physica Acta, 6, 110

Zwicky, F. 1937, ApJ, 86, 217

Acknowledgments

"I can no other answer make, but, thanks, and thanks."
William Shakespeare

Als erstes möchte ich **Eva Grebel** danken, dafür, dass sie mir die Möglichkeit offeriert hat, die Doktorarbeit am Astronomischen Institut in Basel zu schreiben und mir mit Rat die ganzen vier Jahre zur Seite gestanden ist. Ich sage auch danke, dass ich an soviele Konferenzen und Schulen reisen durfte, um meine Arbeit vorzustellen und viele neue Eindrücke zu gewinnen (nicht nur astronomische).

Ich bedanke mich bei **Michael Hilker**, dass er bereit war Co-Referent zu sein für meine Arbeit. Ich durfte zwei intensive Woche bei der ESO und in Bonn verbringen, in denen ich viel über unsere 14 Palomar 14 Sterne und ihre Spektren lernte.

Herzlichen Dank an **Andreas Tammann**, dass er den Vorsitz meiner Prüfung übernommen hat.

Es wurden mehr als 4 Jahre, in denen wir ein Büro teilten. Danke **Katharina**, es war eine geniale Zeit. Ohne dich wäre Heidelberg nicht so angenehm gewesen. Auch an unsere zahlreichen gemeinsamen Konferenzen, Schulen und Reisen denke ich gerne zurück.

A great thanks goes to all the people at ARI in Heidelberg with whom I spent a great time: Thanks to **Denija Crnojevic** for reading many parts of the thesis. Thanks to **Stefano Pasetto**, for initiating the trip to China. Thanks to **Sarah Martell** for reading parts of my thesis and to **Sonia Duffau**, and **Shoko Jin** for being models of how post-docs can be and live. Danke an **Raoul Haschke** und **Johannes Ludwig** für all ihre Fragen und kurzweiligen Diskussionen. Danke an **Matthias Frank** und an **Fabian Zimmer** für eine angenehme Zeit im Büro.

Ich danke auch allen am (ehemaligen) Astronomischen Institut in Basel für eine wunderbare Zeit und für die Unterstützung, die ich auch heute noch erfahre: **Thorsten Lisker, Wolfgang Löffler, Bruno Binggeli, Marco Longhitano** und **Tatjana Hascher**.

Von ganzem Herzen danke ich auch meinen **Eltern**, meiner Schwester **Silvia**, und meinem **Gotti**. Ohne Euch hätte ich nicht Physik studieren und in Astronomie doktorieren können, einfach weil es mir Spass macht. Ihr zeigt immer Interesse an allem was ich mache und unterstützt mich damit sehr!

Ein grosses Dankeschön an **Gerold Betschart**, dass du da in mein Leben getreten bist bedeutet mir sehr, sehr viel.

———

Curriculum Vitae

Education

08/2005 – 08/2009	**PhD in Astronomy** University of Basel Grade: **magna cum laude** Thesis: "Satellites as Probes of Dark Matter and Gravitational Theories" Supervisor: Prof. Dr. Eva K. Grebel
10/2000 – 07/2005	**Diploma in Theoretical Physics**, diploma thesis in astronomy University of Basel Grade of diploma thesis: **6** Grade of exams: **5.3** Thesis: "Empirical Color Transformations between SDSS Photometry and other Photometric Systems" Supervisor: Prof. Dr. Eva K. Grebel
08/1996 – 07/1997	**Exchange year** High School, San Antonio, Texas, USA
08/1995 – 12/1999	**Matura** High School Liestal
08/1990 – 07/1995	Middle School, Sissach
04/1985 – 07/1990	Elementary School, Kaiseraugst (3 years) and Zunzgen (2 years)

During my studies I heard lectures by
Prof. Dr. N. A'Campo, Prof. Dr. C. Bandle, G. Baur, W. Belzig, Prof. Dr. B. Binggeli, Prof. Dr. C. Bruder, Prof. Dr. R. Buser, Prof. Dr. O. Gerhard, Prof. Dr. E. K. Grebel, Prof. Dr. M. Grote, Prof. Dr. H.-J. Güntherodt, Dr. H.-J. Hug, Prof. Dr. H.-C. Im Hof, Prof. Dr. D. Loss, PD Dr. H. Mühry, PD Dr. T. Rauscher, W. Reichel, Dr. J. Schliemann, Prof. Dr. C. Schönenberger, Prof. Dr. I. Sick, Prof. Dr. G.-A. Tammann, Prof. Dr. L. Tauscher, Prof. Dr. F. Thielemann, Prof. Dr. D. Trautmann, H. Walser.

Refereed Publications

K. Jordi, E. K. Grebel, B. Yanny
Search for Extratidal Features around Ursa Minor and Sextans dwarf spheroidal galaxy in the Sloan Digital Sky Survey
to be submitted to A&A

K. Jordi, E. K. Grebel
Search for Extratidal Features Around 17 Globular Clusters in the Sloan Digital Sky Survey
accepted by A&A

K. Jordi, E. K. Grebel, M. Hilker, H. Baumgardt, M .Frank, P. Kroupa, H. Hagi, P. Coté, and S. G. Djorgovski
Testing Fundamental Physics with Distant Star Clusters: Analysis of Observational Data on Palomar 14
2008, AJ, 137, 4586 - 4596

H. Hagi, H. Baumgardt, P. Kroupa, E. K. Grebel, M. Hilker, and **K. Jordi**
Testing Fundamental Physics with Distant Star Clusters: Theoretical Models for Pressure Supported Stellar Systems
2008, MNRAS, 395, 1549 - 1557

M. G. Coleman, **K. Jordi**, H.-W. Rix, E. K. Grebel, A. Koch
A Wide-Field View of Leo II: A Structural Analysis Using the Sloan Digital Sky Survey
2007, AJ, 134, 1938 - 1951

K. Jordi, E. K. Grebel, K. Ammon
Empirical Color Transformations between SDSS Photometry and other Photometric Systems
2006, A&A, 460, 339 - 347

Unrefereed Publications

Katrin Jordi, Eva K. Grebel, Michael Hilker, Holger Baumgardt, Pavel Kroupa, Matthias Frank
Classical or Modified Newtonian Dynamics: Testing MOND in Palomar 14
Abstract for AAS 211th Meeting, Austin, January 2008

K. Jordi, E. K. Grebel
The Search for Tidal Tails of Globular Clusters: NGC 4147
Proceedings of "Globular Clusters – Guides to Galaxies", Concepcion, Chile, March, 2006, ESO Astrophysics Symposia

K. Jordi, E. K. Grebel, K. Ammon
Empirical Color Transformations between SDSS Photometry and other Photometric Systems
2005, AN, 326